

**PREPARATION, CHARACTERIZATION AND  
CATALYTIC APPLICATIONS OF SOME MIXED  
METAL OXIDE CATALYSTS**

**A THESIS  
SUBMITTED TO THE  
UNIVERSITY OF POONA  
FOR THE DEGREE OF  
DOCTOR OF PHILOSOPHY  
(IN CHEMISTRY)**

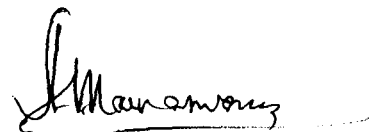
**BY  
A. KESHAVARAJA  
M. Sc**

**CATALYSIS AND INORGANIC CHEMISTRY DIVISION  
NATIONAL CHEMICAL LABORATORY  
PUNE - 411 008 (INDIA)**

**MARCH 1996**

## **CERTIFICATE**

Certified that the work incorporated in the thesis entitled "**PREPARATION, CHARACTERIZATION AND CATALYTIC APPLICATIONS OF SOME MIXED METAL OXIDE CATALYSTS**" submitted by Shri. **A. Keshavaraja** for the degree of Doctor of Philosophy was carried out by the candidate under my supervision in the National Chemical Laboratory, Pune. Such material as has been obtained from other sources has been duly acknowledged in the thesis.



**Dr. A. V. Ramaswamy**

**(Research guide)**

**Dr. A. V. Ramaswamy**

**Head, Catalysis & Inorganic Chemistry Division**

डॉ. आ. व. रामस्वामी

प्रमुख, उत्प्रेरण एवं अकार्बनिक रसायन विभाग

National Chemical Laboratory

Pune-411 008, INDIA

राष्ट्रीय रासायनिक प्रयोगशाला

पुणे-411 008, भारत

## ACKNOWLEDGMENT

*I am deeply indebted to Dr. A. V. Ramaswamy, Deputy Director and Head, Catalysis Division, National Chemical Laboratory, Pune, for giving me an opportunity to work under his inspiring guidance, for my Ph.D degree. But for his guidance I would not have been able to complete the research work. I am particularly thankful to him for giving me full liberty to work out my ideas.*

*I shall be failing in my duty if I do not thank Dr. P. Ratnasamy, Director, NCL, Pune for permitting me to present this work in the form of a thesis. I am greatly indebted to him for his personal interest and concern in my work.*

*I am grateful to Dr. P. Ganguly for stimulating the creative urge in me. I am also grateful to Dr. S. Sivasanker and Dr. S. G. Hegde who took keen interest in my work and helped me at various stages. They have left an indelible imprints in my mind.*

*I owe an enormous debt of gratitude to Dr. K. Vijayamohanan for throwing valuable light on many aspects of my problem in numerous discussions.*

*I shall always remember Dr. K. R. Srinivasan, for showing how valuable is perfection, and giving guidance on how to communicate effectively.*

*I am thankful to Dr. (Mrs.) Veda Ramaswamy for her wise counsel and for motivating me. I shall ever relish the privilege of working with her.*

*I acknowledge with gratitude for the cooperation that I received from my senior colleagues, Dr. H. S. Soni, Mrs. Nalini Jacob, Miss S. Awate, Miss Agashe, Miss Violet and others*

*I am very much thankful to Dr. M.P. Kulkarni, Dr. V.G.Neurgaokar, Dr. B.R.K. Murthy for their support. I am also grateful to Dr. B. S. Rao, Dr. C. Gopinathan and Dr (Mrs.) S. Gopinathan, for their timely advice.*

*My thanks are also due to Dr. S. K. Date, Dr. S. Badarinarayanan, Dr. Murali Sastry, Dr. P. Singh, Dr. R. F. Shinde, and all colleagues of SIL for the help that they gave from time to time.*

*The technical help rendered by Mr. Ramakrishnan, Mr. Purushothaman, Mr. T. Koshy, Mr. T.A.B. Mulla, Mrs. Jyoti, Mr. Mannakatti and Mr. Jadhav, is gratefully acknowledged.*

*My special thanks are due to Mr. Suhas, Mr. C. U. Dinesh, Mr. V. R. Hegde and Mr. Godwin for their enthusiastic help.*

*I am thankful to all my friends: Bhat, Sudhakar, Sathyam, Hari, Anuj, Ramesh, Eric, Kannan, Neepa, Ravi, Raghavan, Deba, Puyam, Rajib, Selvam, Sasi, Naval, Asim, Venkat, Tapas, Tapan, Sahida, Selvaraj, Vinod, Krishanu, Mayya, Anil, Ashok, Robert, Karuna, Bhavana, Ranjeet, Sabde and all the scientific staff of catalysis division, whose support invigorated me.*

*Financial help rendered by Council of Scientific and Industrial Research, New Delhi is gratefully acknowledged.*

*A. Keshavaraja*  
(A. KESHAVARAJA)

# INDEX

Sl. No.	Description	Page No
<b>1</b>	<b>INTRODUCTION</b>	<b>1-24</b>
1.1	Introduction	2
1.2	Classification of Catalysts	3
1.3	Metal oxides as Catalysts	5
1.4	Catalyst Preparation	10
1.5	Strategies for Catalyst Development	14
1.6	Systems chosen in the present study	14
1.7	Objective and Scope	18
<b>2</b>	<b>CHARACTERIZATION TECHNIQUES</b>	<b>25-75</b>
2.1	X-Ray Diffraction	26
2.2	X-ray Scattering Techniques	29
2.3	X-ray Fluorescence Spectroscopy	32
2.4	X-ray Photoelectron Spectroscopy	34
2.5	UV-Vis Spectroscopy	38
2.6	Infrared Spectroscopy	39
2.7	Laser Raman Spectroscopy	45
2.8	Nuclear Magnetic Resonance Spectroscopy	47
2.9	Scanning Electron Microscopy	50
2.10	Transmission Electron Microscopy	52
2.11	Thermal Analysis	55
2.12	Temperature Programmed Reduction	56
2.13	N <sub>2</sub> Adsorption Methods	58
2.14	Sorption Studies	63
2.15	Particle Size Analysis	64
2.16	Cyclic Voltammetry	65
2.17	Gas-liquid Chromatography	67
2.18	Catalytic Test Reactors	68
<b>3</b>	<b>NOVEL FLUORITE TYPE OXIDES AS OXIDATION CATALYSTS</b>	<b>76-164</b>
3.1	Introduction	77
3.2	Mn-stabilized Zirconia	89

3.2.1.	Introduction	89
3.2.2.	A brief literature overview	90
3.2.3.	Experimental	91
3.2.4.	Results and Discussion	94
3.2.5.	Catalytic Activity	129
3.2.6.	General Discussiion	145
3.3	3d-Transition metal oxide-stabilized Zirconia	147
3.3.1.	Introduction	147
3.3.2.	Experimental	148
3.3.3.	Results and Discussion	149
3.3.4.	Catalytic Activity	154
3.4	Summary and Conclusion	159
<b>4</b>	<b>SOL-GEL DERIVED SUPPORTED COPPER CATALYSTS</b>	<b>166-200</b>
4.1	Introduction	166
4.2	Experimental	177
4.3	Results and Discussion	179
4.4	Summary and Conclusion	196
<b>5</b>	<b>SOL-GEL DERIVED METALLOSILICATE CATALYSTS</b>	<b>201-294</b>
5.1	Introduction	203
5.2	Amorphous titanosilicates prepared at different pH	206
5.2.1	Why at Different pH ?	206
5.2.2.	Experimental	206
5.2.3.	Results and Discussion	208
5.3	Amorphous titanosilicates prepared at Neutral pH	227
5.3.1.	Why Neutral medium ?	227
5.3.2.	Experimental	227
5.3.3.	Results and Discussion	230
5.3.4.	Catalytic Activity	255
5.4	Amorphous Aluminosilicates	260
5.4.1.	Why Aluminosilicates ?	260
5.4.2.	Experimental	261
5.4.3.	Results and Discussion	264
5.5.	Summary	288
<b>6</b>	<b>SUMMARY</b>	<b>295-298</b>

# CHAPTER - ONE

## INTRODUCTION

---

*This chapter gives a brief introduction to the entire thesis. It covers various strategic features of catalyst development, methods of preparation and preparation parameters. The scope and objectives of the thesis are also defined.*

## 1.1. INTRODUCTION

Researchers all over the world are ceaselessly attempting to discover catalysts that can initiate and sustain reactions of industrial importance ever since the phenomenon of catalysis was discovered by Berzelius in 1835. Catalysis serves yet another worldwide role, improving our atmosphere and reducing pollution. The commercial examples of environmental catalysis are the catalysts used for controlling automobile emissions, for removing volatile organic compounds (VOCs), and for reducing powerplant emissions.<sup>1</sup>

The world market for heterogeneous catalysts is expected to reach highest peak in the global business in the coming years.<sup>2</sup> The total value of fuels and chemicals derived through the use of catalysts in the US in 1989 was estimated at \$ 891 billion, 17 % of the US GNP for the year.<sup>3</sup> Regardless of slow growth and nominal profit expectations, catalyst suppliers and users are very active in new catalyst development.<sup>4</sup>

Heterogeneous catalyst can be compared to high performance materials which greatly enhance production processes, competitiveness and economics. A new catalyst can amplify process efficiency, reduce production cost and replace existing processes with better ones. The successful exploitation of any material as a catalyst depends on how it is prepared. In spite of numerous scientific studies, preparation of heterogeneous catalysts is regarded as empirical and still remains an art, proceeding through a know-how which is kept as a secret by the catalyst manufacturers.<sup>5</sup> As a result, it is crucial to master catalyst preparation and scale-up from the laboratory to

the manufacturing plant.<sup>6</sup> Each step of the preparation must be characterized not only by physical and chemical techniques, but also by using chemical engineering science.

Catalyst technology is useful in two ways :

- 1) it can be used to eliminate or minimize environmental pollutants;
- 2) it can be used to manufacture value added products with improved yields.

Catalyst development and synthesis is located at the interface of chemistry, chemical reaction engineering and materials science.<sup>7</sup> Research thrusts in design and synthesis of new catalytic materials must strike a balance between the short range structure of the active site and the long range structure of the solid that constitutes the environment surrounding the active site.

While the area of catalysis is replete with many catalysts of great commercial value, there has been a big gap in the understanding of their action. However, the situation has changed in recent years and today the expertise to tailor-make catalysts for specific reactions is available.

## **1.2. CLASSIFICATION OF CATALYSTS**

Many new catalysts have been discovered which can be broadly classified as homogeneous catalysts and heterogeneous catalysts. Catalysts can be further categorized in several ways.

They can be classified according to their physico-chemical nature as follows:

- metal oxides/mixed metal oxides
- supported metals/bimetallic catalysts



- superacids/solid acids
- zeolites/molecular sieves
- clays/heteropolyacids
- metal complexes
- enzyme catalysts

Another interesting way of classifying catalysts is based on their functions, as follows:

- shape selective catalysts
- phase transfer catalysts
- redox catalysts
- acid catalysts

Yet another way of classifying catalysts, based on their behaviour in a particular reaction, is by placing them in to structure sensitive and structure insensitive groups.<sup>8</sup> Rates of structure sensitive catalytic reactions change markedly when the crystallite size of the metal is changed (ammonia synthesis and hydrogenolysis), whereas the rates of other catalytic reactions remain independent of the crystallite size (hydrogenation and carbonylation).

A number of industrially important reactions have been carried out using these catalysts. The industrial use of catalysts can be traced to the contact process for sulphuric acid, which replaced the older chamber process. This was followed by the catalytic synthesis of ammonia from nitrogen and hydrogen. The next stage in the development of catalysis coincided with the advent of petroleum refining and

petrochemical industries. Catalytic cracking, hydroprocessing, reforming and isomerization are among the major processes where catalysts have played major role. Based on the various types of catalysts listed above, a number of new areas have emerged in which catalytic research is vigorously carried out. Some of the prominent reactions are : conversion of methane to liquid fuels, selective conversion of syn gas to chemicals, selective dehydrogenation of alkanes, synthesis of asymmetric structural compounds, control of gaseous emissions from stationary power sources, partial oxidation of olefins and aromatics and homologation of alcohols.

### **1.3. METAL OXIDES AS CATALYSTS**

The vast panorama of heterogeneous catalysts is dominated by metal oxides. Oxides have an ability to bring about electron transfer as well as proton transfer and they can, therefore, be used in both redox and acid base reactions<sup>9</sup> Classifying metal oxides as catalysts is quite tedious since it involves a variety of crystal systems of different compositions with a wide range of physico-chemical properties. An easy and meaningful way of classifying oxide catalysts is based on their applications. The use of oxides in catalysis may thus be classified into four groups.

1. Oxides of main group elements used as acid-base catalysts in the form of solid solutions, oxysalts, oxyacids or bases in heterolytic reactions.
2. Oxides of main group elements, usually used as carriers.
3. Oxides of transition metals used as redox catalysts in reactions in which transfer of electrons takes place across the reactant/catalyst interface (extrafacial reactions) or transfer of atom takes place across the interface (interfacial reactions).

4. Oxides of transition metals used as precursors for the preparation of different active phases like highly dispersed metals or/and metal sulfides.

The utility of metal oxides is in general for catalyzing oxidation reactions on which a large number of industrial processes are based; more than 50 % of the chemical production is due to oxidation reactions catalyzed by metal oxides.<sup>10-17</sup>

Some of the important reactions which require metal oxides as catalysts are:

- oxidation of cyclohexane to cyclohexanone
- oxidative dehydrogenation of ethylbenzene to styrene
- oxidation of n-butane/benzene to maleic anhydride
- oxidation of methane to formaldehyde
- oxidative dehydrodimerization (coupling) of methane to form ethane and ethylene
- oxidation of benzene to phenol and phenol to catechol and hydroquinone
- oxidation of toluene to benzaldehyde
- complete oxidation of hydrocarbons (lower) and carbon monoxide

*The only study  
hydrogenation react  
on supported metal  
oxide*

In metal oxide catalysts it is not just the desired composition that is important; the preparation method is equally crucial. This is because, a minor variation in the preparation method can drastically alter their catalyst properties irrespective of their composition. Therefore, designing metal oxide catalysts involves a judicious selection of metal components and the preparation method.

In general, oxides are prepared in single component or in multiple components; they may be crystalline or amorphous; they may be supported or unsupported. An overview of these aspects is given in the following section.

### ***1.3.1. Single component oxides***

This class of oxides has been known since the emergence of the catalysis as an important area in chemical science and technology. Most of the oxides of the metals known in the periodic table are catalytic in one way or the other. Single component oxides used in the oxidation reactions may belong to one of the following categories:<sup>15</sup>

i) The oxides on which oxygen is adsorbed predominantly in the form of electron-rich species. Transition metal oxides such as NiO, MnO, CoO or Co<sub>3</sub>O<sub>4</sub> in which cations are prone to increase their degree of oxidation and supply adsorbed oxygen molecules or atoms with electrons belong to this category.

ii) Oxides showing a tendency to adsorb oxygen in the form of species less rich in electrons as O<sub>2</sub><sup>-</sup> ions. Oxides such as ZnO, TiO<sub>2</sub>, V<sub>2</sub>O<sub>5</sub> are in this category.

In these metal oxides, two possible states of activated oxygen can be recognized; highly reactive surface states of adsorbed oxygen and less active, lattice incorporated oxygen species. Obviously, the former species are usually considered to be the important ones involved in complete oxidation, and the latter is generally believed to participate in selective partial oxidations. In both the types, the relation between the catalytic activity and physico-chemical properties of metal oxides is understood to conform to the redox model with volcano-type relation.<sup>18</sup>

However, since single component oxides do not come under the purview of the present study, to list a discussion of them in detail is beyond the scope of this chapter.

### 1.3.2. Multicomponent oxides (Mixed metal oxides)

Oxides of two or more different kinds of cations are known as mixed metal oxides. They can be further classified based on whether they are crystalline or amorphous. The name of a group of crystalline mixed metal oxides is derived from the first or the principal compound shown to have a particular type of structure. For instance, the compound  $\text{MgAl}_2\text{O}_4$  which occurs in nature comprises a ccp array of oxide ions where in one eighth of tetrahedral holes are occupied by  $\text{Al}^{3+}$  ions which is the structure of the mineral spinel and are well known as *spinel*s. Similarly, the compound  $\text{FeTiO}_3$  which is closely related to corundum structure is well known as ilmenite. Another class of compounds of the type  $\text{ABO}_3$ , where A being the larger cation with 12 coordination, and B being the smaller cation with 8 coordination are recognized as 'perovskites'. Yet another class is fluorites, of the type  $\text{AO}_2$ , where, A is a cation with 8 coordination and O, the tetrahedral center surrounded by four A atoms. The term fluorite originates from  $\text{CaF}_2$  whose structure is cubic.

The major advantage of the multicomponent oxide is that it is possible to tune oxygen sorption properties by meticulously choosing the required metal components so as to crystallize in a particular structural system. In such cases, the reactivity of oxygen is strongly dependent on the kind of neighbouring metal cations as well as metal - oxygen bonding distance and metal - oxygen bond strength.

Among various types and structures of mixed metal oxides, those with perovskite type ( $\text{ABO}_3$ ) structure is known to be useful for complete oxidation reactions,<sup>19-22</sup> whereas, mixed metal oxides with spinel, scheelite, ilmenite and rutile structure are effective for partial oxidation reactions.<sup>23-26</sup> Furthermore, mixed oxides

with a fluorite type structure based on zirconia, ceria or thoria are interesting owing to their oxygen storage capacity and high oxygen mobility,<sup>27-29</sup> and there is a much to be explored about its potential.

### 1.3.3. Supported metal catalysts

Do they form / come from oxides.

It may look peculiar to consider supported metal catalysts as a type of mixed metal oxides. But in most of the cases, metal oxides are used as precursors for getting supported metal catalysts. Secondly, all the supports themselves are oxides and, therefore, it is appropriate to consider these also as belonging to the mixed metal oxide category.

NO!

In general, supported metals are required for hydrogenation and dehydrogenation reactions.<sup>30-34</sup> Although noble metals like platinum, palladium, rhodium and ruthenium supported on classical materials like silica, alumina or zirconia, are popular among them, non-noble metals like copper and nickel are equally prominent. Once again, from the point of view of catalyst development, there are several aspects to be understood, particularly the role of newer preparation methods in tailoring metal dispersion and metal area and support area.

### 1.3.4. Amorphous mixed metal oxides.

Amorphous mixed oxides are another class of multi-component oxides which merit detailed study with particular emphasis on their behavior in contrast to their crystalline counterparts. Usually, silica based mixed oxides can be obtained in amorphous form and they can generally be called as metallosilicates.

is it correct

Amorphous metallosilicates are among the newly emerging mixed oxides which are not yet well-characterized with emphasis on designing their catalytic properties. Titania - silica mixed oxides which are in this class, have attracted a great deal of attention owing to their utility as catalyst support<sup>35-39</sup> and as catalyst<sup>40-43</sup>

Although our study mainly involves sol-gel and co-precipitation methods, it is pertinent to have a general idea about the various catalyst preparation routes.

## **1.4. CATALYST PREPARATION**

The preparation of a catalyst is considered to be the crucial stage in its development. Several preparation methods have been reported in the literature.

### ***1.4.1. Ceramic method***

The ceramic method involves the mechanical mixing of two or more components followed by heat treatment.<sup>44</sup> Usually, catalyst precursors like metal oxalates or metal carbonates are ground well in an agate mortar in wet or dry condition, which may or may not be followed by ball milling. The mechanically alloyed solid mixtures are then calcined at a very high temperature to get mixed oxides with a single phase.

### ***1.4.2. Complexation method***

The complexation method makes use of chemical reactions which transform slowly and without physical discontinuity (*i.e.* without phase separation) the

homogeneous solution of the catalyst precursor into a homogeneous or amorphous phase.<sup>45,46</sup> This precursor is then dried and calcined to yield more highly intermixed and dispersed oxides than those prepared by the usual precipitation routes. The interesting feature of this method is the use of organic molecules with multiple chemical functionalities as templates for formation of a three dimensional network during the solvent removal step. Removal of the organic ingredient is a crucial step during the catalyst activation.

### ***1.4.3. Sol-gel method***

The sol-gel method is a homogeneous process which results in a continuous transformation of solution into a hydrated solid precursor.<sup>47,48</sup> This method generally involves controlled hydrolysis and polymerization of ionic species in aqueous media. A *sol* is a dispersion of discrete colloidal particles and a *gel* is a colloidal sol normally containing a fluid component and a network internal structure that keeps both the fluid and solid components in a highly dispersed state. The popularity of this method has gained ground in recent times owing to the possibility of controlling the texture, composition, homogeneity and structural properties of the finished solids. The details of the procedure are discussed separately in chapter four.

### ***1.4.4. Combustion synthesis***

Combustion synthesis involves the use of fuels such as hydrazine or carbohydrazide as an additive along with the specific catalyst precursors.<sup>49-52</sup> This method involves a highly exothermic reaction with the liberation of nitrogenous gases



and is, therefore, called combustion synthesis. This method is suitable for getting a highly crystalline powder with single phase. Another kind of combustion synthesis, commonly known as explosion method involves, the use of ammonium bicarbonate for forming the precipitate and dissolving it in acetic acid; this is followed by recovering the precipitate by evaporating acetic acid.<sup>49</sup> The mixture is then transferred to a quartz tube fitted with a frit. It is subsequently heated at about 473 K at which a exothermic reaction occurs resulting in the formation of a powder, which is then calcined at the required temperature. Owing to the exothermicity of the reaction, accompanied by a sudden rise in temperature, a highly crystalline material results.

#### ***1.4.5. Freeze drying technique***

This method involves the drying of the catalyst precursors under freezing conditions.<sup>53</sup> This requires low pressure, preferably, pressure of the order of  $10^{-3}$  to 1 torr. Typically, the required catalyst precursors are mixed in aqueous or non-aqueous solvents which are then quenched suddenly in liquid nitrogen. The solid thus obtained is kept under low pressure in a freeze dryer and kept overnight. The final step is drying and calcination which is carried out as usual.

#### ***1.4.6. Spray drying technique***

The spray drying technique is particularly useful for coating the catalyst on a support and requires spray drying equipment.<sup>53,54</sup> A slurry of the catalyst precursor is prepared and passed through a ceramic support kept in a spray drier at a high

temperature (above 537 K). While passing through the spray drier, the precursor is heated, dried and coated on the support.

#### ***1.4.7. Hydrothermal method***

The hydrothermal method is particularly useful for making zeolitic materials<sup>55</sup> or mixed metal oxides.<sup>56</sup> Hydrothermal treatment in presence of an organic template gives a porous material with a high surface area and pore volume. It is possible to engineer the pore size by choosing an appropriate template.

#### ***1.4.8. Co-precipitation method***

In the co-precipitation method, a precipitating agent, which is often a hydroxide or a carbonate of ammonia or sodium, is added to a solution containing the precursor compounds.<sup>57-59</sup> Hydroxides or carbonates of the metal ions are precipitated out of the solution, which are filtered, washed and calcined to form the oxide. The homogeneity and the degree of the atomic mixing of the metal ions in the precipitates depend upon the solubility product of the compounds involved. Several conditions such as the pH of the precipitation, rate of addition of the precipitating agent, concentration of the metal salt solution, stirring and the temperature influence the structure and properties of the final product to a large extent.

The deposition-precipitation method of catalyst synthesis comprises application of the active components on to an existing support through a chemical reaction. This reaction gives rise to the formation of an insoluble compound containing the active element. This method can give rise to uniformly distributed active components over the support surface even at high loadings.

## ***1.5. STRATEGIES FOR CATALYST DEVELOPMENT***

There are basically two ways for developing catalyst materials. The first one is to prepare a certain material and look for its catalytic utility. Alternatively, the second is to tailor the desired properties of a material in such a way that it would be catalytically active in the target reaction. The second method is a challenging one and, therefore, is of great interest. To understand the various crucial aspects of catalyst development, several metal oxide systems, prepared by different routes and with diverse properties and applications were included in the present study. The typical systems chosen are given here.

## ***1.6. SYSTEMS CHOSEN IN THE PRESENT STUDY***

In the present investigation, various catalysts systems are chosen in such a way that all of them are branches of a big family of mixed metal oxides. Particularly, three types of systems were chosen, *viz.*, zirconia based oxides with fluorite type structure prepared by the co-precipitation method for complete oxidation reactions, copper catalysts supported on silica prepared by the sol-gel method for hydrogenation reactions, and amorphous titanosilicates and aluminosilicates prepared by the sol-gel method at controlled pH for oxidation of fine chemicals. A detailed account of these catalyst systems is given in the introductory section of the subsequent chapters, and a brief literature overview of each system is given below.

### ***1.6.1. Zirconia based oxides for oxidation reactions.***

Zirconium dioxide (zirconia) is an oxide with a high melting point (about 3000 K), a low thermal conductivity and a high resistance to corrosion, which has been used

for refractories, pigments, piezoelectric devices, ceramic condensers and oxygen sensors.<sup>60</sup> The development of fully and partially stabilized zirconia with a high mechanical strength has opened up new applications in fine ceramics. Recently, attempts have been made to use zirconium dioxide as catalysts for various reactions both in the form of single oxide and combined oxides.<sup>61</sup>

As a single component,  $ZrO_2$  has been found to be useful as catalysts for several organic reactions. Reactions such as the synthesis of  $\alpha$ -olefins from alcohols; formation of 1-butene from 2-butanamine, acetonitrile from triethylamine; allyl alcohol from epoxide and reduction of aldehydes, carboxylic acids and esters with alcohols, have been carried on zirconia catalysts.<sup>62</sup> On the other hand, zirconia as a part of the multiple component oxide is considered to be the emerging catalytic material with potential applications. In fact, a galaxy of modified zirconia catalysts have been reported in recent times.

For instance, Wokaun et. al. have reported  $Au/ZrO_2$  catalysts prepared by the co-precipitation method for hydrogenation of carbon dioxide.<sup>63</sup> They found that the crystallization of zirconia and segregation of gold occurred after calcination and that was the major reason for the enhanced activity. Another kind of catalyst, based on zirconia for hydrogenation reaction is the Mn-Zr mixed oxide, made by Chung and co-workers.<sup>64</sup> Their studies revealed that the type of Mn present in the mixed oxide affected the selectivity pattern of CO hydrogenation. Ni-zirconia catalysts are also known to be useful for hydrogenation reactions.<sup>65</sup> Another area of interest where the oxygen ion conducting properties of zirconia have been exploited is solid electrolytes.<sup>66</sup> Recently, efforts to use zirconia-based oxides for environmental applications,

particularly for NO<sub>x</sub> removal, have been reported.<sup>67-69</sup> However, design and development of zirconia based oxides suitable for oxidation reactions are not known as per the knowledge of the investigator.

Oxidation reactions are of two types : partial oxidation and complete oxidation, of which, both in general, require noble metal catalysts. In addition, in several cases, use of metal oxides as catalysts at higher temperature is found to be feasible. Depending on the nature of the reaction and their mechanism, it is possible to tailor-make a particular metal oxide catalyst for a specific application.

Keeping in view of the importance of the catalytic route for cleaner environment, particularly for removal of noxious emissions from autoexhaust, the present study was restricted only to complete oxidation of hydrocarbons (n-butane) and carbon monoxide. Although, a wide spectrum of catalysts is reported in the literature, an attempt was made to develop oxide materials with novel properties which can act as an alternative to the noble metal catalysts. The current approach involved the preparation of a stabilized zirconia with a novel stable structure, high surface area, reliable thermal stability, mechanical properties, resistance to sintering and with considerable catalytic activity and long life.

### ***1.6.2. Supported Cu catalysts for hydrogenation and dehydrogenation reactions.***

Similar to oxidation, hydrogenation and dehydrogenation reactions are also important both from fundamental as well as industrial point of view. Supported metal catalysts are being used for this purpose. These can be classified into two categories:

noble metals and non-noble metals. Since the present interest was to study the impact of preparation methods, a simple system comprising of copper metal dispersed on a silica matrix was chosen, which was relatively cheaper than that of other metal catalysts. Copper based catalysts are useful in a variety of industrial processes.<sup>70-75</sup> They are conventionally prepared by impregnation, deposition precipitation, or ion exchange technique.<sup>76,77</sup> More recently, the sol-gel method has also been applied to get supported metal catalysts.<sup>78-80</sup> However, the use of the sol-gel method is not yet reported for the preparation of copper catalysts. In addition, a systematic investigation of the role of sol-gel preparation on the crystallite size, metal area and dispersion of the metal, and on the properties of the support, and their impact on catalytic properties would be interesting and require a detailed study.

### ***1.6.3. Amorphous titano-silicates and aluminosilicates***

Titanium silicates have recently been shown to be in crystalline form which, when prepared hydrothermally in presence of organic nitrogenated templates, crystallize into a series of molecular sieves like TS-1, TS-2, Ti-MCM 41 and Ti-ZSM 48, depending on the templates used. Similar is the case with crystalline aluminosilicates known as zeolites. In all these metallosilicates, it is the presence of isolated active sites located within the channels that impart catalytic properties to them. For the first time these materials have been used as catalysts in shape selective oxidations. Thus, shape selectivity and high activity due to isolated active sites in the zeolite channel make it attractive for fundamental studies and industrial applications.

However, amorphous analogs of these molecular sieves are yet to be investigated thoroughly.

An attempt in this direction has been tried by several investigators. Particularly, studies on the effect of the type of preparation on the catalytic properties of titania-silica mixed oxides is one such attempt, in which various preparation techniques, such as complex-assisted sol-gel technique, co-precipitation, hydrogel kneading and xerogel kneading have been applied and their properties compared.<sup>81</sup> It was found that the complexing assisted sol-gel method gives titania-silica mixed oxides with the formation of the Ti-O-Si bond. Similarly, the influence of sol-gel and drying conditions on structure properties have been reported recently.<sup>82</sup> It was accordingly found that titania-silica mixed oxide, prepared at a low temperature by supercritical drying, possessed mesoporosity combined with high Ti dispersion and structural stability, rendering this aerogel most suitable for use in liquid phase epoxidation. Another important parameter to be controlled during sol-gel preparation is the pH, and nothing has been reported so far on its role in obtaining isolated Si-O-Ti linkages in titania-silica mixed oxides. The same rationale can also be applied where a systematic study on the influence of pH during the sol-gel preparation of acidic aluminosilicates on catalytic properties would be interesting.

## 1.7. OBJECTIVES AND SCOPE

In the present investigation, therefore, an attempt has been made *to design and develop fluorite type mixed metal oxides for use as complete oxidation catalysts*. The preparation method followed here is *co-precipitation* method because of



numerous advantages and simplicity. In view of the importance of generation of *highly dispersed metal* supported on a high surface area support material, application of *sol-gel method* to prepare *copper-silica catalysts* is dealt with. The present investigation is also confined to *amorphous titanosilicates and aluminosilicates* since catalytic exploitation of these materials are scarcely available in the literature. Once again, the role of preparation method is studied with particular emphasis on *sol-gel* conditions in designing amorphous metallosilicates and their impact on physicochemical and catalytic properties. The investigation is thus aimed at generating isolated active sites in amorphous materials so as to develop a new family of amorphous catalysts.

Handwritten note: *Handwritten note: 1/2 or 5 or active sites*

The objective and scope of the present thesis are to understand :

- The role of preparation method on the structure, properties and the catalytic activity of the materials, particularly the mixed metal oxides;
- the importance of the structural stabilization of fluorite type oxide materials for complete oxidation activity;
- the advantage of the sol-gel method of preparation in getting highly dispersed metal, with nano scale particle size, which are highly active in the selective hydrogenation reaction; and
- the generation of isolated active sites in metallo-silicate materials, particularly, amorphous aluminosilicates and amorphous titanosilicates.

Accordingly, the thesis is divided in to *six* chapters.



A brief introduction of various aspects of metal oxide catalysts is provided in *Chapter I*. *Chapter II* gives a description of various experimental techniques used.

*Chapter III* deals with synthesis, characterization and catalytic applications of novel stabilized zirconia with fluorite type structure. The preparation of these oxide materials by the co-precipitation method and their physico-chemical characterization are described. The utility of these novel materials in the complete oxidation of hydrocarbon and carbon monoxide is also discussed in this chapter.

*Chapter IV* deals with the studies of a supported metal catalyst, Cu-silica, prepared by the sol-gel method. The catalyst was characterized by various techniques and its application in the hydrogenation reaction was studied. The sol-gel derived copper silica was compared with catalysts prepared by the conventional co-precipitation route. The improved activity and selectivity associated with long life was explained in terms of constrained grain growth model.

*Chapter V* describes the synthesis, characterization and catalytic applications of micro-meso porous amorphous titanosilicates and amorphous aluminosilicates. Titanosilicates, synthesized at ambient conditions in the absence of nitrogenated organic bases, were amorphous (XRD). They possessed a bimodal, narrow pore size distribution with pore widths around 0.8 and 3.6 nm and surface area of about 500 - 700 m<sup>2</sup> g<sup>-1</sup>. An absorption bands at 960 cm<sup>-1</sup> (IR) and 220 nm (UV); a radial electron density distribution pattern also indicated the presence of isolated TiO<sub>4</sub> units in a silica matrix. It was and catalytically active and substantially selective in the oxidation of benzene, toluene and phenol. Similarly, the study on novel amorphous alumino-

silicates prepared by the sol-gel method at two different pH conditions, their distinct properties as reflected by FTIR, NMR and other techniques, and their catalytic behavior in the isomerization of mesitylene are also described in this chapter. Thus, the role of sol-gel preparation condition in getting the *isolated active species* is discussed in detail.

An overall summary of the thesis is given in *Chapter VI*.

## References

1. J. N. Armor, *Appl. Catal. B*, **1** (1992) 221.
2. S. Wilkinson and D. Hunter, *Chem. Week*, **144** (1989) 24.
3. Roth. J. F., Catalysis science and technology, S. Yoshida, N. Takezawa, T. Ono, (Eds), Kodansha Ltd., Tokyo, 1991, Vol-1, p-3
4. L.L Hegedua, Ed, *Catalyst Design*: Wiley Interscience, 1987.
5. B. Delmon and Coll (Eds) *Scientific Bases for the preparation of heterogeneous catalysts, Vol-1 to VI*, Elsevier, Amsterdam, 1980
6. E. F. Sanders and E. J. Schlossmacher, *Catalysis*, **1** (1983) 31.
7. J. J. Burton, R. L. Garten, Ed. 1977, *Advanced materials in Catalysis*, Academic press, New York.
- 8.. M. Boudart, *Adv. Catal.*, **20** (1969) 153.
9. .J. Haber, in J. A. Thomas and K. I. Zamaraev (Eds), *Perspectives in Catalysis*, Blackwell Scientific Publications, 1992, p-371.
10. A. Bielanski and J. Haber, *Oxygen in Catalysis*, Dekker, New York 1991;
11. *New Developments in Selective Oxidations*, G. Centi and F. Trifiro Eds (Elsevier 1990).
12. R. K. Grasselli and J. D. Burchington, *Advan. Catal.*, **30** (1981) 133.
13. J. Haber, in *Surface properties and Catalysis by Non-metals*, J. Bonnelle, B. Delmon and E. Derouane (Eds), Reidel, Dordrecht 1983 p-1.
15. A. Bielnski and J. Haber, *Catal. Rev.*, **19** (1979) 1.
16. D. B. Dadyburjor, S. S. Jevur and E. Ruckenstein, *Catal.. Rev.* **19** (1979) 293.
17. H. H. Kung, *Transition metal oxides - surface chemistry and catalysis*, Elsevier 1988.
18. A. A. Balandin, *Advan. Catal.*, Vol-10, Academic press, New York, 1958, p-95.
19. J. L. G. Fierro, *Catal. Today*, **8** (1990) 201.
20. M. Mizuno, *Catal. Today*, **8** (1990) 221.
21. H. M. Zhang, Y. Teraoka and N. Yamazoe, *Appl.Catal.*, **41** (1988) 137.
22. M. Machida, K. Eguchi and H. Arai, *J. Catal.*, **103** (1987) 385.
23. T. Seiyama, N. Yamazoe, and K. Eguchi, *Ind. Eng. Chem. Prod. Res. Dev.*, **24** (1985) 19.
24. N. Yamazoe, S. Hidaka, H. Arai, and T. Seiyama, *Oxid. Commun.*, **4** (1983) 287.
25. J. Haber and G. Grzybowska, *J. Catal.*, **28** (1973) 489.
26. J. Haber, *Int. Chem. Eng*, **15** (1975) 21.
27. P. S. Gelling and H. J. M. Boumeester, *Catal. Today*, **12** (1992) 1.
28. R. G. Silver and J. G. Ekerdt, *J. Catal.*, **118** (1989) 400.
29. F. Zamar, A. Trovarelli, C. D. Leitenburg, and G. Doletti, *J. Chem. Soc. Chem. Comm.*, (1995) 965.
30. G. J. Hutchings, F. King, I. P. Okoy, and C.H. Rochester, *Appl. Catal.*, **83** (1992) L7.
31. G. Carturan, G. Facchin, G. Cocco, G. Navazio, and C. Gubisota, *J. Catal.*, **82** (1983) 56.

32. Y. Watanabe, Y. Tsuji, T. Ohsumi, and R. Takeuchi, *Bull. Che. Soc. Jpn.*, **57** (1988) 2867.
33. G. C. Bond, *Chem. Soc. Rev.*, **20** (1991) 441.
34. R. J. Grau, A. E. Cassano, and M. A. Baltanas, *Catal. Rev. Sci. Eng.*, **30** (1988) 1.
35. A. Baiker, P. Dollenmeier, P. Glinski, and A. Reller, *Appl. Catal.*, **35** (1987) 365.
36. R. A. Rajadhyaksha, and H. Knozinger, *Appl. Catal.* **51** (1989) 81.
37. J. S. Reick, and A. T. Bell, *J. Catal.*, **99** (1986) 262.
38. E. I. Ko, J. P. Chen, and J. G. Weissman, *J. Catal.*, **105** (1987) 511.
39. M. A. Cauqui, J. J. Calvino, G. Cifredo, L. Esquivias and J. M. Rodriguez-Izquierdo, *J. Non-Cryst. Solids*, **147/148** (1992) 758.
40. S. Imamura, H. Tarumoto, and S. Ishida, *Ind. Eng. Chem. Res.*, **28** (1989) 1449.
41. M. Niwa, M. Sago, H. Ando, and Y. Murakami, *J. Catal.*, **69** (1981) 69.
42. R. Neumann, M. Chava, and M. Levin, *J. Chem. Soc. Chem. Comm.*, (1993) 1685.
43. A. Keshavaraja, V. Ramaswamy, H. S. Soni, A. V. Ramaswamy and P. Ratnasamy, *J. Catal.*, **501** (1995) 645.
44. A. K. Cheetam and P. Day, *Solid State Chemistry Techniques*, Oxford University Press, 1987.
45. C. Marcilly, P. Courty and B. Delmon, *J. Amer. Ceram. Soc.*, **53** (1970) 56.
46. C. N. R. Rao and J. Gopalakrishnan, *Acc. Chem. Res.*, **20** (1987) 228.
47. S. Komarneni, R. Roy, U. Selvaraj, T. Sano, K. Maeda, and H. Shoji, *J. Mater. Res.*, **4** (1994) 1131.
48. L. Hench and J. K. West, *Chem. Rev.*, **90** (1990) 33.
49. L. Wachowski, S. Zielinski and A. Burewicz, *Acta Chimica Academiae Scientiarum Hungaricae*, **104** (1980) 141.
50. R. Gopichandran and K. C. Patil, *Mater. Lett.* **12** (1992) 437.
51. H. K. Varma, P. Mukundan, K. G. K. Warriar and A. D. Damodaran, *J. Mater. Sci. Lett.*, **10** (1991) 666.
52. S. S. Manoharan and K. C. Patil, *J. Amer. Ceram. Soc.*, **75** (1992) 1012.
53. D. W. Johnson, P. K. Gallagher, F. Schrey, W. W. Rhodes, *Am. Ceram. Soc. Bull.*, **55** (1976) 520.
54. J. G. M. Delau, *Amer. Ceram. Soc. Bull.*, **49** (1970) 572.
55. P. Barteau, B. Delmon, J. L. Dallons, and van Gysel, *Appl. Catal.*, **70** (1991) 307.
56. H. Cheng, J. Ma, Z. Zhao, D. Qiang, *J. Amer. Ceram. Soc.*, **75** (1992) 1123.
57. P. Courty, C. Marcilly, in Preparation of catalysts I, B. Delmon, P. A. Jacobs, and G. Poncelet (Eds), *Stud. Surf. Sci. Catal.*, **1** (1976) 119.
58. K. R. Barnard, K. Fogar, T. W. Turney and R. D. Williams, *J. Catal.*, **125** (1990) 265.
59. D. G. Klissrski and E. L. Uzunova, *Chem. Mater.*, **3** (1991) 1060.
60. A. Pathak, D. K. Mukhopadhyay and P. Pramanik, *Mater. Res. Bull.*, **27** (1992) 155.
61. T. Yamaguchi, *Catal. Today*, **20** (1994) 199.
62. K. Tanabe and T. Yamaguchi, *Catal. Today*, **20** (1994) 185.
63. R. A. Koepfel, A. Baiker, C. Schild and A. Wokaun, *J. Chem. Soc. Farad. Trans.*, **87** (1991) 2821.

64. D. J. Koh, J. S. Chung, Y. G. Kim, J. S. Lee, I. S. Nam, and S. H. Moon, *J. Catal.*, **138** (1992) 21.
65. C. Schild, A. Woukan, R. A. Koepfel and A. Baiker, *J. Phys. Chem.*, **95** (1991) 6341.
66. I. S. Metcalfe, *Catal. Today*, **20**, (1994) 283.
67. H. C. Zang, J. Lin, W. K. Teo, J. C. Wu, and K. L. Tan, *J. Mater. Res.*, **10** (1995) 545.
68. K. Eguchi, M. Watanabe, S. Ogata and H. Arai, *Bull. Chem. Soc. Jpn.*, **68** (1995) 1739.
69. K. A. Bethke, D. Alt and M. C. Kung, *Catal. Lett.*, **25** (1994) 37.
70. E. G. M. Kuijpers, R. B. Tjepkema, W. J. J. Van der Wal, C. M. A. M. Mesters, S. F. G. M. Spronck and J. W. Geus, *Appl. Catal.*, **25** (1986) 139.
71. M. Kobayashi, N. Takazawa, C. Minochi, and K. Takahashi, *Chem. Lett.*, (1980) 1197.
72. K. Takahashi, N. Takazawa, and H. Kobayashi, *Appl. Catal.*, **2** (1982) 363.
73. D. M. Monti, M. S. Wainwright, D. L. Trimm, and N. W. Cantt, *Ind. Eng. Chem. Prod. Res. Dev.*, **24** (1985) 377.
74. D. M. Monti, N. W. Cant, D. L. Trimm, and M. S. Wainwright, *J. Catal.*, **100** (1986) 17.
75. K. Klier, *Advan. Catal.*, **31** (1983) 243.
76. T. A. Doorling, B. W. J. Lynch and R. L. Moss, *J. Catal.*, **20** (1971) 190.
77. C. J. G. Van der Graft, P. J. Elberse, A. Mulder and J. W. Geus, *Appl. Catal.*, **59** (1990) 275.
78. T. Lopez, P. Bosch, J. Navarrete, M. Asomoza and R. Gomez, *J. Sol-gel Sci. Technol.*, **1** (1994) 193.
79. T. Lopez, P. Bosch, M. Asomoza and R. Gomez, *J. Catal.*, **133** (1992) 247.
80. W. Zai and R. D. Gonzalez, *Catal. Lett.*, **12** (1992) 73.
81. M. Toba, F. Mizukami, S. Niwa, T. Sano, R. Maeda, A. Annala and V. Komppa, *J. Mol. Catal.*, **91** (1994) 277.
82. D. C. M. Dutoit, M. Schneider and A. Baiker, *J. Catal.*, **153** (1995) 165.

## CHAPTER - TWO

# Characterization Techniques

---

*This chapter deals with the experimental and interpretational aspects of various physico-chemical characterization techniques adopted in the present investigations.*

## Introduction

Catalyst characterization is one of the crucial aspects of catalyst design since it gives information about crystallinity, surface structure, nature of the active sites, particle size and morphology, acidity, and other characteristic features. In this regard all the modern tools of characterization such as the spectroscopic techniques, adsorption techniques and analytical techniques are very important.

The present chapter gives a brief account of the experimental techniques used in the subsequent chapters. This is only a compilation of various instrumental and theoretical aspects relevant to provide a background to the present study.

### *2.1. X-Ray Diffraction (XRD)*

X-Ray diffraction (XRD) is one among the prominent characterization tools applied for studying the structure of the catalyst. X-rays have wavelength in the range of 1 - 10 Å and are adequately energetic to penetrate solids and probe their internal structure, to identify bulk phases and to estimate crystallite sizes.<sup>1</sup>

X-ray diffraction is the elastic scattering of X-ray photons by atoms in a periodic lattice. The scattered monochromatic X-rays that are in phase give constructive interference. Fig. 2.1a illustrates how diffraction by crystal phase allows one to derive lattice spacing,  $d$ , by measuring the angle  $2\theta$ , under which constructive interfering X-rays with wavelength  $\lambda$ , leave the crystal by using the Bragg relation,

$$n\lambda = 2d \sin\theta. \text{-----(i)}$$

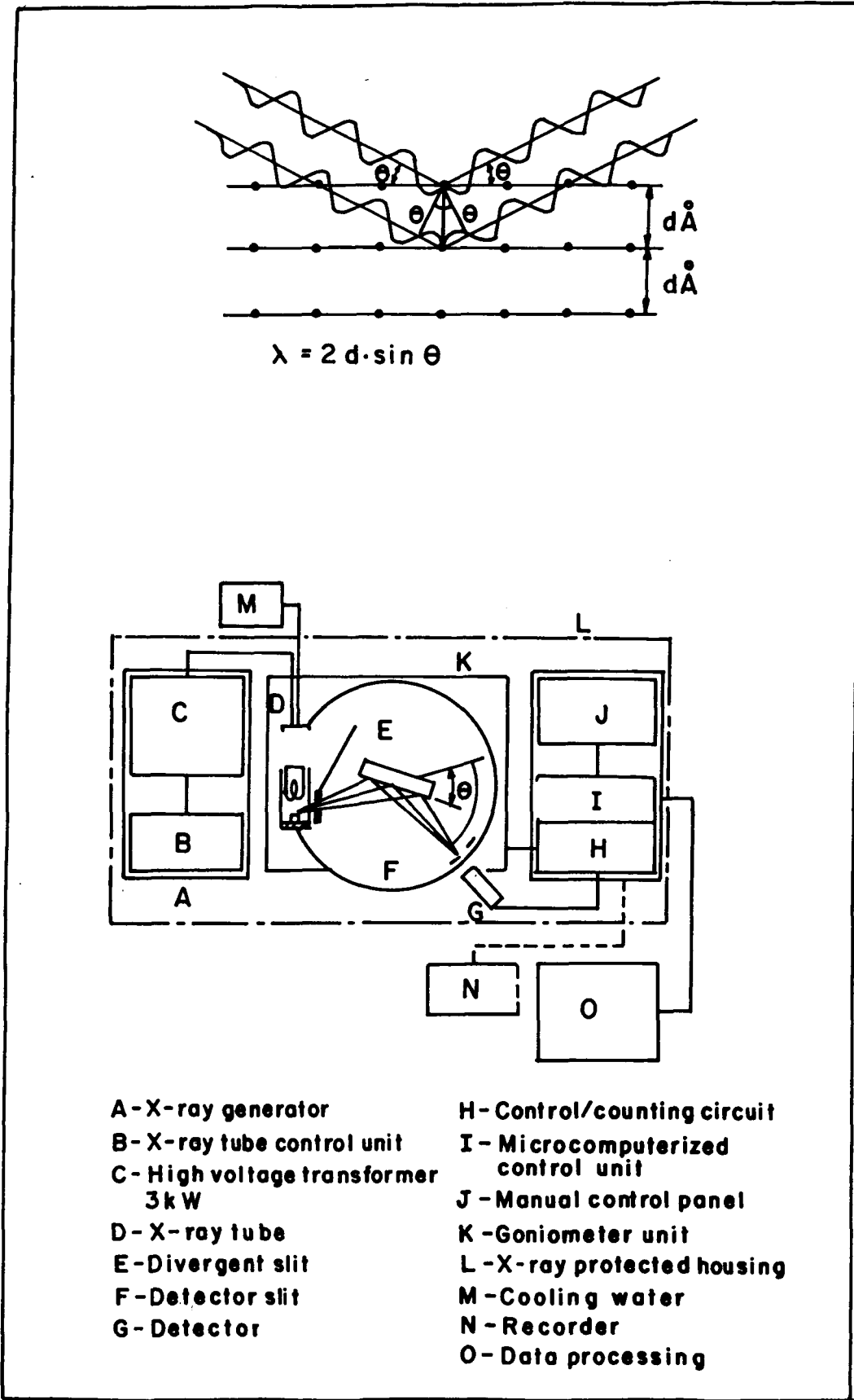


Fig. 2.1: Bragg's phenomenon (a); a schematic diagram of X-ray diffraction unit (b).



The XRD pattern of a powdered sample is measured with a stationary X-ray source (like Cu-K $\alpha$ ) and a movable detector, which scans the intensity of the diffracted radiation as a function of the angle  $2\theta$  between the incident and the diffracted beams. When working with a powdered sample an image of diffraction line occurs because a small fraction of the powdered particles will be oriented such that by chance, a certain plane (hkl) is at the right angle with the incident beam for constructive interference. A schematic diagram of the XRD unit used in the present investigation is depicted in Fig. 2.1b.

The diffraction patterns can be used to identify various phases in a catalyst. The width of diffraction peaks carries information on the dimensions of the reflecting planes. Diffraction lines from the perfect crystals are very narrow. For crystals with size below 100 nm, line broadening occurs due to incomplete destructive interference in scattering directions where the X-rays are out of phase. The Debye-Scherrer formula,<sup>2</sup>

$$\langle L \rangle = K\lambda/\beta\cos\theta \text{ ----- (ii)}$$

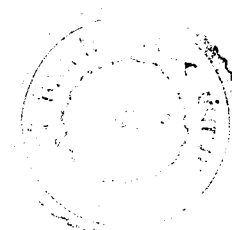
is used to estimate the crystallite size, where  $\beta$  is peak width,  $K$  is a constant and  $\langle L \rangle$  is volume averaged thickness of crystallite size.

It is possible to find out the symmetry and cell constant of a given powder by X-ray diffraction technique. As an illustration, indexing of a cubic pattern by their  $\sin^2\theta$  ratios is discussed here.

According to Bragg equation and the expression for an interplanar spacing of a cubic crystal, two reflections ( $h_1 k_1 l_1$ ) and ( $h_2 k_2 l_2$ ) satisfy equations

$$\sin^2\theta_1 = (\lambda^2/4a^2) (h_1^2 + k_1^2 + l_1^2) \text{ ----- (iii)}$$

$$\sin^2\theta_2 = (\lambda^2/4a^2) (h_2^2 + k_2^2 + l_2^2) \text{ ----- (iv)}$$



dividing (iii) by (iv) gives

$$\sin^2\theta_1 / \sin^2\theta_2 = m_1 + m_2 \text{ ----- (v)}$$

where  $m_1$  and  $m_2$  are integral sum of the square of the respective miller indices.

For some constant spacing 'd', a value of  $\sin^2\theta$  for one wavelength is related to  $\sin^2\theta$  for second wavelength as follows :

$$\sin^2\theta_1 / \sin^2\theta_2 = \lambda_1^2 / \lambda_2^2$$

This relationship follows directly from the square of the Bragg's law written for two wavelengths.

From the observed  $\sin\theta$  value of any line in an indexed cubic pattern, the unit cell dimension can be determined by employing the Bragg's equation in the form

$$a = \{(\lambda/2)/(\sin\theta)\}(h^2+k^2+l^2)^{0.5}$$

$$a = d (h^2+k^2+l^2)^{0.5}$$

Similarly, it is possible to estimate unit cell parameters of other systems also.

The X-ray diffraction unit used in the present investigation is 'Rigaku' Model D-Max III VC, Japan, with Ni filtered Cu-K $\alpha$  radiation having curved graphite crystal monochromator and NaI scintillation counter.

## 2.2. X-Ray Scattering Techniques

The elastic X-ray scattering from the amorphous solids can be interpreted in terms of the radial electron distribution function (REDF)  $4\pi^2 \rho(r)$ , where  $\rho(r)$  will tend towards the *average number density function* over large distance of  $r$ ,  $\rho(r)$  will tend towards the average number density  $f_0$  of the sample.<sup>3</sup> The ratio of  $\rho(r)/\rho_0 = g(r)$  is usually called the pair probability function (PPF).

The REDF and PPFs are obtained from the intensity observed on the amorphous sample through several corrections for air scattering, polarization and absorption effects. The intensity thus corrected is converted to electron units per atom by normalization process. Then the theoretical values of the incoherent scattering due to Compton effect are subtracted from the corrected measured values. This resultant intensity only includes the coherent scattering which is related with the structure factor or the interference function  $s(\varphi)$ , the average radial distribution function  $4\pi r^2 f(r)$ , which specifies the density of atoms or electrons as a function of the radial distance from any reference atom or electron in the system and the average pair distribution function  $g(r)$  of the sample can be calculated. Therefore, the areas under the peaks of REDF give the respective numbers of nearest neighbors at several radial distance,  $r$ . In order to carry out the Fourier transformation, the value at zero  $Q$  must be evaluated, which is estimated by smoothly extrapolating the observed intensity curve  $s(\varphi)$  to the value at zero.

**Theory :**

The intensity corrected for the absorption and polarization effects is given by the sum of coherent and incoherent scattering :

$$I_s(\varphi) = \beta [ I_{ev}^{coh}(\varphi) + I_{ev}^{incoh}(\varphi) ],$$

where,  $\varphi = 4\pi \sin\theta/\lambda$ ,  $\beta$  is proportionality factor called normalization constant,  $I_{ev}^{coh}$  and  $I_{ev}^{incoh}$  are the coherent and incoherent scattering intensities from the sample.

$$I^{coh}(\varphi) = \langle f^2 \rangle + \langle f \rangle^2 \int 4\pi r^2 [\rho(r) - \rho_0] \sin\varphi r \cdot dr / \varphi r \text{ ---- (ii)}$$

where,  $\langle f^2 \rangle = [\sum c_i f_i]^2$ , mean of the square of the scattering factor in the  $n$  comp. System,  $\langle f \rangle^2 = [\sum c_i f_i]^2$ , the square of the mean scattering factor,  $\rho_r$  is the average number density function,  $\rho_0$  = average number density of the sample.

The average structure factor or interference function  $s(\varphi)$  is :

$$s(\varphi) = [ I_{ev}^{coh}(\varphi) - \{ \langle f^2 \rangle + \langle f \rangle^2 / \langle f^2 \rangle \} ] \text{ ----- (iii)}$$

The fourier transformation of  $\varphi[s(\varphi)-1]$  gives the average reduced distribution function  $G(r)$ .

$$G(r) = 2/\pi [s(\varphi)-1] \sin \varphi r . d\varphi \text{ ---- (iv)}$$

from the function  $G(r)$ , the radial distribution function is computed as,

$$4\pi r^2 \rho(r) = rG(r) + 4\pi r^2 \rho_0 \text{ ----- (v)}$$

The average pair probability function  $g(r) = \rho(r)/\rho_0$  ----- (vi)

The X-ray scattering experiment gives fingerprint data on the nature of the samples from the differential redf  $[G(r)]$  and the pair probability function  $[g(r)]$ .

In a typical experimental procedure, the X-ray specimen was prepared by pressing the powder into an aluminium holder at 25 mm diameter and 1.5 mm thickness. X-ray measurements were made with Cu  $K_\alpha$  radiation on a computer controlled Rigaku XRD (Model D-MAX III VC) equipped with a NaI scintillation counter, a curved graphite crystal monochromator and a nickel filter. The diffracted intensities were collected from 3.5 to 130° (2θ) range at a scan rate of 0.5° min<sup>-1</sup>. The intensities were corrected for air scattering by scanning blank sample and subtracting, for polarization and absorption effects and then normalized to convert the corrected intensities to the electron units. The mean atomic density  $\rho_0$  is computed from the relationship,  $\rho_0 = Nd/A * 10^{24}$ , where, d is the density in g/cm<sup>3</sup>, N is Avagadro's number and A is the atomic weight.

This technique is particularly used to study amorphous titanosilicate samples the details of which are discussed in chapter V.

### 2.3. X-Ray Fluorescence Spectroscopy (XRF)

When a sample is irradiated with powerful primary X-rays emitted from an X-ray tube, secondary X-rays (fluorescence X-rays) will come out from this sample. The secondary X-rays are then separated into its spectral components so as to selectively take out specific fluorescent X-rays caused by the aimed element and thereby qualitative and quantitative analysis is carried out.<sup>4</sup>

A schematic block diagram of X-ray fluorescence spectrometer is presented in Fig. 2.2a. It consists of :

- (i) *X-ray generator*: a unit designed to generate stable high voltage (10 kV - 100 kV) to be applied to the X-ray tube;
- (ii) *spectrometer assembly* : a unit designed to perform spectral work on fluorescent X-rays emitted from the sample;
- (iii) *electronic circuit panel* : a unit designed to count and record signals detected by the spectrometer assembly.

The basic structure of the X-ray tube is a diode which consists of a filament as the cathode generating X-rays by intercepting the accelerated electrons by means of the positive potential near the target. The window to pass X-ray to the out side tube is of the 'end-window' type, as shown in the Fig. 2.2 b.

The wavelength ( $\lambda$ ) of emitted X-rays and the atomic number  $Z$  is related by the formula,  $(1/\lambda)^{0.5} = C (Z-8)$ . Thus, it is possible to know the atomic number of a specimen when the wavelength of fluorescent X-rays emitted from a specimen is measured.

When the incident X-ray or electron beam strikes an electron in the K-shell and knocks it out from its orbit, the position of the electron in the orbit becomes vacant.

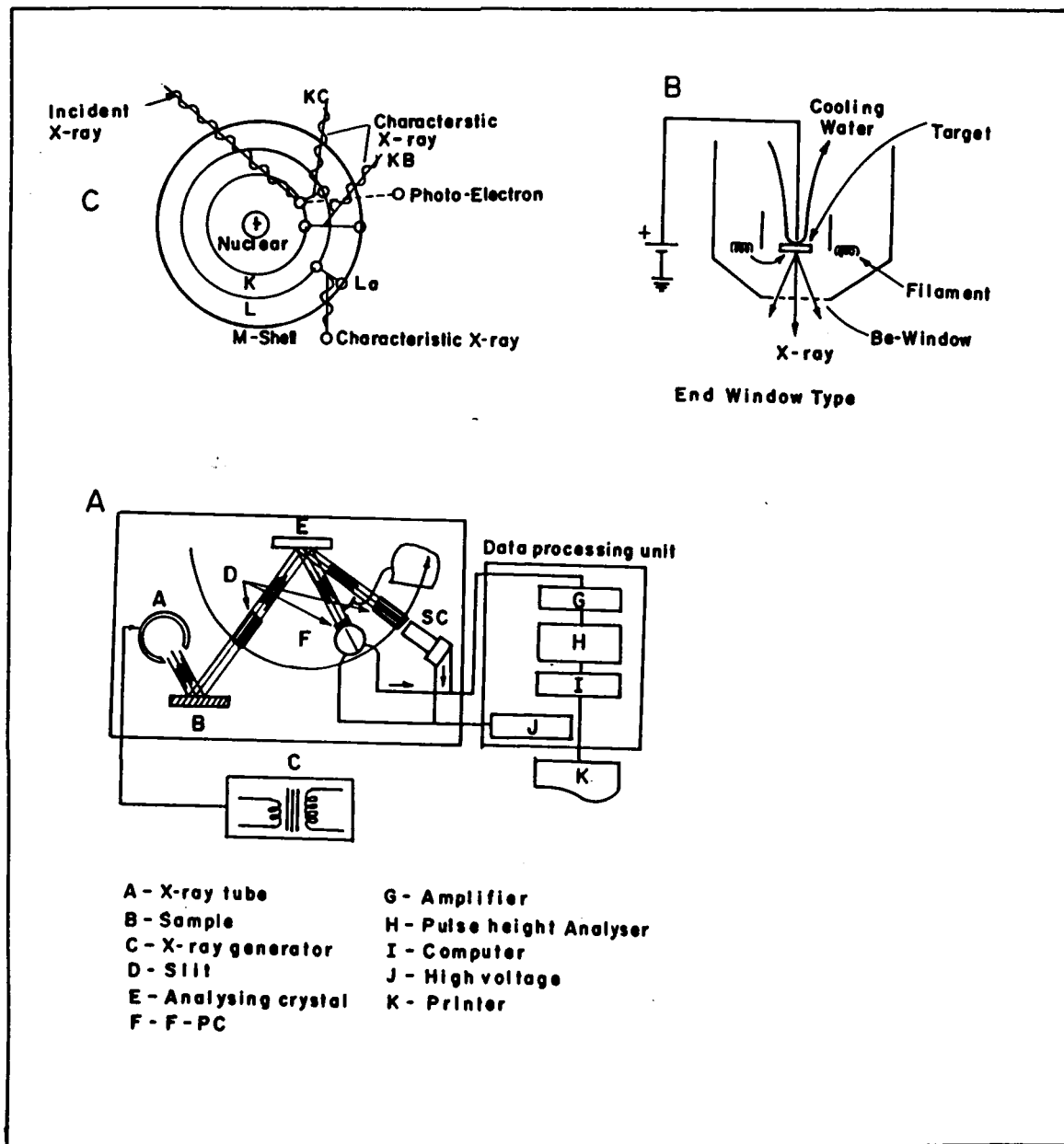


**Fig. 2.2 :** a) A schematic block diagram of X-ray fluorescence spectrophotometer;  
 b) end-window type window to pass X-ray; c) X-ray fluorescence phenomenon.

At this time, the electron moves to the K shell from the outer shell and cause the characteristic X-rays corresponding to the energy difference between the outer shell and K-shell (see Fig. 2.2 c).

In a typical experimental procedure, the sample was fused by 'Rigaku' bead sampler unit at 1523 K with lithium tetraborate and KBr as nonwetting agent in a platinum crucible. Standards were prepared under the same conditions as the sample from analytical grade metal oxides. The calibration curves for various elements were prepared keeping suitable measurement parameters under vacuum. It relies on the availability of a set of matrix matched standards, whose concentrations are accurately known and which cover a small concentration range around that of unknown sample. In addition, bulk solids should have the same surface finish and powdered solids should have similar particle size distribution and packing density.

The intensity of the analyte line (corresponding to the element to be analyzed) of the standards are measured and the data is used to prepare a calibration graph of intensity versus analyte concentration. The intensity of the analyte line of the unknown sample is then measured.

The instrument used in the present investigation is sequential X-ray Fluorescence Spectrometer, Rigaku-Model 3070, having End Window X-ray tube with Rhodium target.

## ***2.4. X-Ray Photoelectron Spectroscopy (XPS)***

X-ray photoelectron spectroscopy is based on the photoelectric effect. An atom absorbs a photon of energy  $h\nu$ , and subsequently, a core or valence electron with binding energy  $E_b$  is ejected with kinetic energy,  $E_k = h\nu - E_b$ .

An atom which has been ionized in one of the inner states may return to its electronic ground state *via* one of the following processes<sup>5</sup> (Fig. 2.3 a and b):

i) An electron of an energetically higher level, jumps in to core hole, the energy thereby released is emitted as a quantum of characteristic X-ray radiation; ii) the core hole is filled by an outer electron, but the available energy is transmitted in a radiationless process to a second electron which may then leave the atom with a characteristic kinetic energy, called Auger process; iii) as an electron moves through matter, it may suffer an inelastic collision. It will then appear in the spectrum with lower kinetic energy. These loss features are studied by electron energy loss spectroscopy (EELS) and contain information regarding the dielectric properties of the surface.

In XPS one measures the intensity of photoelectrons  $N(E)$ , as a function of their kinetic energy,  $E_k$ . Because each element has a characteristic spectrum of binding energy, XPS can be used to analyze the composition of sample.

The X-ray photoelectron spectrometer consists of the following basic components

(i) *Source* : In general  $MgK_{\alpha}$  or  $AlK_{\alpha}$  soft X-ray sources are employed since they yield reasonable resolutions needed for studying chemical shifts. The energies of these sources (1253.6 and 1486.6 eV, respectively) are sufficient for probing the core levels of the commonly observed elements.

(ii) *Sample preparation chamber*: The sample to be investigated is mounted inside the sample preparation chamber, which has to be at ultra high vacuum. Calcination, reduction and other pretreatment can be carried out in this chamber.



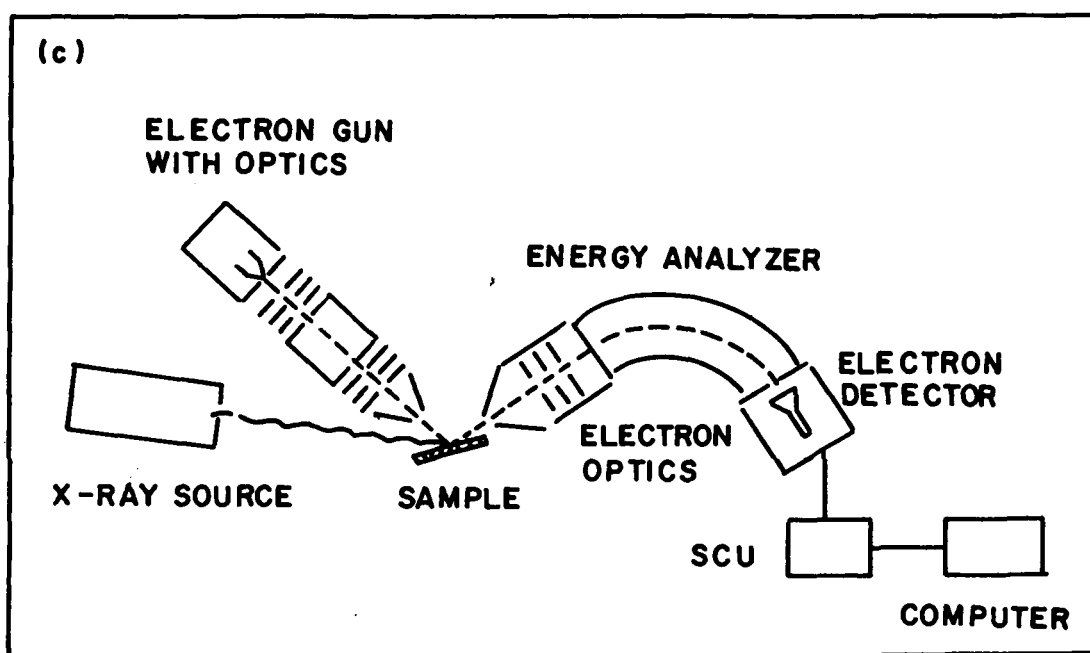
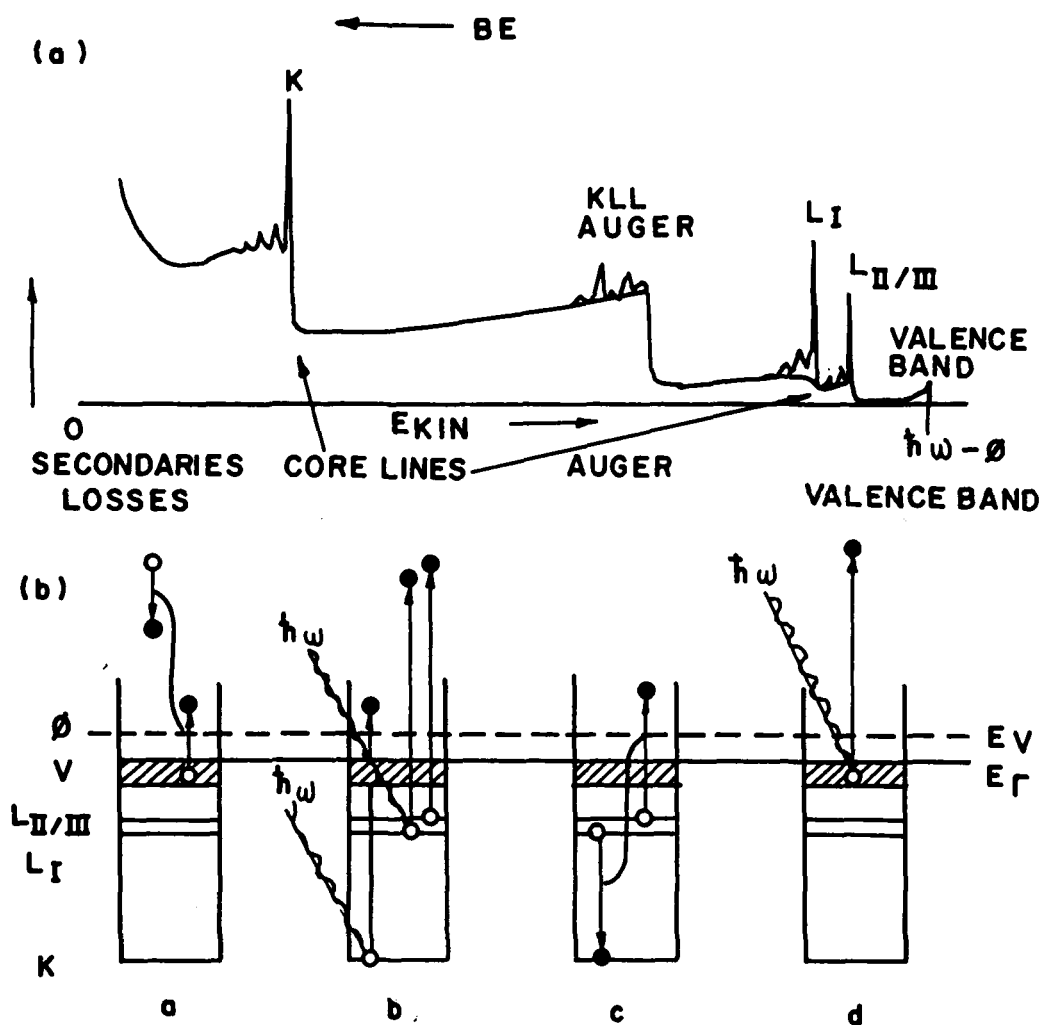


Fig. 2.3 : a) Emitted electron distribution curve under X-ray irradiation.  
 b) Physical mechanism explaining peaks occurring in Fig. 2.3 a.  
 c) A schematic diagram of XPS instrument

(iii) *Spectrometer analysis chamber* : After pretreatment of the surface, the sample is transferred to the spectrometer chamber for analysis. The chamber is equipped with the X-ray source, an electron gun and the electron energy analyser.

(iv) *Electron energy analyzer*: The most often used types are hemispherical and cylindrical mirror analyzers and they are capable of energy analysis in a wide range of electron energy, 0 eV - 2000 eV.

(v) *detector* : A simple electron collector with electrometer amplifier is suitable for currents higher than  $10^{-14}$  amp. An electron multiplier, often referred to as channel electron multiplier is commonly employed in various commercial spectrometers.

(vi) *data acquisition system* : The signal from the electron multiplier (channeltron) is fed to a computer for further data analysis.

A block diagram of the ESCA machine is given in Fig. 2.3 c.

### *Quantitative analysis*<sup>6,7</sup>

The photoelectron current for constant X-ray flux is given by

$$I = KN\sigma\lambda\tau,$$

where, I is photoelectron current for a given peak, K, a constant, N is density of atoms in analyzed layer,  $\sigma$  is photoelectron cross section,  $\lambda$  is electron inelastic mean freepath and  $\tau$  is spectrometer transmission function. If one assumes a weak energy dependence of  $\lambda$ , the relative atomic concentrations of two elements A and B can be evaluated from

$$N_A/N_B = I_A\sigma_B/I_B\sigma_A$$

Estimates of the photoelectron intensity is made by the computer integration of peaks with corrected base line. The photoionization cross sections are taken from tables.

The XPS measurements were carried out in a VG Scientific ESCA-3 MK2 electron spectrometer with an Al  $K_{\alpha}$  X-ray source.

## 2.5. UV-vis Spectroscopy

Information on the valence state of the ions incorporated in solid matrices, especially on their coordination and on the type of transitions involved can be obtained by spectroscopic investigations in the UV-Vis region (200 - 1000 nm).

The main components of the spectrophotometer<sup>8</sup> are schematically presented in Fig. 2.4

- i) The light source, L ( a deuterium lamp for UV and tungsten filament lamp for visible region);
- ii) Monochromator-MC consisting of a quartz prism or of a diffraction grating;
- iii) A system of mirrors for focalization of the light beam, M;
- iv) A device of mirrors for diffuse incident radiation- C;
- v) A detection system, D consisting of photosensitive cells in UV and the visible regions;
- vi) a system for registration, R.

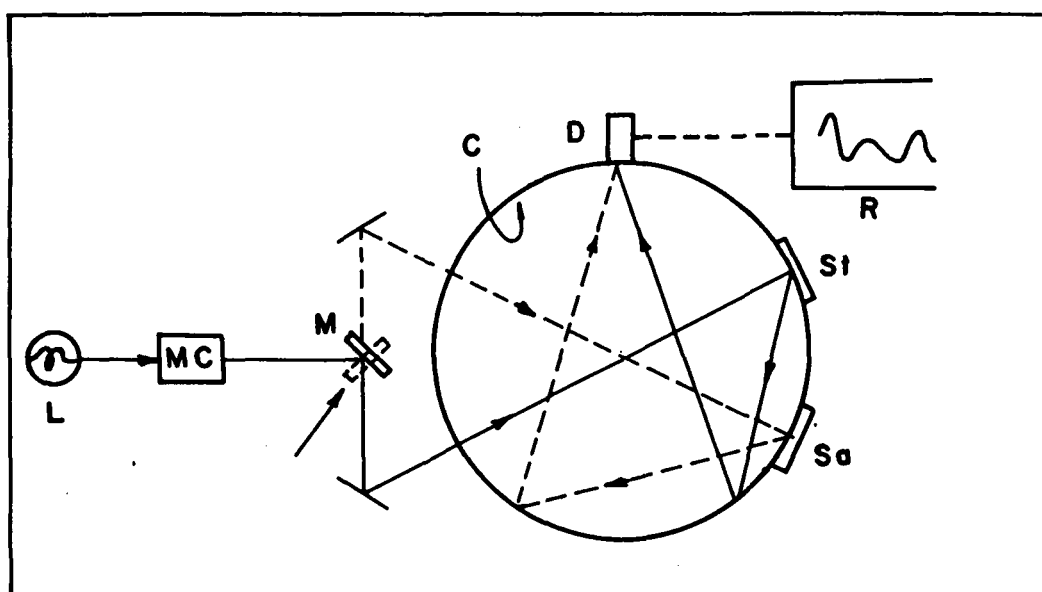


Fig. 2.4 : A schematic representation of diffuse reflectance device.

The measurements of the reflectance ability of the sample is carried out relative to the reflectance of a standard, BaSO<sub>4</sub> on a Shimadzu UV-2101 PC spectrophotometer equipped with an integral sphere.

## ***2.6. Infrared Spectroscopy (FTIR)***

IR radiation is an energy range that corresponds to transition between the vibrational energy levels of molecules. When IR radiation is incident on a sample, energy from the beam is absorbed by the molecule for the vibrational transition and an absorption band at corresponding frequency results. The most used portion of the infrared band lies in the region between 4000 - 400 cm<sup>-1</sup> where resonances with molecular vibrations occur. The frequencies, frequency shifts and the band intensities of the infrared spectra are sensitive to the local bonding state, orientation and physical environments of the catalyst surface.

The most common application of infrared spectroscopy in catalysis is to identify adsorbed species and to study the way in which these species are chemisorbed on the surface of the catalyst.<sup>9, 10</sup> More specifically, IR spectroscopy has been used to study the adsorption of typical probe molecules like ammonia, pyridine and other bases, hydrocarbons, carbon dioxide which can monitor either the acidic or basic sites on oxide catalysts.<sup>11</sup>

*The IR Spectrophotometer* : The design of the FTIR spectrophotometer is shown in the Fig. 2.5. Michaelson's interferometer lies at the heart of the FTIR instrument, in which the IR beam is split into two and then recombined. The division of the beam is

achieved by a beam splitter (commonly germanium coated KBr window) which transmits 50 % and reflects the rest. One part of the beam goes to a fixed mirror at a distance  $L$  and the other to a mirror which moves around the same length, thus introducing a varying path difference. When the beams are recombined an interference pattern is obtained. The intensity of the recombined signal can be expressed as:

$$I(x) = \sum_{n=1}^{N-1} S(w_i) \cdot \cos(2 \pi x w_i)$$

where  $w_i$  are the wave numbers of all the frequencies present and  $S(w_i)$  the intensity of the monochromatic line at wavenumber  $w_i$ . The interferogram is measured by recording the detector signal as a function of the path difference  $x$ , which contains all frequencies simultaneously as illustrated in Fig. 2.6a. This is achieved by using a helium-neon laser of accurately known frequency as a reference, in which the interferogram is measured at a series of discrete points, *eg.* The data point separation which is equal to the laser wavelength, so as to digitize very precisely the IR-interferogram (Fig. 2.6b).

Th 8458

The interferogram is then converted into a spectrum of the discrete frequencies by means of a Fourier Transformation (FT)<sup>13</sup>:

$$S(k\Delta w) = \sum_{n=0}^{N-1} I(n\Delta x) \cdot \exp(i2\pi nk/N)$$

The function  $S$  consists of the so-called Fourier coefficients, with which one can reconstruct the interferogram into intensities vs its wave numbers (Fig. 2.6c).

Advantages offered by FTIR are

- i) all frequencies can be measured simultaneously;
- ii) it offers high precision of IR wave number;

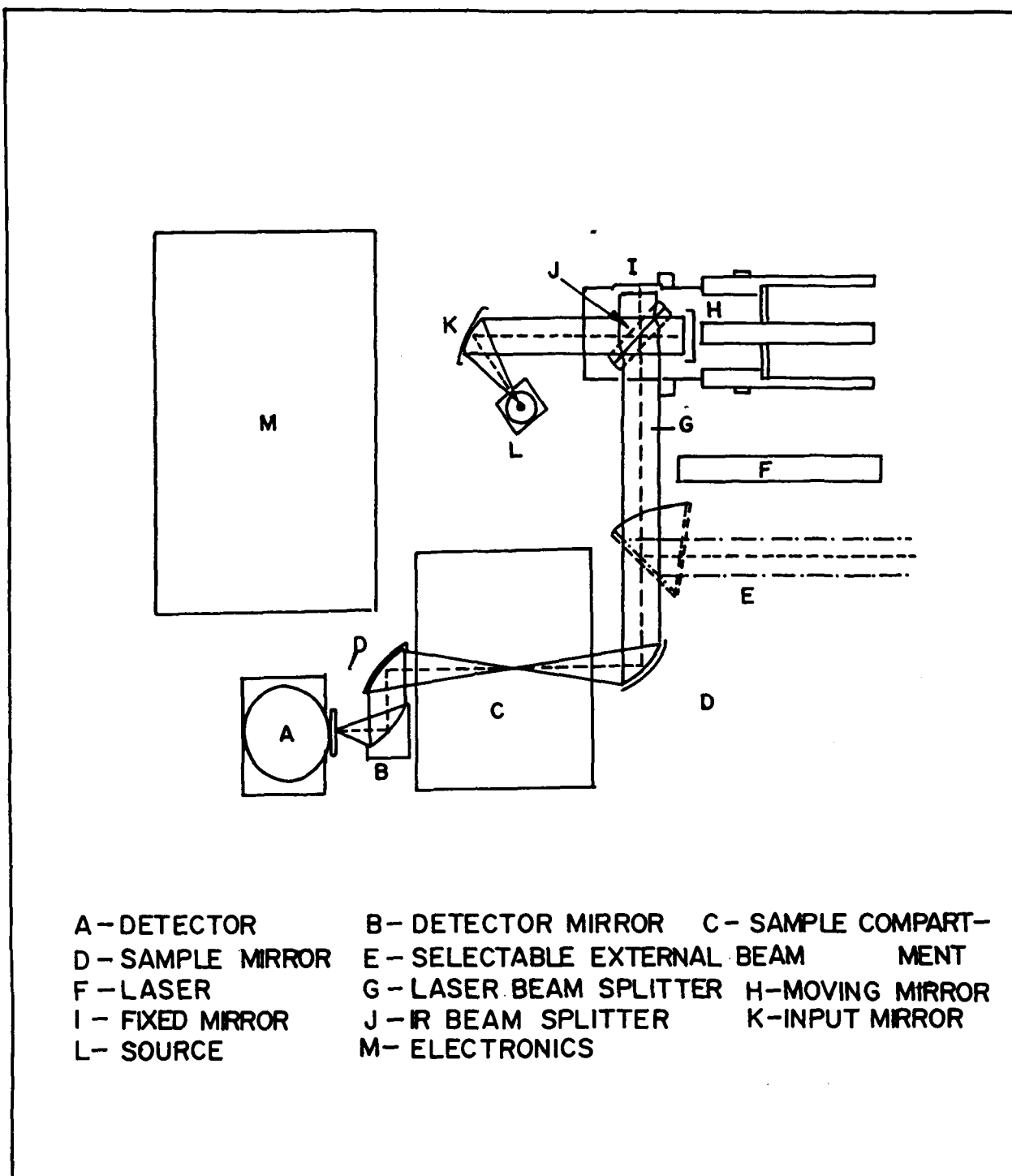


**Fig. 2.5** A schematic diagram of FTIR spectrophotometer based on a Michelson's interferometer.

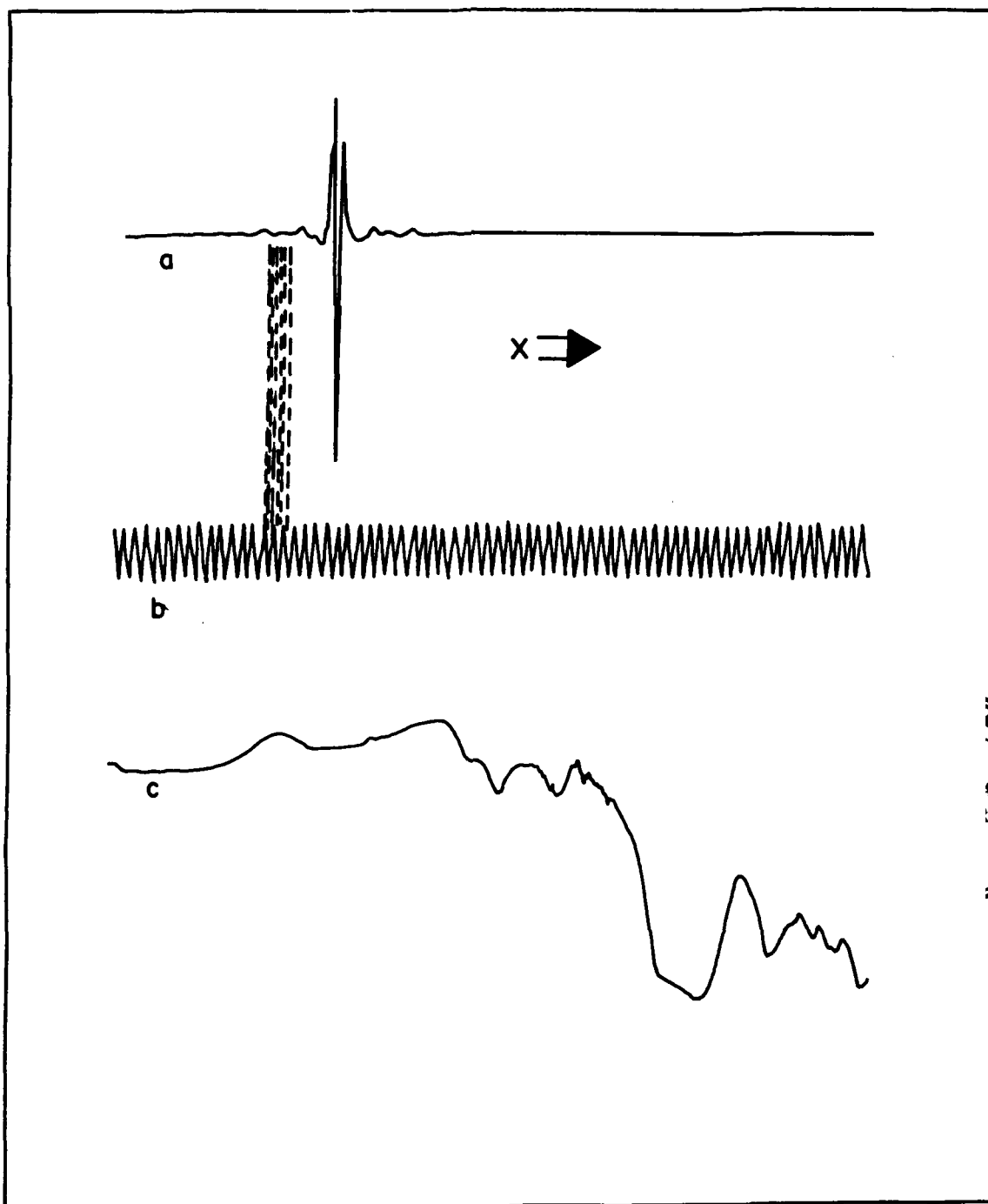


**Fig. 2.6** a) Interference patterns of a broad band source; b) He/Ne laser signal; and c) FTIR spectrum.

iii) it is possible to achieve high signal to noise ratio in shorter time because of the high energy throughput of the radiation.

*Sample preparation :*

Finely powdered samples are pressed under high pressure (10,000 - 20,000 psi) in a metal die in to a thin wafer which is placed in a sample holder inside an IR cell. The sample thickness should be optimum to provide many layers of adsorption sites but thin enough to allow the transmission of IR beam. Normally 10 - 20 mg cm<sup>-2</sup> is enough.

*The Infrared cell*

The design of the IR cell is schematically shown in Fig. 2.7. For the study of the adsorbed species, it should be possible to evacuate the cell at least up to 10<sup>-6</sup> torr and connect to a gas handling system for various treatments. In addition, there should be provision for heating or cooling the sample.

The framework IR spectra of the solid samples were recorded in a Nicolet (60 SXB) FTIR instrument, after deposition of the sample as a thin film on a Si plate and subsequent removal of background vibration due to Si.

The FTIR spectra of the adsorbed pyridine were used to identify the type of acid sites and relative amount of Lewis and Brönsted acidity. The IR spectra of the adsorbed pyridine were obtained using self supported wafers of the sample (5 mg/cm<sup>2</sup>). The sample was outgassed *in situ* at 673 K under vacuum (10<sup>-6</sup> torr) for 6 h and cooled to 373 K. The spectra were averaged for 500 scans with 2 cm<sup>-1</sup> resolution. Then the sample was equilibrated in pyridine vapour (10 mm v-p) for 1 h and excess pyridine was evacuated at 373, 473, 573 and 673 K for 1 h before recording the spectra.



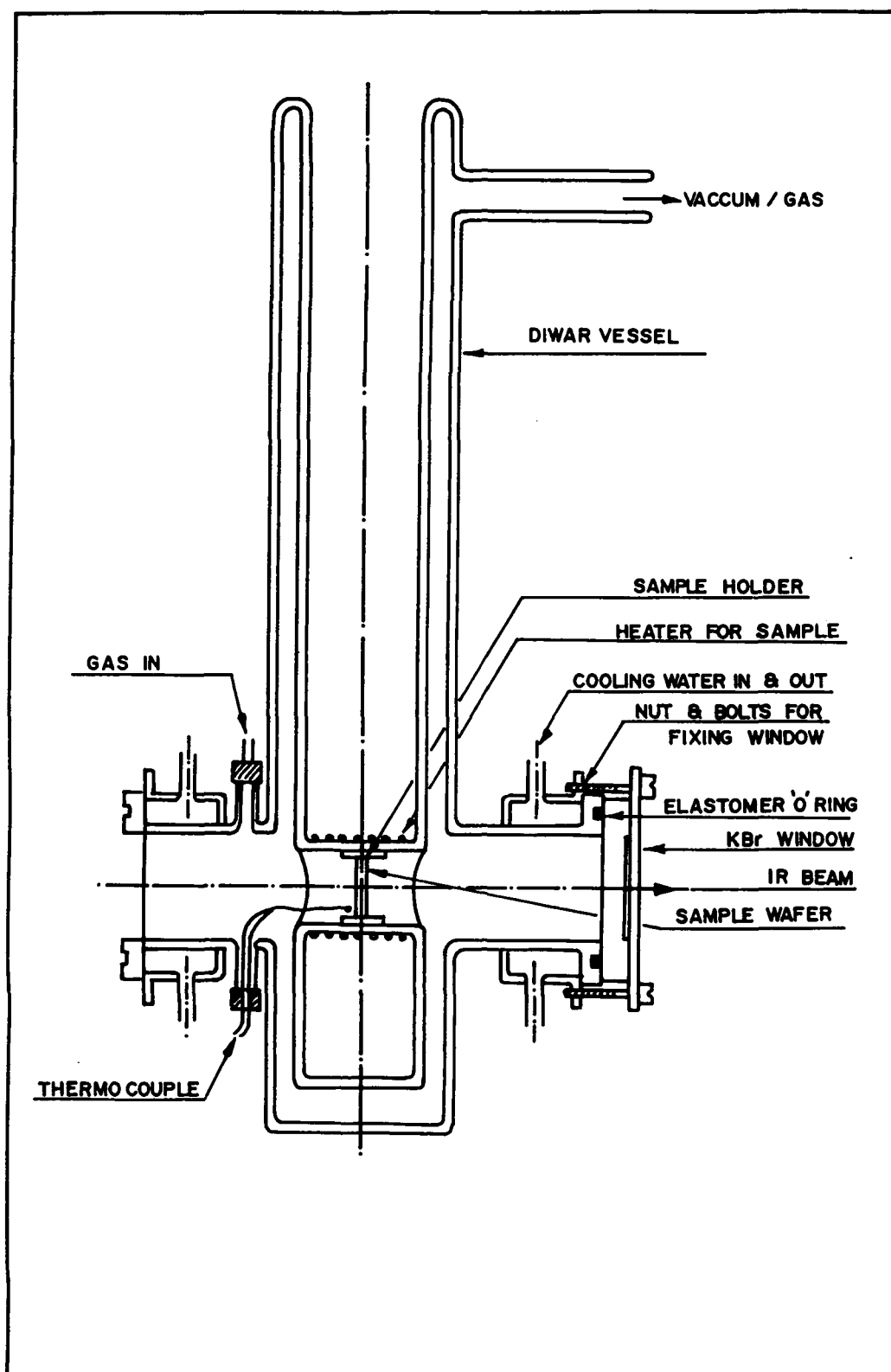


Fig. 2.7 Schematic diagram of a typical FTIR cell.

## ***2.7. Laser Raman Spectroscopy***

The laser Raman spectroscopic technique is closely related to vibration-rotation spectroscopy, since in these experiments the molecules are prepared in well defined vibration-rotation-translation states, before their interaction with the surface and after collision with the surface the final states are analyzed to deduce the dynamical processes that have taken place during molecule - surface interaction.

In these studies, one uses a supersonic molecular beam with almost all the molecules occupying the first few rotational levels of the vibrational ground state, and also with a very narrow, well defined velocity distribution, corresponding to less than few Kelvin temperature. The molecules are then brought in to the desired vibration-rotation state by excitation with a narrow band tunable infrared laser and the excited molecules are allowed to undergo collision with the required surface. The scattered molecules are analysed for their angular distribution, translational energy changes, and changes in internal energy distribution.<sup>13-15</sup>

A schematic diagram of the Laser-Raman spectrometer is shown in Fig. 2.8. The Raman scattering measurements were performed in the region  $100 - 810 \text{ cm}^{-1}$  in the back scattering mode using SPEX 1403 reflection grating type double spectrometer. The SPEX 1442 third monochromator, slaved in tandem to the double monochromator was used to reduce the Rayleigh light and other background effects. The data were collected in the photon counting mode using the RCA C31034 GaAs photo-multiplier detector system and SPEX DM1 DATAMATE spectrometer controller and data processor. The radiation of wavelength 514.5 nm from the Argon-ion laser (Spectra Physics

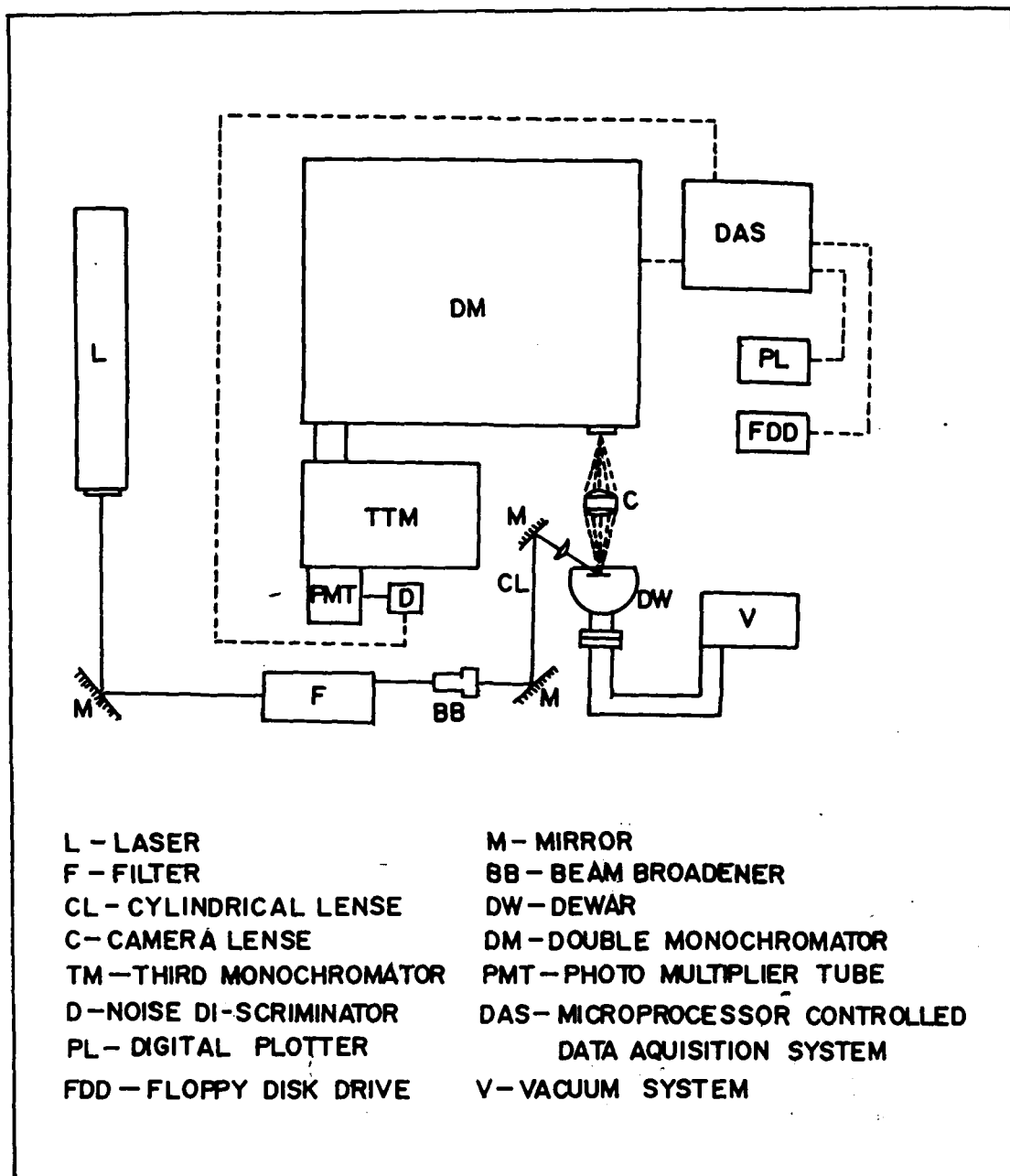


Fig. 2.8 A schematic diagram of laser Raman spectrometer.

model 165-B), filtered through the SPEX lasermate was allowed to fall on the sample in a line focus geometry (about 1 cm x 0.005 cm area) with the help of a cylindrical lens. The intensity of the radiation incident on the sample was 250 mW. The scattered radiation collected and focused onto the spectrometer slit using a Minolta camera lens (55 mm,  $f/1.2$ ). The polarization of the incident radiation was kept fixed in the horizontal plane. The actual positions, intensities and widths of the various Raman bands were measured after a light smoothing of the raw data by using the in-built software of the DM1 data processor. The ultimate resolution at the 250  $\mu\text{m}$  wide exit slit was about  $\pm 2 \text{ cm}^{-1}$ .

## ***2.8. Nuclear Magnetic Resonance Spectroscopy***

NMR technique is applicable to all nuclei having non-zero nuclear spins. When a sample with such nuclei is placed in a strong magnetic field, magnetic polarization of the nuclei takes place and only two possible nuclear energy states, *i.e.* those with magnetic moments aligned parallel or anti parallel to the applied field exist. The parallel orientation is more stable by a small amount of energy  $2\mu H_0$ , where  $\mu$  is the magnetic moment and  $H_0$  is the magnetic field at the site of the nucleus. An NMR experiment involves the introduction of transition between the lower to the higher state by the application of a radio frequency field of frequency  $\nu_0$  such that  $\nu_0 = g H_0$ , where  $g$  is the gyromagnetic ratio.

A schematic diagram of NMR spectrometer is given in Fig. 2.9 a. A typical NMR spectrometer consists of four major components i) a magnet and a device for stabilizing the magnetic field; magnet must be capable of giving intense stable magnetic

field with a homogeneity of the order of parts per billion; ii) a sample probe which houses the sample and allows resonance to take place; a schematic diagram of the sample probe is shown in Fig.2.9b. The probe will allow the sample tube to be spun, usually by an air jet directed towards a spinner turbine. iii) a source and a detector of radio frequency radiation; radio frequencies are generated by electronic multiplication of the natural frequency of quartz crystal contained in a thermostated block and iv) a data recorder.<sup>16</sup>

### MAS NMR :

In solids, since the molecules are rigidly bound to the lattice, all anisotropic interactions are present in full strength and the spectrum is broader. The dominant contribution to the line broadening arises from the dipole-dipole interactions. This type of broadening can be suppressed by the so-called 'Magic Angle Spinning' (MAS)<sup>17</sup> According to this technique, the dipolar coupling of any two spins can be reduced to zero on an average by spinning the sample about an axis making an angle  $\theta$  with the magnetic field such that  $(3\cos^2\theta-1)/2 = 0$ . This corresponds to the value of  $\theta$  equal to  $54.7^\circ$  and is called the *Magic Angle* since it produces miraculous effects in the line widths of the NMR spectra in the solid state.

Solid state MAS NMR spectra were obtained with a 'Bruker AM 300' high resolution multinuclear NMR spectrometer.  $[\text{Al}(\text{H}_2\text{O})_6]^{3+}$  and trimethyl silane were used as external standards for  $^{27}\text{Al}$  and  $^{29}\text{Si}$  NMR, respectively. The spectra were recorded at room temperature. The  $^{29}\text{Si}$  MAS NMR spectra were obtained at 79.5 MHz at a spinning rate of 3 kHz with a radio frequency pulse of 2.3 microseconds. The  $^{27}\text{Al}$  MAS NMR spectra were obtained at 104.3 MHz at a spinning rate of 4 kHz with a radio frequency pulse of 4 microseconds.

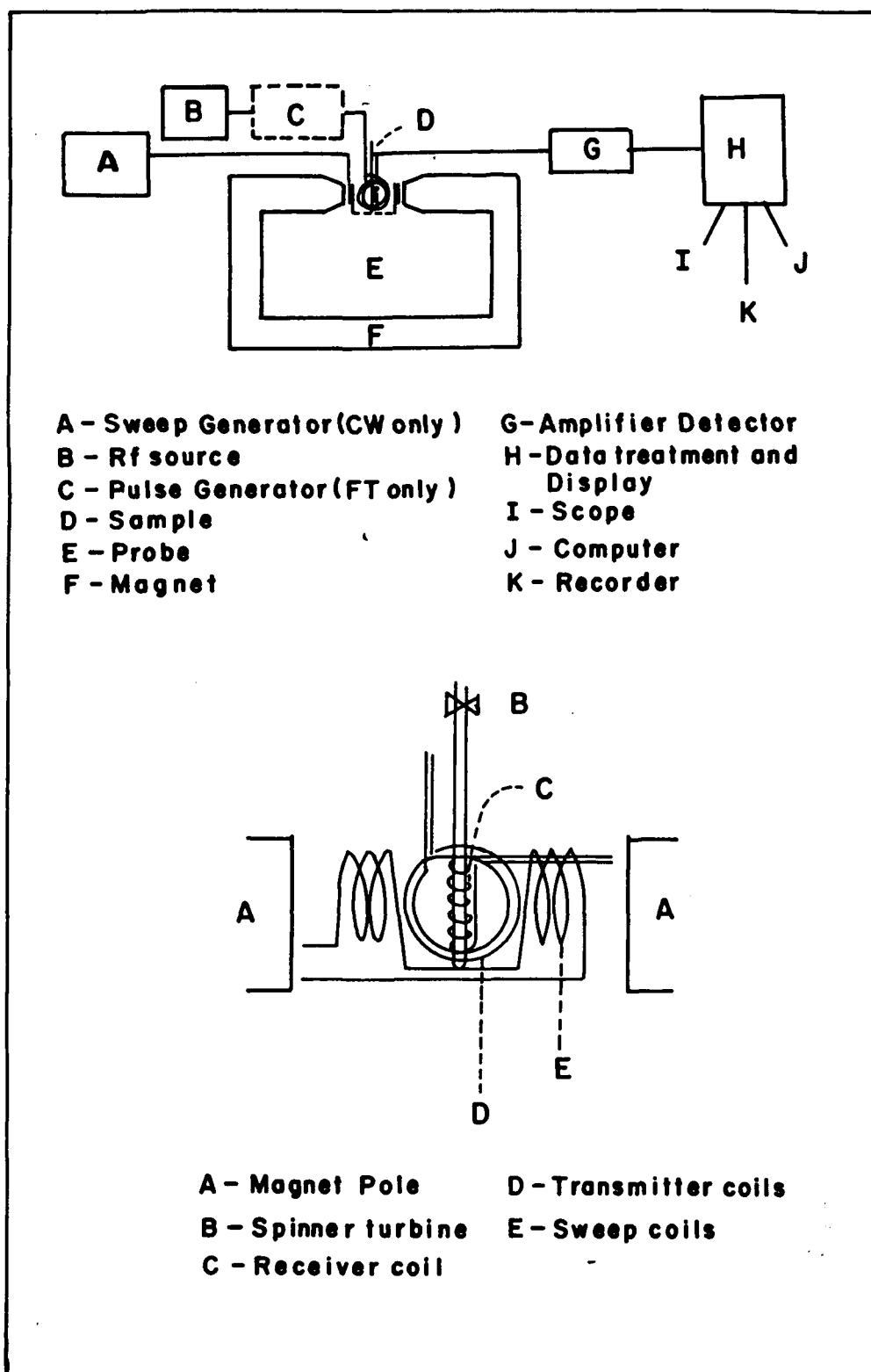


**Fig. 2.9** (a) A schematic diagram of NMR spectrometer;  
 (b) Sample probe used in the experiment.

## ***2.9. Scanning Electron Microscopy (SEM)***

Scanning electron microscopy (SEM) is considered to be a powerful tool to look mainly at the morphology and particle size. SEM is carried out by rastering a narrow beam over the surface and detecting the yield of either secondary or back scattered electrons as a function of the position of the primary beam.

A schematic block diagram of a scanning electron microscope is presented in Fig. 2.10. It consists of three major parts;<sup>18</sup>

- i) electron optical column
- ii) vacuum system
- iii) electronic and display system

The source of illumination is the invisible beam of electrons produced by the process of thermionic emission by heating a V shaped tungsten filament electrically to about 2700 K. To accelerate the electrons away from the filament, a high negative voltage (typically 2 to 25 kV) is applied between the filaments. This electron beam emerges in 10-50  $\mu\text{m}$  in diameter. To remove the most of the gas molecules from the beam's path a vacuum system is connected. The condenser lenses control the diameter of the beam and reduce it to around 5 nm. This then passes through the objective lens to ensure that the beam has its smallest diameter when it strikes the specimen surface. This results in electron emission from the specimen, which are collected by the detector and subsequently they are converted in to a small electron signal. The beam is thus systematically moved point by point along a line and reflected electron signal is collected. Usually one complete scan consist of one thousand lines, each of one

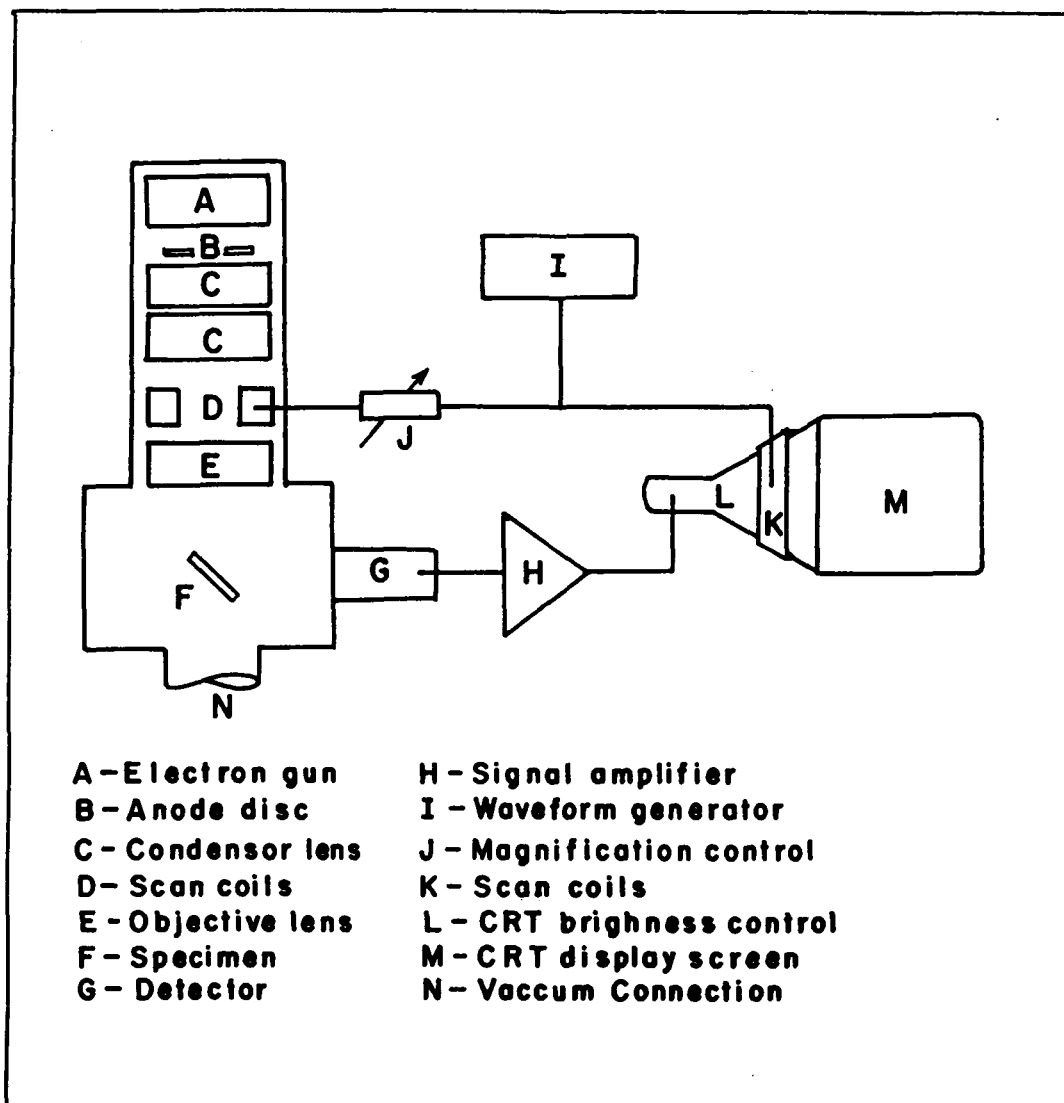


Fig. 2.10 : A schematic block diagram of scanning electron microscope.



thousand points called a 'frame'. Two pairs of scan coils at right angles to the beam supplied with specially shaped current wave forms produced in the wave from the generator makes the beam to scan in this way. A 'cathode ray tube' (CRT) is used to present the signal in an instantly recognizable form, a picture.

For most practical purposes, the SEM's display screen is limited to about 20 cm<sup>2</sup> and the resolution limit is 0.1 μm, and maximum magnification possible is about 20,000 times.

*Sample preparation:* Dry samples are fixed into small holders called 'stubs'. Non-conductive specimens are coated with uniform conductive layers, preferably gold. Coating is usually done by sputtering or evaporation prior to recording SEM photographs. The instrument used in the present study is 'Jeol Model 5200' unit.

## ***2.10. Transmission Electron Microscopy (TEM)***

Information obtained by TEM is derived from the scattering process that takes place when electron beam travels through the specimen. The basic reason for utilizing the electron microscope is its superior resolution resulting from the very small wavelength as compared to other forms of radiation.

The transmission electron microscope can be operated to form images by bright field, dark field or lattice image phase contrast modes. In addition, it is also possible to form diffraction patterns by using selected area apertures and focusing the intermediate lens on the diffraction pattern formed in the back focal plane of the objective lens.<sup>19</sup>

A schematic ray diagram of TEM operated for imaging and selected area diffraction ( SAD ) is shown in Fig. 2.11. It consists of an electron gun, which

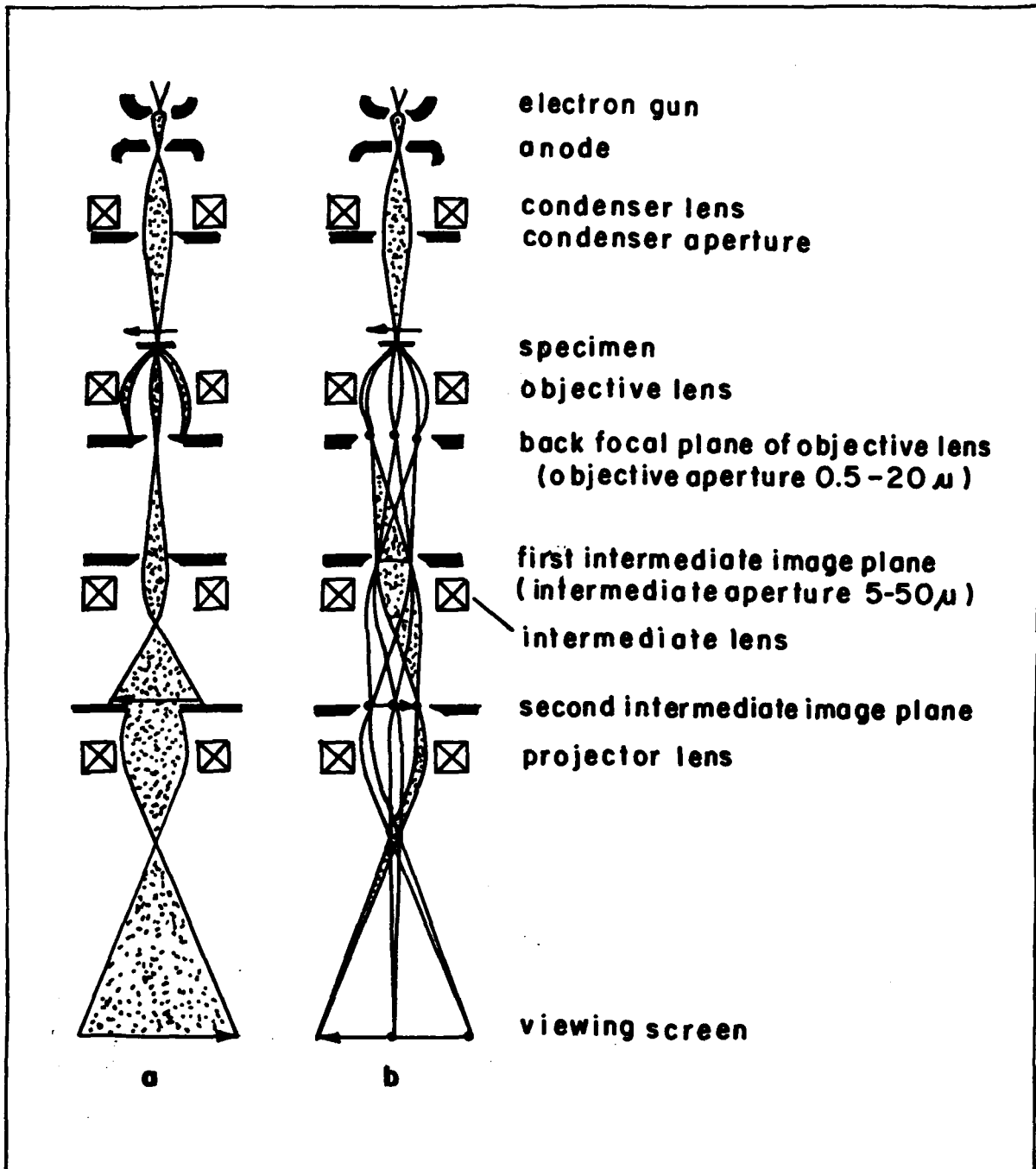


**Fig. 2.11** A schematic ray diagram for a three lens imaging microscope operated for (a) imaging and (b) selected area diffraction.

produces partially collimated electron of required energy ( 100 keV ). As the collimated beam of electrons passes through the sample, it is scattered according to Bragg's law. The beams that are scattered at small angles ( 1 to 2 degree ) to the transmitted beam are focused by the objective lens to form a diffraction pattern at its back focal plane. When the intermediate and the projector lens system are properly focused, a magnified image of the back focal plane of the objective lens will be projected on the viewing screen. The intermediate selected area diffraction (SAD) aperture makes it possible to obtain diffraction patterns from small portion of the specimen. This technique is very useful, since a correlation can be readily made between the morphological and crystallographic information of very small areas. The technique is of particular importance if more than one phase is present in the specimen.

Apart from the selected area diffraction, direct lattice imaging may also be used to calibrate magnification greater than 2,00,000 times. From a lattice image of known standard specimen (gold), the magnification may be determined by measuring the interplanar spacing on the microscope plate and comparing this value with the known d-spacing of the material.

When the image is formed by the diffracted beam, the imaging technique is called *the dark field technique*. By this technique, it is possible directly to resolve the structure images of individual atoms. This method is very useful in the characterization of complex microstructure. Alternatively, amplitude contrast is obtained by deliberately excluding the diffracted beam and hence the phase relationship. From the imaging sequences by the use of suitably sized aperture, a back focal plane of the objective lens is placed and such an image is called *bright field image*.

TEM and electron diffraction of the sample were carried out in a Jeol (Model 1200 EX) electron microscope. Typical operating conditions of a conventional TEM instrument is 100 keV electrons,  $10^{-6}$  m bar vacuum, 0.5 nm resolution and a magnification of 300,000.

## 2.11. Thermal Analysis

Thermal method of study gives the simultaneous recording of weight change (TG), differential weight change (DTG) and differential heat change (DTA) of solid sample (catalyst precursors) as a function of temperature under any gaseous atmosphere.

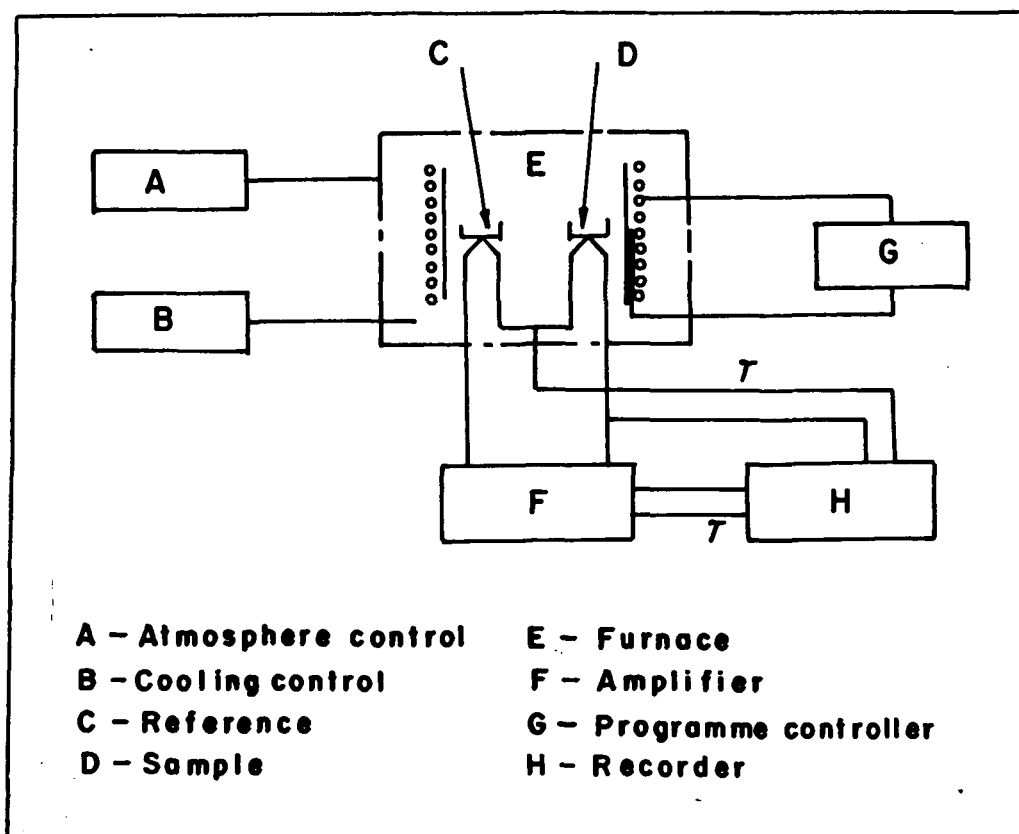


Fig. 2.12 : A schematic diagram of TG-DTA system.

A schematic diagram of the TG-DTA system is given in Fig. 2.12. It consists of following components.

- i) sample holder assembly; (ii) furnace; (iii) temperature programmer
- iv) recording device; (v) atmospheric control; (vi) cooling control

The details of the instrumental aspects are given elsewhere.<sup>20</sup>

The thermal analysis of the catalyst precursors was carried out on TG-DTA-92 (Setaram, France) instrument at a heating rate ranging from 2 to 10 K min<sup>-1</sup> under flowing air. Sensitivity of the instrument with respect to TG is 2 mg, DTA is 0.1 mV and DTG is 0.2 mV.

## ***2.12. Temperature Programmed Reduction (TPR)***

TPR is a technique used for the reductive chemical characterization of solids. The essence of the technique is the reduction of a solid by a gas at the same time that the temperature of the system is changed in a predetermined way.<sup>21</sup> The solid is reduced by flowing hydrogen, the concentration of which is monitored down the stream of the reactor. The analysis of the record is simply the hydrogen consumption due to reduction and is usually displayed as a function of temperature.

A schematic diagram of the TPR instrument with thermal conductivity detector is represented in Fig. 2.13.

A weighed amount of the sample is placed in the reactor which is connected to the apparatus. Before the actual TPR measurements the sample may be subjected to a variety of pretreatment. For reduction, 5 % H<sub>2</sub> in Ar is used. This passes through the

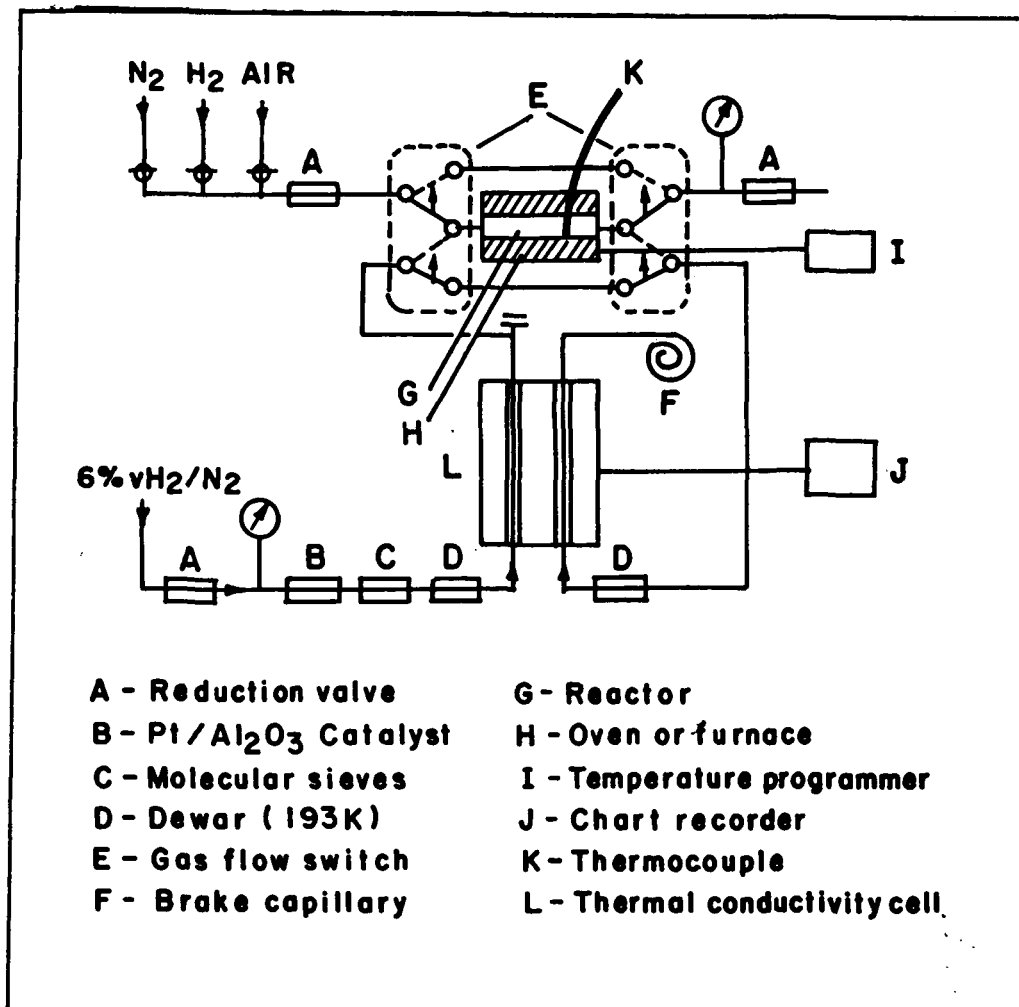


**Fig. 2.13** A schematic diagram of temperature programmed reduction apparatus.

system at a flow rate of usually 600 - 1200 ml h<sup>-1</sup> and an over pressure of 0 - 0.5 atm. The reducing gas is passed through a deoxygenation catalyst, a cold trap, through one arm of the thermal conductivity cell and then through the reactor, which is heated at a linear programmed rate (usually 1 -20 K min<sup>-1</sup>) then once again through a cold trap to the other arm of the thermal conductivity cell where any change in the hydrogen concentration is monitored. The change in the hydrogen concentration with time is displayed on the recorder. Distinct reduction process in the sample shows up as TPR profile.

### ***2.13. N<sub>2</sub> Adsorption methods***

In this technique the total volume of gas delivered or withdrawn from the sample is calculated by multiplying the flow rate by total experimental time. The volume adsorbed by the sample is calculated by subtracting the "dead space" volume, *i.e.*, the volume of the manifold, holder, and sample. This volume can be calculated by two different methods depending on the type of analyzer.

#### ***Instrumental description :***

The schematic diagram of the N<sub>2</sub> adsorption unit is given in Fig. 2.13. It consists of an outgassing section and a physisorption section. The temperature in the outgassing section is varied as per the requirements. Three capacitance type pressure transducers (MKS Baratron) are provided in the sorption section to monitor the sample pressure and the saturation pressure. The vacuum in the system is measured with a Penning gauge. The physisorption section contains the sample port and the reference port which is used for monitoring the saturation pressure of the adsorbate.

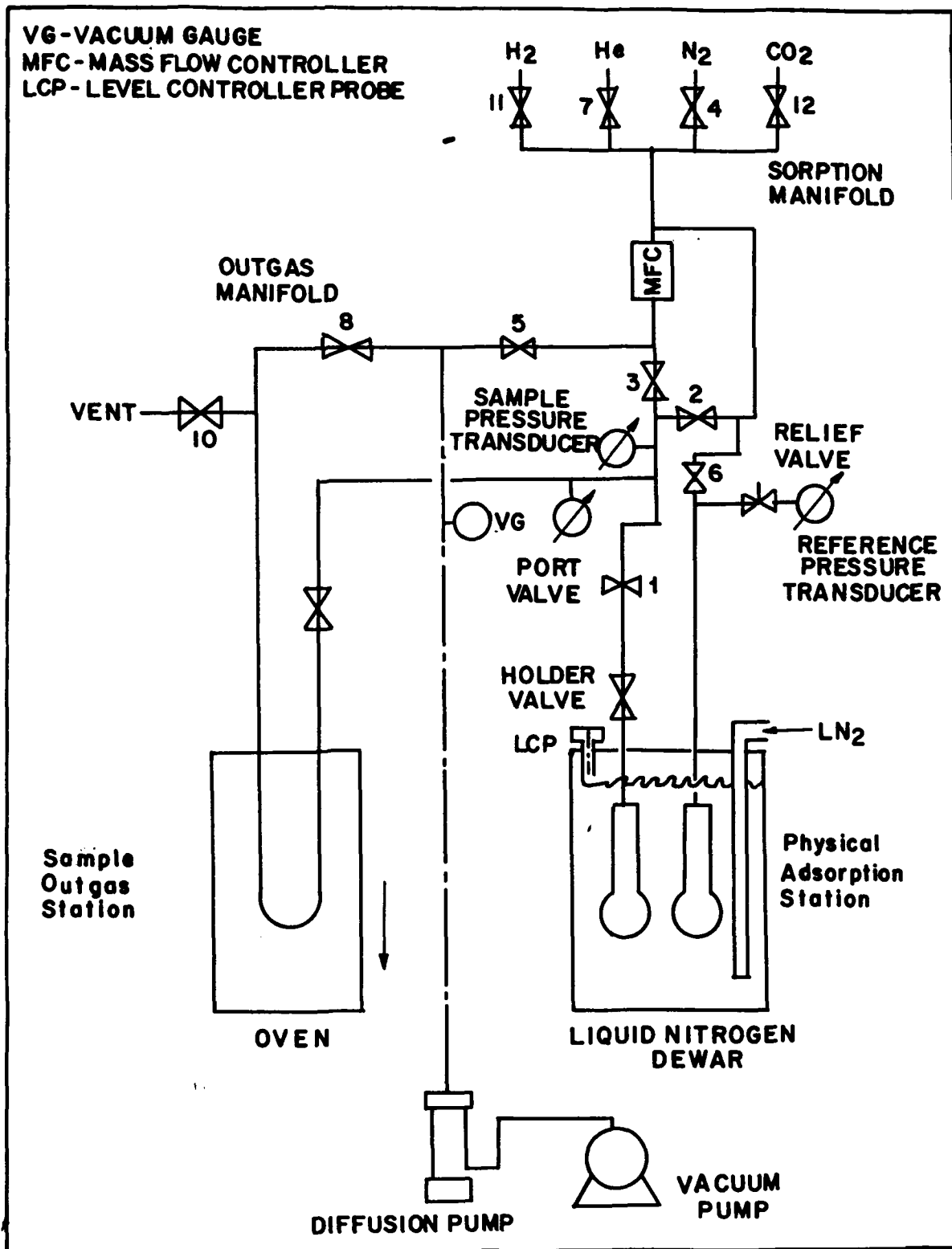


Fig. 2.14 : A schematic diagram of N<sub>2</sub>/Ar surface area analyzer (Omnisorp 100 CX).



The sample is immersed in the liquid nitrogen contained in the Dewar provided with the unit. Interfacing between the instrument and the computer is done by two interfacing cables. The data is acquired using an A/D converter.

***Adsorption isotherm and BET surface area :***

By knowing the volume adsorbed ( $V_s$ ) by the sample at different pressures ( $X_p$ ) and the saturation pressure ( $p_o$ ), the adsorption isotherm will be given by plotting  $V_s$  versus the partial pressure of nitrogen,  $X_p/P_o$ . The surface area of the sample is obtained by using the adsorption isotherm and linearized BET equation, which is given below :

$$X_p/V_s(P_o - X_p) = 1/V_m C + [(C-1)/V_m C] * (X_p/P_o),$$

where  $V_m$  is the monolayer capacity and  $C$  is the BET constant related to the enthalpy of adsorption. By plotting the left side of the equation versus  $X_p/P_o$  (the relative pressure of adsorbate), a straight line will result from which the following information is obtained.

$$\text{Slope} = S = (C-1)/V_m C$$

$$\text{Intercept} = I = 1/V_m C$$

$$C = (S/I) + 1$$

$$V_m = 1/S + I$$

The BET surface area is calculated using the following equation :

$$SA = V_m \cdot N \cdot A_m$$

where  $SA$  is the surface area of the sample,  $V_m$  is the volume adsorbed by a monolayer,  $N$  is the Avagadro's number and  $A_m$  is the cross sectional area of the adsorbate. For nitrogen, a value of  $16.2 \text{ \AA}^2$  for  $A_m$  was used, and after applying the appropriate conversion factors, equation will be simplified to

$$SA = 4.35 * V_m \quad m^2 g^{-1}$$

*T-plot analysis* : To differentiate between the adsorption mechanism in micropore and that occurring in meso and macropores, the t-plot analysis developed by Lippens and de Boer was applied.<sup>22</sup> The method consists of plotting the adsorption isotherm in terms of the volume of the gas adsorbed versus the statistical film thickness, t.

The t-plot consists of two regions separated by a transition region. The first linear region represents both micropore filling and surface coverage of larger pores. The second linear region gives the layer by layer adsorption taking place in meso and macropores and not in micropores. The *micropore volume* is obtained by extrapolating the second linear region to the y-axis. The y-axis intercept multiplied by the ratio of the gas and liquid densities of adsorbate (0.00156 for nitrogen) will provide micropore volume in cc per gram of the solid. The meso and macropore area is given by the slope of the second linear region.

#### *Pore size distribution and pore volume*

The pore size distribution is obtained from the analysis of the desorption isotherms by applying the BJH model<sup>23</sup> which involves the area of the pore walls and uses the Kelvin equation to correlate the partial pressure of nitrogen in equilibrium with the porous solid to the size of the pores where the capillary condensation takes place. Similarly, the micropore size distribution is calculated by applying Horwath-Kawazoe model.<sup>24</sup>

The values of the different constants needed to calculate the pore size distribution parameters are given below

Surface tension of nitrogen, = 8.855 mN/m; Molar volume,  $V_m = 34.6 \text{ cm}^3 \text{ mole}$

Normal boiling point of  $N_2 = 77.3 \text{ K}$  Ideal gas constant =  $8.31 * 10^7 \text{ erg/mole}$ .

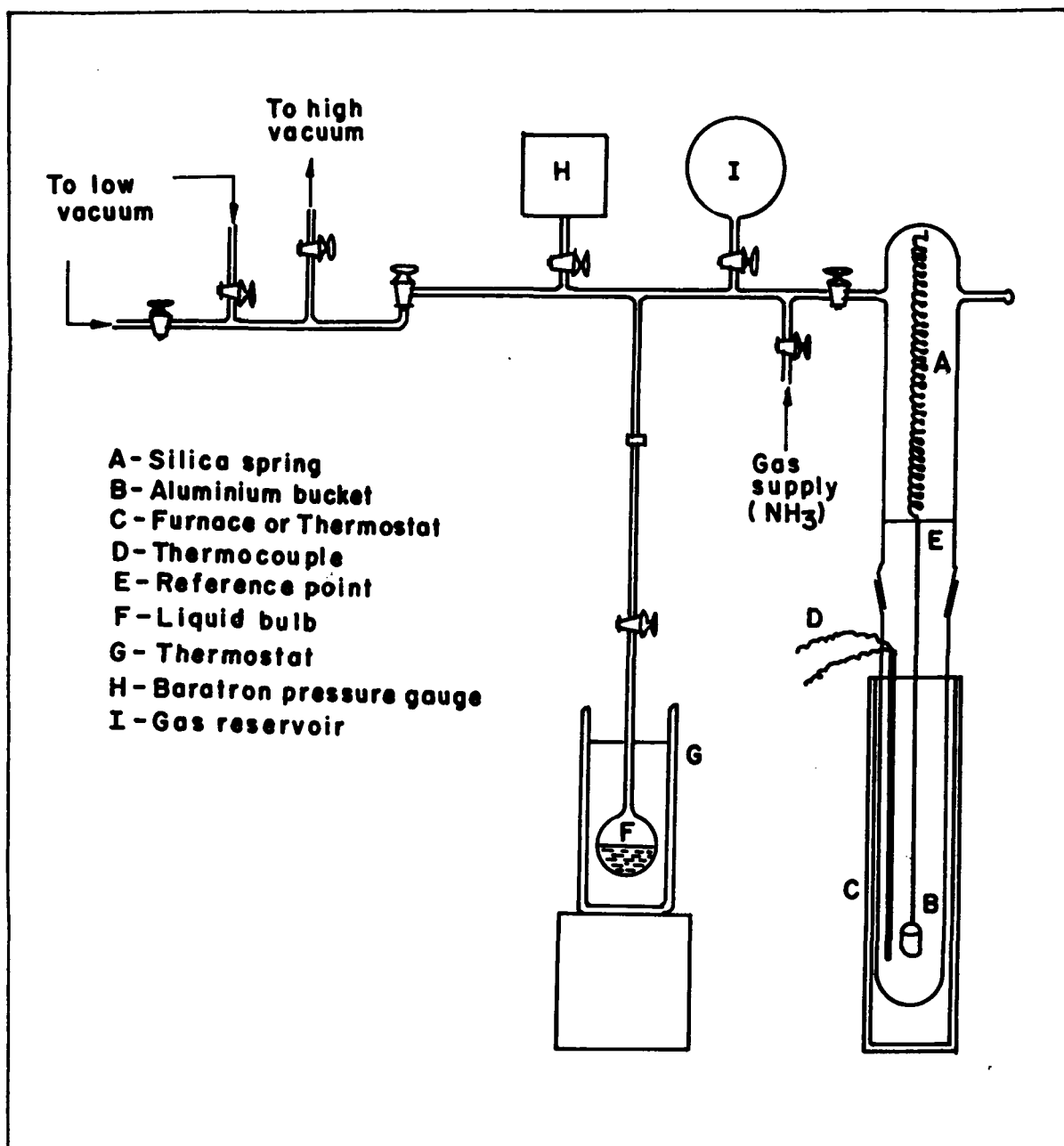


Fig. 2.15 Gravimetric adsorption unit

Conversion factor for gas STP to liquid volume = 0.00156

N<sub>2</sub> adsorption studies were carried out on Omnisorp analysers using the continuous sorption technique to obtain the gas adsorption or desorption isotherm for a solid sample.

## ***2.14. Sorption studies***

The sorption measurements for hydrocarbons in the pores of mixed metal oxide catalysts were conducted on McBain type gravimetric unit (Fig 2.15)

A sensitive silica spring was used for the measurement of weight changes. About 100 mg of sample was pressed in to a pellet and weighed in to an aluminium bucket suspended to a silica spring. The assembly was evacuated by means of a two stage rotary pump and an oil diffusion pump to a vacuum of 10<sup>-6</sup> torr. The sample was activated at 673 K by continuous pumping till a constant weight was obtained. After the sample had reached a constant weight, the temperature of the sample was lowered to the desired value. To study the equilibrium sorption capacity, the sorbate (like H<sub>2</sub>O, benzene, n-hexane, mesitylene, 1,3,5-triisopropylbenzene) was introduced to the sample at a constant temperature and partial pressure of the sorbate and the weight gain was recorded on a catherometer as a function of time. After recording the equilibrium sorption, the catalyst was evacuated and outgased to 673 K at 10<sup>-6</sup> torr, and used for the next sorption measurement.

## 2.15. Particle Size Analysis

The particle size analysis is done on the basis of photoextinction phenomenon and Stoke's law of sedimentation on micron photosizer.

A light beam passes through the suspension and particles in it extinct the light. As the particles undergo sedimentation, the intensity of the light becomes stronger as a function of time. From this phenomenon, micron photo size analyzer determines the particle size distribution. In order to improve the sedimentation speed of fine particles, a centrifuge is used in the process of measurement.

According to Stoke's law, sedimentation speed is related to the particle diameter by  $V = [0.03267(\rho_p - \rho_f)(X)^2] / \mu_f$

where,  $V$  is sedimentation rate in  $\text{mm min}^{-1}$ ,

$\mu_f$  is viscosity of the liquid in centi poise.

$X$  is particle diameter in microns

$\rho_p$  and  $\rho_f$  are the density of the particle and the liquid.

If  $h$  is the depth from the surface and  $T$  is the sedimentation time, then

$$h = VT = T[0.03267(\rho_p - \rho_f)(X)^2] / \mu_f$$

Thus, by knowing the sedimentation time, particle diameter can be calculated.

In a typical procedure, 50 mg of the sample was put into 100 ml of water contained in a beaker. About 0.5 mg of sodium meta phosphate was added as a dispersing agent. The beaker was subsequently kept in the ultrasonic vibrator for 20 minutes. In the meanwhile, the input conditions (details of the particle density, medium density, height of the cell, etc.) was fed to the computer and the time chart was taken and the blank measurement was carried out.

The well dispersed sample was then poured into the sample cell and mounted inside the measurement chamber. The measurement was then started.

After the completion of the measurement of the light intensity during the natural sedimentation, the sample cell was subjected to centrifugation, the RPM of which is as prescribed in the time chart. Then the sample cell was again kept in the measurement chamber and the intensity of light was measured.

The particle size analysis is carried out using a Micron Photo sizer instrument, (Seishen, Japan). The average particle size was estimated by applying the above formula.

## ***2.16. Cyclic Voltammetry***

Cyclic voltammetry is a dynamic electrochemical method for demonstrating redox process on different materials, in which the potential applied to a working electrode. The resulting current - potential curve at a fixed sweep rate can be used to understand the nature and the extent of the redox processes on the surface of catalyst in conjunction with the electrolyte system. A typical three electrode cell used for this purpose is presented in Fig. 2.16a, where reference electrode, counter electrode and a working electrode are clearly indicated separately.

The input to the electrochemical cell is triangular, or cyclic waveform (Fig. 2.16a inset) and the potential scan is programmed to begin at an initial value where no Faradaic process can occur. The scan continues at the desired linear scan rate to the switching potential and then reverses in direction to return to the initial potential. The scan rate can be chosen over a wide range, typically from  $1 \text{ mV s}^{-1}$  to  $500 \text{ V s}^{-1}$ . The resultant voltammograms are interpreted in terms of the cyclic reversibility, number

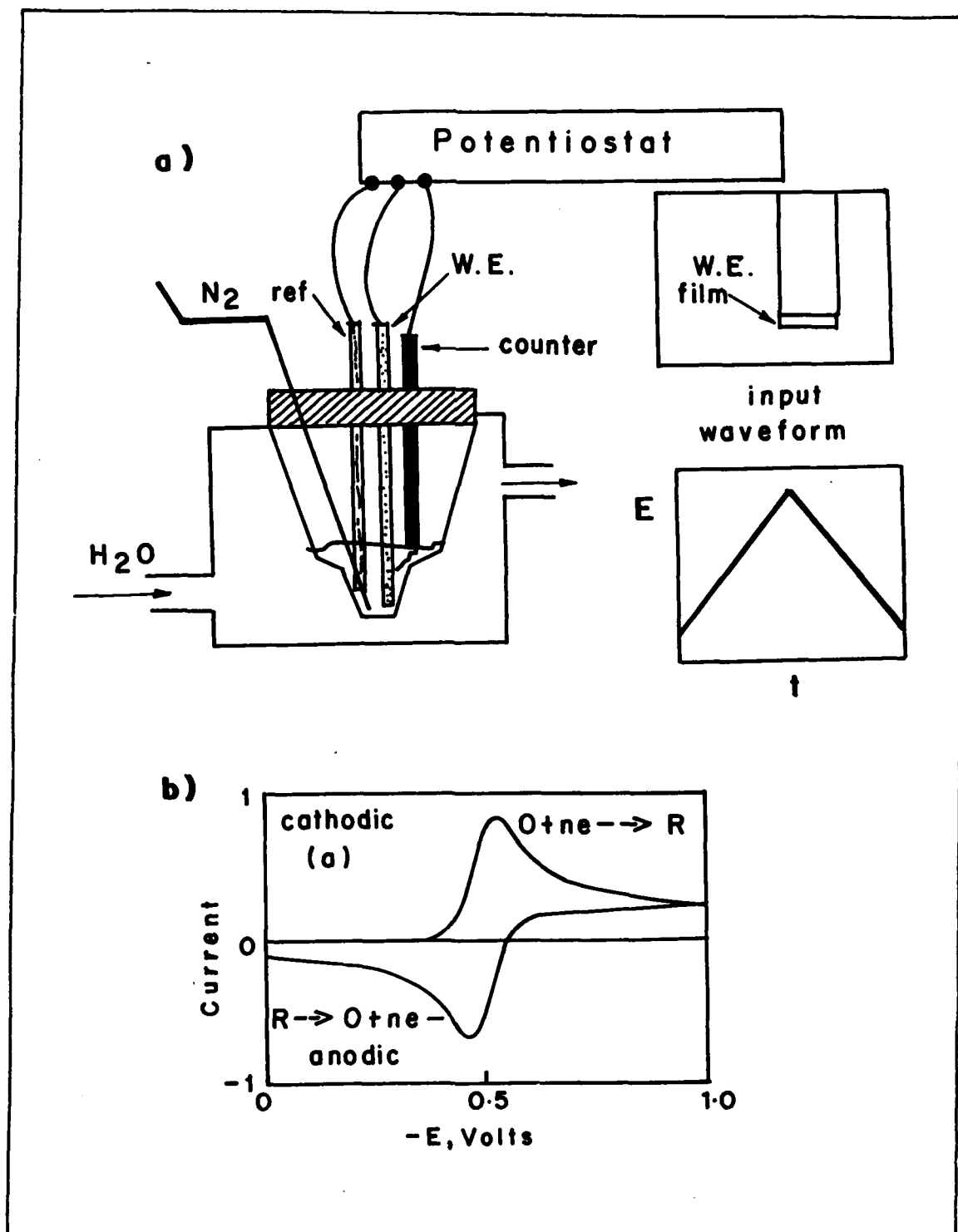
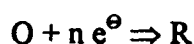


Fig. 2.16 : a) A three electrode cell applicable to studies of materials; inset : a film coated working electrode and the cyclic voltammetric wave form; b) Ideal shape of cyclic voltammogram for a reversible diffusion controlled reaction.

of electrons involved and the free energy change corresponding to the redox transformation.

Consider a solution containing electro active species O in the vicinity of the working electrode. This solution also contains a large concentration of inert electrolyte to lower the cell resistance and to minimize the migration current. If O is reversible and rapidly reduced, we have the following reaction:



where, n is the number of electron transferred from electrode to O. In this reaction, the cell current is governed by the rate of diffusion of O to the electrode and therefore is called as diffusion controlled.

A typical CV corresponding to a complete reversible process is presented in Fig. 2.16.

Cyclic voltammetry experiments were carried out at room temperature using a three electrode single compartment electrochemical cell consisting of a pellet sample as the working electrode, large area platinum foil as the counter electrode and standard calomel electrode as the reference electrode in a representative electrolyte of 0.1 M KOH.

## ***2.17. Gas - liquid chromatography***

The gas liquid chromatography was used extensively for the product analysis during the investigation of various catalytic test reactions.

When the sample is injected in the GC, the mixture to be separated is vaporized and sent through a column by flowing inert gas such as hydrogen or helium (carrier



gas). The column is packed with a solid on the surface of which is adsorbed a liquid of very low volatility. This liquid serves as the fixed phase. The components of the mixture moves through the column at different rates due to selective phase distribution between the two phases and thus get separated.

The detection system consists of catherometer which measures changes in the thermal conductivity of the gas stream. The instrument consists of an electrically heated wire which forms one arm of the whetstone's bridge. The wire assumes a steady temperature and resistance when the pure carrier gas flow over it. As the separated component reaches the wire, its temperature increases as a result of decrease in thermal conductivity of its surroundings. The consequent change in resistance is measured by the bridge. The change in resistance is proportional to the concentration of the component.

Thermal conductivity of  $H_2$  and He are six to ten times greater than that of organic compounds. The presence of even a trace amount of other material causes a large decrease in thermal conductivity.

Another kind of detector is flame ionization detector. Many organic compounds when pyrrolysed at the temperature of the hydrogen/air flame, ionic species are produced and the resultant ionic current are directly proportional to the amount of the specific component present in the sample.

## ***2.18. Catalytic test reactors***

Catalytic test reaction is one of the important tools which bridges the gap between the fundamentals of catalysis and its industrial application. In the present

investigation, mainly, two types of reactors have been used, viz., a batch reactor and a plug flow reactor.<sup>26</sup>

### i) *Batch reactors*

Reactors which are operated batchwise are called batch reactors. This type of reactor is useful for carrying out reaction at liquid phase in presence of a solvent. It is usually used for the production of high value added products in limited amounts. In a typical reaction procedure, a batch reactor is loaded with a batch of reactants and the reaction is started by adding required amount of catalyst or by increasing the temperature. Both the unconverted reactant and the reaction products are held in the reactor during the reaction. Thus, the composition of the reaction mixture changes as a function of time. Mechanical stirring ensures good mixing as well as a sufficient heat exchange with the surroundings.

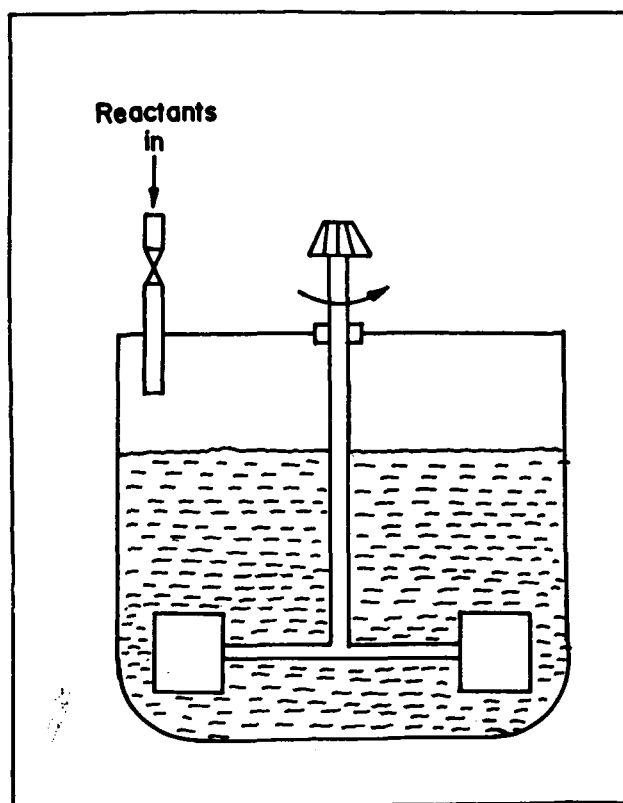


**Fig. 2.17 :** A typical batch reactor.

A schematic diagram of a stirred batch reactor used in the present investigation is shown in Fig. 2.17. In the case of perfect mixing, both temperature and composition are uniform throughout the reactor. Mass balance for a component A over the complete reactor can be written as :

$$dn_A/dt = R_{v,A}V$$

where,  $n_A$  is the amount (in mol) of A,  $t$  is time in seconds,  $R_{v,A}$  is the volumetric production rate of A expressed in  $\text{mol m}^{-3} \text{s}^{-1}$  and  $V$  is the reaction volume in  $\text{m}^3$ .

The degree of conversion of A is given by,

$$X_A = (n_{A0} - n_A)/n_{A0}$$

i.e., the amount of A which has reacted,  $n_{A0} - n_A$ , is related to the amount added to the reactor,  $n_{A0}$ .

### (ii) *Plug Flow Reactor*

Plug flow reactors are most suitable for carrying our reaction in the gaseous phase. The reaction is performed by feeding the reactants continuously to the cylindrical tubes packed with catalyst, the length of which is 10 to 1000 times larger than the diameter. The mixture of unconverted reactants and the reaction products is continuously withdrawn at the reactor outlet. Hence, constant concentration profiles of reactants and products as well as a temperature profile are established between the inlet and outlet of the tubular reactor. In view of the high length-to-diameter ratio of most tubular reactors the flow through them can be adequately described as plug flow.

In a plug flow reactor the mass balance for a component A over an infinitesimal reactor element is given by

$$(F_A + dF_A) - F_A = R_{w,A}dW$$

where,  $F_A$  is the molar flow rate of A,  $R_{W,A}$  is the specific production rate of A in  $\text{mol kg}^{-1} \text{sec}^{-1}$  and  $dW$  is the catalyst mass in the reactor.

Similar to the batch reactor, a fractional conversion of a reactant A can be defined as :  $X_A = (F_{A0} - F_A)/F_{A0}$  , where,  $F_{A0}$  is the molar flow rate of A at the reactor inlet,  $\text{mol s}^{-1}$

The advantages of the plug flow reactors are :

- simple set-up, basically a tube with packed catalyst bed;
- variation of  $W/F_{A0}$  by changing the amount of catalyst  $W$  or  $F_{A0}$  allows a broad range of conversions to be covered.

The reactor systems used in the present investigation is presented in Fig. 2.18 and 2.19 for gas-liquid reactions and gas phase reactions respectively.

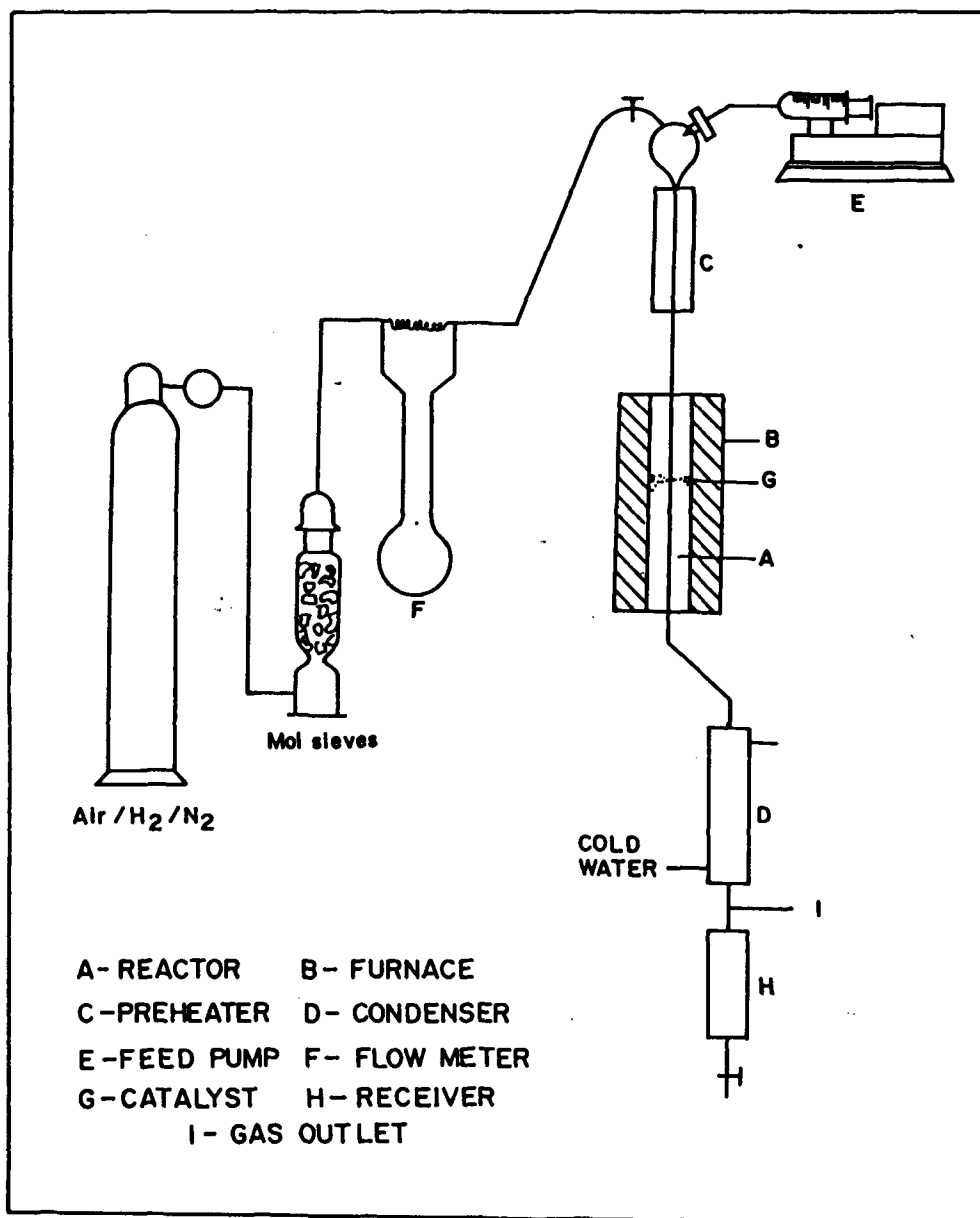


**Fig. 2.18 :** Fixed bed plug-flow reactor used for hydrogenation reactions in the vapour phase (chapter four).

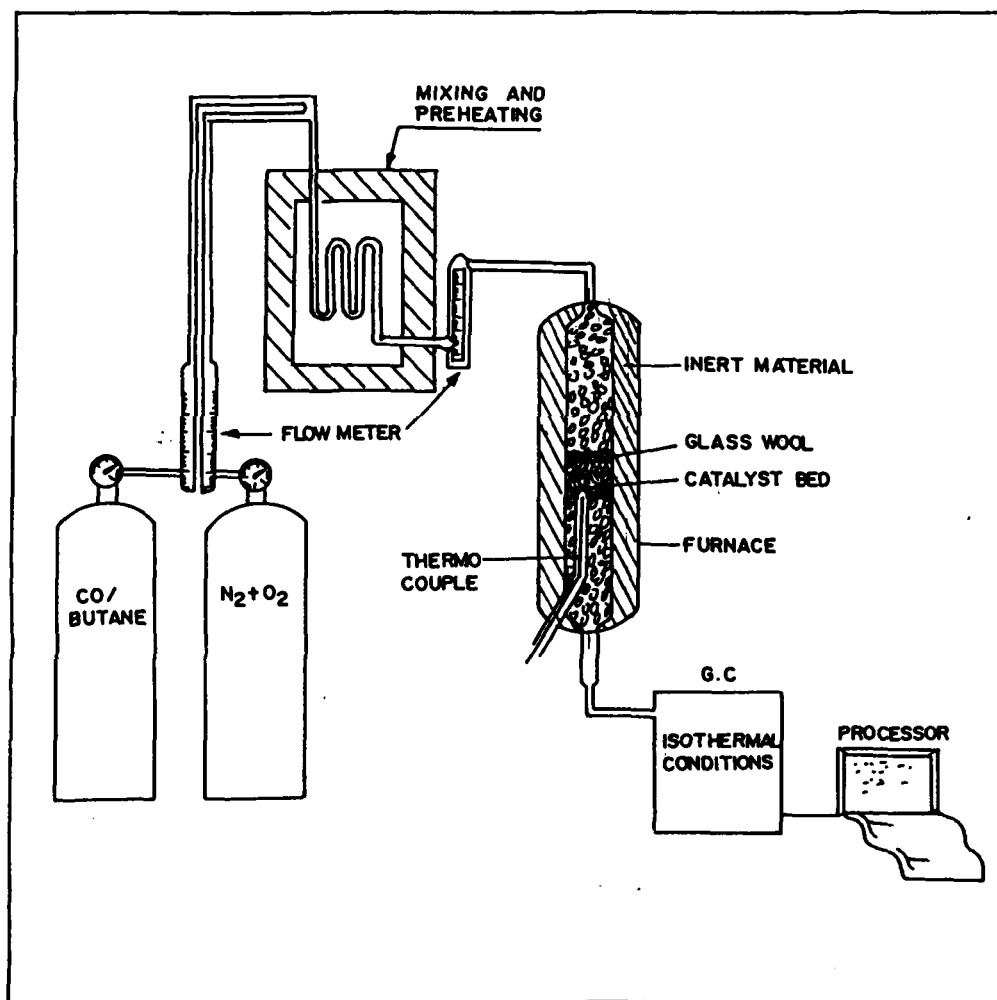


**Fig. 2.19:** Fixed bed plug-flow reactor used for oxidation reactions in the gas phase (chapter three).

## References

1. J. B. Cohen and L. H. Schwarz, *Diffraction from materials*, Academic press, New York, 1977.
2. H. P. Klugg and I. E. Alexander, in *X-ray diffraction procedures for polycrystalline and amorphous materials*, 2<sup>nd</sup> Edition, Wiley, New York.
3. P. Ratnasamy and A. J. Leonard, *Catal. Rev.*, **6** (1972) 293.
4. G. Ewing (Ed), *Instrumental methods of chemical analysis*, Tokyo, Mcgrah Hill, Kogakusha Ltd., 1975.
5. *Characterization of heterogeneous catalysis*, Ed. F. Delannay (Marcel Dekker Inc.) N. Y. 1984, p-225.
6. R. S. Swingle, *Anal. Chem.*, **47** (1975) 21.
7. H. P. C. E. Kuipers, H. C. E. Van Leuven and W. M. Visser, *Surface and Interface Anal.*, **8** (1986) 235.
8. G. Kortum, *Reflectance Spectroscopy*, Springer Verlag, Berlin, 1969.
9. A. Fadini and F. M. Schbepet, *Vibrational Spectroscopy*, Ellis Horwood Ltd., Chichester, 1989.
10. M. D. Baker, *Catal. Rev. Sci. & Eng.* **29** (1987) 269.
11. M. C. Kung and H. H. Kung, *Catal. Rev. Sci. & Engg.* **27** (1985) 425.
12. J. Hager and H. Walther, *Ann. Rev. Mater. Sci.*, **19** (1989) 265.
13. J. L. Birman, H. Z. Cummins, and K. K. Rebane (Eds), *Light Scattering in Solids*, Plenum Publishing Corporation, New York, 1979.
14. M. C. Lin and G. Ertl, *Ann. Rev. Phys. Chem.*, **37** (1986) 587
15. H. Zacharias, *Appl. Phys.*, **47** (1988) 37.
16. D. A. R. Williams, in D. J. Mowthorpe (Ed) *Nuclear Magnetic Resonance Spectroscopy*, John Wiley and Sons, New York, 1986..
17. E. R. Andrew, A. Bradbury and R. G. Eades, *Nature*, **182** (1958) 1659.; I. J. Lowe, *Phys. Rev. Lett.*, **20** (1959) 285.
18. Grahame Lawes in Arthur M James (Ed) *Scanning Electron Microscopy and X-Ray micro analysis*, John wiley and Sons, New York, 1987.
19. G. Thomas and M. J. Gorinje, *Transmission Electron Microscopy of Materials*, Wiley Interscience, John Wiley and Sons, New York.

20. J. W. Dodd and K. H. Tonge, in B. R. Currell, (Ed), *Thermal Methods*, John Wiley and Sons, New York, 1987.
21. Alan Jones and B. McNicol, *Temperature Programmed Reduction for solid materials characterization*, Marcel Dekker, Inc, New York, 1986.
22. B. C. Lippens and J. H. de Boer, *J. Catal.*, (1965) 319.
23. E. P. Barret, L. G. Joyner and P. H. Halenda, *J. Amer. Chem. Soc.*, **73** (1951) 373.
24. J. Horwath and K. Kawazoe, *J. Phys. Soc. Jpn.*, **16** (1983) 470.
25. J. F. Rusling and S. L. Suib, *Advan. Mater.*, **6** (1994) 922.
26. J. A. Moulijn, P. W. N. M. Van Leeuwen and R. A. Van Santen, (Eds), *Catalysis*, Elsevier Science Publisher, 1993.



## CHAPTER - THREE

# NOVEL FLUORITE TYPE OXIDES AS OXIDATION CATALYSTS

This chapter deals with the preparation, characterization and catalytic applications of a novel zirconia based oxides consisting of 3d-transition metal oxides as solid solution stabilized in cubic phase with fluorite type structure.

---

*Details given in this chapter are published in parts in J. Mater. Res., 9 (1994) 837;  
J. Chem. Soc. Chem. Commun. (In press); Thermochemica Acta, 254 (1995) 267;  
Appl. Catal. (B) Environmental, (in press).*

---

## 3.1. INTRODUCTION

---

### *3.1.1. Automotive pollution*

Air pollution is recognized as a major problem in urban and heavily industrialized areas, where the flow of clean air from the surrounding areas is insufficient to dispel the accumulation. When we look at the sectorwise distribution of pollutants, motor vehicles account for more about 64 % of the anthropogenic emissions of carbon monoxides, hydrocarbons and nitrogen oxides (Fig. 3.1). Carbon monoxide is an opprobrious poison which has an affinity for hemoglobin 210 times greater in the blood than that of oxygen. Prolonged exposure to a level of above 9 ppm can lead to reduced mental acuity. Hydrocarbons and oxides of nitrogen lead to photochemical smog in the presence of sunlight giving rise to ozone and pollutants like nitrogen dioxides and peroxyacyl nitrates. An exposure to these oxidants above 0.08 ppm causes eye irritation and impairment of lung functions in persons suffering from pulmonary diseases. These oxidants also cause damage to vegetation and rubber.

It is estimated that ambient air of Bombay contain about 4,76,700 tonnes of carbon monoxide, 1,72,800 tonnes of hydrocarbons and about 8,00,000 tonnes of NO<sub>x</sub>. A detailed cost-benefit analysis carried out during a study has established that the air pollution in Bombay alone costs around Rs. 16,000 million for the year 1991

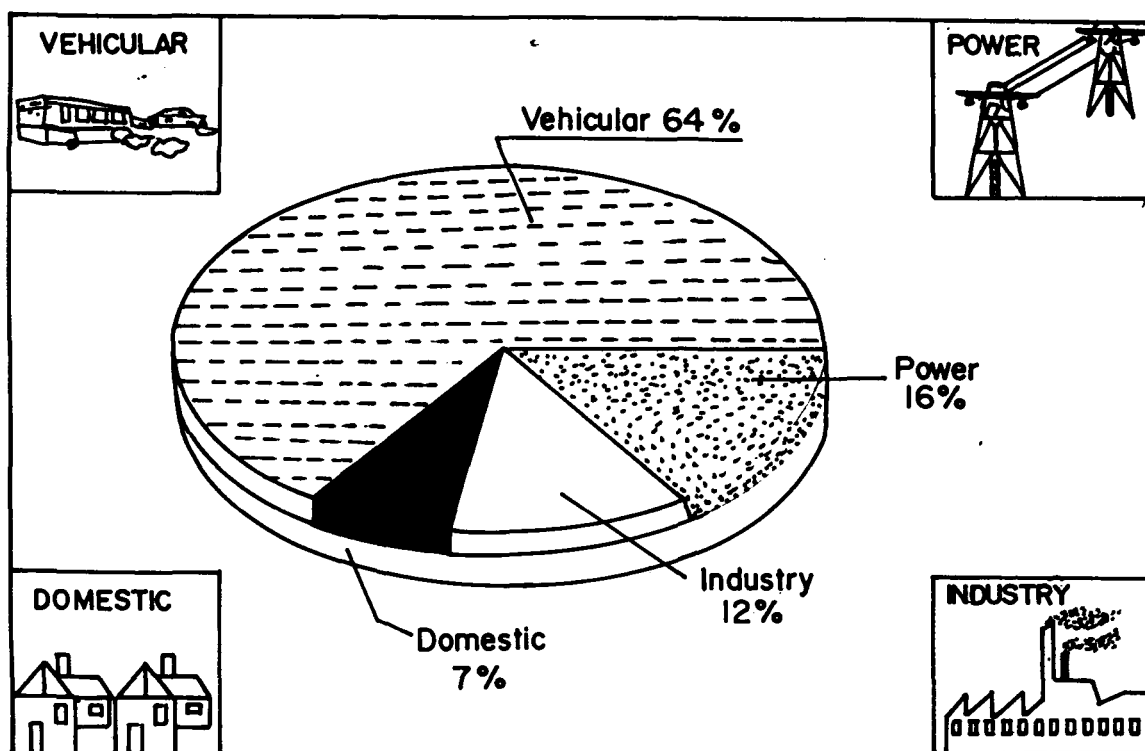


Fig. 3.1 : Sectorwise distribution of pollutants

in terms of mortality and morbidity of population and related economic loss due to the loss of wages. According to another survey, about 30 % of Delhi people are suffering from respiratory ailments due to the hazardous effects of around 2000 tonnes of air pollutants spewed out in atmosphere every day from 25 lakh vehicles plying in Delhi roads. The control of automotive exhaust emissions has therefore become a matter of serious consideration.

### ***3.1. 2. Worldwide regulatory measures***

California Air Resources Board (CARB) has decided to implement even more stringent emission limits in California to be generally effective from the year 2000 and the programme is referred to as regulations for ULEV (Ultra Low Emission Vehicles and ZEV (Zero Emission Vehicles).<sup>1</sup> Similarly, Indian emission standards to be met by this year is given in Table 3.1

**Table 3.1 Indian Emission Standard (1996)<sup>2</sup>**

Cylinder capacity, cc	CO, g./km	HC + NO <sub>x</sub> , g/km
< 1400	8.7	3.0
>1400 <2000	11.2	3.8
> 2000	12.4	4.4



### ***3.1.3. Generation of pollutants ?***

The major components of the pollutants emitting from automotive vehicles are carbon monoxide, hydrocarbons and nitrogen oxides. Carbon monoxide is a typical

product of high temperature combustion in presence of oxygen. This gas is therefore produced if rich air-fuel mixture is affected into the engine at any operating stage of the engine. Alternatively, if the fuel is not mixed sufficiently with the air or if the engine operates at lower than the stoichiometric ratios then the chances of emission of carbon monoxide from the exhaust are very high. Hydrocarbons are known to be contrived by the extinct layer that may result if the flame front is the extinguished fraction of the cold wall. The presence of the unburnt hydrocarbons is also due to crevice between the piston and the cylinder wall or piston ring. Also, if the engine operates with very lean mixture, the number of missing cycle increases, resulting in higher hydrocarbon emissions. Nitrogen oxides are formed during the high temperature ignition in the cylinder (above 800 K) by the reaction of oxygen atoms with the nitrogen molecule. These are complex reactions.

### ***3.1.4. How to get rid of these pollutants ?***

These poisonous pollutants can be abated by two ways: primary pollution control and secondary pollution control. The former route involves improvements in the engine design and improvement in the fuel in such a way that there should be complete burning of the fuel there by reducing the emission level and it is the concern of automobile engineers. In the latter case the various options available for the control of emissions from the automobiles are

- \* Use of thermal reactors
- \* Exhaust gas regulation system (EGR)
- \* Catalytic converters

Of these, catalytic converters hold a greater promise and flexibility compared to other options because, catalytic combustion offers several advantages over conventional combustion, such as lower emission levels of contaminants such as nitrogen oxides, better fuel efficiency and lower peak temperatures.

### ***3.1.5. Known catalysts***

The first and foremost attempt to develop a catalytic process for achieving this purpose was reported by Houdry.<sup>3a</sup> His pioneering efforts stimulated many others for their research efforts in the area of automotive catalysis. In addition, the clean air act of 1970 set some norms which spurred very intensive research. Over 350 million vehicles (passenger cars and trucks) have been equipped with catalytic converters throughout the world as the principle means of exhaust emission control. The application of catalytic converters has been one of the prominent scientific achievements of the recent years.<sup>3b</sup> In conjunction with the unleaded fuel, the catalytic converter is a remarkable device in what it achieves and it is rated among the top ten inventions of this century.<sup>4</sup>

Furthermore, to meet the emission norms proposed for 1996, which are more stringent, it is necessary to intensify this research. The most successful class of active catalysts for both oxidation and reduction is the noble metals : silver, gold, ruthenium, rhodium, palladium, osmium, iridium and platinum. However, a relatively high cost and a shortage in the domestic supply of noble metals may in future, necessitate the development of non-noble metal catalysts for automobile emission control.

Base metal oxide catalysts were investigated as early as in 1970's for the control of automotive emissions.<sup>5,6</sup> These include mixture of oxides of copper and chromium in equal amounts. Also, oxides of nickel, manganese, cobalt, vanadium and iron are also prominent. Rare earth oxides of perovskite family, such as lanthanum cobaltates, lanthanum lead manganites, have also been investigated for the complete oxidation of hydrocarbons and carbon monoxide.

Among the non-noble metal catalysts studied so far, several types of metal oxides have been exploited for complete oxidation purposes. The major active components include compositions such as copper/chromium, cobalt, nickel, manganese and other materials. Another breed of oxides investigated recently are Y-Ba-Cu-O superconductors. Jiang and co-workers reported 90 % conversion of carbon monoxide at 533 K using  $\text{YBa}_2\text{Cu}_3\text{O}_{7-x}$  catalyst.<sup>7</sup> It has been found that the carbon dioxide yield reaches a maximum within the first stages of the reaction (typically first 20 min) and then steadily decreases as the reaction time increases. Otamiri *et al* studied the oxidation of carbon monoxide over Co and Al substituted  $\text{YBa}_2\text{Cu}_3\text{MeO}_{7-x}$ , where Me = Co or Al and found that an increasing degree of substitution in the B-site by active component (Co) and inactive one (Al) results in lower activity.<sup>8</sup>

Among the new generation catalysts, ceria based oxides have been reported to be useful for oxidation of lower hydrocarbons by Trovarelli and co-workers.<sup>9</sup> They correlated the increase in the oxidation activity to higher oxygen mobility at lower temperature for fluorite structured metal oxides compared to pure  $\text{CeO}_2$ . It is also related to lower reduction temperature of  $\text{Ce}^{\text{IV}}$  and thus the increased ability of  $\text{CeO}_2$  to shift between  $\text{Ce}^{\text{IV}}$  and  $\text{Ce}^{\text{III}}$  at much lower temperatures. This could expedite the

creation of oxygen ion vacancies and their subsequent reactions with oxygen from the gas phase. Annulment of oxygen vacancies with formation of oxygen-hole centers has been recently invoked to elucidate the role of defects and oxygen ion migration in the catalytic activity of doped lanthanum oxide in oxidation reactions.<sup>10,11</sup> Another such material which was explored for its activity for oxidation of carbon monoxide in 70's is the mixed conducting oxide based on  $ZrO_2$  and  $ThO_2$ . Berkstresser *et al*<sup>12</sup> compared catalytic activity of  $ZrO_2$ ,  $Zr_{0.91}Ca_{0.09}O_{1.91}$  and  $Th_{0.85}La_{0.15}O_{1.925}$  for the oxidation of CO by oxygen. Their explanation for higher activity includes the possibility of enhanced adsorption sites for one of the reactants involved in the rate limiting process where the reactants may be either polarized or ionized.

Although considerable effort has been expended to understand the working of the catalysts, exact strategic measures to be followed for designing new catalysts are still lacking.

### ***3.1.6. Limitations of existing catalysts***

Most of the known oxides have not been shown to be sufficiently active under demanding and realistic conditions. The major drawbacks are their lack of durability and the detrimental effects of poisons and high temperatures on catalyst life. Specifically, loss of surface area of the support and the active ingredient due to sintering, destruction of catalyst material by crushing, attrition, phase transition and melting are the prominent factors.<sup>13</sup> Base metal oxide catalysts require long time to heat up to operating temperature, therefore, they could not achieve the performance required to meet the more stringent cold-start emission standards.



### ***3.1.7. The present strategy***

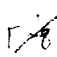
There is considerable upsurge in the quest for alternative catalytic materials. The important consideration in designing these is the tailoring of the oxygen mobility required for the easy redox process. For an oxidation catalyst, filling of the surface oxygen vacancies by incorporation of oxygen from the gas phase does not necessarily take place at the same site from which the surface oxygen is extracted during the desorption of oxygenated products. Therefore, a high value of coefficient of diffusion of oxide ion in the catalyst lattice or over its surface is often an important condition for the catalyst to show high activity. Tailoring the surface properties of an oxide catalyst may be achieved in several ways.

- synthesis of the catalyst in the form of crystallites exposing mainly those crystal phases constituting atoms in a spatial arrangement most appropriate for the formation of required adsorbed intermediates;
- introduction of aliovalent ions that are substitutional or interstitial to the crystal lattice and adjust the position of the Fermi level to a value which would secure the appropriate exchange of electrons between the adsorbed reactants and the catalyst, and regulate the occupancy of the frontier orbitals to modify the HOMO and the LUMO character;
- adjustment of redox properties of the gas phase by changing its composition to generate defects, and induce such a valance state of transition metal ions at the catalyst surface which is required for the formation of reactive surface intermediates;
- mixing different oxides to create interfaces where certain crystal phases may be stabilized to generate a new catalytic active sites.

*Taking into account all these possibilities, an attempt has been made to develop a novel series of catalytic materials based on zirconia consisting of some 3d-transition metal ions and belonging to the fluorite family.*

Zirconia and its solid solutions are materials of current technological and scientific interest owing to their widespread applications in high technology ceramics and ionic conductors. Recent efforts in extending the application of zirconia-based solid solutions in the area of heterogeneous catalysis stimulated us to design a series of catalyst composites of zirconia doped with various transition metal ions at different loadings.

### **3.1.8. Fluorites ?**

The term fluorite is originally due to the  $\text{CaF}_2$  which has a cubic structure. The schematic diagram of fluorite lattice with cubic symmetry is shown in fig. ~~Fig.~~ 

3.2. It is a compound  $\text{RX}_2$  in which R is octahedrally coordinated to oxygen atoms and X (in this case oxygen) forms the tetrahedral center surrounded by R.

The idealized structure of cubic zirconia is based on that of fluorite with space group  $\text{Fm}\bar{3}\text{m}$ , metal atoms on 4(a)(0,0,0) and oxygen on 8(f) (1/4, 1/4, 1/4). For the unit cell dimension,  $a = 5.175 \text{ \AA}$ , of the zirconia with cubic symmetry, the average metal-oxygen distance is  $[5.175 \times (3)^{0.5}]/4 = 2.241 \text{ \AA}$ . With approximately 10 % of the oxygen sites vacant we may expect that in a given cube the coordination of the metal will be 8, 7, 6 or even lower and it is interesting to consider the extent to which the valance of each metal ion is satisfied in these environments. To do this bondlength-bond valance relationship can be made use of.<sup>14</sup> This relationship assumes

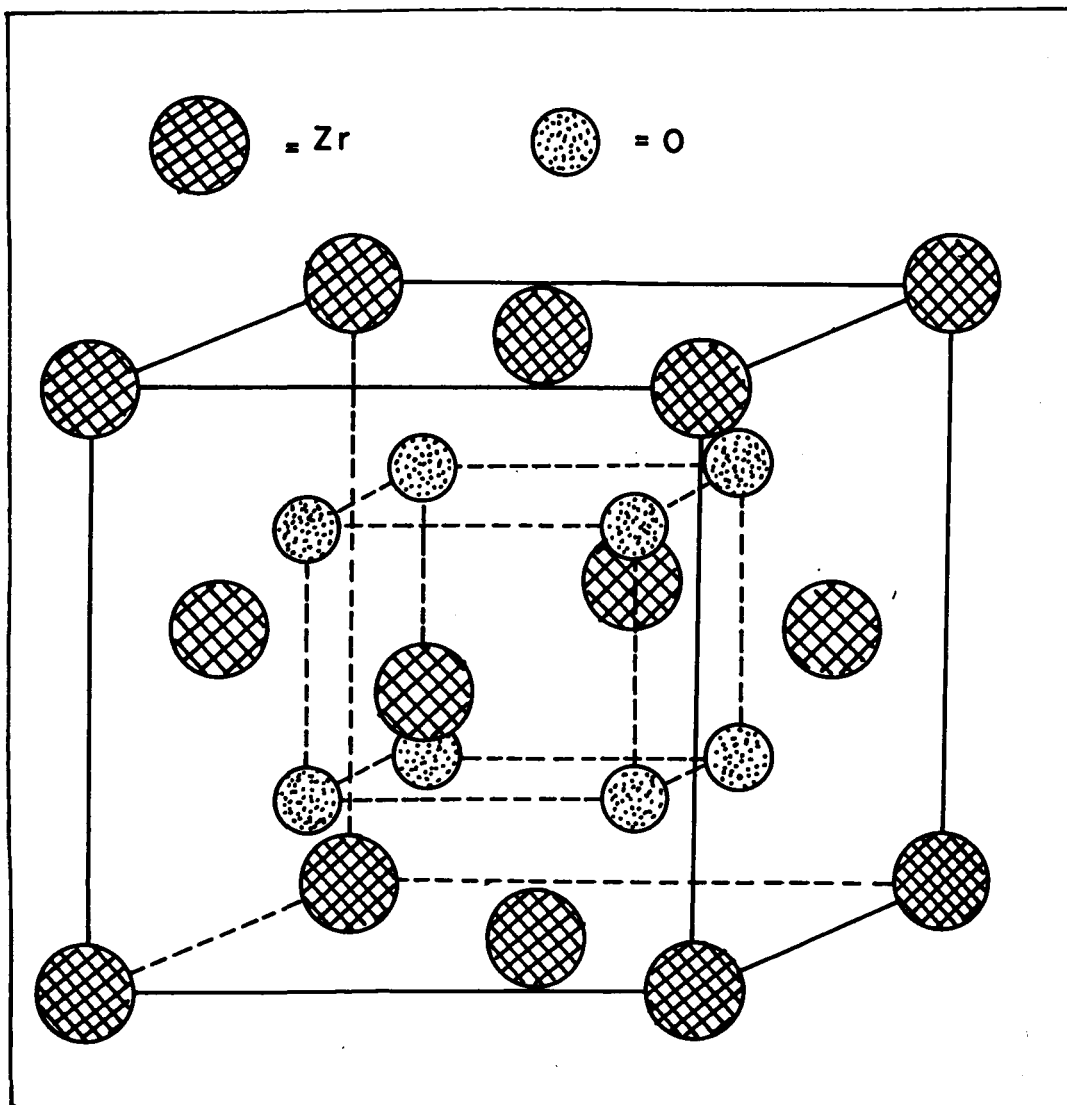


**Fig. 3.2 :** Idealized cubic structure of zirconia

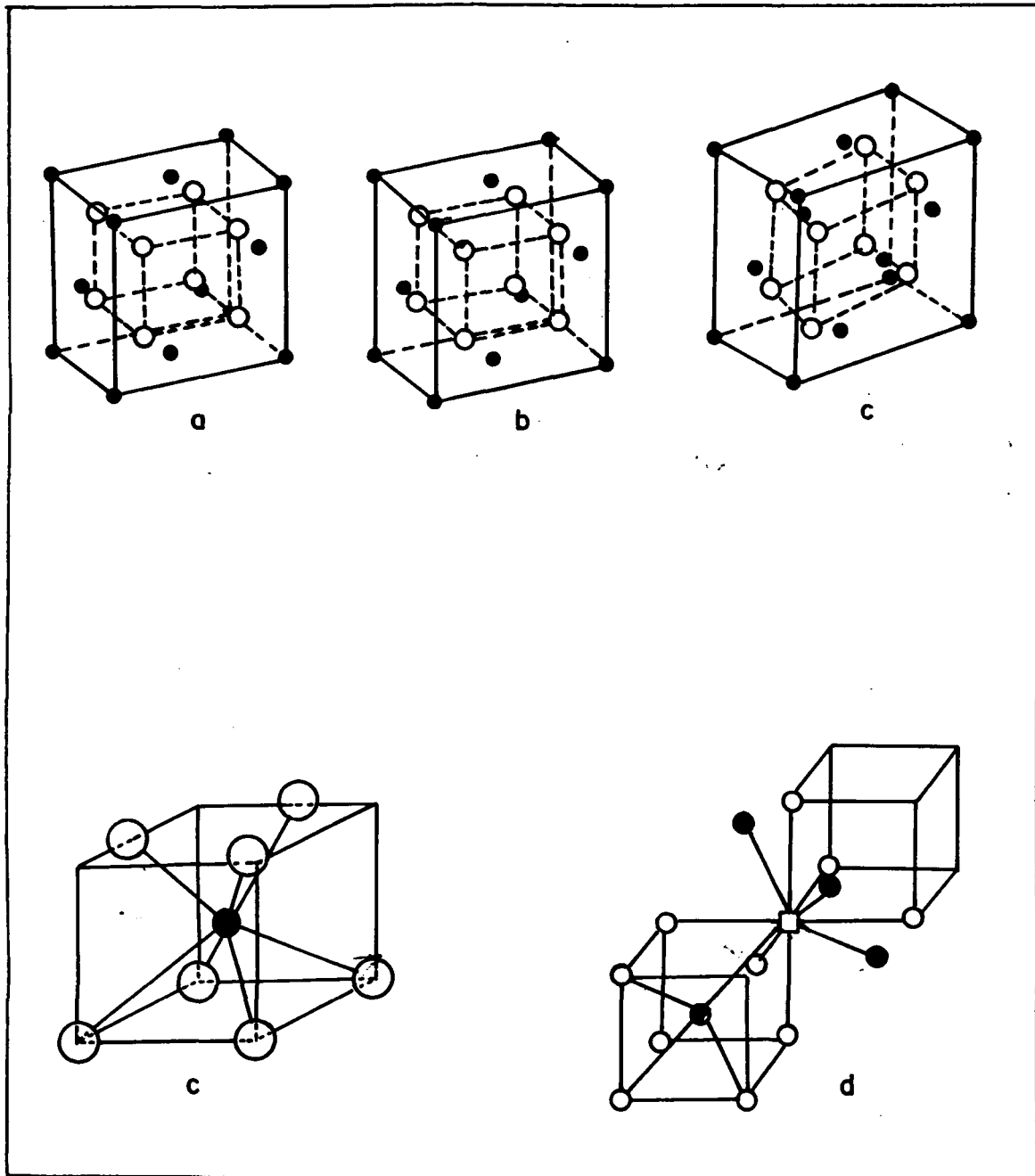


**Fig. 3.3 :** Various polymorphs of zirconia: cubic (a), tetragonal (b), monoclinic (c) and stabilized zirconia (d)

that the contribution  $S$ , to the valence of a particular ion by a bond to another ion is given in terms of bond length, 'd' by the empirical exponential form

$$s = \exp[(r_0-d)/B]$$

where,  $r_0$  and  $B$  are empirically determined parameters, many of which have been tabulated.<sup>15</sup> The total valence  $V_i$  of a given atom,  $i$  may be obtained by summing the overall neighbouring atoms,  $j$  contributing to the bonding, *i.e.*,

$$V_i = \sum_j \exp [(r_0-d_{ij})/B]$$

Thus, it is possible to estimate the preferred metal oxygen distance required for getting idealized cubic structure.<sup>16</sup>

Metal oxides such as  $ZrO_2$ ,  $CeO_2$ , and  $ThO_2$  forms fluorite type structure under certain conditions. At room temperature,  $ZrO_2$  has a deformed structure with monoclinic or tetragonal symmetry (Fig. 3.3) By doping with lower valent ions such as calcium or yttrium, the cubic structure is stabilized and remains viable down to room temperature. In the stabilized zirconias, the oxygen vacancies, which are present as the ionic majority defects are randomly distributed over the identical crystallographic oxygen positions. In particular, the ordering effects may occur at high dopant concentration depending on the ratio of the radii of the  $Zr^{4+}$  to dopant cation. Usually, metal oxides such as  $La_2O_3$ ,  $Y_2O_3$ ,  $MgO_2$  and  $CeO_2$  are known to stabilize zirconia into cubic/tetragonal structure.<sup>17</sup> However, our interest is the stabilization of zirconia by a 3d-transition metal oxide so as to make it a suitable oxidation catalyst. Alternatively, it may be just reverse, *i.e.*, stabilization of the transition metal oxides in the zirconia lattice!



---

## 3.2.

### Mn - STABILIZED ZIRCONIA

---

#### 3.2.1. INTRODUCTION

Among various oxides of the group IV B,  $ZrO_2$  is unique in its properties, such as permeability, thermal shock resistance and ionic conductivity and finds applications as catalysts, gas sensors, gas turbines, thermal barrier coatings, etc<sup>18-21</sup> The three polymorphs of zirconia, viz., monoclinic, cubic, and tetragonal have been well characterized.<sup>22</sup> Among them, the cubic form is known to play a significant role in the field of ceramics and refractory oxides. Apart from this, it can also act as a good catalyst.<sup>23-25</sup> For all these reasons, considerable work has been done to stabilize zirconia into cubic phase. The various polymorphs of zirconia can be made stable or metastable even at room temperature by manipulating the method of preparation or by the addition of some metal oxides. Solid solutions of zirconia and various metal ions have been widely investigated. It has been reported that the addition of alkaline earth oxides such as CaO and MgO, group III B metal oxides such as  $Sc_2O_3$  and  $Y_2O_3$  and rare earth oxides such as  $La_2O_3$  and  $Ce_2O_3$  stabilize zirconia in to cubic (fluorite) phase.<sup>17,18,26</sup> Recently, Co(II), Ru(IV)- and La(III)-stabilized zirconia solid solutions have been reported.<sup>27-28</sup> Although the cubic phase stabilization of zirconia using other transition metal oxides such as MnO, NiO,  $Cr_2O_3$ ,  $Mn_2O_3$ , CuO and  $Fe_2O_3$  have

earlier been reported,<sup>18, 29</sup> they require either a very high temperature (1275 K) of calcination or the presence of some other metal oxide, such as  $\text{TiO}_2$  as an adduct. To tailor  $\text{ZrO}_2$  for catalytic applications, a lower calcination temperature is preferable in order to get a high surface area, apart from the creation of oxygen ion vacancy and a stable single phase.

### 3.2.2 A BRIEF LITERATURE OVERVIEW

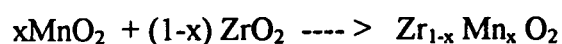
Manganese compounds are considered to be suitable materials for catalysing several reactions involving surface or bulk oxygen. Use of bulk manganese oxides for complete oxidation reactions is known for a long time. However, manganese when doped on the surface of a suitable matrix shows a tremendous improvement in its catalytic behaviour. For instance,  $\text{MnO}_x$  modified alumina is known to possess special properties due to the development of highly reactive basic sites and a presumable development of activated Bronsted acid sites.<sup>30</sup> The presence of  $\text{MnO}_x$  is reported to render meritorious effect on alumina when it is used as a catalyst for oxidative coupling of methane<sup>31</sup> and deep oxidation of hydrocarbons.<sup>32</sup> Similarly,  $\text{MnO}_x$  supported on silica is known to be an effective catalyst for oxidative coupling of methane.<sup>33</sup> The major advantage of using manganese in these supports is believed to be the possibility of getting multivalent Mn species. But, the disadvantage is that, Mn-oxides segregate on the support due to sintering resulting in crystal growth and consequent decrease in the activity. This warrants some alternative way where long life of the catalyst is also assured apart from high activity and reasonable selectivity. This motivated us to initiate preparing Mn - oxide catalysts stabilized on some stable

crystalline matrix. To the best of our knowledge, the successful stabilization of zirconia by Mn-oxide was reported by us for the first time.<sup>34</sup> Later, Dravid and co-workers also reported the stabilization of cubic zirconia with manganese oxide.<sup>35</sup> Recently, Eguchi and co-workers have used Mn- Zr mixed oxides for the removal of nitrogen oxides by adsorption.<sup>36</sup> Once again, our continuous effort in successful application of Mn-stabilized zirconia in complete oxidation of hydrocarbon (butane) is described in a recent communication.<sup>37</sup>

### 3.2.3 EXPERIMENTAL

#### 3.2.3.1. *Preparation of Mn-stabilized zirconia*

The Mn- stabilized zirconia was obtained by a co-precipitation method using high purity zirconyl nitrate (99.9%, Loba Chemie) and manganese acetate (99.9%, Loba Chemie). Required quantities of solutions of these two salts were mixed and the hydroxides were precipitated at room temperature by a slow addition of tetramethylammonium hydroxide (25 % aqueous solution) with constant stirring till the pH of the mixture reached 8. The hydroxide gel thus formed was filtered, washed well with water and acetone, dried at 383 K under vacuum and finally calcined at temperature between 773 K and 1073 K in air for 8 h to 36 h. The formation of stabilized oxide can be expressed as:



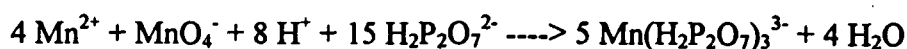
Zirconia samples with 5, 10, 15, 20, 25 and 30 mole % of Mn were thus prepared. For comparison, a sample with 10 mole % MnO<sub>2</sub> in zirconia was prepared by solid state reaction, taking a mixture of the two oxides (99.9% pure, Aldrich, USA) grinding



under acetone and subsequently drying and calcining at temperature between 773 and 1273 K.

### ***3.2.3.2. Chemical Analysis***

The total amount of manganese was determined by method described by Vogel<sup>38</sup> for determination of manganous ions with permanganate in a neutral pyrophosphate solution.



The amount of Mn(III) and Mn(IV) was determined by a method according to Fyfe by using acetyl acetone as complexing agent. The detailed procedure is given elsewhere.<sup>39</sup> Then Mn(II) was determined from the difference {total manganese - (Mn(III)+ Mn(IV))}.

### ***3.2.3.3 Characterization***

The synthesized samples were analyzed for quantitative and qualitative phase identification in a 'Rigaku' (Model D/Max III VC, Japan) X-ray powder diffractometer using Ni-filtered Cu-K<sub>α</sub> radiation ( $\lambda = 1.5406 \text{ \AA}$ ) at a scanning speed of 1 degree per minute. The lattice parameters were calculated by the least square refinement using a computer program (PDP 11, Universita di Trieste, Italy). The thermal analysis of the sample was carried out on a simultaneous TG-DTA instrument (model 92, Setaram, France). About 40 mg of the powder hydroxide precursor was placed in a platinum sample holder, 8 mm in diameter and 10 mm in height. The experiments were carried out at a uniform heating rate of 10 K min<sup>-1</sup> up to 1273 K and at 100 cm<sup>3</sup> min<sup>-1</sup> flow

of air or nitrogen. The BET surface areas were measured in an 'Omnisorb-100 CX' (Coulter, USA) analyzer using nitrogen as the adsorbate under continuous flow mode. The IR spectra of two representative samples were recorded in nujol in a 'Perkin Elmer' (model 5300) IR spectrometer. XPS measurements were carried out in a 'V.G.Scientific ESCA-3-MK-II' electron spectrometer fitted with an Mg-K $\alpha$  ( $\lambda=1253.6$  eV) X-ray source. The temperature-programmed reduction experiments were carried out on a 'Sorbstar' (Hungary) TPR unit using 10 % H $_2$  in N $_2$  and at a heating rate of 18 K min $^{-1}$ . The redox ability of the samples was studied by cyclic voltammetry, the details of which are given in chapter two.

#### ***3.2.3.4. Catalytic test reactions***

The catalytic test reactions for complete oxidation of n-butane were carried out using a micro-reactor operated in a steady state plug-flow mode. The powdered catalyst was pelleted, crushed and then sieved to 16 to 20 mesh before use. The reaction mixtures [n-butane (4%), N $_2$  (76% and O $_2$  (20%)] were admitted to the reactor at a GHSV of 36000 h $^{-1}$ . The products (CO $_2$  and H $_2$ O) were analyzed by an on-line GC using poropak Q column. The reaction rate (expressed as micro moles g $^{-1}$  sec $^{-1}$ ) was evaluated from the slope of the linear correlation between the conversion and W/F, where W is the weight of the catalyst and F is the flow rate of the reactants under the steady state conversion maintained at less than 20 %. The schematic diagram of the reactor used is depicted in chapter two (Fig. 2.19).

### 3.2.4. RESULTS AND DISCUSSION

#### 3.2.4.1. Chemical Analysis

The results of chemical analysis are presented in Table 3.2. It can be seen that, there is reasonable agreement between the input Mn amount and the Mn content obtained by the chemical analysis. This shows that, the present preparation method promotes the homogeneous mixing of the components. Furthermore, the samples contain,  $Mn^{4+}$ ,  $Mn^{3+}$  and  $Mn^{2+}$  in varying amounts. At lower level of Mn-doping (5 to 10 mole %), the sample contained  $Mn^{2+}$  in a relatively higher amount. However, at 20 mole % of Mn loading and above the  $Mn^{4+}$  was found to be dominating.

**Table 3.2.**

**Chemical analysis results of Mn-stabilized zirconia**

Mn content (mole %) input	Mn content (mole %) (chemical analysis)	Mn (II) mole %	Mn (III) mole %	Mn (IV) mole %
5	4.8	2.8	1.3	0.7
10	9.0	3.8	2.2	3.0
20	19.8	6.9	4.0	8.9
30	29.6	8.3	5.0	16.3

#### 3.2.4.2. TG-DTA studies

The co-precipitation as hydroxide is a better route for getting mixed oxides of zirconium and other elements due to its simplicity and the ease of formation of

requisite microstructure and texture after calcination. Accordingly, the present preparation method follows a similar procedure to get stabilized zirconia with manganese in the lattice.<sup>34</sup> Since the preparation of this new material is mainly aimed at getting a good catalyst with high surface area, it is important to optimize the temperature of calcination. An understanding of the mechanistic aspects of the thermal decomposition of these precursors is hence relevant. The present study is aimed at such an understanding through a systematic TG-DTA investigation of the mixed hydroxides of zirconium and manganese. In addition, an attempt has been made to account for the role of manganese and the effects of various hydrolyzing agents on the thermal stability of zirconia.

### *TG and DTA of the oxide hydroxides*

Figures 3.4 and 3.5 show the TG and DTA plots, respectively of the zirconium oxide hydrate (curve a), the Zr-Mn mixed oxide hydrates containing 5 to 30 mole % of Mn (curves b to e, respectively) and the pure manganese hydroxide (curve f), all obtained by precipitation using ammonium hydroxide. The major weight loss in each case extending upto 573 K is due to dehydration of the oxide hydrate. The observed weight loss given in Table 3.3 agrees very well with the theoretical values of weight loss calculated from an assumption of the initial composition to be  $Zr_{1-x}Mn_xO(OH)_2$  where x is in the range of 0 to 0.3. From an analysis of standard enthalpies of decomposition of different metal oxides and extrapolation to standard enthalpy of formation of  $Zr(OH)_4$ , it has been recently suggested that only  $ZrO(OH)_2$  or  $ZrO_{1.5}O(OH)$  is stable and that  $Zr(OH)_4$  is not stable at room temperature.<sup>40</sup> In the case of

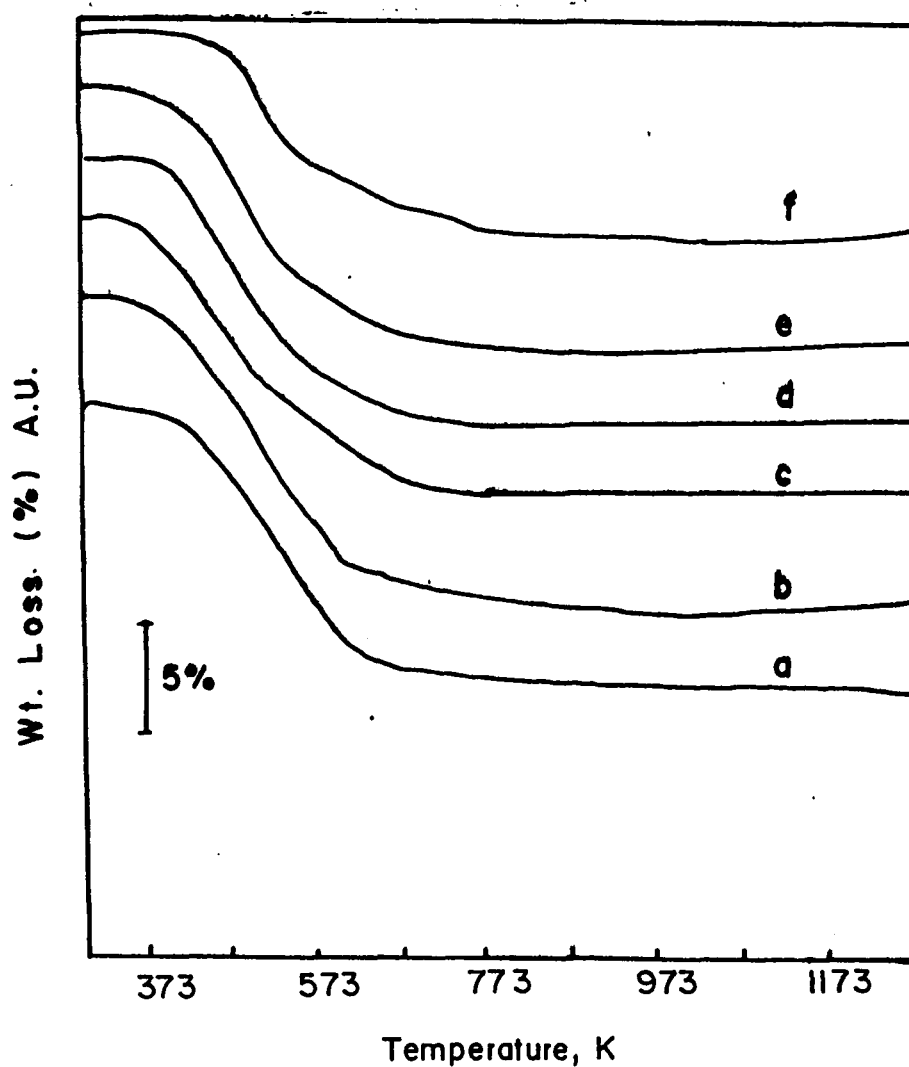


**Fig. 3.4 :** TG profiles of decomposition of pure zirconium oxide hydrate (a), Mn-Zr co-precipitated oxide hydrate with 5 (b), 10 (c), 20 (d) and 30 mole % of Mn (e) and pure manganese hydroxide (f).

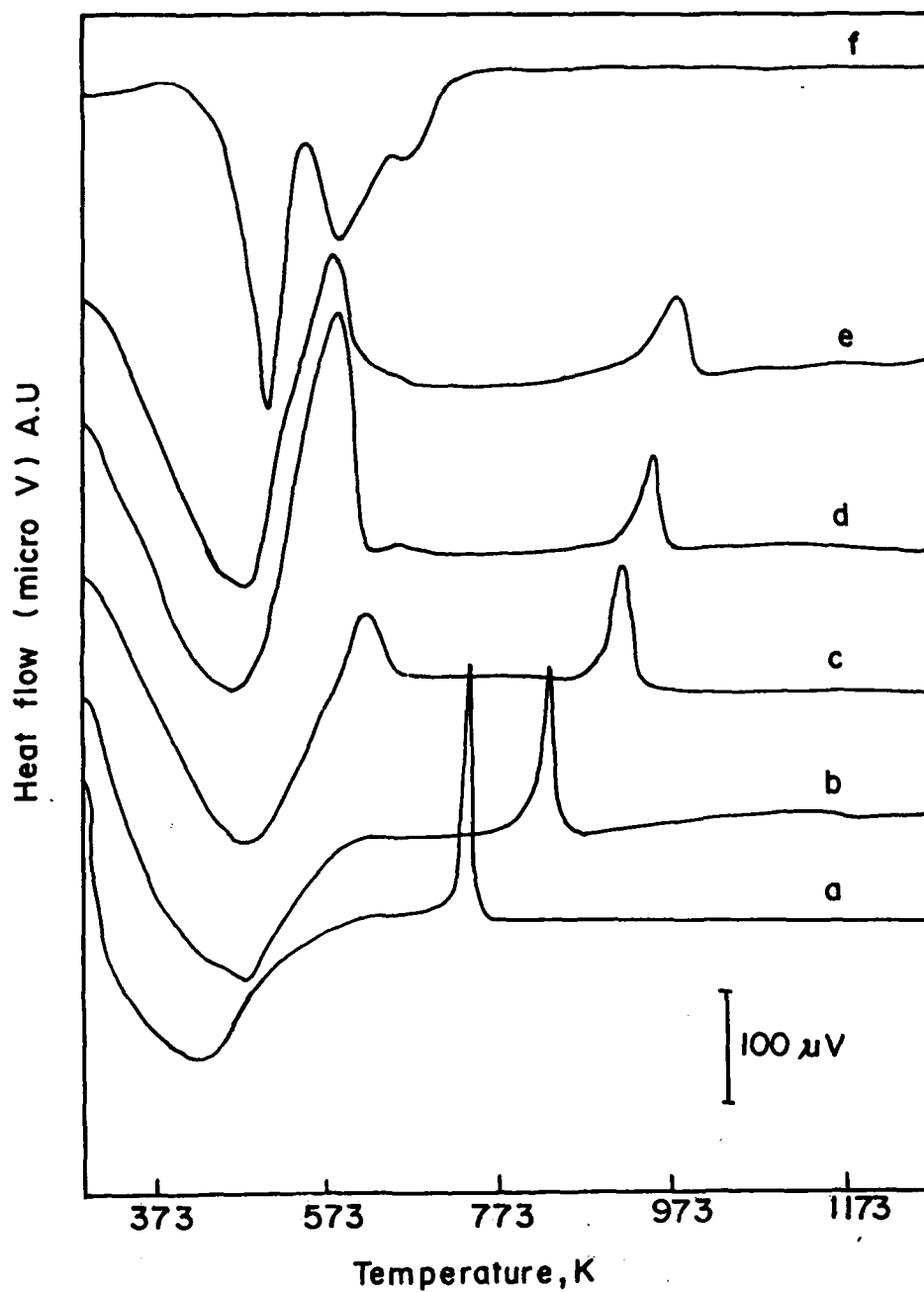


**Fig. 3.5 :** DTA profiles of the decomposition of zirconium oxide hydrates, Mn-Zr oxide hydrate and manganese hydroxide. (Details of the samples are given in Fig.3.4)

Mn mixed Zr oxide hydrates, the agreement between the calculated and observed values confirms the initial composition to be an oxide hydroxide.

**Table 3.3**

**Weight loss, peak maxima, and enthalpy of crystallization of zirconium oxide hydrates with different manganese prepared by co-precipitation.**

Precursor hydrate sample	Weight loss (observed), wt %	Weight loss (calculated, wt %)	Peak maxima, K		Enthalpy, kJ mol <sup>-1</sup>	
			Endo	Exo	Endo	Exo
Zr oxide hydrate	12.55	12.69	438	740	-121	28.2
Zr-Mn (5) <sup>b</sup>	12.70	12.90	451	818	-142	22.6
Zr-Mn (10)	13.05	13.08	453	876	-120	16.7
Zr-Mn (20)	13.40	13.44	446	940	-129	12.1
Zr-Mn (30)	13.80	13.81	416	960	-65	12.1

<sup>b</sup> *Figures in the parenthesis indicate the Mn content in mole %*

For both zirconium oxide hydroxide and mixed oxide hydroxide of manganese and zirconium, the dehydration is accompanied by a large endothermic peak in the temperature range of 373 to 573 K. The peak maxima are recorded between 423 and 453 K for all the samples and the calculated heats are in the range of 120 to 142 kJ mol<sup>-1</sup> (Table 3.3). The samples with higher Mn loading, viz. 20 and 30 mole % of Mn in <sup>\*</sup>ZrO<sub>2</sub> show 2 endothermic peaks which are not well resolved (Fig. 3.5). This

probably is due to separate or individual dehydration of the oxide hydroxides of manganese and zirconium from the mixed phase.

### *Crystallization and the glow exotherms*

After the dehydration is almost complete, the transition from amorphous to crystalline phase is accompanied by an exothermic peak in the temperature range of 723 to 873 K for all the samples except for manganese hydroxide (Fig. 3.5). Similar observations have been reported in the preparation of  $Y^{3+}$  stabilized zirconia.<sup>41</sup> The exothermic peak temperature for all the samples are given in Table 3.3. The water content at the initiation temperature of the exotherm was very small in all the cases. The shift between the initial and peak temperature of all the exotherms increases with manganese content. The difference between the initial and the final temperature also increases showing broadening of the exothermic peaks. The enthalpy of crystallization calculated from the integrated intensity of the DTA exotherms was found to be 28 kJ mole<sup>-1</sup> for pure zirconia and this value agrees well with that reported by Livage et al.<sup>42</sup> From pure zirconium oxide to mixed Zr-Mn oxide samples containing different concentrations of manganese, there is a tendency for the exotherms to shift to higher temperatures. Considering the peak maxima, there is a linear increase in the exothermic peak temperature with increasing manganese content in the zirconia as seen in Fig. 3.6. A similar observation with yttria stabilized zirconia is reported recently by Tagawa et al.<sup>40</sup> Prima facie, this indicates that the crystallization is hindered by the presence of manganese in the amorphous zirconia. On the other hand, the enthalpy of crystallization decreases progressively from 28 kJ mole<sup>-1</sup> of ZrO<sub>2</sub> for the pure ZrO<sub>2</sub> sample to 12.1 kJ mole<sup>-1</sup> of ZrO<sub>2</sub> for samples with 20 mole % of Mn in



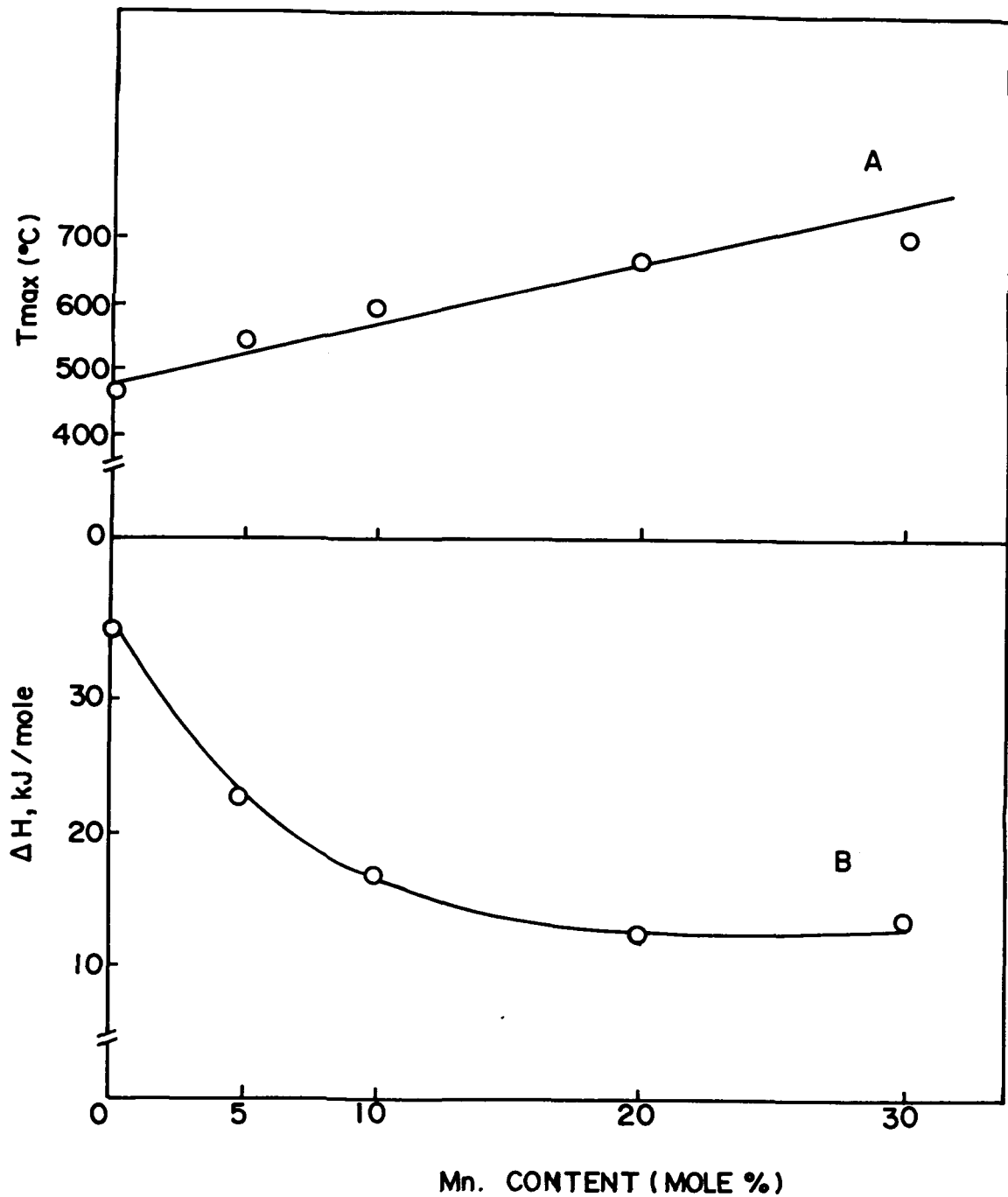


**Fig. 3.6 :** Influence of manganese content in zirconium oxide hydrate on (A) the exothermic (crystallization) peak maxima, and (B) the enthalpy of crystallization

zirconia and stabilized at the same value for 30 mole % of manganese containing sample (Table 3.3). This phase transformation from amorphous to crystalline phase occurs just after the completion of the dehydration step in all the samples, since no weight loss is observed in this region. This exotherm can be a characteristic feature of either the crystallization alone or the glow phenomenon<sup>43</sup> or both of these occurring simultaneously. When the manganese oxide hydrate alone is decomposed, no exothermic peak is observed and no amorphous material is formed. It is, therefore, possible that when Mn-oxide is dissolved in amorphous zirconia, enthalpy of crystallization of amorphous to crystalline, cubic phase decreases.

In the case of pure zirconium oxide hydrates, the observed exotherm at around 743 K is very sharp. A similar observation was reported earlier<sup>42</sup> and has been attributed to both a glow phenomenon and crystallization occurring together. Such a kind of exotherm was also observed for other metal oxides like ferric oxide and chromium oxide.<sup>44</sup> The glow phenomenon is believed to be a visible manifestation of the coalescence of primary colloidal particles into larger masses with consequent release of surface energy.<sup>45</sup> In the case of pure zirconium oxide hydrates, such a crystallization leads often to a monoclinic  $ZrO_2$  phase (XRD). A decrease in the enthalpy of crystallization with increase in manganese content indicates that the glow phenomenon slowly decreases with increasing manganese content. Thus, manganese contributes significantly towards decreasing the exothermicity of the glow and crystallization resulting in the formation of cubic phase. Similar quelling of glow was attributed to adsorption of one oxide on the surface of the other when two oxides were

mixed together<sup>45</sup> In the present case, it is the formation of solid solution of oxides of zirconium and manganese which is probably responsible for the decrease in glow.

### ***Texture and phase transformation***

The controlled calcination of the precursors leads to transformation of the amorphous to crystalline phase. This process may be treated as proceeding in two steps : the first is the formation of the initial crystalline phase and the second, the sintering of the small crystallites into bigger crystals. A large enthalpy of crystallization will facilitate the second step. Since the glow phenomenon results in crystal growth, a loss of surface area and profound alteration in the electronic properties of the crystalline materials can be expected. Hence, it is essential to control this phenomenon. The incorporated manganese in zirconia appears to control this phenomenon and as a result, there is a substantial increase in the surface area of the samples formed. With increasing manganese content, the surface area increases (from 70 to 110 m<sup>2</sup> g<sup>-1</sup>) of the samples calcined at 773 K. In the X-ray diffraction profiles of the samples, significant peak broadening is observed with increase in manganese content, indicating a decrease in the crystallite size. Hence, this exothermic peak observed in DTA can be ascribed to the phase transformation from amorphous to crystalline phase and not to the glow phenomenon. Apart from the formation of the small crystallites, presence of the mesopores was also observed in the Mn-stabilized zirconia samples. These are stable in cubic phase upto 1023 K and are found to be active in the total oxidation of hydrocarbons (C<sub>4</sub>) and carbon monoxide.

### 3.2.4.3. X-Ray Diffraction studies

#### *Effect of Mn content:*

The X-ray diffraction patterns of representative samples are given in Fig. 3.7. The profile *a* corresponds to a sample prepared by mixing 10 mole % MnO<sub>2</sub> with ZrO<sub>2</sub> (solid state mixture) and calcined at 1273 K. Individual oxide phases denoted by 'm' and 'z' (corresponding to MnO<sub>2</sub> and ZrO<sub>2</sub>, respectively) are seen. No single phase is formed by this procedure. On the contrary, the hydroxide gel route leads to the incorporation of Mn in to ZrO<sub>2</sub> to form a cubic phase in samples calcined at 773 K, as seen from the XRD profiles of samples with 10, 20 and 30 mole % of Mn in ZrO<sub>2</sub> (profiles b, c and d, respectively). However, when the Mn content increased up In pure zirconia, both cubic and monoclinic phases are observed. The metastable cubic phase may be due to the surface hydroxyls present in ZrO<sub>2</sub>. When it was doped with 5 mole % of Mn, the major phase found is cubic along with a fraction of monoclinic phase. As the amount of Mn is increased up to 30 mole %, only cubic phase is found to exist. When the reaction is brought through the co-precipitated hydroxide, the formation of the stabilized oxide takes place probably through a labile hydroxy complex. The formation of such a hydroxy complex which subsequently decomposes to a disordered oxide phase is shown to be feasible in the La<sub>2</sub>O<sub>3</sub> stabilized cubic zirconia.<sup>26</sup> A similar mechanism may be applicable to the Mn-stabilized zirconia, particularly, in the pH condition of our study.

Another evidence for the incorporation of Mn in the lattice of zirconia can be had by looking at the Fig. 3.8. A decrease in the lattice parameter with increase in Mn

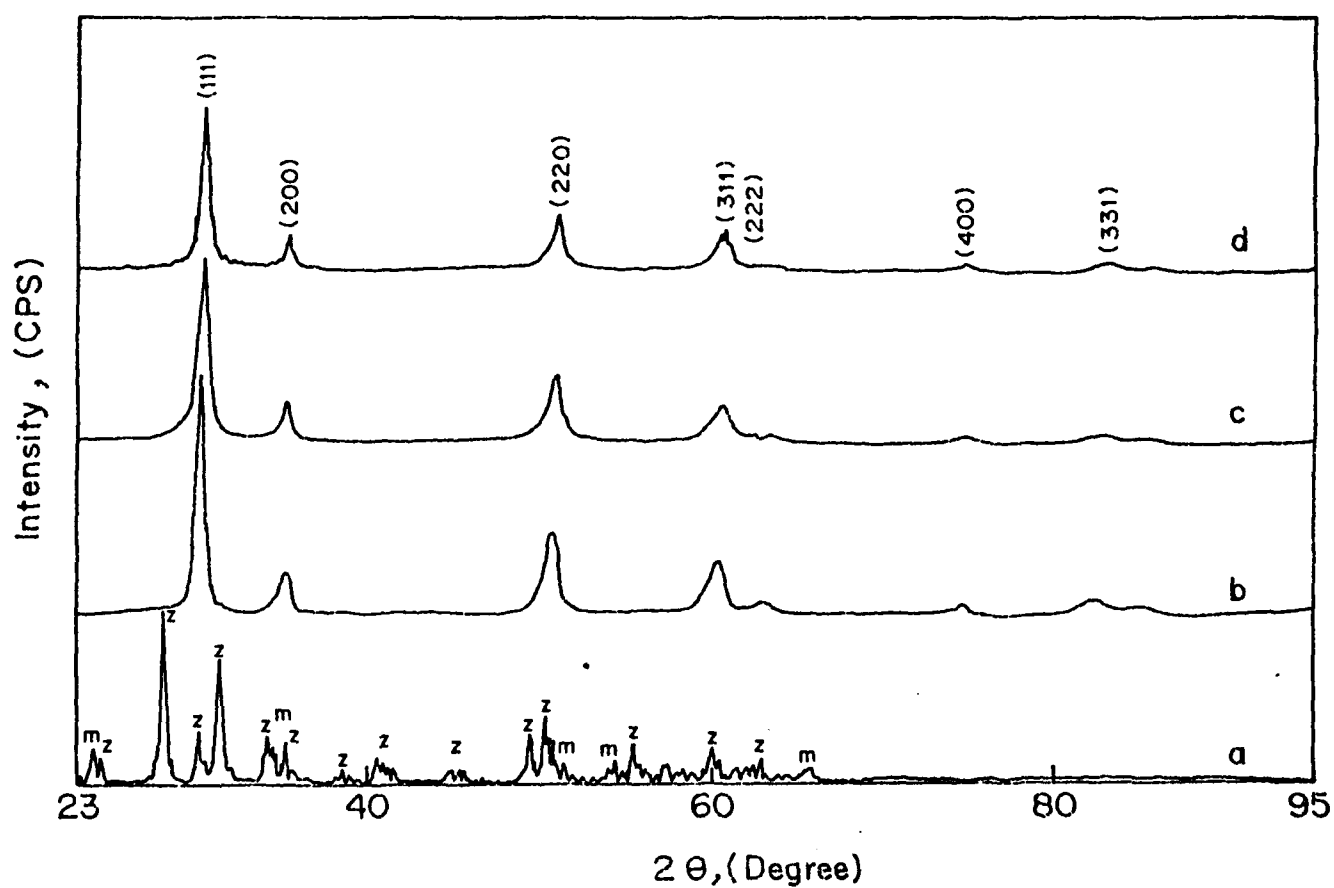


**Fig. 3.7 :** A comparison of the XRD patterns of a solid state mixture of ZrO<sub>2</sub> and 10 mole % of MnO<sub>2</sub> calcined at 1273 K (a), and ZrO<sub>2</sub> with 10, 20 and 30 mole % of Mn prepared by co-precipitation method and calcined at 773 K (profiles b, c and d, respectively). Peaks marked *m* and *z* refers to individual phases of MnO<sub>2</sub> and ZrO<sub>2</sub>, respectively.

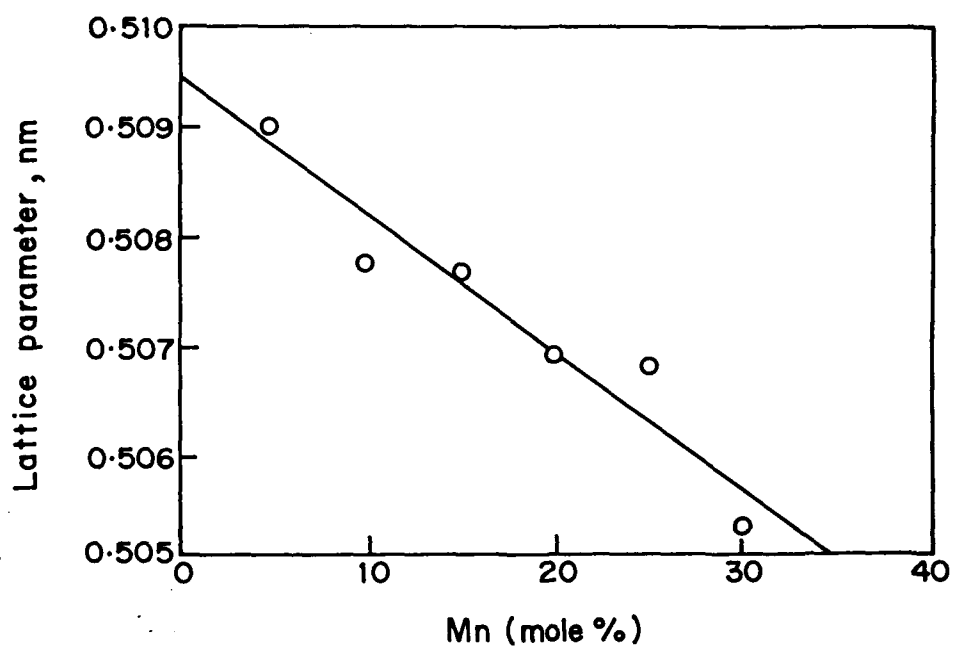


**Fig. 3.8 :** Variation of lattice parameter with Mn content in Mn-stabilized zirconia.

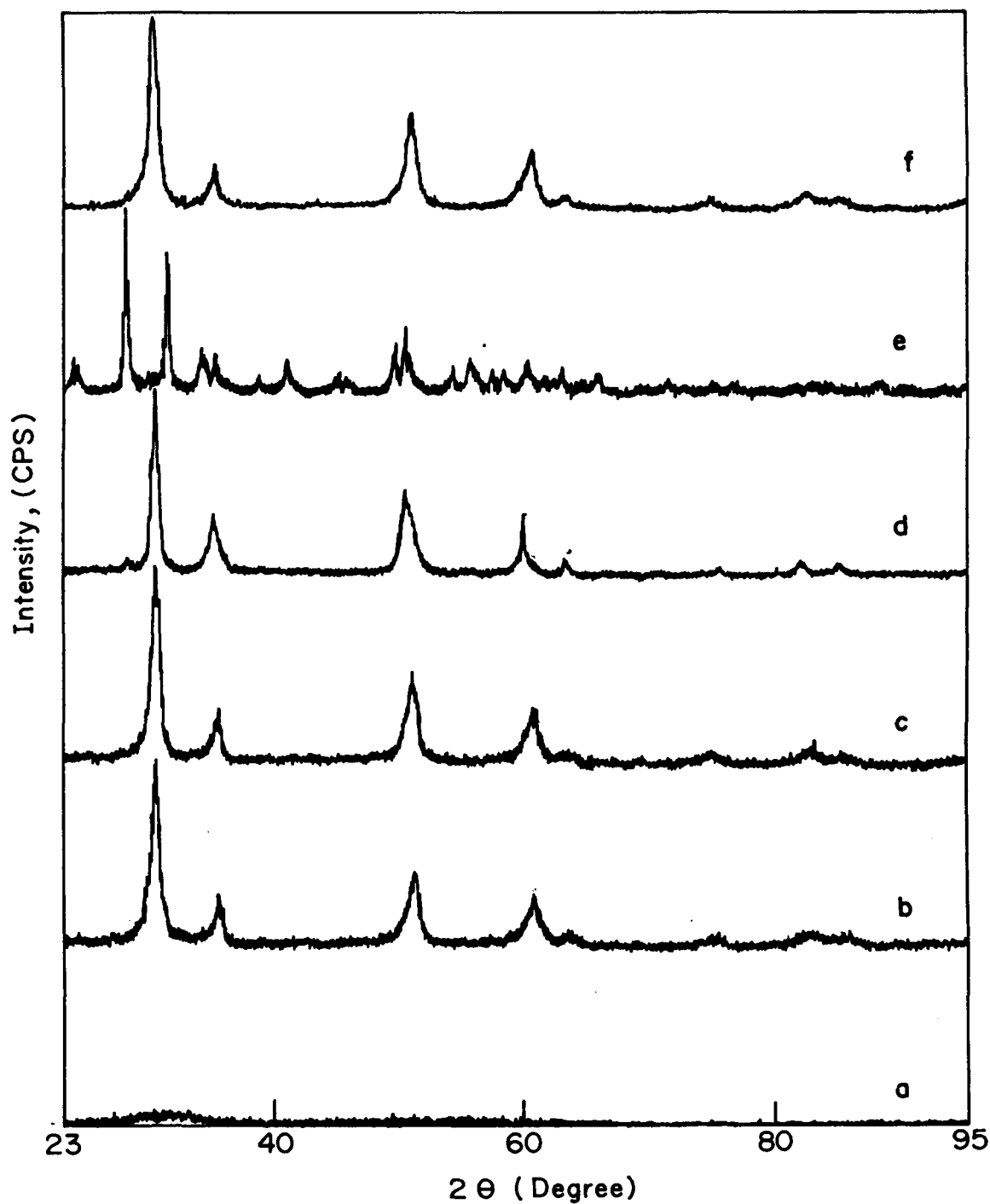


**Fig. 3.9 :** X-ray powder diffraction profiles of  $\text{Zr}_{0.9}\text{Mn}_{0.1}\text{O}_2$  calcined at 673, 773, 873, 973 and 1073 K (profiles a to e, respectively) and treated in  $\text{H}_2$  at 1073 K (profile f).

content (Table 3.4 ) shows that the larger  $Zr^{4+}$  cation sublattice is substituted with the smaller  $Mn^{4+}$  ions, causing lattice contraction with a linear correlation.

### Effect of calcination

The effect of calcination on the structure of one of the representative sample (with 10 mole % Mn) as reflected by X-ray diffraction studies is shown in Fig. 3.9. The samples calcined upto 673 K were found to be amorphous (Fig. 3.9, profile 'a'). Above 673 K, broad peaks corresponding to the formation of a crystalline phase begin to appear and the crystallization is complete at 773 K (Fig. 3.9, profile 'b'). The samples were further calcined in air upto 873 K for 12 and 36 h to examine the crystallization of any minor impurity phase. It is seen that the XRD lines are sharper due to increased crystallite size (Fig. 3.9, profile 'c'), but still belong to a single cubic phase without any impurity oxide phases. The indexing of the lines for samples with various Mn content confirms the presence of cubic phase without any impurity oxide.

**Table 3.4**  
**Physical properties of Mn-stabilized zirconia**

Mn content (mole %)				
Initial	By titrimetry	Phases	Lattice parameter (nm)	Surface area (m <sup>2</sup> /g)
0	0	cubic + mc	0.5090	75
10	8.96	cubic	0.5089	80
20	19.76	cubic	0.5069	105
30	29.56	cubic	0.5052	73



The  $2\theta$  and  $d$  values of these samples are almost similar to that of  $\text{La}^{3+}$  stabilized zirconia, with a small deviation. The lattice parameters (accurate to  $\pm 0.0001$  nm) of the samples are given in Table 3.4.

#### **Effect of reducing atmosphere on the structure**

The effect of heat treatment under reducing atmosphere at various temperatures and reoxidation on the structure of a representative sample of Mn-stabilized zirconia (10 mole % of Mn) as identified by X-ray diffraction studies is shown in Fig. 3.10. As such, the sample is cubic (Fig. 3.10, a). When reduced at 773 K its structure remains intact (Fig. 3.10, b) with a little increase in the lattice parameter (Table 3.5). When the same sample was reoxidized at the same temperature, the lattice parameter value reverted back almost to the original value, while the structure remains cubic only (Fig. 3.10, c). However, when the same sample was reoxidized at 1073 K, there is disruption in the structure with the emergence of monoclinic phase of zirconia, thus causing destabilization (Fig. 3.10 d). When the same sample was reduced at 1073 K, once again the structure remains intact, with a significant expansion in the lattice parameter (Fig. 3.10 e). This sample, when reoxidized at 773 and 1073 K, the cubic structure remains intact (Fig. 3.10 e and f). Thus, calcination in  $\text{H}_2$  at 773 K and above stabilizes  $\text{ZrO}_2$  in the cubic phase, probably by  $\text{Mn}^{2+}$  ions, as the lattice parameter increases to 0.5094 nm for this sample. This indicates the importance of the ionic size of the dopant on the structural stabilization of zirconia. From the Shannon's ionic radii values,<sup>45b</sup> one can see that lower valent manganese,  $\text{Mn}^{2+}$ , which is most probably present during reduction at 1073 K, has the ionic size somewhat equivalent to that of  $\text{Zr}^{4+}$ . While, the samples calcined at 773 K and those reoxidized at 773 and

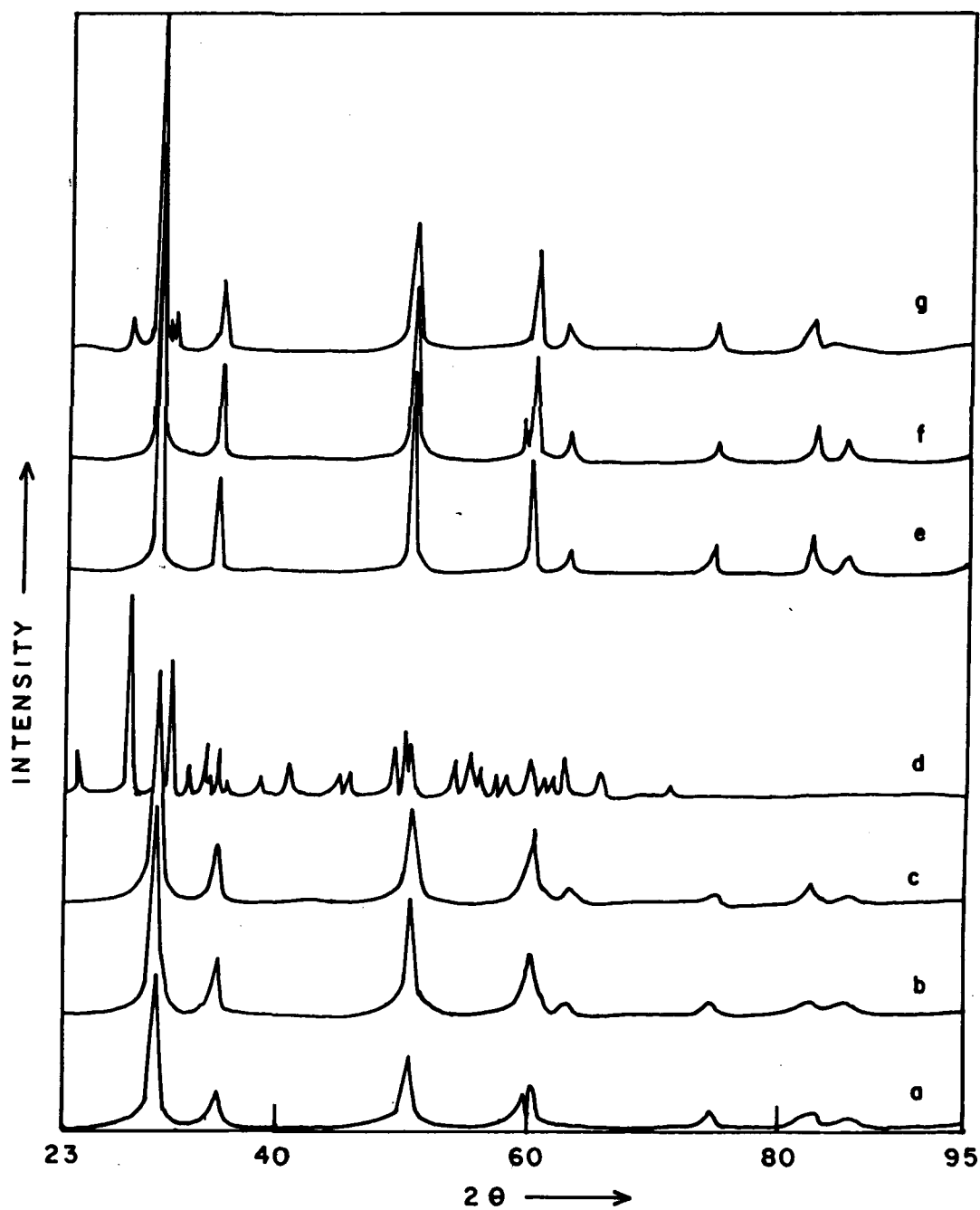


**Fig. 3.10 :** Effect of reduction and reoxidation of Mn-stabilized zirconia (with 10 mole % Mn) as evidenced by XRD studies: as prepared sample after calcining at 773 K denoted by A (a), A reduced at 773 K to get B, (b) B reoxidized at 773 K to get C (c), B reoxidized at 1073 K to get D (d), A reduced at 1073 K to get E (e) and E reoxidized at 1073 K. 773 K and D reoxidized at 1073 K.

1073 K contains multivalent manganese and the structure gets destabilized at higher temperature (1073 K). This indicates that higher valent manganese is not favourable for the stabilization.

**Table 3.5**

**XRD parameters of Mn-zirconia under reduction and reoxidation**

Notation	Conditions	Phases	Lattice parameter, nm
A	Mn zirconia calcined at 773 K	cubic	0.5080
B	A reduced at 773 K	cubic	0.5090
C	B reoxidized at 773 K	cubic	0.5085
D	B reoxidized at 1073 K	monoclinic	
E	A reduced at 1073 K	cubic	0.5104
F	E reoxidized at 773 K	cubic	0.5095
G	E reoxidized at 1073 K	cubic	0.5085

#### **3.2.4.4. N<sub>2</sub> Adsorption studies**

The BET surface areas of the Mn containing zirconia are included in Table 3.6. A surface area of about 100 m<sup>2</sup> g<sup>-1</sup> is observed for samples with 15 and 20 mole % of Mn. The particle size of the samples was in the range of 0.4 to 1.1 μm. The area calculated from the t-plot of the N<sub>2</sub> adsorption isotherm.<sup>46</sup> was about the same as the BET area. Hence, the area contribution is understood to be mainly from the mesopores in these samples and not due to external surfaces. This is an important consideration for the application of these materials as catalysts in oxidation reactions.

The effect of manganese on the nature of pores and their distribution can be understood by viewing at their adsorption-desorption isotherms and their pore size

**Table 3.6**

**N<sub>2</sub> physisorption data of Mn-stabilized zirconia**

Mn (mole %)	Isotherm type	Hysteresis type	S <sub>BET</sub> (M <sup>2</sup> /g)	V <sub>p</sub> (cm <sup>3</sup> /g)	t-area (m <sup>2</sup> /g)	Av. pore radius (Å)	Crystallite size (Å)
0	II	B	50	0.057	48	28	90
5	IV	E	78	0.068	64	17	85
10	IV	E	80	0.075	77	18	78
20	IV	E	107	0.102	101	19	66
30	IV	E	73	0.070	73	19	51

distribution. Full adsorption-desorption isotherms of the samples with 10, 20 and 30 mole % of Mn and also of pure zirconia is shown in Fig. 3.11. The pure zirconia has a type II isotherm, with hysteresis of type B, whereas Mn-stabilized zirconia samples shows isotherms of type IV (BDDT classification) and hysteresis loop of type E.<sup>47, 48</sup> This confirms the presence of well developed porous network. E type hysteresis is generally associated with 'ink bottle' type pores, spheroidal pores or voids between close packed spherical particles.<sup>49,50</sup> On the otherhand, type B hysteresis loop is characteristic of cylindrical pores. All the samples are found to be mesoporous, pure zirconia with pore radii of about 28 Å and Mn-stabilized zirconia with pore radii around 19 Å. Fig. 3.12 shows the effect of thermal treatment on the pore size

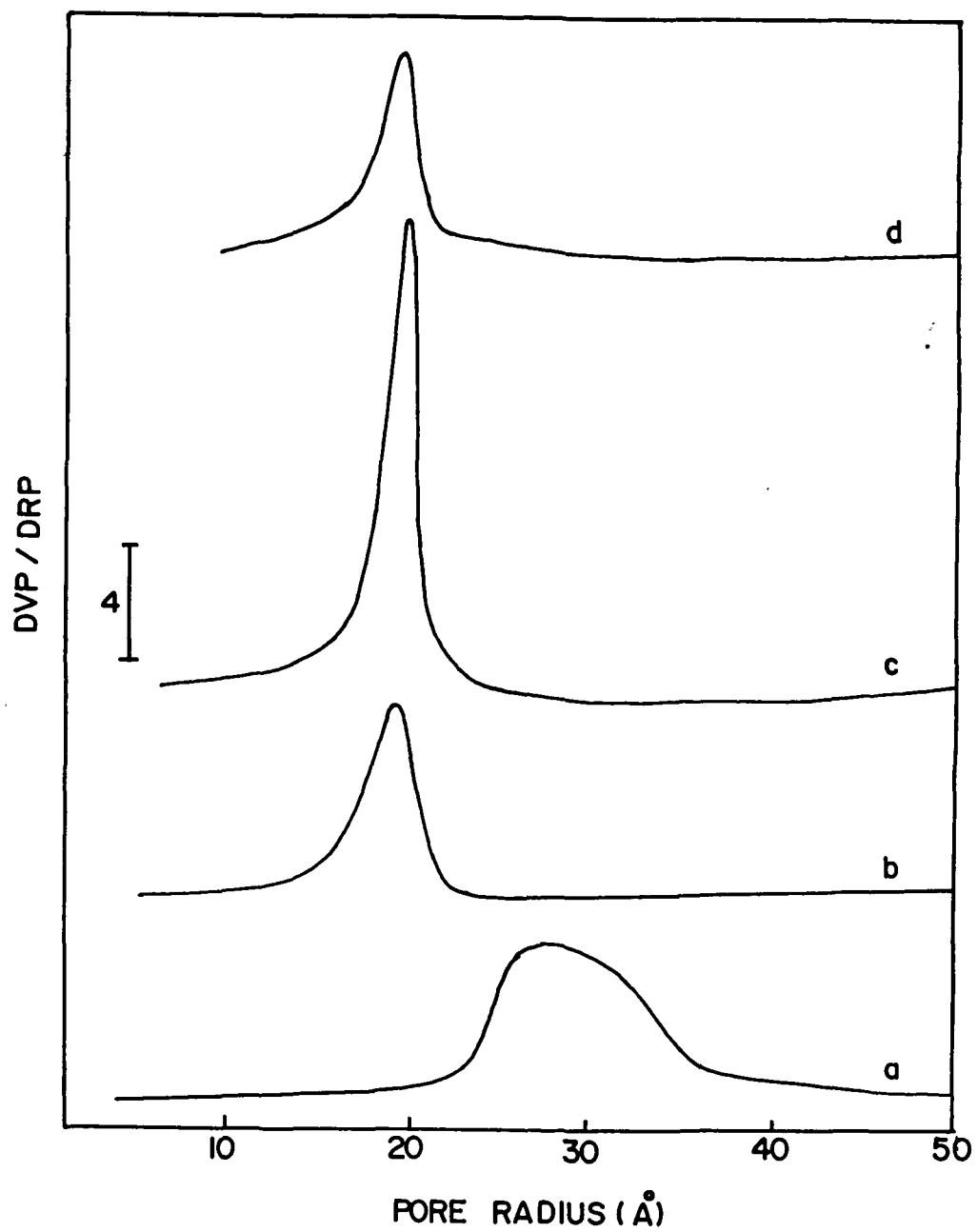


**Fig. 3.11 :** Pore size distribution of pure zirconia (a), and Mn-stabilized zirconia with 10, 20 and 30 mole % of Mn (b, c, and d, respectively)

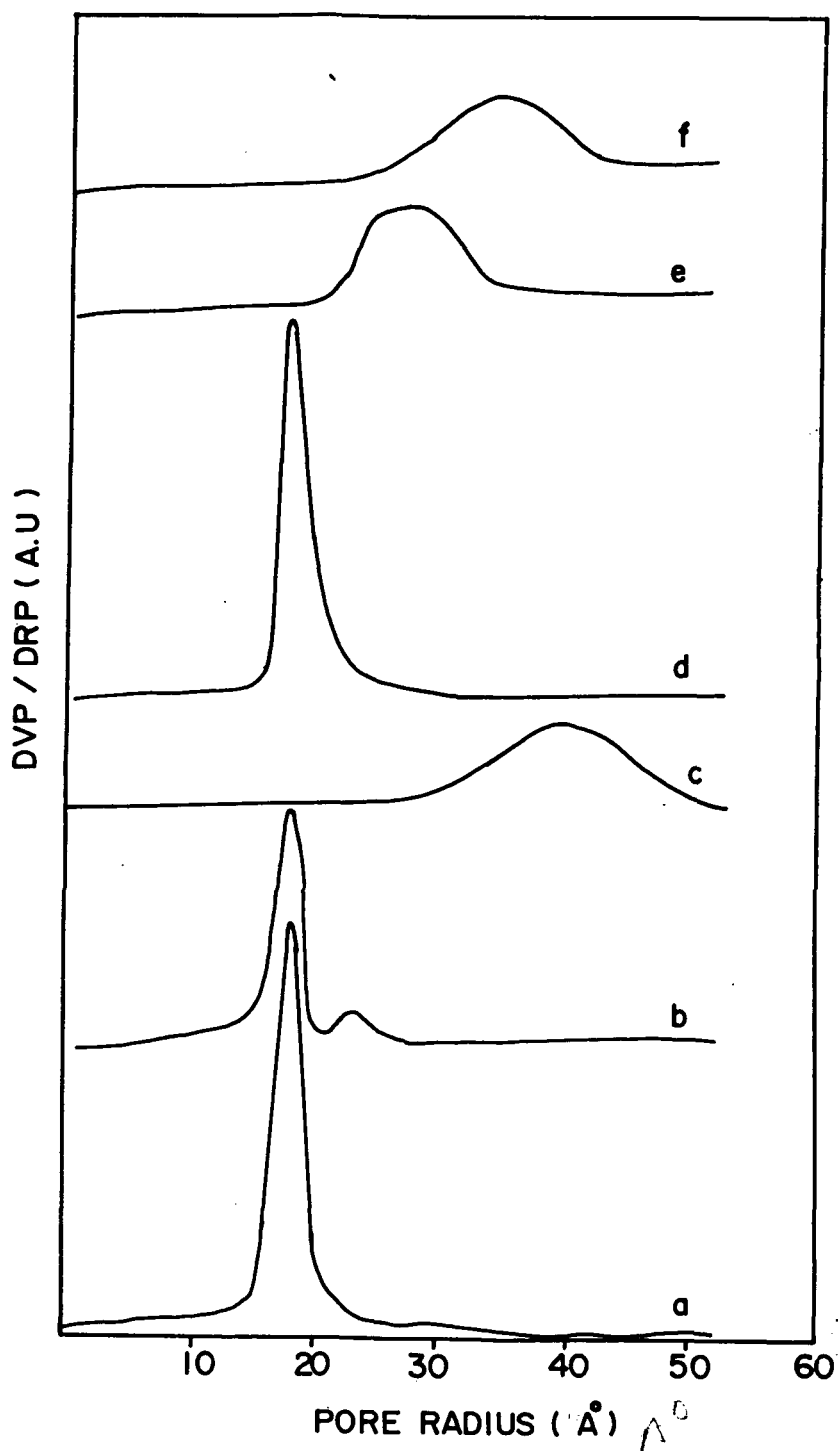


**Fig. 3.12 :** Pore size distribution of Mn-stabilized zirconia calcined at 773, 873 and 973 K (a, b, and c, respectively) and corresponding pore size distribution of pure zirconia (d, e, and f, respectively).

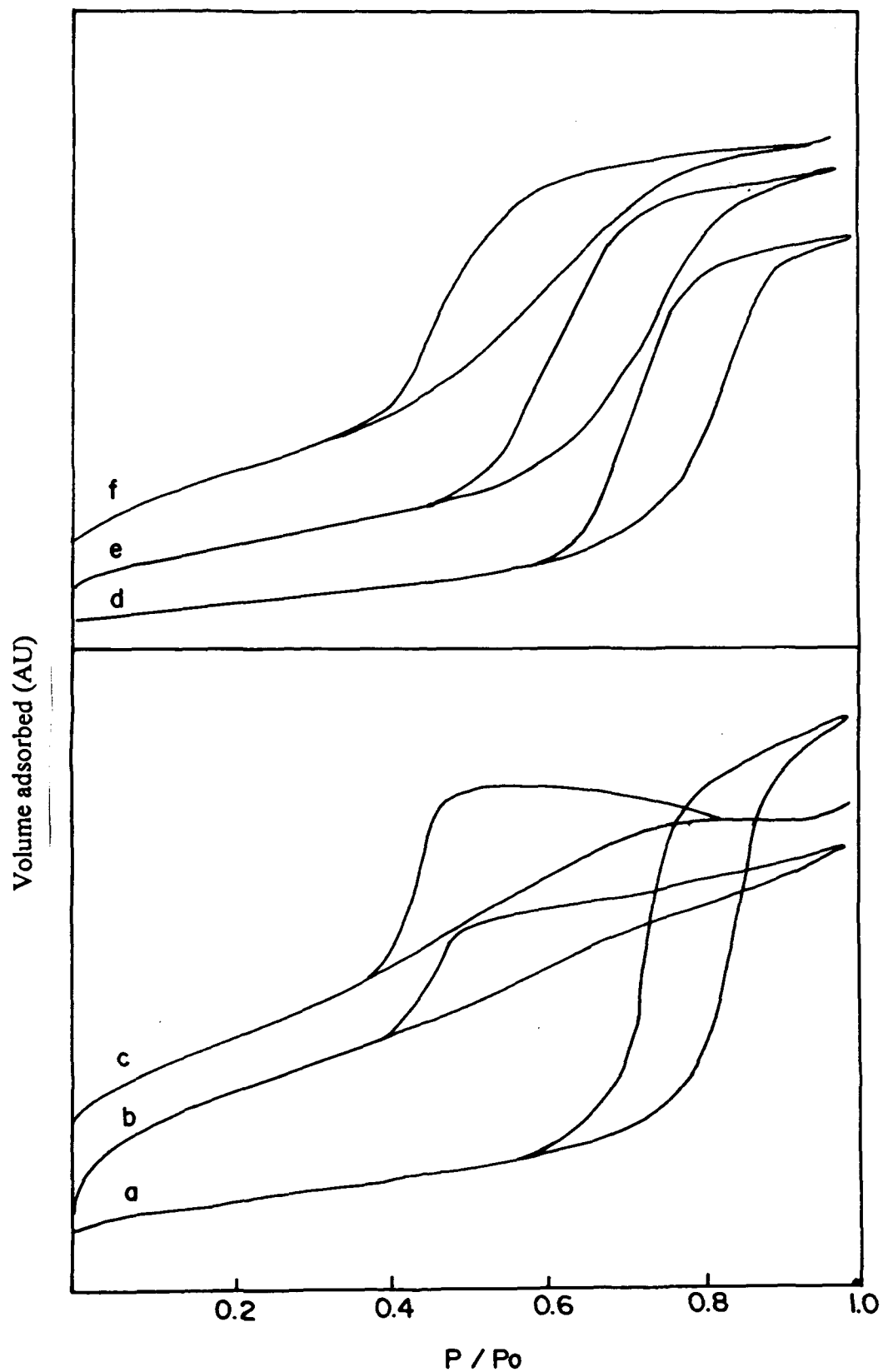


**Fig. 3.13 :** Adsorption - desorption isotherms of Mn-stabilized zirconia (20 mole % of Mn) and pure zirconia calcined at 773, 873 and 973 K, respectively (a to f).

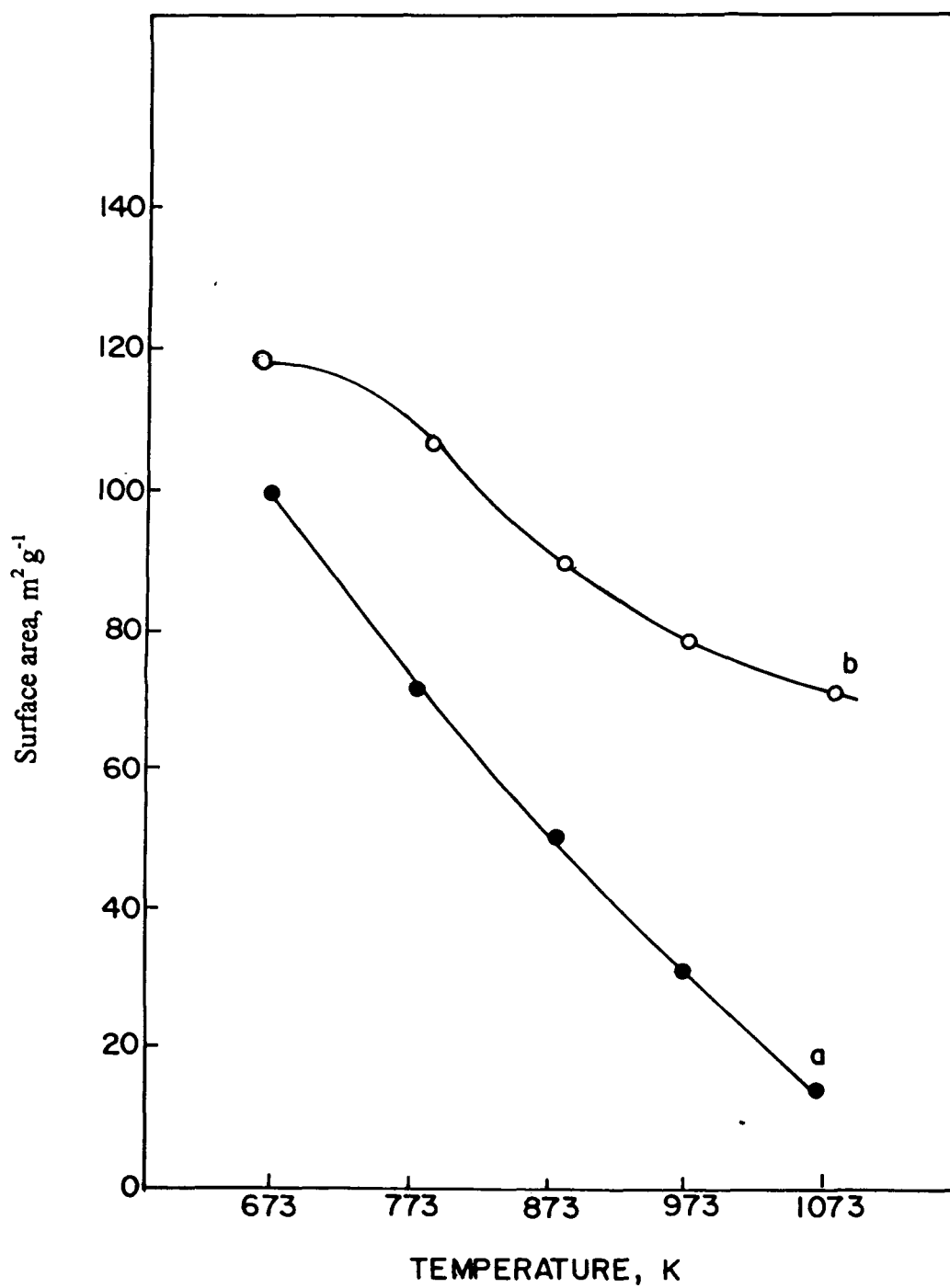


Fig. 3.14 : Variation of surface area with calcination temperature of pure zirconia (a) and Mn-stabilized zirconia (b).



distribution and the corresponding adsorption desorption isotherms are presented in Fig. 3.13. These two indicate that in pure zirconia, the porous net work collapses at an earlier temperature while the presence of Mn seems to stabilize the porous nature and the internal surface area of the sample. This is further illustrated in Fig. 3.14, where the variation of surface area of pure zirconia and Mn-stabilized zirconia against calcination temperature is plotted. The rate of decrease in surface area is drastic for zirconia while for the latter, the surface area remains quite high even after calcining at 1073 K. Thus, the the role of manganese in inhibiting the sintering phenomenon is in agreement with that of an earlier observation.<sup>51</sup> Apart from the internal surface, there a significant influence of the external surface on the surface area as reflected by the variation in the respective crystallite sizes which decreases with increasing manganese content.

The formation of zirconia through calcination of zirconium hydroxide is well documented.<sup>52-54</sup> It eventually involves three steps : loss of loosely bound water and terminal hydroxo groups, oxolation of OH bridges to form embryonic oxide nuclei, and finally the growth of the nuclei to form observable crystallites. The presence of Mn-hydroxide may hinder the growth of embryonic oxide nuclei and thus causing the smaller crystallites. In addition, it also controls the pore volume to a significant extent, thus stabilizing the surface area.

### **3.2.4.5 XPS studies**

Although the samples contain bi-, tri-, and tetravalent manganese, the XPS results indicate the presence of Mn<sup>4+</sup> ions on the surface of all the samples. The

binding energy value (Mn 2p<sub>3/2</sub>) in the range of 641.8 to 642.5 eV (Table 3.7) for the samples calcined in air upto 873 K is typical of Mn<sup>4+</sup> species. There is no evidence for

**Table 3.7**

**XPS data of Mn-stabilized zirconia**

Mn content mole %	Binding energy (eV)			Zr/Mn Ratio	
	Zr3d <sub>5/2</sub>	Mn2p <sub>3/2</sub>	O1s	theoretical	experimental
10	184.6	641.5	529.6	10.00	9.44
20	181.9	641.9	529.9	4.00	3.94
30	179.3	642.1	529.7	2.33	1.68

the presence of Mn<sup>2+</sup> or Mn<sup>3+</sup> ions on the surface. However, chemical analysis data showed the presence of lower valent manganese to a significant level. The XPS spectra of Zr3d<sub>5/2</sub> electrons of Mn-stabilized zirconia with Mn content ranging from 10 to 30 mole % is presented in Fig. 3.15. The corresponding Mn2p<sub>3/2</sub> and O1s peaks are presented in Fig. 3.16 and Fig. 3.17.

The binding energy of Zr3d core lines has been found at 182.4 eV in agreement with other data reported in the literature.<sup>55, 56</sup> The spin orbit splitting between Zr3d<sub>5/2</sub> and Zr3d<sub>3/2</sub> is 2.4 eV. The FWHM, as obtained from the deconvolution of the Zr3d core lines using a gaussian curve is 1.35 eV for Zr3d<sub>5/2</sub> lines and 1.25 eV for Zr3d<sub>3/2</sub> lines.

The Mn2p spectra are reported in Fig. 3.16 spectrum a, b and c correspond to 10, 20 and 30 mole % of Mn respectively. The spin orbit splitting is found to be in the range of 11 - 12 eV. The corresponding binding energy values show an increasing

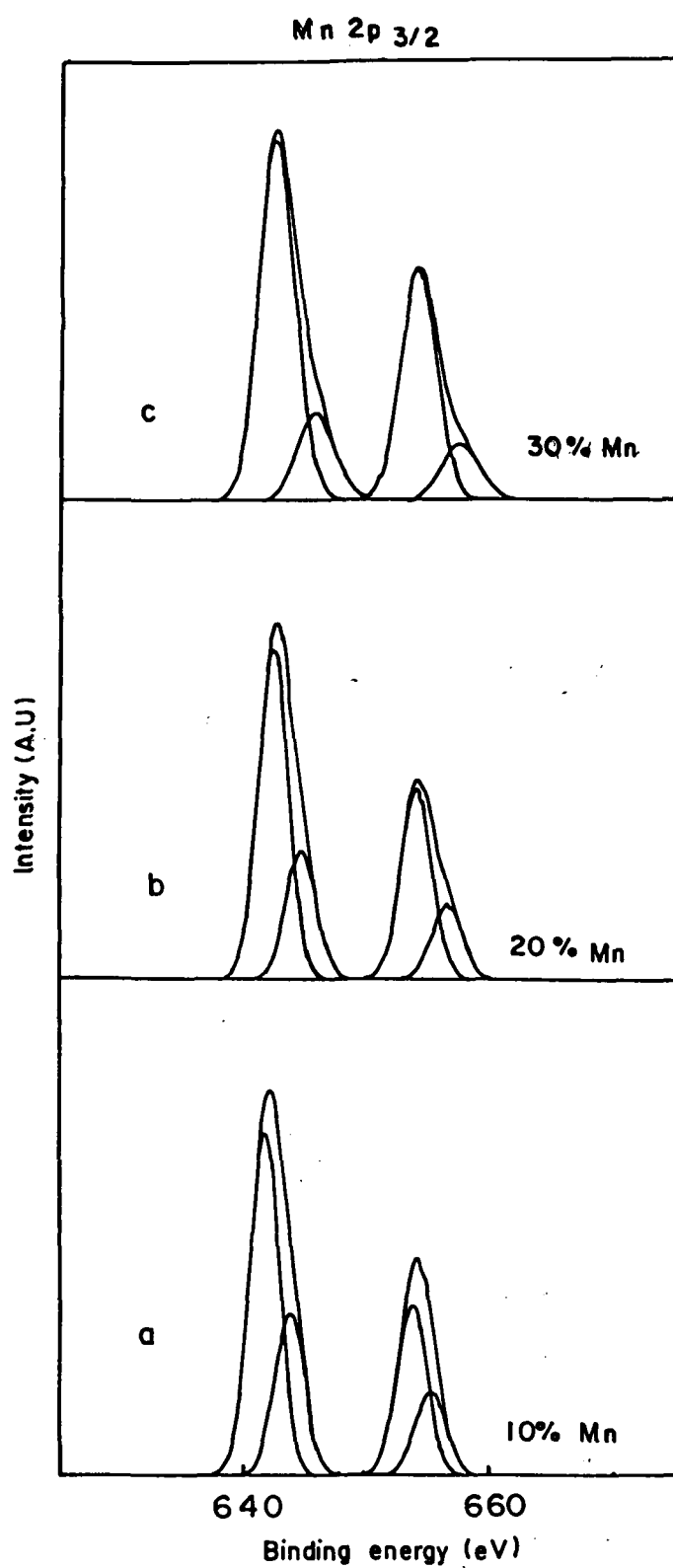


**Fig. 3.15 :** Mn  $2p_{3/2}$  photoelectron spectra of Mn-stabilized zirconia with 10, 20 and 30 mole % of manganese. (a, b, and c, respectively).

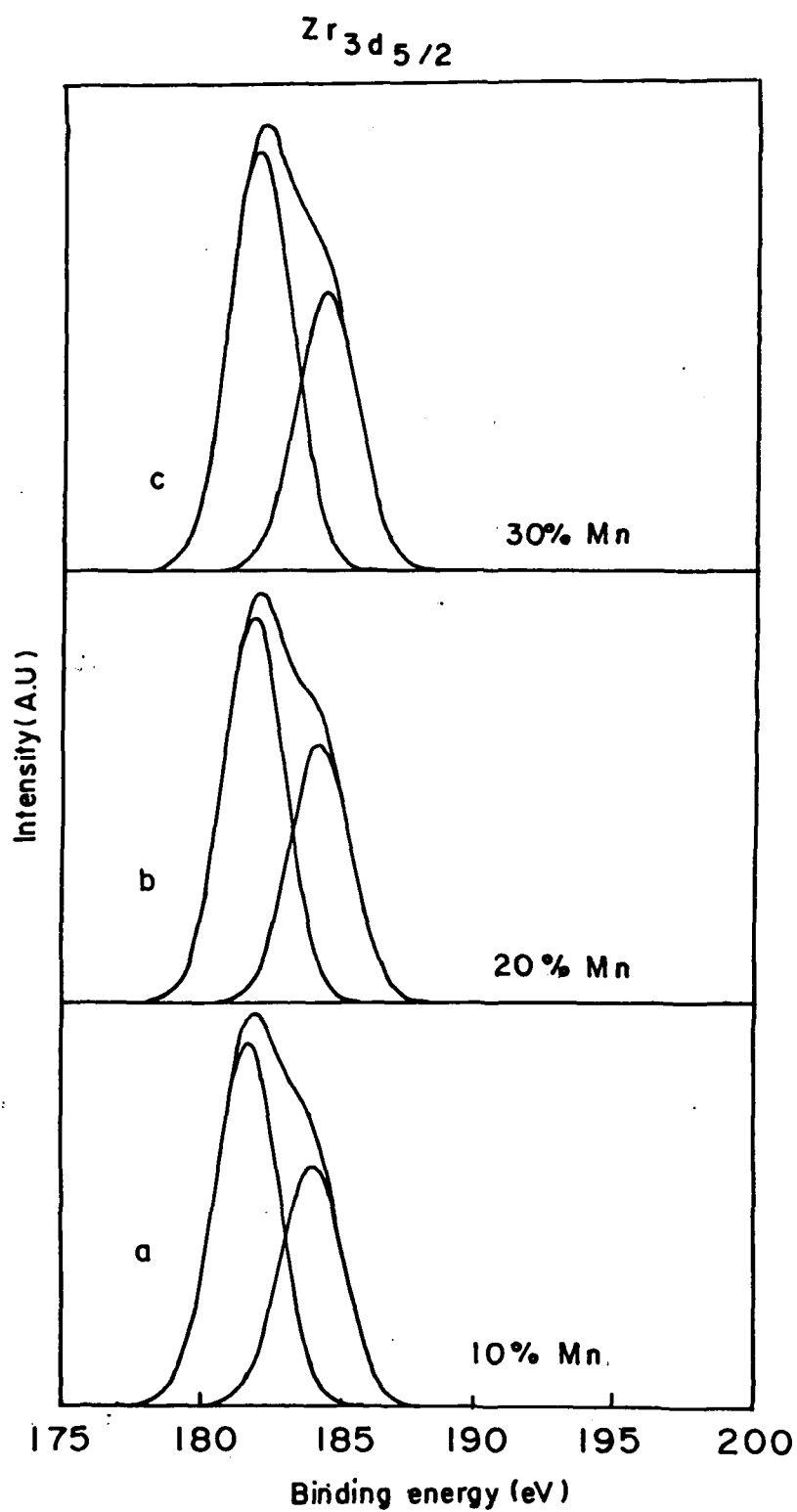


**Fig. 3.16 :**  $Zr\ 3d_{5/2}$  photoelectron spectra of Mn-stabilized zirconia with 10, 20 and 30 mole % of manganese. (a, b, and c, respectively).

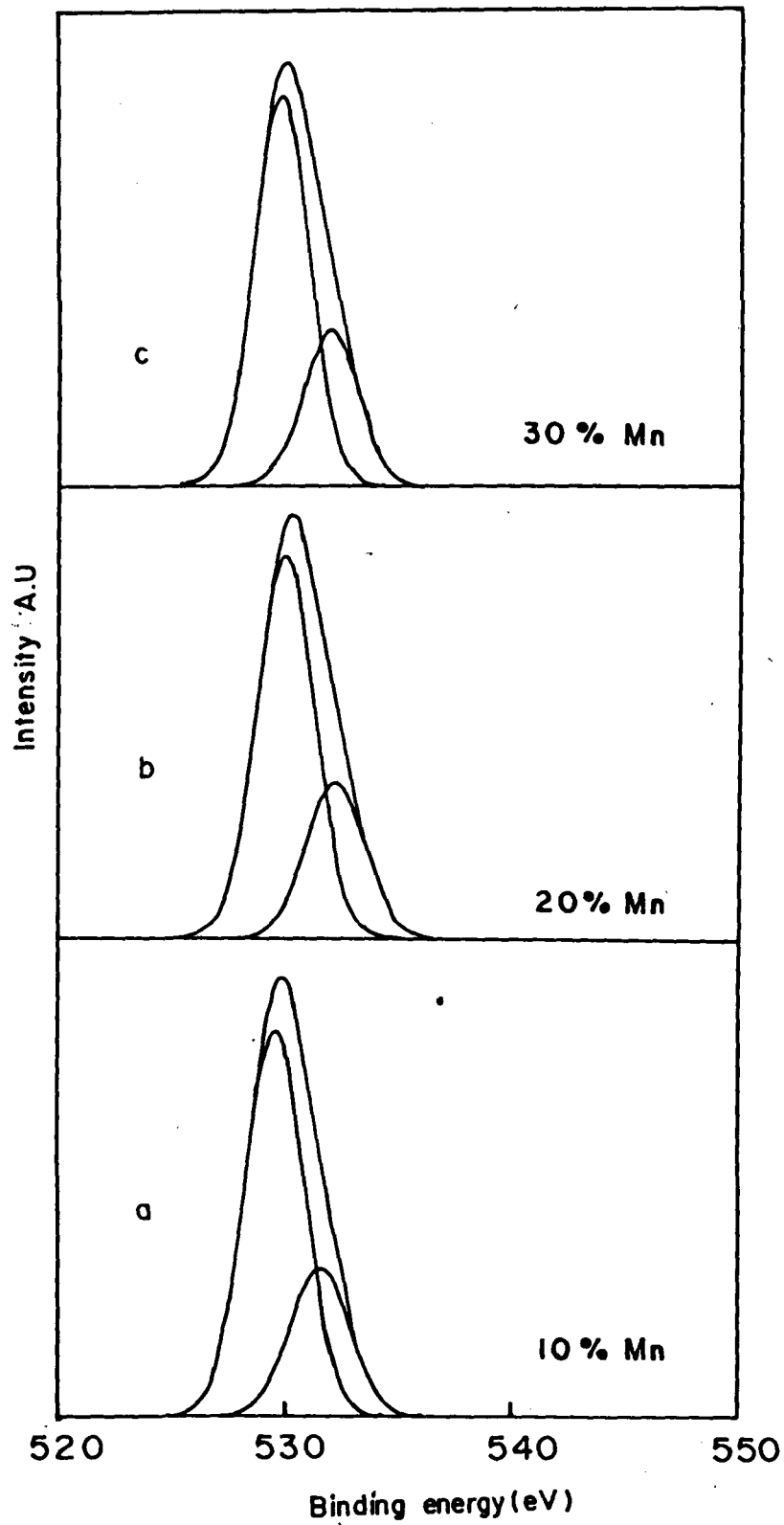


Fig. 3.17: O 1s photoelectron spectra of Mn-stabilized zirconia with 10, 20 and 30 mole % of manganese. (a, b, and c, respectively).

trend with increasing Mn content. This BE shift can be attributed to the formation of a solid solution of zirconia and manganese. The lower BE of the sample with lower Mn content indicates the presence of lower valent Mn, i.e.,  $Mn^{2+}$  in considerable amount than that of other samples. This is in agreement with the chemical analysis data and TPR studies.

Fig. 3.17, shows the O1s core lines measured on three samples. All the O1s spectra exhibit a secondary line at around 529.9 eV apart from the main line at around 530.5 eV. A second component observed in all the O1s spectrum is attributed to the possible oxygen surface disorder produced by the fracturing process of the crystals.

It is recognized that in oxide systems, changes of the metal - oxygen bond length or coordination number lead to significant shift of the core line binding energies and/or shapes. Same thing was observed for Mn-stabilized zirconia.

On increase in Mn content from 5 to 30 mole %, the number of structural oxygen vacancies introduced in the zirconia lattice will change proportionately. In several crystallographic models based on the fluorite structure, vacancies are randomly distributed and  $Zr^{4+}$  with different coordination number should be present in the lattice. This could be reflected by distinct binding energy values and FWHM of the Zr3d lines when different Mn contents are considered.

Several models for the possible oxygen distribution and corresponding oxygen displacements of the oxygen ions from the ideal fluorite sites have been proposed for yttria stabilized zirconia.<sup>57-60</sup> Similar model can be applied to Mn-zirconia also. As the Mn content increases, the concentration of oxygen vacant site increases and the metal-oxygen distances and the metal - oxygen coordination number could change.

Particularly, the oxygen ion vacancies introduced by the manganese in the zirconium lattice could be partially or completely coordinated to  $Zr^{4+}$  ions. It is known that the full width at half maximum (FWHM) and the binding energy values of X-ray photo emission lines measured on oxides are significantly influenced by the local order around the atom.<sup>61,62</sup> Thus XPS could be effective in detecting possible modifications of Mn-stabilized zirconia.

#### ***3.2.4.6. FTIR studies***

Additional evidence for the formation of cubic phase of the Mn-stabilized zirconia is obtained by comparing the IR spectra of zirconia with 10% of Mn prepared by both the methods, i.e., precipitation and solid state reaction. The IR spectrum of the monoclinic  $ZrO_2$  is reported to show six bands in the region 300 to 800  $cm^{-1}$ . On the other hand,  $Y_2O_3$  stabilized zirconia in cubic phase consisted of a broad band in the same region.<sup>63</sup> which indeed is observed in the present samples (Fig. 3.18).

#### ***3.2.4.7. Raman Spectra***

Additional evidence for the formation of cubic phase is also given by laser Raman spectroscopy. Fig. 3.19 shows the Raman spectra of pure zirconia (a) and Mn-stabilized zirconia with 10 and 20 mole % of Mn (b and c, respectively). A sharp band around 465  $cm^{-1}$  observed in the Mn-stabilized zirconia samples is characteristic of fluorite type oxides with cubic symmetry.<sup>64, 65</sup> Furthermore, after the substitution of manganese, there is a shift in the Raman wave number to lower bond strength

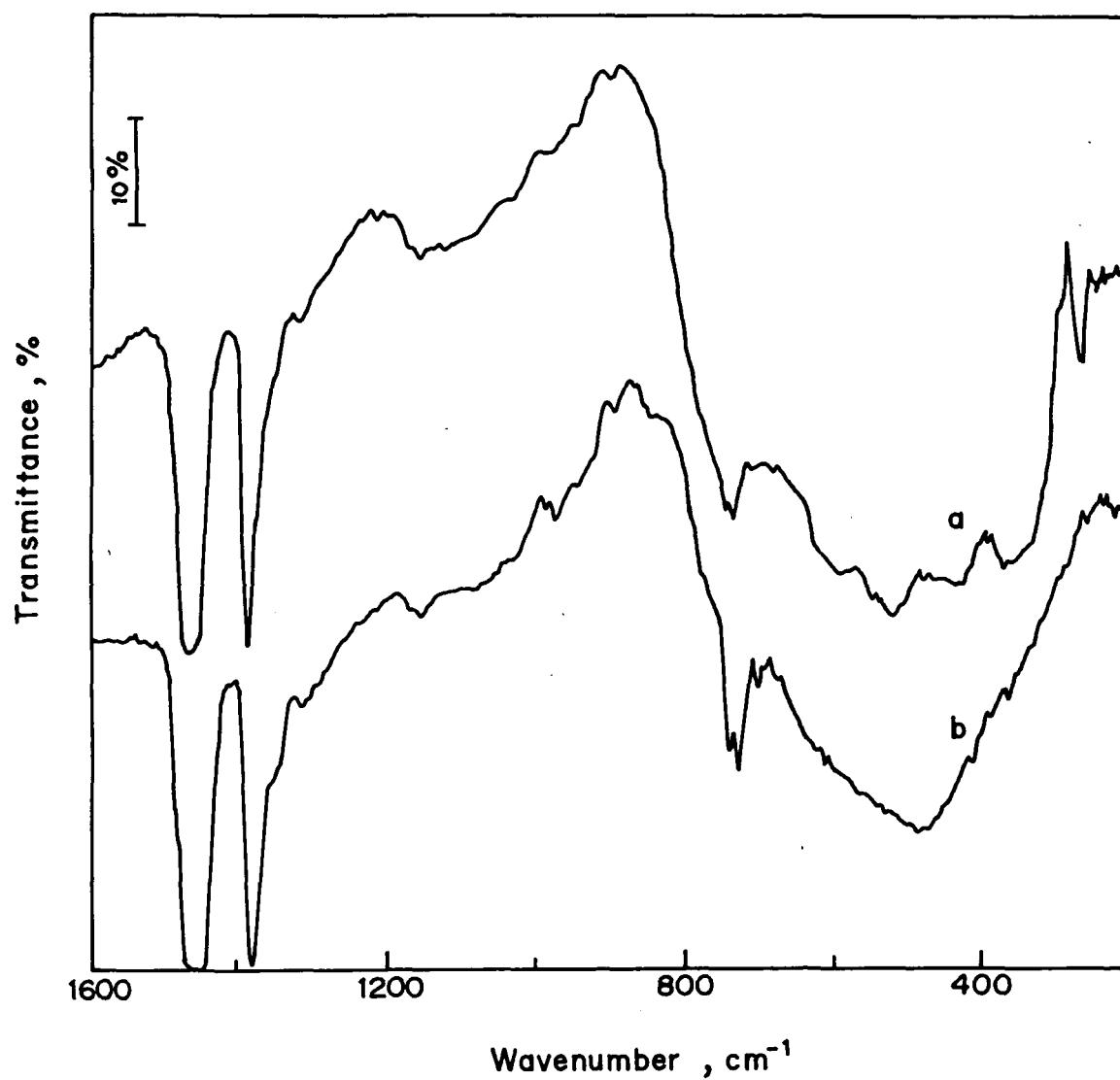


**Fig. 3.18 :** Framework IR spectra of solid state mixture of 10 mole % of  $\text{MnO}_2$  in zirconia (curve a) and of cubic stabilized zirconia with same amount of Mn (curve b).



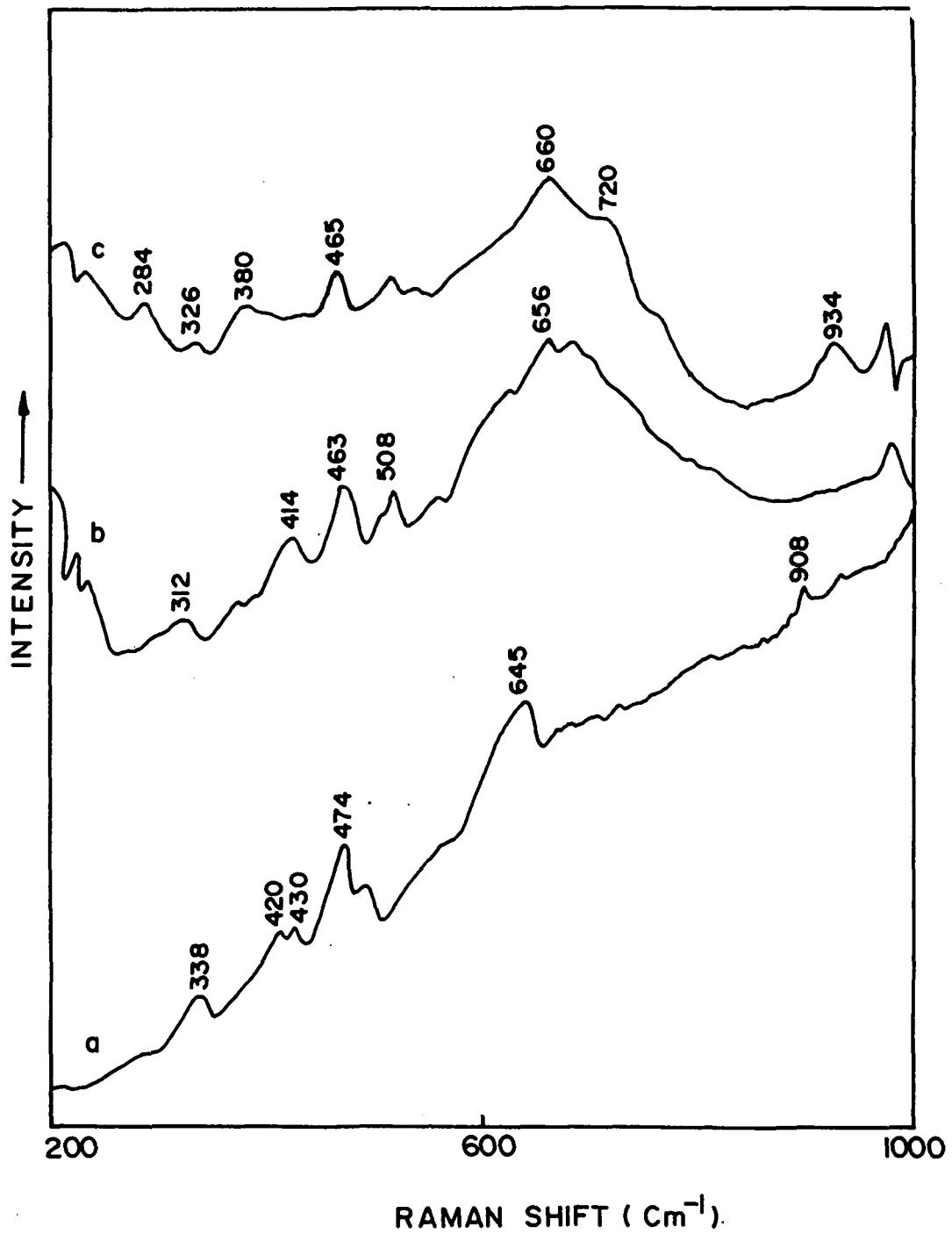


Fig. 3.19 : Raman spectra of pure zirconia (curve a), and Mn-stabilized zirconia with 10 and 20 mole % of Mn (curves b and c, respectively).

compared to that of pure zirconia. This can be attributed to the formation of solid solution, different local bonding environments of dopant cation and increasing number of oxygen vacancies.<sup>66</sup>

### 3.2.4.8. TPR studies

The temperature programmed reduction (TPR) profiles of a physical mixture of MnO<sub>2</sub> and ZrO<sub>2</sub> (0.1 mole of MnO<sub>2</sub>) and the one prepared by the hydroxide gel route with 10, 20 and 30 mole % of manganese are represented in Fig. 3.20. (curves 'a' to 'd', respectively). The TPR chromatograms show distinct T<sub>max</sub> and H<sub>2</sub> consumption for all the samples for the reduction process indicating the presence of multivalent manganese with different proportions of Mn<sup>2+</sup>, Mn<sup>3+</sup> and Mn<sup>4+</sup> in the bulk. The overall reduction process of all the samples upto 1075 K appear to be governed by not a simple two stage reduction of Mn<sup>4+</sup> ----> Mn<sup>3+</sup> --> Mn<sup>2+</sup>,

**Table 3.8 : Quantitative TPR data**

Sample	H <sub>2</sub> consumed (theoretical), μ mole g <sup>-1</sup>		H <sub>2</sub> consumed (Expt), μ mole g <sup>-1</sup>	
	Step I	Step II	Step I	Step II
10 Mn-ZrO <sub>2</sub>	418.1	418.1	352	612
20Mn-ZrO <sub>2</sub>	862.4	862.4	837	617
30Mn-ZrO <sub>2</sub>	1335	1335	1216	461.2

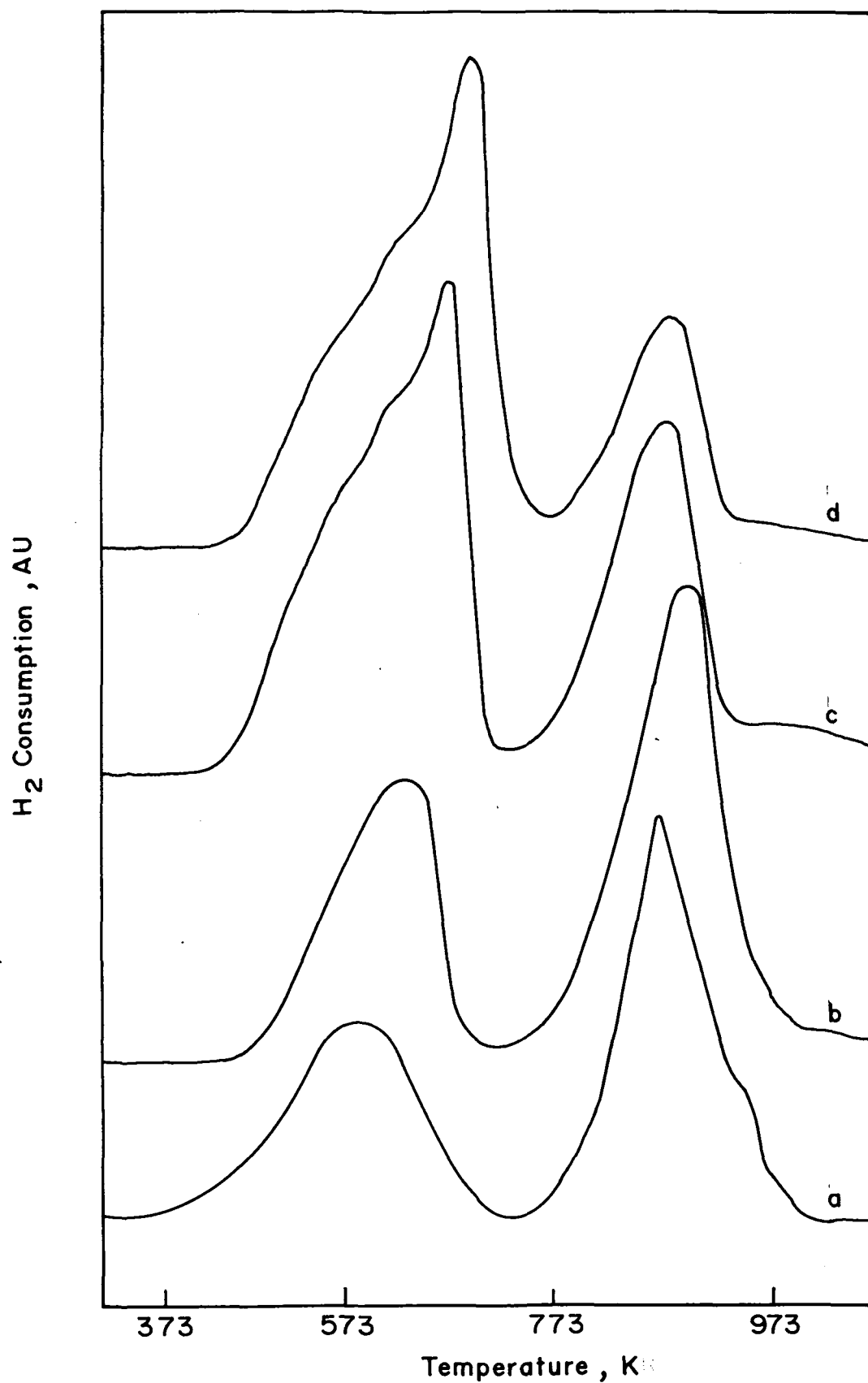


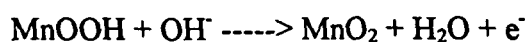
**Fig. 3.20 :** TPR profiles of solid state mixtures of  $\text{MnO}_2 + \text{ZrO}_2$  (a) and Mn-stabilized zirconia with 10, 20, 30 mole % of manganese (b, c, and d, respectively).

but by further solid state transformations. Quantitative data are shown in Table 3.8. An increase in the H<sub>2</sub> consumption in the first stage with increasing amount of manganese indicate that at higher Mn loadings, Mn<sup>4+</sup> is relatively more in agreement with chemical analysis results.

### 3.2.4.9. Cyclic Voltammetry

The cyclic voltammograms of Mn-stabilized zirconia can be used to understand the relative ease of oxidation state changes of Mn as manifested by the redox waves under potential sweep conditions, since the zirconia sample is electrochemically silent under the potential window of - 800 mV to + 800 mV.

Voltammograms of pure zirconia and Mn-stabilized zirconia with 10, 20 and 30 mole % of manganese is presented in Fig. 3.21.(a to d). No peaks are observed for pure zirconia (a), while, on the surface of Mn-stabilized zirconia, various reversible and irreversible redox waves are observed. For example, in sample with 10 mole % of manganese, a strong irreversible cathodic peak at around -650 mV corresponds to the presence of stable Mn<sup>2+</sup> species, while a reversible couple at around -150 mV may be due to the interconversion of Mn<sup>4+</sup> and Mn<sup>3+</sup> species according to the reaction<sup>67, 68</sup>



On the other hand, the main redox wave with the cathodic peak at 600 mV can be attributed to the oxidation of Mn<sup>4+</sup> to higher valent manganese. As the Mn content is increased, the irreversible cathodic peak vanished showing the diminution of lower valent manganese. This is already confirmed by chemical analysis and temperature programmed reduction studies, where there is a decrease in the amount of Mn<sup>2+</sup> with

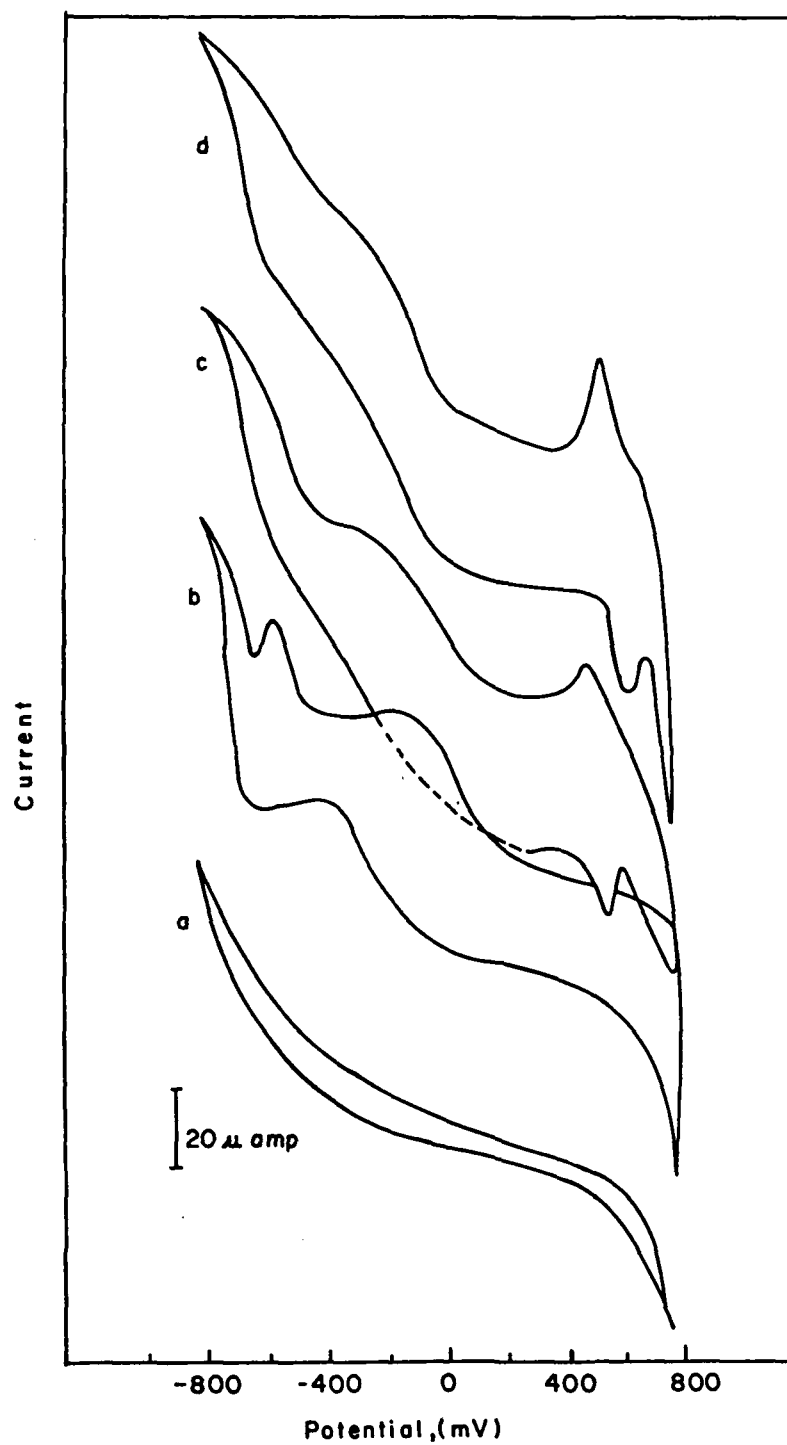


**Fig. 3.21 :** Cyclic voltammograms of pure zirconia (a), and Mn-stabilized zirconia with 10, 20 and 30 mole % of manganese (b, c and d, respectively).

increasing Mn content. However, the quasi-reversible couple at around -200 mV remained intact for all the sample irrespective of Mn content. In addition, the redox couple at about 600 mV also showed an increase in the peak current values.

An interesting observation in this study is that the difference between the anodic and cathodic peak potential is smaller for sample with lower amount of manganese suggesting more facile redox reactions at the composite electrode. This is indeed observed in the TPR study, where, the ease of redox ability was directly dependent on the amount of manganese present in the zirconia lattice. Thus, site isolation by solid solution approach looks to be an attractive way in the direction of catalyst development.

Although, this electrochemical way of analysis is a befitting method to confirm the redox ability of various species present on the surface of the solid catalyst, the results cannot be directly correlated with observed catalytic activity without taking precautions such as solvent induced changes, presence of electric field at the interface, interference from the reaction at the counter electrode, etc.

### **3.2.5 Catalytic Activity of Mn-stabilized zirconia**

#### ***3.2.5.1 Complete Oxidation of n-butane***

Results on the catalytic activity of Mn-stabilized zirconia in the complete oxidation of n-butane, which is one of the major components of hydrocarbons of automotive emission is interesting. The role of Mn content, the effect of calcination

temperature and the importance of stabilized cubic structure on the catalytic activity are described .

The results of the catalytic activity of Mn-stabilized zirconia in the complete oxidation of butane as a function of Mn content is presented in Table 3.9 The catalytic activity is compared with reference to the rate of the reaction and also expressed in

**Table 3.9.**

**Catalytic activity of Mn-stabilized zirconia in complete oxidation of n-butane**

Mn content (mole %)	$T_{50}^a$	$T_{100}^b$	Rate <sup>c</sup>
0	653	823	0.98
5	566	668	6.35
10	480	565	10.4
20	445	523	26.85
30	460	532	24.60
50	510	592	13.22

terms of the temperature required for 50 % conversion ( $T_{50}$ ) and 100 % conversion ( $T_{100}$ ). Fig.3.22 presents the conversion of n-butane with temperature in presence of pure zirconia (curve e) and stabilized zirconia containing varying amounts of Mn (curves a to d for 20, 10, 30 and 5 mole % of Mn, respectively). The rate increases almost linearly with Mn content and reaches a maximum at 20 mole % of Mn in zirconia and then starts declining slowly, as shown in Fig. 3.23. An increase in rate with Mn content up to 20 mole % and then a decline shows that the activity depends

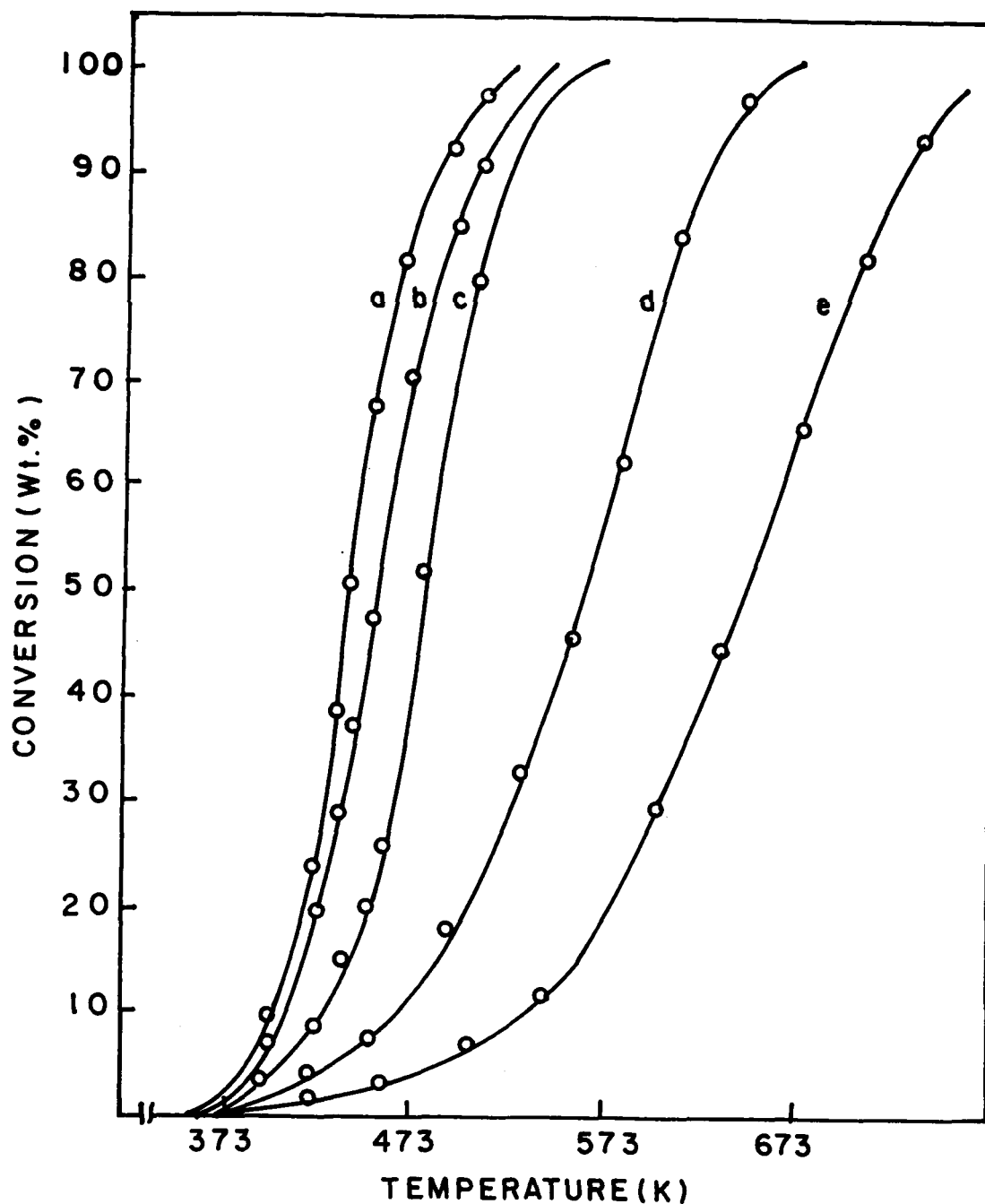


Fig. 3.22 : Light-off curves for the oxidation of n-butane over pure zirconia (curve 'e') and Mn-ZrO<sub>2</sub> samples with Mn content of 20, 30, 10 and 5 mole % ('a' to 'd', respectively). Feed composition : n-butane (4%), N<sub>2</sub> (76%) and O<sub>2</sub> (20%); GHSV : 36000 h<sup>-1</sup>.



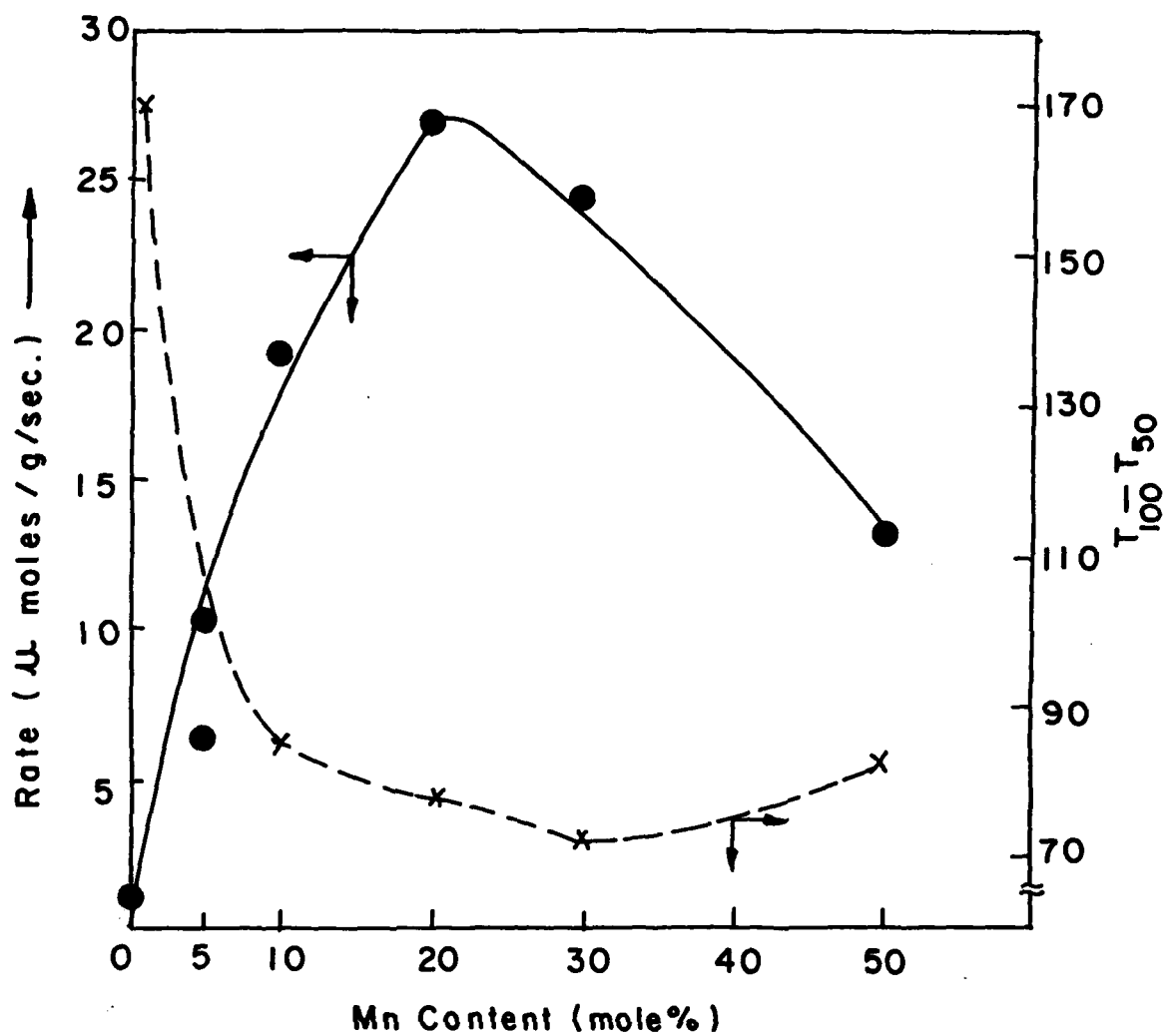
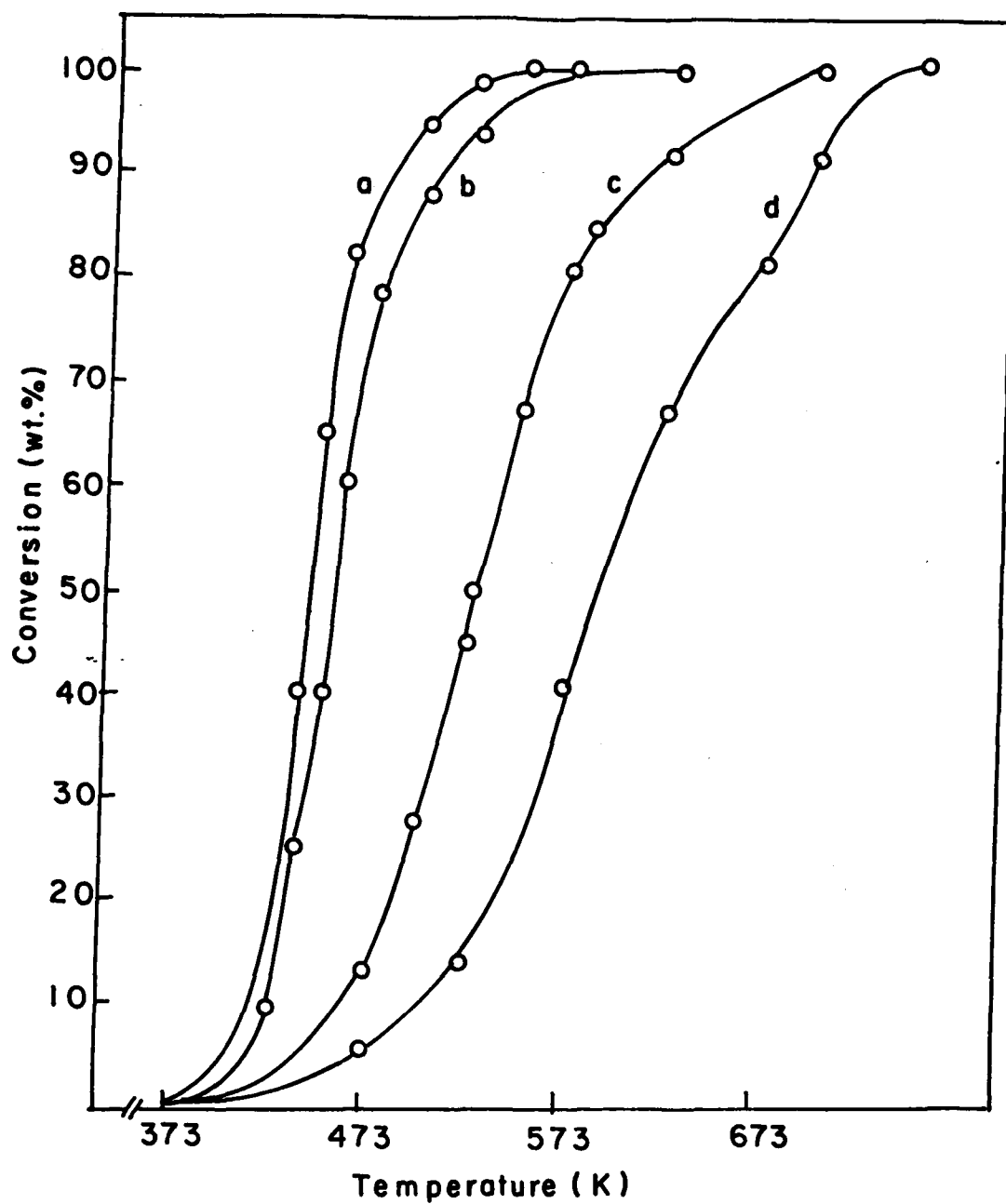
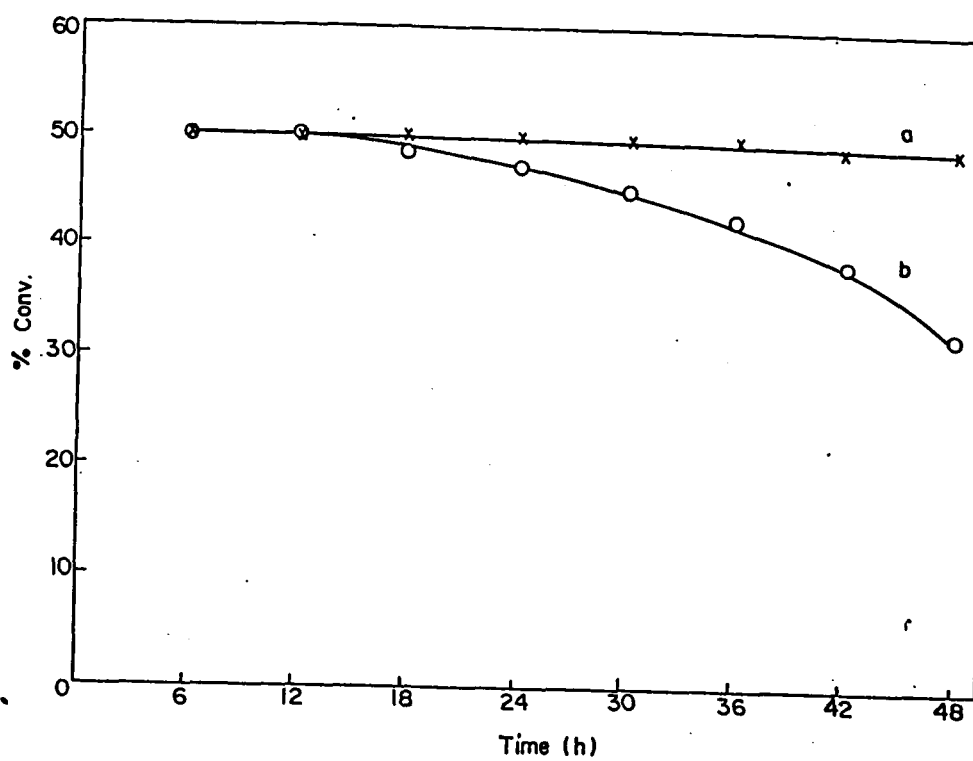


Fig. 3.23 : Variation of reaction rate and  $T_{100} - T_{50}$  for oxidation of n-butane as a function of Mn content in Mn-stabilized zirconia.

mainly on the stable structure of the catalyst by an optimum amount of Mn rather than on the surface area or the amount of active element. An alternative proposition for the higher activity of Mn-stabilized zirconia relatively at lower temperatures includes the possibility of enhanced adsorption sites for one of the reactants involved in the rate limiting process. This would be logical if oxygen vacancies or oxygen vacancy - acceptor pairs at, or near the surface were the adsorption sites. Fig. 3.23 also shows the variation of  $T_{100} - T_{50}$  as a function of Mn content, where  $T_{100}$  and  $T_{50}$  are the temperature required for 100 % and 50 % conversion of n-butane. We have chosen this as a relative measure of the activity response to inlet temperature. It can be seen that the temperature response to the rate of oxidation of n-butane over samples with Mn content ranging from 10 to 30 mole % is similar to that found in precious metal catalysts with a steep rise in activity with a lower light off temperature.<sup>69</sup> However, the behavior of the catalyst with lower and higher amount of Mn is similar to that of perovskite type or binary oxides with a lower slope. It is likely that the rate determining step depends on the optimum amount of Mn content required to get the solid solution. Since the catalysts are active at lower temperatures It is apparent that the rate equation which is most fitting is  $T_r = kP_{C_4}$ , where, the reaction rate largely depends on the n-butane partial pressure. Although, the participation of the lattice oxygen can not be ruled out, the reaction is mainly operated by adsorbed oxygen in the present case and the reaction is facile at lower temperatures. The rate dependence on the oxygen partial pressure and the possible mechanism of oxidation involving multivalent Mn in the lattice will be presented in detail later. Apart from the optimum amount of active element, the calcination temperature also plays an important role in



**Fig. 3.24 :** Effect of calcination temperature on the n-butane oxidation activity of Mn-stabilized zirconia with 20 mole % of Mn. Curves 'a' to 'd' correspond to samples calcined at 773, 873, 973 and 1073 K, respectively.



**Fig. 3.25 :** A comparison of activity - stability of Mn-stabilized zirconia ( $Zr_8Mn_2O_2$ ) with fluorite structure at 450 K (a) and  $LaMnO_3$  with perovskite structure at 550 K (b) in the oxidation of n-butane at a GHSV of  $36000\text{ h}^{-1}$ .

controlling the structure and texture which in turn show significant influence on the catalytic activity. This is illustrated in Fig. 3.24, where the oxidation activity of Mn-stabilized zirconia (20 mole % Mn) sample calcined at different temperatures (curves a,b,c and d correspond to the catalysts calcined at 773, 873, 973 and 1073 K, respectively) are represented. The catalysts calcined at 773 and 873 K where a single cubic phase exists, are quite active. Then, the activity gradually declines as the calcination temperature is increased to 973 K, when the structural transformation of fluorite (cubic) to monoclinic phase begins with a consequent reduction in the surface area. At 1073 K, the material transforms completely to monoclinic phase and the activity further deteriorates. An interesting feature of the above studies is that it is the optimum amount of Mn which could stabilize zirconia in to cubic phase that is important for getting better activity. When monoclinic zirconia was impregnated with the same amount of Mn, the activity was meagre. Also, a sample with very low amount of Mn with monoclinic zirconia impurities and the one with very high amount of Mn as a separate phase of  $\text{MnO}_2$  along with cubic zirconia were not active.

Fig. 3.25 compares Mn-ZrO<sub>2</sub> in the fluorite structure and the perovskite oxide ( $\text{LaMnO}_3$ ) for their long term activity. The fluorite based material shows a lower tendency to deactivate compared to the perovskite material. This can be attributed to the role of Mn in the inhibition of sintering, particularly when it is present in the fluorite lattice. In addition,  $\text{LaMnO}_3$  contains only trivalent Mn whereas, the Zr-MnO<sub>2</sub> contains multivalent manganese ions in the fluorite lattice, as confirmed by TPR studies and chemical analysis, thus facilitates the redox ability of the catalysts.

The major point to be discussed here is what makes the Mn-stabilized zirconia with cubic structure so active. The fundamental phenomenon behind the stabilization and the ensuing activity is the oxygen mobility. This type of oxygen mobility arises due to the creation of defect sites. Such a creation of defect sites will have a tremendous impact on the catalytic properties.<sup>70,71</sup> If a foreign ion in a crystalline lattice has a net charge difference from that of the host ion it replaces, an ionic defect must be introduced for charge compensation. As a result of the increase in the concentration of ionic defects, the ionic conductivity is increased. To achieve this through the creation of defect sites, introduction of lower valent ions of yttrium, magnesium or calcium is known in the literature. In the present case, the advantage of using multivalent Mn is two fold. First of all, it generates defect sites enhancing the oxygen mobility and secondly, it undergoes easy redox cycle due to its ease of reduction when present as a part of the zirconia lattice which is confirmed by our TPR studies. This is particularly due to the presence of  $Mn^{2+}$ ,  $Mn^{3+}$  and  $Mn^{4+}$  ions in the zirconia lattice.<sup>72,73</sup> It is inferred that adsorption of butane and oxygen occurs simultaneously on the catalyst surface so that, at one site  $Mn^{2+}$  and/or  $Mn^{3+}$  gets oxidized to  $Mn^{4+}$  and at the other site  $Mn^{4+}$  gets reduced to  $Mn^{3+}$  and/or  $Mn^{2+}$ . Thus, a reduction-oxidation cycle is facilitated. In a some-what similar kind of studies on Mn-MgO system both  $Mn^{3+}$  and  $Mn^{4+}$  dispersed on MgO were found to be more favorable for the complete oxidation of carbon monoxide compared to that of pure oxides.<sup>69</sup> But, unlike the supported Mn oxide, in our samples Mn appears to be a part of the  $ZrO_2$  cubic structure.

### 3.2.5.2. Deep oxidation of carbon monoxide

Carbon monoxide is usually the most toxic component of the auto exhaust emissions and catalytic route is preferred to curb it. A number of investigators have studied catalytic oxidation of carbon monoxide in recent times.<sup>72</sup> Among single component oxides, having potential application as CO oxidation catalysts,  $\text{CO}_3\text{O}_4$ , NiO and  $\text{MnO}_2$  are prominent.<sup>73</sup> However, they deactivate faster due to sintering. Mixed metal oxides such as perovskites were found to be effective.<sup>74-76</sup> Among all the metal oxides used for this purpose, those with vital oxygen mobility is known to be useful. In recent times, serious attempts have been expended by many investigators to develop novel catalysts with high oxygen mobility for using as CO oxidation catalysts. For example, Berkstresser and coworkers studied the oxidation of CO on calcia stabilized zirconia and thoria stabilized lanthana.<sup>77</sup> Similarly, van Dijk and co-investagtors have studied the effective utility of oxides with fluorite structure for the oxidation of carbon monoxide.<sup>78</sup> Anderson and Courtine *et al* have further added a number of metal oxides with a good oxidation activity to the big family of oxidation catalysts.<sup>79, 80</sup>

Similar to the earlier studies on hydrocarbon oxidation, an attempt has been made to use Mn-stabilized zirconia for the complete oxidation of carbon monoxide. Fig. 3.26 shows the light-off curves of CO oxidation over pure zirconia (curve e) and Mn-stabilized zirconia containing 5, 10, 20 and 30 mole % of manganese.(curves d, b and c, respectively). Similar trend was also observed in the case of n-butane oxidation. Catalyst with 20 and 10 mole % of manganese was found to be more active as reflected by lower light off temperature. Both these samples could convert carbon

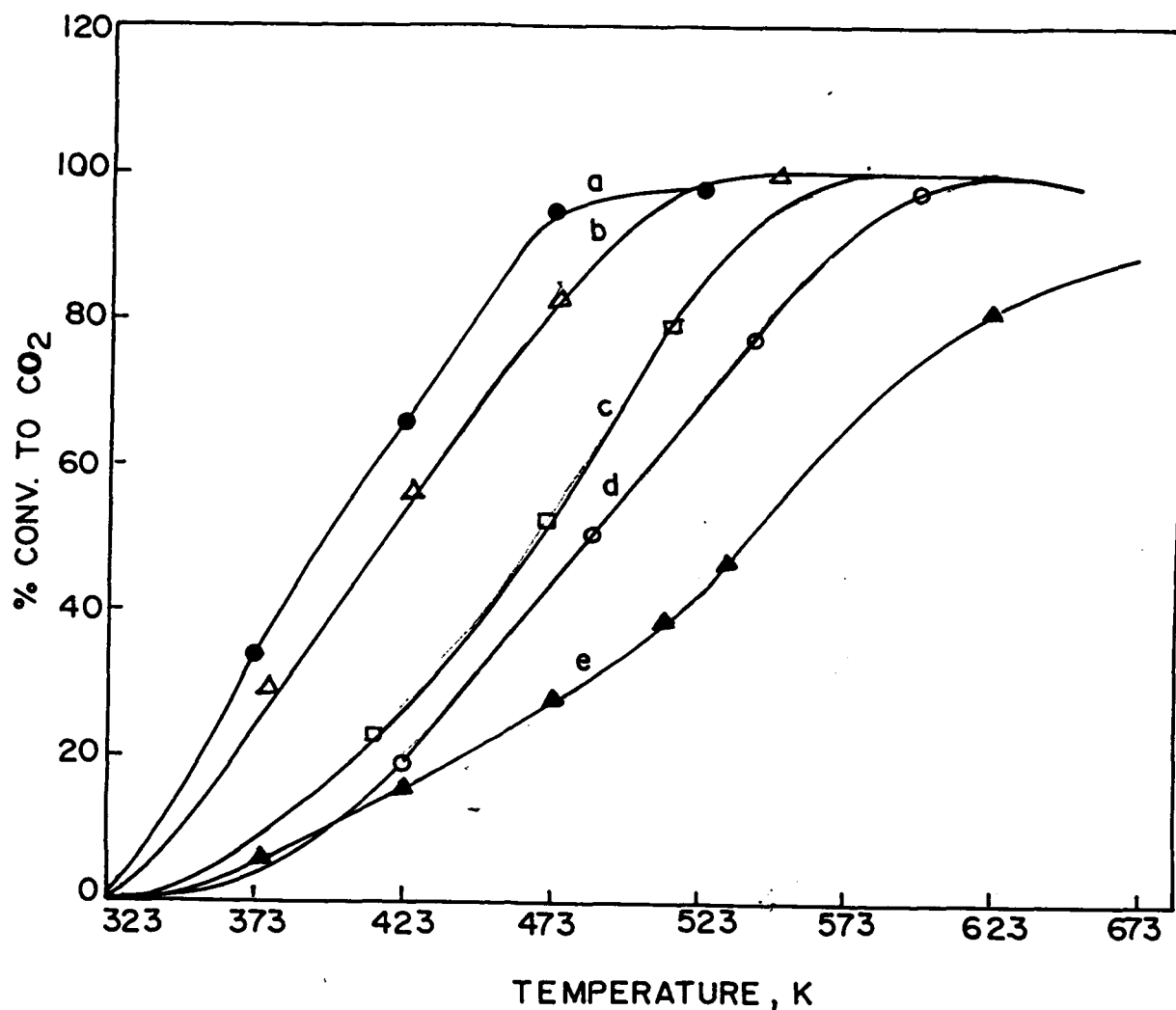


**Fig. 3.26 :** Light-off curves for the oxidation of CO over pure zirconia (curve 'e') and Mn-ZrO<sub>2</sub> samples with Mn content of 20, 10, 30, and 5 mole % ('a' to 'd', respectively). Feed composition : CO (5%), N<sub>2</sub> (90 %) and O<sub>2</sub> (5 %); GHSV : 36000 h<sup>-1</sup>.



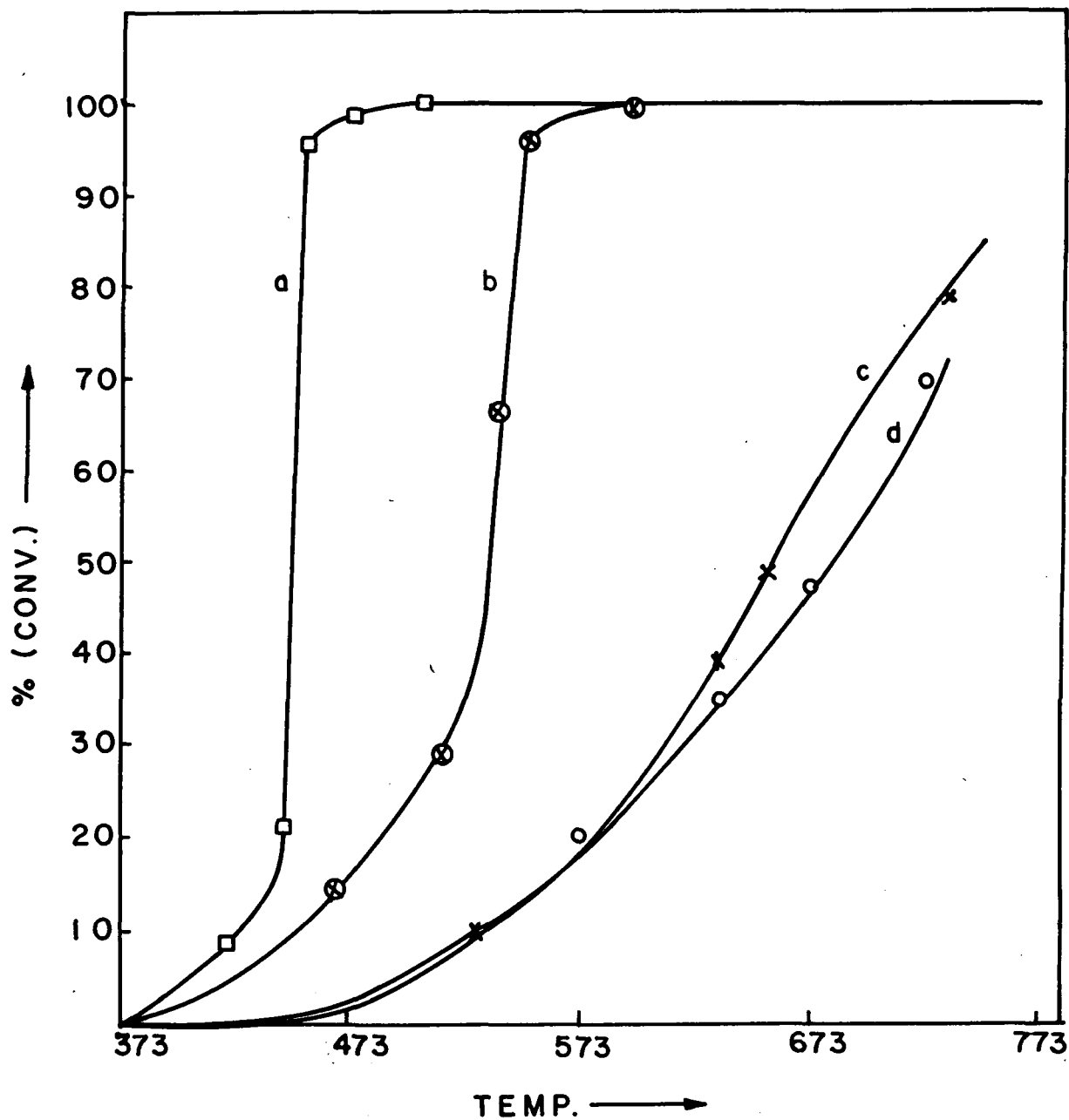
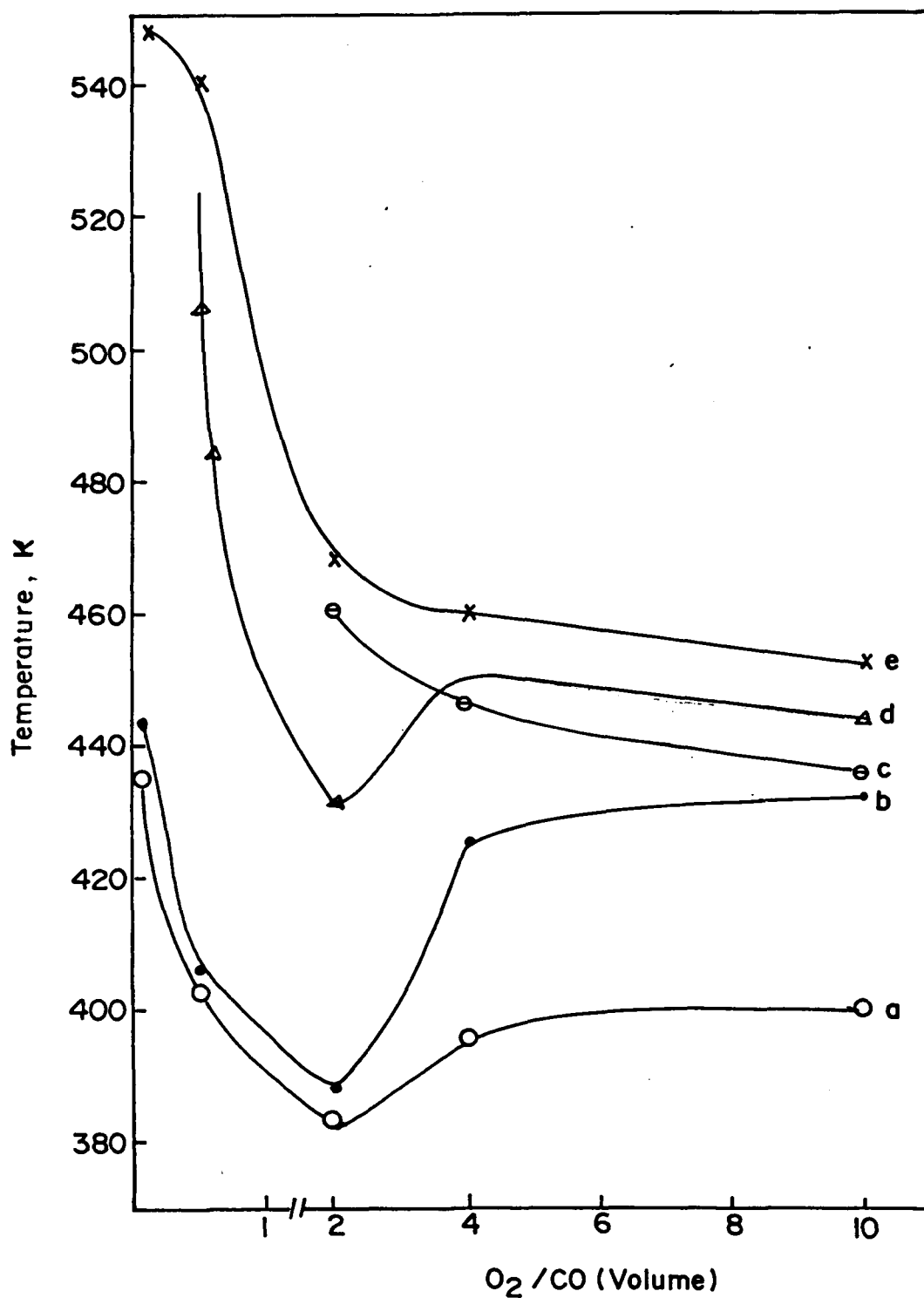
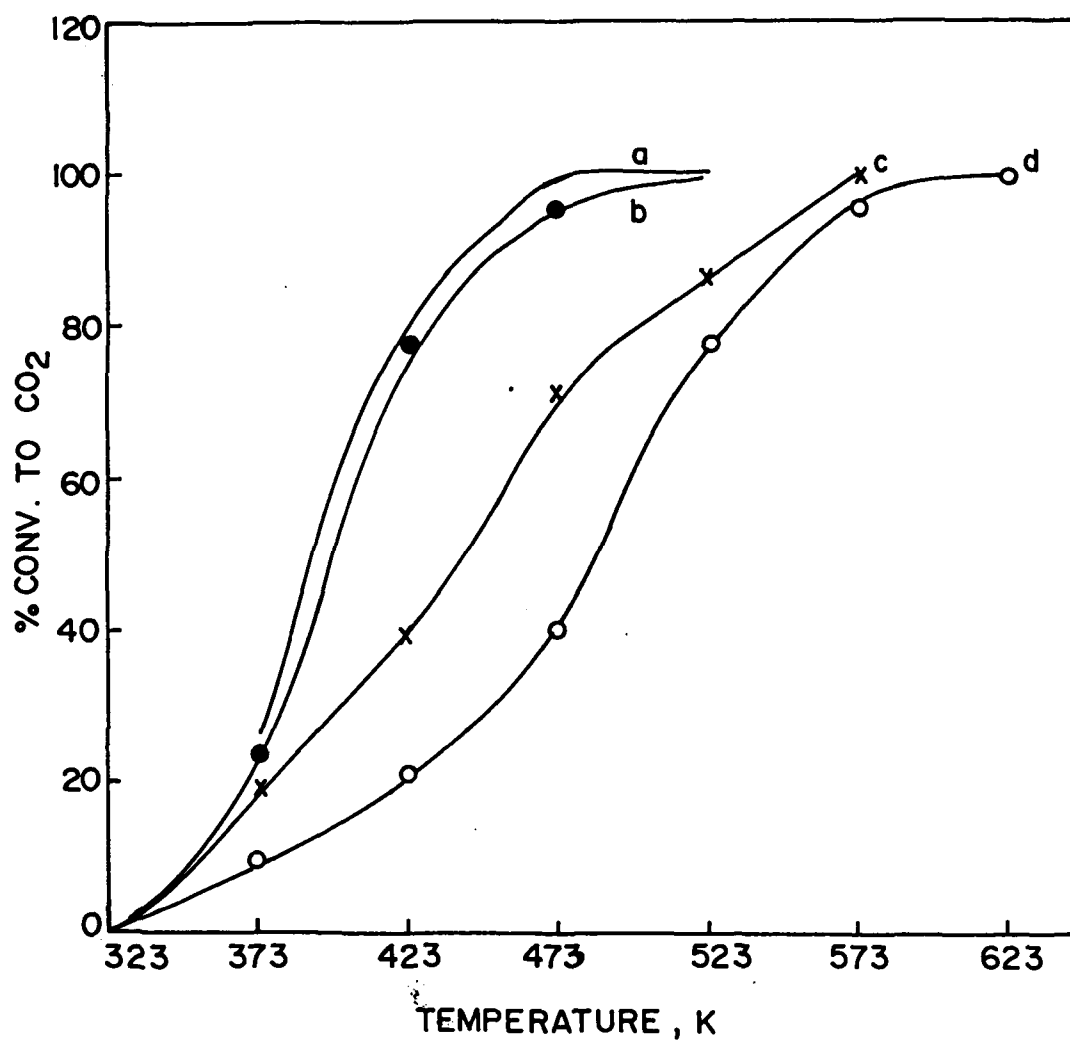


Fig. 3.27 : A comparison of CO oxidation activity over Mn-stabilized zirconia with 10 mole % of Mn (curve 'b') with that of Pt/ZrO<sub>2</sub> (curve 'a'), LaMnO<sub>3</sub> (curve 'c') and solid state mixtures of MnO<sub>2</sub> - ZrO<sub>2</sub> (curve 'd').



**Fig. 3.28 :** Effect of O<sub>2</sub>/CO (volume ratio) on temperature required for 50 % conversion of carbon monoxide over pure zirconia (curve 'e') and Mn-stabilized zirconia with 20, 10, 30 and 5 mole % of manganese. (curves 'b' to 'e', respectively).



**Fig. 3.29 :** Effect of calcination temperature on the CO oxidation activity of Mn-stabilized zirconia with 20 mole % of Mn. Curves 'a' to 'd' correspond to samples calcined at 773, 873, 973 and 1073 K, respectively.

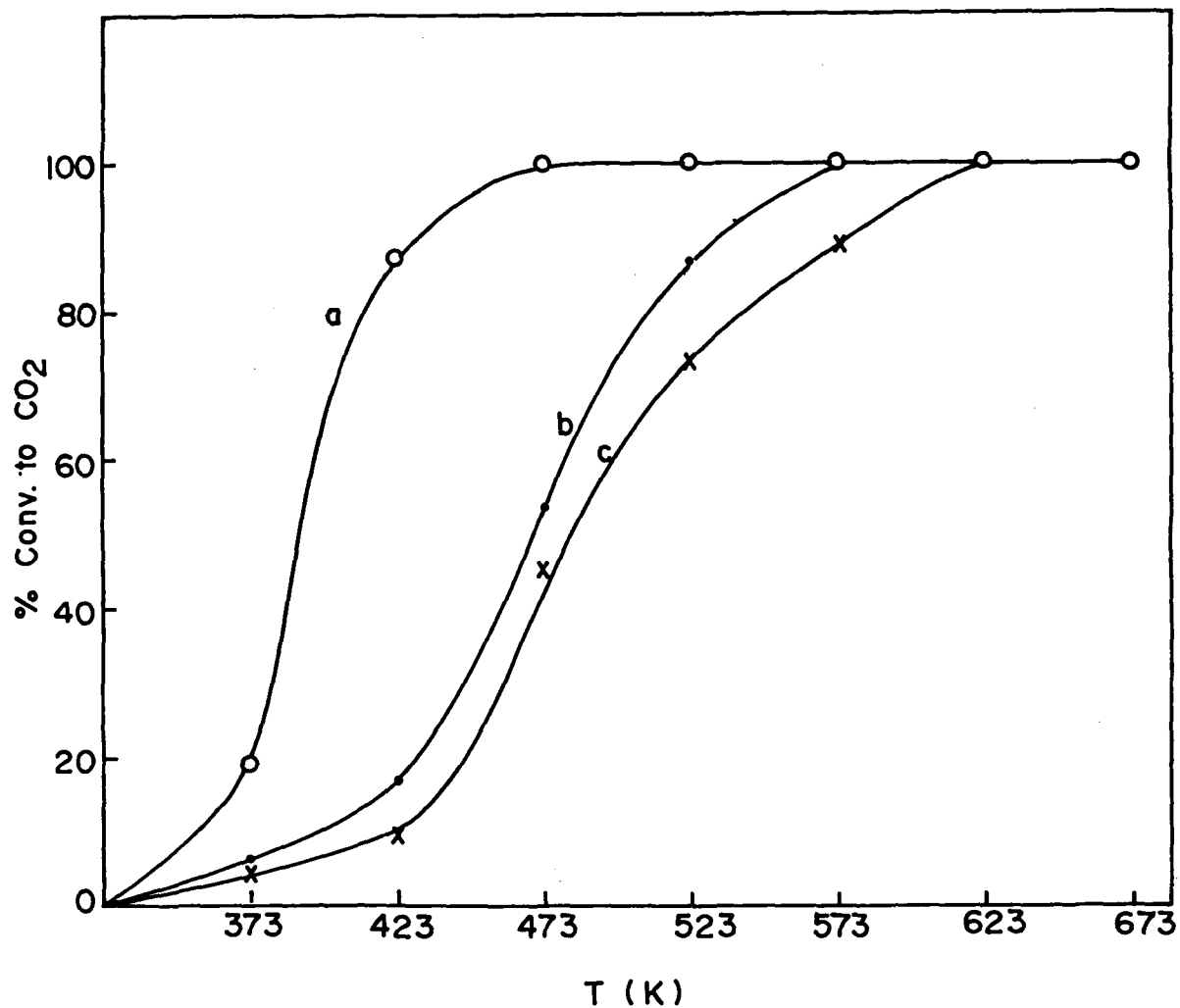


**Fig. 3.30 :** Performance of a variety of Mn-based catalysts (20 mole % ) in the complete oxidation of carbon monoxide. Curves a to c correspond to Mn-stabilized zirconia, and Mn-impregnated ZrO<sub>2</sub> and amorphous Mn-silica.

monoxide to the extent of 100 % at temperature as low as 473 K. Whereas, the sample with very low amount (5 mole %) and relatively higher amount of Mn (30 mole %) could convert CO only to the extent of 50 %. The sample with out Mn (pure  $ZrO_2$ ) shows poor activity as expected.

Fig. 3.27 compares the CO oxidation activity of Mn- $ZrO_2$  sample (curve 'b') with that of Pt/ $SiO_2$  with 0.01 wt % of Pt (curve a), solid state mixture of  $MnO_2$  and  $ZrO_2$  (curve c) and  $LaMnO_3$  (curve d). It is found that, the present catalyst is almost similar to that of noble metal catalysts in its activity and far better than conventionally prepared catalysts and perovskite type of metal oxides.

The effect of oxygen content on the oxidation activity of Mn-stabilized zirconia sample with varying amount of manganese is represented in Fig. 3.28, where, the ratio  $O_2/CO$  is plotted against the temperature required for 50 % conversion of CO. The optimum volume ratio,  $O_2/CO$  required for oxidizing CO was found to be 2 in all the cases. However, even when oxygen below the stoichiometric level was used, there is significant conversion of carbon monoxide. This may be attributed to the availability of lattice oxygen species present in the high surface area metal oxide for facile oxidation reaction.

The effect of the calcination temperature on the CO oxidation activity is presented in Fig. 3.29. The trend is similar to that observed for butane oxidation. Samples calcined at 773 and 873 are almost similar in activity (curve a and b) with 100 % conversion of CO at temperature as low as 473 K. At higher calcination temperatures (973 K and 1073) the complete conversion of CO can be achieved only above 573 K.

Fig. 3.30 shows a comparison of catalytic performance of Mn-stabilized zirconia (curve a), Mn-impregnated zirconia prepared by incipient wet technique method (curve b) and amorphous Mn-silica (curve c), where the Mn content is 20 mole % in all the cases. The distinct behaviour of the three samples shows that, it is not the Mn-content but the Mn residing in a stable matrix which is important. Both Mn-impregnated zirconia is relatively poor than the Mn-stabilized zirconia. Although amorphous Mn-silica catalysts have higher surface area, they are not very active. Thus, one can say that active sites, (Mn in the present case) when stabilized in the fluorite matrix shows beneficial effects.

### 3.2.6. General discussion

Catalytic oxidation reactions on metal oxides are often described in terms of interfacial process which may proceed *via* redox mechanism or push-pull mechanism<sup>81</sup>.<sup>82</sup> This is schematically represented in Fig. 3.31. The former involves the reaction between the reactant and oxide to give oxygenated products and partially reduced catalysts, and reoxidation of the reduced catalyst with the gaseous oxygen to restore the catalyst to its initial state. Thus, in this kind of process, the reduction part and the oxidation part are considered to be separate processes and hence called as 'redox reaction'. In this case, the two processes may simultaneously occur at different site. On the other hand in the case of push-pull mechanism both oxidation and reduction processes takes place consecutively at the same site. The efficacy of Mn-stabilized zirconia in the complete oxidation of n-butane and carbon monoxide can therefore be attributed to the ease of redox processes, which is already illustrated by TPR studies, XPS investigation and cyclic voltammetric studies.

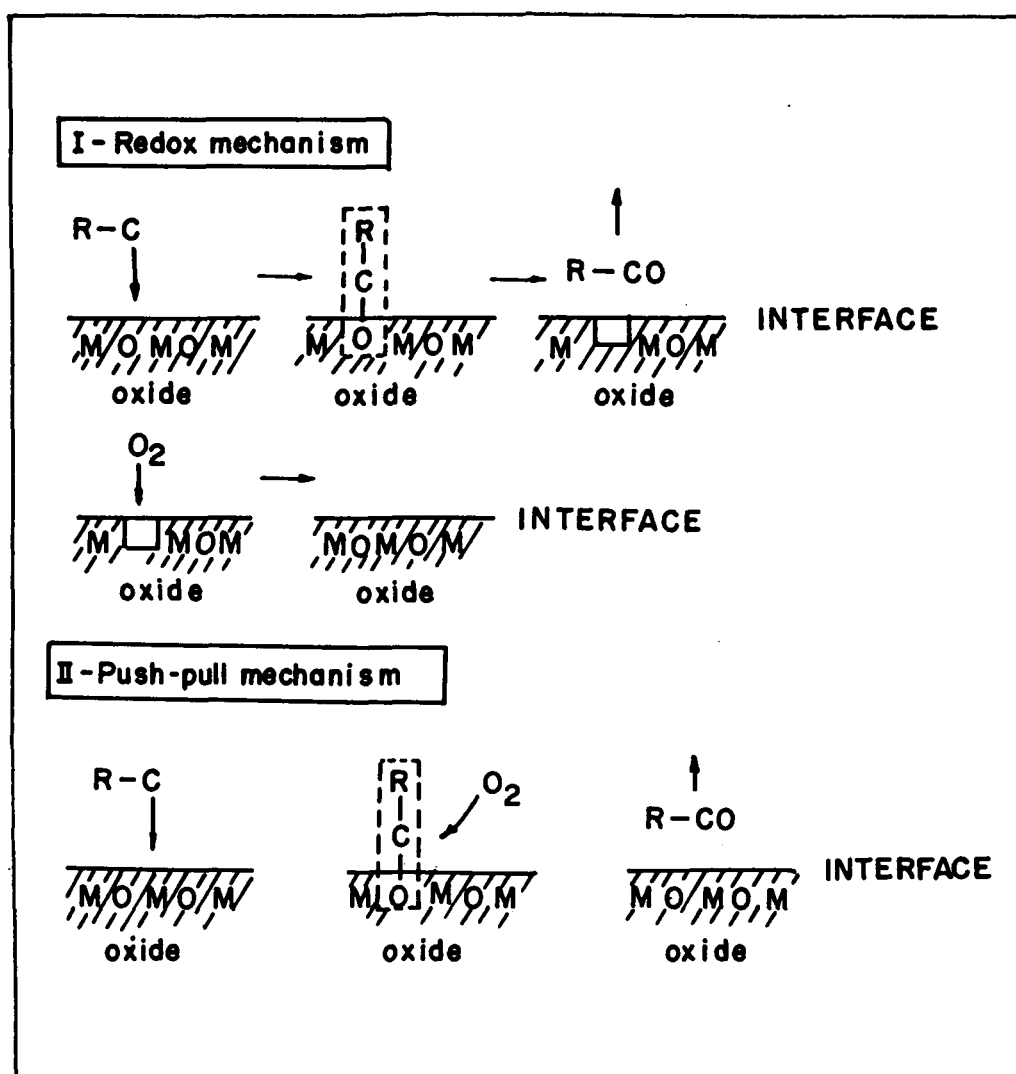


**Fig. 3.31 :** A schematic diagram of 'redox' and 'push-pull' mechanism of CO and n-butane oxidation over metal oxide catalysts.

---

### 3.3.

## 3d-TRANSITION METAL OXIDE-STABILIZED ZIRCONIA

---

### 3.3.1. INTRODUCTION

In the previous section it has been demonstrated that, multivalent manganese when present as a part of the zirconia lattice can act as a befitting site for the complete oxidation of pollutants such as n-butane and carbon monoxide. This motivated us to extend the same methodology to other 3d transition metals also. Accordingly, stabilization of zirconia by oxides of Cr, Fe, Co and Ni is dealt with in this section.

It has already been established that oxides of 3d-transition metals such as Cr, Mn, Fe, Co as a single component oxide or when crystallized as perovskite phase ( $ABO_3$  type) are quite effective for the complete oxidation of carbon monoxide and hydrocarbons. Our maiden attempt to crystallize cubic type of fluorite lattice using various 3d transition metal oxides and their application as complete oxidation reaction are found to be an attractive way of getting higher oxidation activity and better stability to the catalyst. Therefore, this section is centered on zirconia stabilized with 20 mole % each of oxides of Cr, Mn, Fe, Co and Ni. Although, Mn-stabilized zirconia is already discussed in detail in the previous section, one of them (with 20 mole % Mn) is once again included here for comparison with other samples.



## **3.3.2. EXPERIMENTAL**

### ***3.3.2.1. Preparation***

The 3d transition metal oxide - stabilized zirconia samples were prepared by mixing an aqueous solution of zirconyl nitrate and one of the nitrate of Cr, Mn, Fe, Co and Ni in the molar ratio of 0.8 to 0.2, to which aqueous tetramethylammonium hydroxide (25 %) was added under vigorous stirring until the pH reached 8. The resultant precipitate was washed with deionized water, dried at 383 K for 24 h and subsequently calcined at 773 K for 8h. Although Mn-stabilized zirconia is already discussed in detail with various level of Mn-loading in the previous section, a sample with 20 mole % of Mn is once again considered here for comparing with that of samples containing same amount of Cr, Fe, Co and Ni, respectively.

The present section presents the physico-chemical and catalytic properties of these materials in the complete oxidation of n-butane to carbon dioxide and water. An attempt has been made to correlate the catalytic activity to some intrinsic properties of the material.

### ***3.3.2.2. Characterization and Catalytic test reactions***

The physico-chemical characterization of the catalysts were carried out by XRD, TG-DTA, TPR, and adsorption (BET) techniques.

The oxidation of n-butane and carbon monoxide were separately carried out in a tubular, quartz micro-reactor of the down flow fixed bed type in the temperature range 423 to 723 K using 200 mg of stabilized zirconia as the catalyst. After

preheating the catalyst at 673 K for 12h, the reaction mixtures [n-butane (4%), N<sub>2</sub> (76%) and O<sub>2</sub> (20%)] were admitted to the reactor at GHSV ranging from 10000 to 36000 h<sup>-1</sup>. Similarly, in the oxidation of carbon monoxide, the feed composition was adjusted to [CO(1%), N<sub>2</sub> (91%) and (8%)]. The complete oxidation products of n-butane such as water and carbon dioxide and unreacted n-butane were analyzed with an on-line gas chromatograph using a 10m long Porapak-Q column. In the case of carbon monoxide, molecular sieve 5 A column was used.

### 3.3.3. RESULTS AND DISCUSSION.

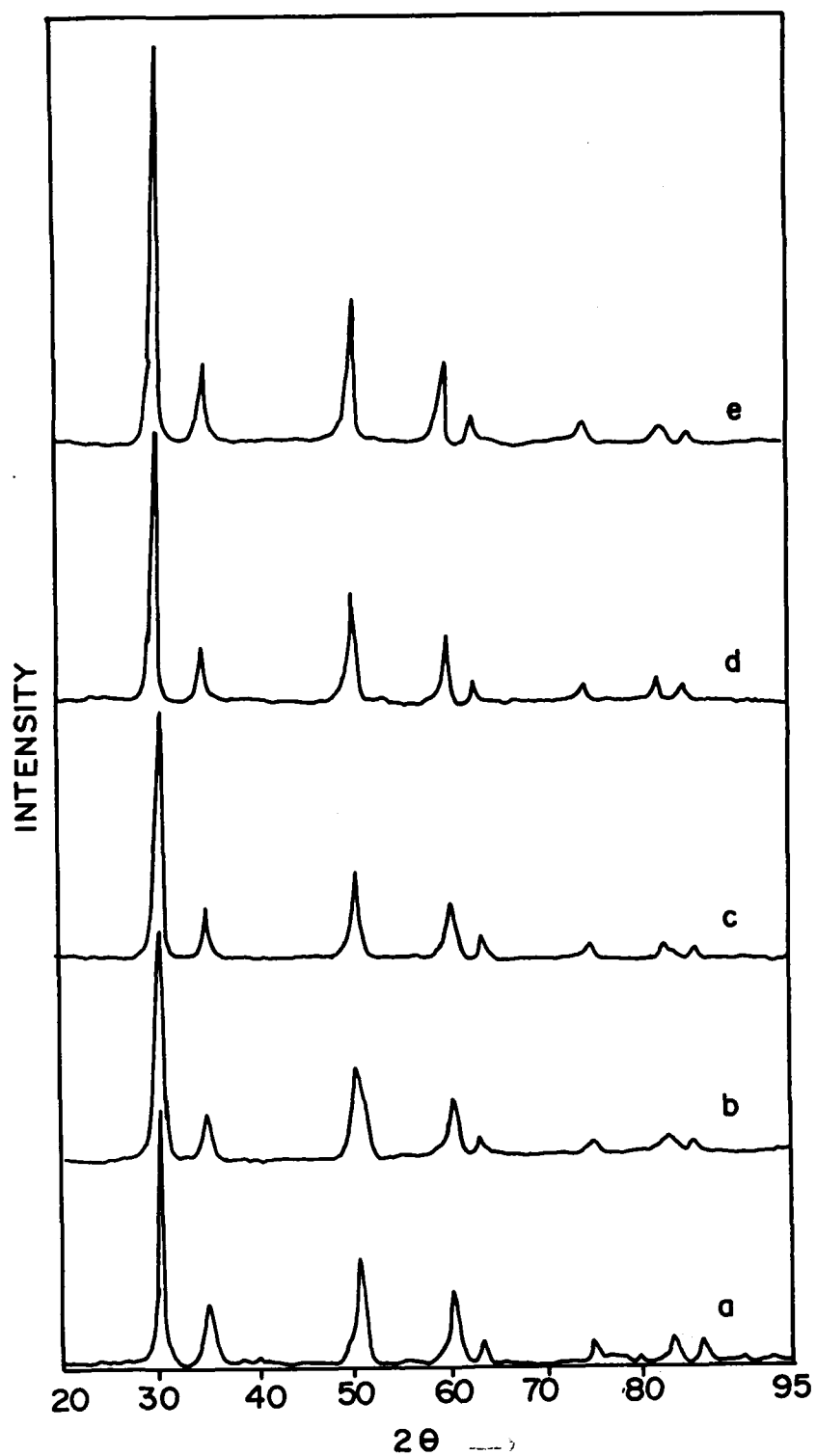
#### 3.3.3.1. X-Ray diffraction

Table 3.10 gives the physico-chemical characteristics of the new series of zirconia based oxides, modified with several 3d transition metal incorporations.

Table 3.10

Physico-chemical properties of 3d-transition metal oxide-stabilized zirconia

Sample	surface area, m <sup>2</sup> g <sup>-1</sup>	lattice constant, nm	Conversion of n-butane at 573 K
Zr <sub>0.8</sub> Cr <sub>0.2</sub> O <sub>2</sub>	118	0.5067	80
Zr <sub>0.8</sub> Mn <sub>0.2</sub> O <sub>2</sub>	107	0.5065	100
Zr <sub>0.8</sub> Fe <sub>0.2</sub> O <sub>2</sub>	102	0.5059	91
Zr <sub>0.8</sub> Co <sub>0.2</sub> O <sub>2</sub>	98	0.5089	97
Zr <sub>0.8</sub> Ni <sub>0.2</sub> O <sub>2</sub>	96	0.5083	47



**Fig. 3.32 :** A comparison of the XRD patterns of zirconia stabilized with Cr, Mn, Fe, Co and Ni prepared by co-precipitation method and calcined at 773 K (profiles 'a' to 'e', respectively).

Since the sample contain lower valent cations in the lattice, the exact oxygen stoichiometry need not be 2. All of them are crystalline with cubic symmetry and the lattice parameter varies with the size of the dopant ion; in the case of Mn-stabilized zirconia, it also varies with the amount of the dopant ion. Typical powder X-ray diffraction patterns of Cr-, Mn-, Fe-, Co-, and Ni-stabilized zirconia calcined at 773 K are shown in the Fig. 3.32 (a to e). The corresponding lattice parameter values were presented in table 3.10. In all the cases no evidence for the presence of single component oxides like  $\text{MnO}_2/\text{MnO}$ ,  $\text{Fe}_2\text{O}_3$ ,  $\text{Cr}_2\text{O}_3$ , NiO or CoO were obtained.

### ***3.3.3.2. TG-DTA studies***

Similar to Mn-stabilized zirconia, the formation of zirconia stabilized with other transition elements like Cr, Fe, Ni and Co was followed by the thermal decomposition of the corresponding oxide hydrates. The most significant result of the thermal analysis is the DTA profile shown in the Fig. 3.33, in which the crystallization exotherms can be seen. In contrast to the oxide hydrate of pure zirconia with an exothermic peak around 723 K (profile f), the mixed oxide hydrates on thermal treatment gives an exotherm at substantially higher temperature (profiles a to e corresponding to mixed oxide hydrates of Zr with Cr, Mn, Fe, Co and Ni). Detailed discussion of the DTA studies is already done in section 3.2.4.2. and the same methodology is valid here.

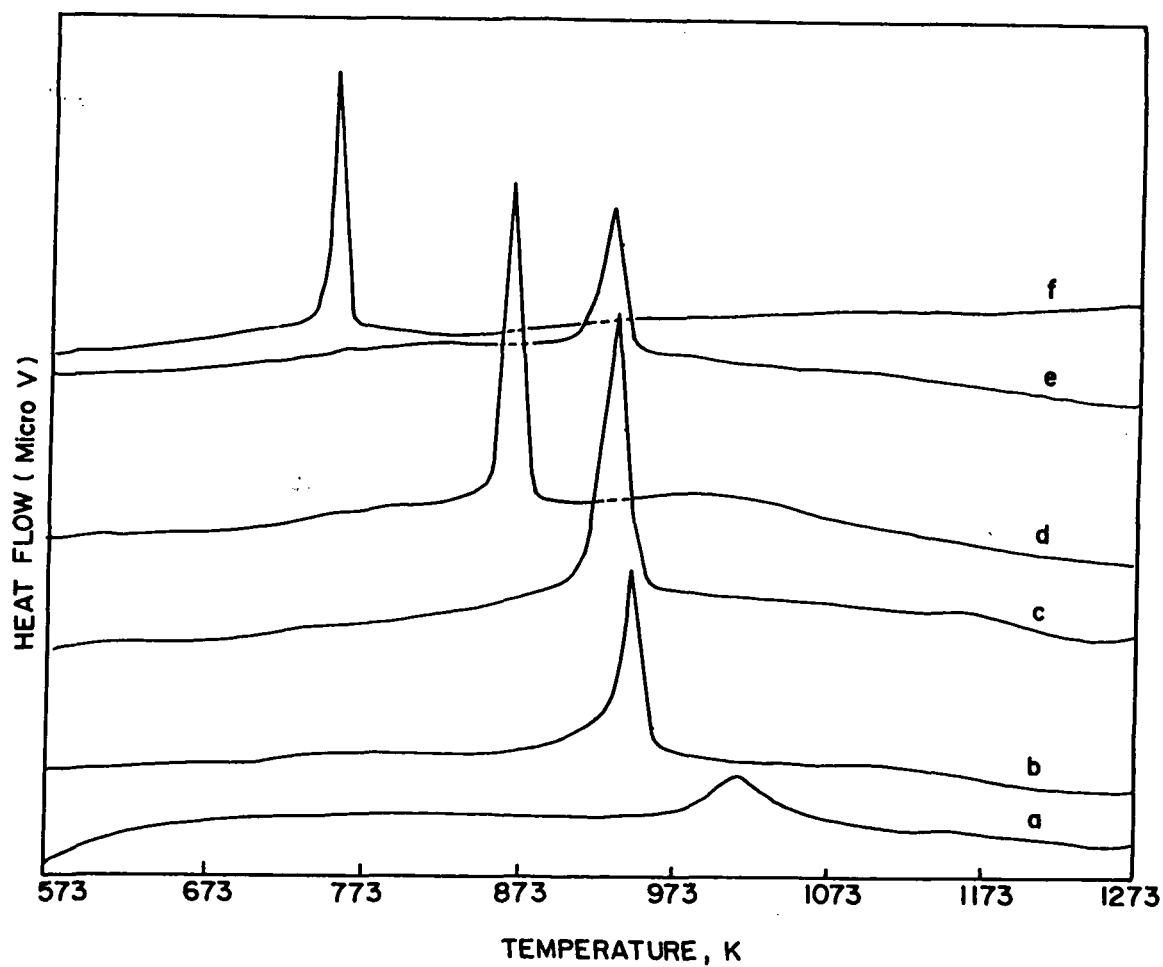


**Fig. 3.33 :** DTA profiles of the decomposition of M-Zr oxide hydrates, where M refers to 20 mole % of Cr, Mn, Fe, Co or Ni (a to e) and that of pure zirconium oxide hydrate (f).

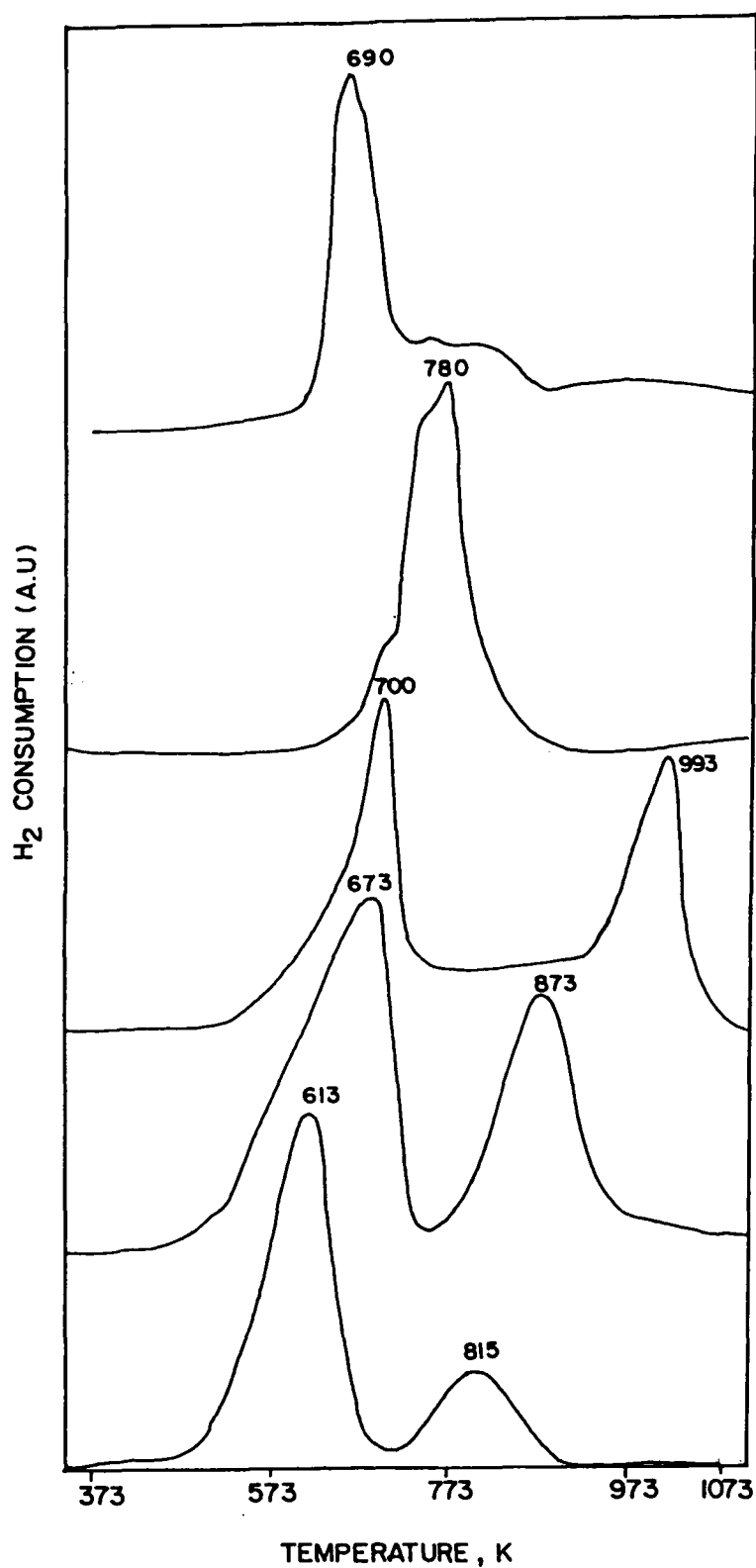


**Fig. 3.34 :** TPR profiles of zirconia stabilized with Cr, Mn, Fe, Co and Ni prepared by co-precipitation method and calcined at 773 K (profiles 'a' to 'e', respectively).

### ***3.3.3.3. TPR profiles***

Temperature programmed reduction profiles of the various stabilized zirconia samples with 20 mole % of Cr, Mn, Fe, Co and Ni are depicted in Fig. 3.34. One can see the ease of reducibility at relatively lower temperature than that of the corresponding bulk oxides. While the samples with multivalent elements like Mn, Cr and Fe show two stages of reduction, with hydrogen consumption proportional to their quantity; Co and Ni stabilized zirconia samples show a single step reduction which can be attributed to the + 2 states of Co and Ni.

### ***3.3.4. Catalytic Activity***

Fig. 3.35 compares the activity of Pt/ZrO<sub>2</sub> (curve a) with that of various stabilized zirconia samples (curves b to f) and of pure zirconia (curve g) in the complete oxidation of n-butane as a function of inlet gas temperature. The Pt-zirconia has the lowest light-off temperature, whereas the pure zirconia (monoclinic) and Cr- and Ni-stabilized zirconia show a catalytic response only at higher temperature. However, the performance of Mn-stabilized zirconia (Fig. 3.35 b) is nearly as good as that of noble metal doped zirconia while Co- and Fe-stabilized zirconia have medium activity. A better way to compare the activity of the samples is to find the temperature required for fixed conversion. Table 3.11 presents the temperatures at which 50 and 100 % conversion of butane to CO<sub>2</sub> occurs under the conditions above. The rate data presented in the Table 3.11 indicate that the activity is not related to the surface area of the catalyst but to some other intrinsic properties.

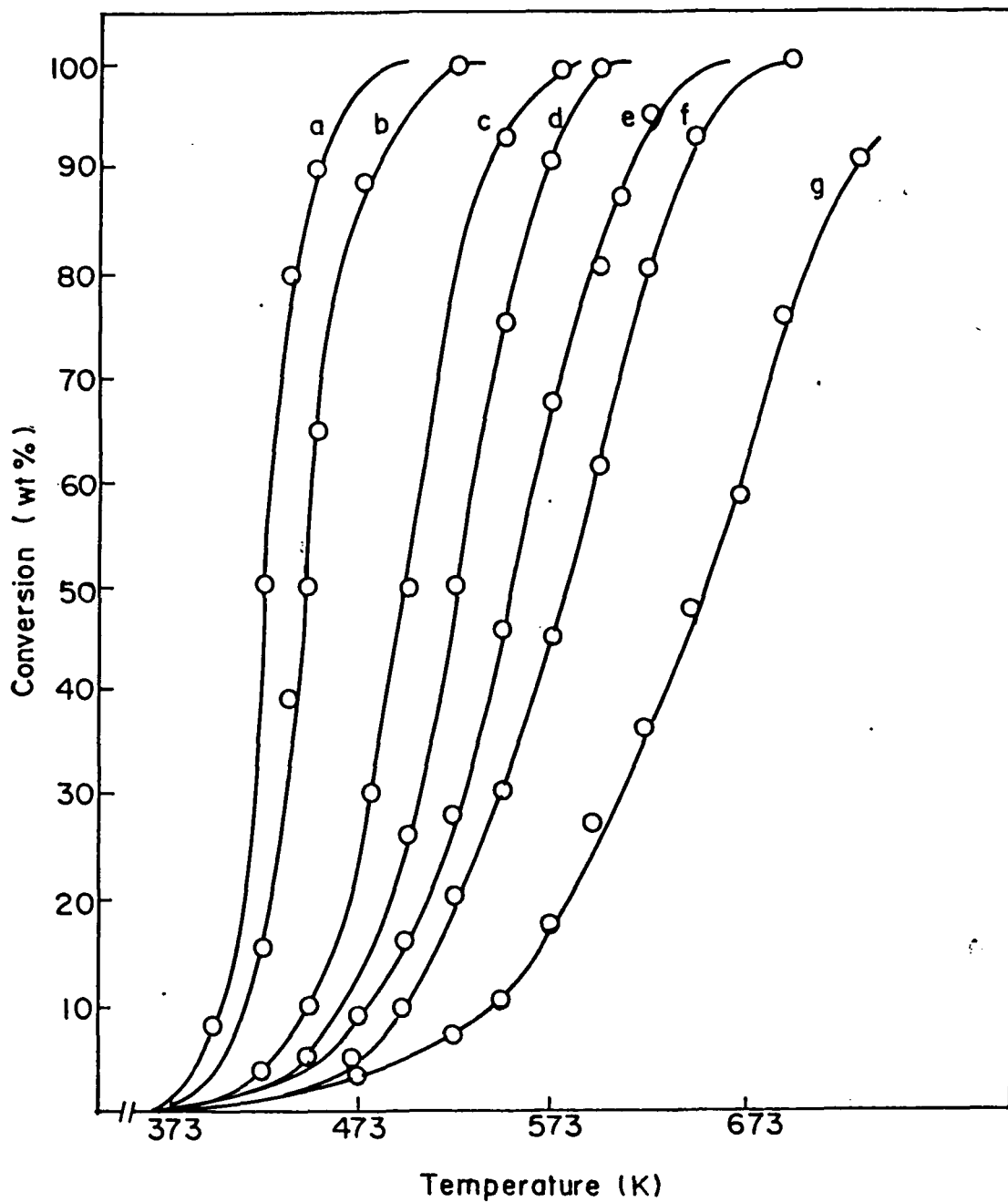


**Fig. 3.35 :** Conversion of n-butane as a function of temperature over Pt/ZrO<sub>2</sub> (a), Mn (b), Co (c), Fe (d), Cr (e) and Ni (f) stabilized zirconia and pure zirconia (g). Feed composition : butane (4%), N<sub>2</sub> (76%), O<sub>2</sub> (20 %); GHSV 36000 h<sup>-1</sup>.



**Table 3.11**  
**Catalytic properties of fluorites, perovskites and Pt/ZrO<sub>2</sub>**

Catalyst	Phase	Surface area (m <sup>2</sup> g <sup>-1</sup> )	T <sub>50</sub> <sup>a</sup> /K	T <sub>100</sub> <sup>b</sup> /K	Rate <sup>c</sup>
ZrO <sub>2</sub>	monoclinic	56	653	823	0.98
Zr <sub>0.8</sub> Cr <sub>0.2</sub> O <sub>2</sub>	fluorite	118	550	648	10.42
Zr <sub>0.8</sub> Mn <sub>0.2</sub> O <sub>2</sub>	fluorite	105	445	523	26.85
Zr <sub>0.8</sub> Fe <sub>0.2</sub> O <sub>2</sub>	fluorite	102	523	603	18.60
Zr <sub>0.8</sub> Co <sub>0.2</sub> O <sub>2</sub>	fluorite	98	498	583	22.35
Zr <sub>0.8</sub> Ni <sub>0.2</sub> O <sub>2</sub>	fluorite	96	581	698	12.69
LaCoO <sub>3</sub>	perovskite	26	573	763	4.96
LaMnO <sub>3</sub>	perovskite	28	558	703	5.20
Pt/ZrO <sub>2</sub>	monoclinic	48	423	475	30.12

<sup>a</sup> Temperature required for 50 % conversion of n-butane.

<sup>b</sup> Temperature required for 100 % conversion of n-butane.

<sup>c</sup> Rate of the reaction (μmol g<sup>-1</sup> s<sup>-1</sup>) was evaluated from the slope of the linear correlation between the conversion and  $m/f$ , where,  $m$  is the mass of the catalyst and  $f$  is the flow rate of the reactant under steady state conversion maintained at < 20 %.

<sup>d</sup> Pt/ZrO<sub>2</sub> was prepared by doping 0.5 mass % of Pt metal on zirconia by the incipient wet technique.

As a control experiment, the oxidation activity of well known perovskite type oxide containing Mn and Co were also tested and the results are also included in Table 3.11. By comparing the activity exhibited by bulk oxides of manganese and cobalt to those of Co- and Mn- containing perovskites (ABO<sub>3</sub>) it is clear that the present

catalyst series is superior and particularly, the activity of Mn-stabilized zirconia is fairly close to that of Pt-doped zirconia, with Co- and Fe- stabilized zirconia showing somewhat less activity. It is thus evident that the mere presence of an element which is redox active is not the only criterion for obtaining improved activity. Probably, a stable structure coupled with fairly high surface area, the presence of oxygen ion vacancies and an accessible redox pair leads to high oxidation activity.

For complete oxidation reactions, surface  $O^-$  or  $O_2^-$  are the required species that need to be generated.<sup>82</sup> Incorporation of the oxygen from the gas phase on the oxide surface or in the lattice does not necessarily take place at the same site so that the oxygen mobility is required. Such mobility is known to be created in zirconium oxide when the  $Zr^{4+}$  ion is partly substituted by another metal ions such as  $Y^{3+}$ ,  $Mg^{2+}$ ,  $Ce^{4+}$ ,  $Ca^{2+}$ , etc<sup>83-85</sup> although these particular elements do not substantially enhance reactivity. Incorporation of transition-metal ions such as Mn or Co increases the activity mainly due to the creation of defect sites as a consequence of the charge imbalance. It has been confirmed by TPR studies that 3d-transition elements residing in the fluorite lattice are more readily reduced at lower temperature due to the site isolation. Whereas, metal ions within the individual oxides or those belonging to the perovskite family require higher temperature for the same job.

The pseudo-free electrons resulting from the oxygen ion removal can reduce the valance state of the cation residing in the lattice as well as on the surface. Thus, during the steady state hydrocarbon oxidation, a type of redox mechanism is operative in which anion point defects are essential for oxygen adsorption and reversible valance changes at the cations make them suitable adsorption sites for hydrocarbon species.

Such a situation is more favourable in the fluorite type of systems mainly due to its oxygen ion vacancy.

In a fluorite structure, each metal atom is surrounded by eight oxygen atoms and each oxygen is the tetrahedral centre surrounded by four metal atoms. In general, zirconia is found to be a distorted fluorite with monoclinic symmetry with seven coordination. However, on doping lower valent metal ions such as  $Y^{3+}$ ,  $Mg^{2+}$  or  $Ca^{2+}$ , stabilization into the cubic phase is possible with generation of oxygen ion vacancy. Applications of such materials as high temperature refractories, gas sensors, thermal barrier coatings, etc. are extensively reported in the literature. Yet, they have not found much use as oxidation catalysts mainly because of the requirement of the very high temperature for the operation of the redox mechanism. This means that a mere presence of oxygen ion vacancy, as in the case of known fluorite type oxide is not adequate. In the present case, it is the presence of oxygen ion vacancy coupled with an easily pliable pair of redox transition metal ions in the zirconia matrix at a relatively lower temperature seems to be responsible for the higher activity in the oxidation of hydrocarbons. The complete oxidation of carbon monoxide is also feasible in similar way, with a temperature response akin to that of hydrocarbons.

### 3.4. Summary and Conclusion

In summary, the co-precipitation of Mn and Zr (Mn = 0.05 to 0.3 mole) as hydroxide gel followed by calcination in air at 773 K stabilizes zirconia in the cubic (fluorite) phase, as evidenced by XRD and IR data. The present preparation method also enables one to get stabilized zirconia with a surface area of about  $100 \text{ m}^2 \text{ g}^{-1}$ . The preliminary results of XPS and TPR measurements reveal the presence of  $\text{Mn}^{4+}$  on the surface of stabilized  $\text{ZrO}_2$ . The possibility of inducing multi-valent Mn in the fluorite system, with a fairly high surface area may extend its application to interesting catalytic reactions. Further studies on the oxygen ion vacancy, reducibility (stabilization of  $\text{ZrO}_2$  in cubic phase by  $\text{Mn}^{2+}$  at higher temperatures), thermal behavior, magnetic susceptibility and catalytic activity of these samples may form the subject of future research work

In the manganese containing zirconium oxide hydrates (0 to 0.3 mole of Mn) prepared by co-precipitation method using ammonium hydroxide, the initial composition corresponds to  $\text{Zr}_{1-x}\text{Mn}_x\text{O}(\text{OH})_2$  as seen from the TG results of the decomposition of these hydroxides. There is a tendency for manganese to hinder the crystallization of zirconia to a cubic phase, as the DTA peak maxima of the exotherms shift progressively to higher temperatures when Mn content increases in the samples. Still, the enthalpy associated with the crystallization process decreases with manganese content. On heating, a solid solution of manganese in amorphous zirconia leads to the formation of  $\text{Zr}_{1-x}\text{Mn}_x\text{O}_2$  stabilized in the cubic phase with fluorite structure, having higher surface area and smaller crystallite size.

These Mn-stabilized zirconia solid solutions with multivalent manganese in the zirconia lattice is a suitable catalyst for the complete oxidation of n-butane. The catalytic activity is sensitive to the structure rather than to the texture or the amount of active element. The increased activity is believed to be due to the oxygen ion mobility, the origin of which could be ascribed to the creation of defect sites in the lattice. The easy redox ability of Mn in the  $ZrO_2$  lattice also plays a synergistic role in achieving better activity in the oxidation reaction.

Thus a series of novel catalysts belonging to fluorite family prepared by a simple route are active as complete oxidation catalysts. The successful development of fluorite oxides for such an application is mainly due to the synergistic action of an easily pliable redox couple and the defect sites caused by oxygen ion vacancy. Further experimental studies to explore the mechanistic features would help one to understand the intricacies of the role of catalysis for automotive pollution abatement.

## Referencres

1. Motor Vehicle Emission Regulation and Fuel Specification, Concawe report No. 4/94, 1994.
2. Notification of mass emission standards for petrol driven vehicles effective from 1<sup>st</sup> April, 1996, Ministry of Surface Transport, Government of India, 15 September, 1993)
- 3a. E. Houdry, *Advan. Catal.* **9** (1957) 499.
- 3b. M. P. Walsh, *Plat. Met. Rev.* **30** (3) (1986) 106..
4. J. J. Mooney, Exhaust Control, automotive, Kirk-Othmer Encyclopaedia.
5. R. L. Klimisch, I<sup>st</sup> National Symposium on Heterogeneous Catalysis for control of air pollution, Philadelphia, 1968.
6. G. R. Lester, The development of auto exhaust catalysts, ACS symposium series, **222** (1983) 415.
7. A. R. Jiang, Y. Peng, Q. W. Zhon, P. Y. Gao, H. Q. Yuan and J. F. Deng, *Catal. Lett.* **3** (1989) 235.
8. J. C. Ottamiri, J. F. Crow and S. L. T. Anderson, *J. Catal.*, **138** (1992) 562.
9. F. Zamar, A. Trovarelli, C. De. Leitenberg and G. Dolcetti, *J. Chem. Soc. Chem. Commun.*, 1995 965.
10. J. A. Kilner and B. C. H. Steele in Nonstoichiometric oxides, ed. O. T. Sorensen, Academic press, p 233, 1981.
11. D. J. Ilet and M. S. Islam, *J. Che., Soc. Farad. Trans.* **89** (1993) 3833.
12. G. W. Berkstresser, R. J. Brook and J. M. Whelan, *J. Mater. Sci.* **9** (1974) 491.
13. J. T. Kummer, *J. Phys. Chem.*, **90** (1986) 4747.
14. I. D. Brown, Structure and Bonding in crystals, Vol-II, pp-1-30, Academic press, New York (1981).
15. I. D. Brown and D. Altermatt, *Acat. Crystillogr.*, **41** (1985) 244.
16. Welberry *et al*, *J. Solid State Chem.*, **100** (1992) 71.
17. H. Ishizawa, O. Sakurai, N. Mizutani and M. Kato, *Am. Cer. Soc. Bull.*, **65** (1986) 1399.
18. T.H. Etsell and S.N. Flengas, *Chem. Rev.*, **70** (1970) 1970.

19. R.S. Garvie, R.H. Hannink and R.T. Pascoe, *Nature*, **258** (1975) 703.
20. G. Fischer, *Ceram. Bull.*, **65** (1986) 1355.
21. T. Yokoyama, T. Setoyama, N. Fujita, M. Nakajima, T. Maki and K. Fujii, *Appl. Catal.* **88** (1992) 149.
22. O. Ruff and F. Abert, *Z. Anorg. All. Chem.*, **180** (1929) 19.
23. H.C. Yao and M. Bettman, *J. Catal.*, **41** (1976) 349.
24. B.H. Davis, *Appl. Surf. Sci.*, **19** (1984) 200.
25. R.G. Silver, C.J. Hou and J.G. Ekerdt, *J. Catal.*, **118** (1989) 400.
26. A.M. George, N.C. Mishra and N.C. Jayadevan, *J. Mater. Sci. Lett.*, **11** (1992) 404.
27. Ping Wu, R. Kershaw, K. Dwight and A. Wold, *Mater. Res. Bull.*, **23** (1988) 475.
28. Y.C. Long, Z.D. Zhang, K. Dwight and A. Wold, *Mater. Res. Bull.*, **23** (1988) 631.
29. M. Hoch and M. Mathur, *J. Am. Cer. Soc.*, **45** (1962) 373.
30. M. I. Zaki, A. K. H. Nohman, G. A. M. Hussein and Y. E. Nashed, *J. Mater. Sci. Lett.*, **14** (1995) 1442.
31. R. Burch, S. Chalker, G. D. Squire and S. C. Tsang, *J. Chem. Soc. Faraday Trans.*, **86** (1990) 1607.
32. R. Prasad, L. Kennedy and E. Ruckenstein, *Catal. Rev. Sci and Engg.*, **26** (1984) 1.
33. M. Marcezewski and H. Marcezwaska, *Polish J. Chem.* **69** (1995) 956.
34. A. Keshavaraja and A. V. Ramaswamy, *J. Mater. Res.*, **9** (1994) 837.
35. V. P. Dravid, V. Ravikumar, M. R. Notis, C. E. Lymzo, G. Dhalenne and A. Revcolevsch, *J. Amer. Ceram. Soc.*, **77** (10) (1994) 2758.
36. K. Eguchi, M. Watabe, S. Ogata, and H. Arai, *Bull. Chem. Soc. Jpn*, **68** (1995) 1739.
37. A. Keshavaraja and A. V. Ramaswamy, *Appl. Catal. (B) Environmental*, (in press)
38. A. I. Vogel, "A text book of Quantitative analysis including elementary instrumental analysis" Third Ed. P 360, Longman, London, 1961
39. W. S. Fyfe, *Nature*, **164**, (1949) 790; Fyfe, *Anal. Chem.*, **23**, (1951) 174.
40. H. Tagawa, J. Mizusaki, H. Narita and H. Takeuchi, *Thermochimica Acta*, **63** (1990) 303.
41. E. D. Whitney, *J. Am. Ceram. Soc.*, **53** (1970) 697.

42. J. Livage, K. Doi and C. Mazires, *J. Am. Ceram. Soc.*, **51** (1968) 349.
43. R. Srinivasan and B. H. Davis, *J. Colloid & Interface Sci*, **156** (1993) 400-405.
44. J. D. Carruthers, K. S. W. Sing and J. Feenerty, *Nature*, **213** (1967) 66.
45. M. Sorrentino, L. Steinbrecher and F. Hazel, *J. Colloid & Interface Sci.*, **31** (1969) 307.
- 45b R. D. Shannon and Pevitt, *Acta Crystallogr.*,
46. J.C.P Broekhoff and B.G. Linsen, in "Physical and Chemical Aspects of adsorbents and Catalysis" (B.G. Linsen, Ed.), Chapter 1, pp. 1-62, Academic Press, New York, 1970
47. S. J. Gregg and K. S. W. Sing, Adsorption, surface area and porosity, 2<sup>nd</sup> Ed, Academic press, London, 1982.
48. K. S. Sing, D. H. Everette, R. A. W. Haul, L. Moscou, R. A. Pierotti, J. Rouquerol, and T. Siemieniewska, *Pure and Appl. Chem.*, **57** (1985) 603.
49. J. H. DeBoer,, in D. H. Everette and F. S. Stone (Eds), The structure and properties of porous materials, Butterworths, London, 1958, p-68.
50. A. J. Lecloux in J. R. Anderson, and M. Boudart (Eds), Catalysis Science and Technology), Springer-Verlag, Berlin, 1981, p-171.
51. A. Keshavaraja, N. E. Jacob and A. V. Ramaswamy, *Thermochimica Acta*,
52. E. D. Whitney, *J. Am. Ceram. Soc.*, **53** (1970) 697.
53. J. Livage, K. Doi, and C. Mezeres, *J. Am. Ceram. Soc.*, **51** (1968) 349.
54. C. J. Norman, P. A. Goulding, and I. McAlpine, *Catal. Today*, **20** (1994) 313
55. D. D. Sarma, and C. N. R. Rao, *J. Electron Spectroscopy and Rel. Phenomenon.*, **20** (1980) 25.
56. F. Parmigiani, L. E. Depèro, L. Sangaletti and G. Samoggia, *J. Elec. Spec. Rel. Pheno.*, **63** (1993) 1.
57. D. Steele, B. E. F. Fender, *J Phys. C.*, **7** (1974) 1.
58. C. R. A. Catlow, A. V. Chadwick, G. N. Greaves, and L. M. Moroney, *J. Am. Ceram. Soc.*, **69** (1986) 272.
59. B. W. Veal, A. G. McKale, A. P. Paulikas, S. J. Rothman, and L. J. Nowicks, *Physica. B*, **150** (1988) 234.
60. S. Suzuki, M. Tanaka, and M. Ishigama, *J. Phys. C.*, **20** (1987) 2963.



61. F. Parmigiani, G. Pacchioni, C. R. Brundle, D. E. Foulter and P. S. Bagus, *Phys. Rev. B*, **43** (1991) 3695.
62. P. S. Bagus, C. R. Brundle, G. Pacchioni and F. Parmigiani, *Chem. Phys. Lett.*, **196** (1992) 3695
63. N.T. McDevitt and W.L. Baun, *J. Am. Cer. Soc.*, **47** (1964) 622.
64. D. P. C. Thackeray, *Spectrochim. Acta*, **30** (1974) 549.
65. V. G. Keramidas, W. B. White, *J. Chem. Phys.* **59**, (1973) 1561.
66. D. J. Kim, H. Jung, and I. Yang, *J. Amer. Ceram. Soc.*, **76** (1993) 2106.
67. M. Uchiyama, S. Slane, E. Plichta, and M. Saloman, *J. Electrochem. Soc.*, **136** (1989) 36.
68. D. Belanger and G. Laperriere, *J. Electrochem. Soc.*, **137** (1990) 2355.
69. J. Wei, *Adv. Catal.*, **24** (1975) 57.
70. S. Becker and M. Berns, *J. Catal.*, **128** (1991) 512.
71. J. L. Dubois, B. Rebours and C. J. Cameran, *Appl. Catal.*, **67** (1990) 73.
72. M. P. Rosynek, *Catal. Rev. Sci. Eng.* **16** (1977) 111.
73. P. K. Coattures, J. M. Badie, and R. Berjam, *High Temp. Sci.*, **13** (1980) 331.
74. H. Arai, T. Yamada, and T. Seiyama, *Appl. Catal.*, **26** (1986) 265.
75. Y. F. Y. Yao, *J. Catal.*, **36** (1975) 266.
76. T. Nitadori and M. Misono, *J. Catal.*, **8** (1985) 459.
77. W. Berkstresser, R. J. Brook, and J. M. Whalen, *J. Mater. Sci.*, **9** (1974) 491.
78. M. P. Van Dijk, *Mater. Res. Bull.*, **19** (1984) 1149.
79. A. Anderson, *J. Catal.*, **69** (1981) 465.
80. P. Courtine, thermodynamics and structural effects in mild oxidation catalysts, in solid state chemistry in catalysis, (Ed) R. K. Grassilli, J. F. Brazadil.; ACS Symp sereies 279, Washington DC, ACS, 1985, 37.
81. P. Mars and D. W. Van Krevelan, *Chem. Eng. Sci.*, **3** (1954) 41.
82. A. Bielanski and J. Haber, in Oxygen in Catalysis, Marcel Dekker, New York, 1991.
83. N. Matsui, *Solid State Ionics*, **18** (1986) 888.
84. P. Berthet, J. Berthon, and A. Revcolevschi, *Phys. Rev. B*, **158** (1989) 506.
85. P. J. Alonso, R. Alcalá, J. Casas-Gonzalez, R. Cases, and V. M. Orera, *J. Phys. Chem. Solids*, **50** (1989) 1185.

## CHAPTER- FOUR

# Sol-gel derived Supported Copper Catalysts

---

*In this chapter, supported copper catalysts prepared by sol-gel method are investigated in comparison to the catalysts prepared by co-precipitation method. The importance of high surface area of the support, crystallite size, metal area and inhibition of sintering on hydrogenation /dehydrogenation activity and selectivity are studied.*

## 4.1. INTRODUCTION

Recently a great deal of interest has been shown in the application of sol-gel chemistry in various fields of technology. Although the basic principle of sol-gel chemistry was known more than a hundred years ago,<sup>1</sup> its technological applications have come to the light only in the last ten years.<sup>2,3</sup> However, a majority of the materials prepared using the sol-gel method till recently were confined to ceramics, refractories and glasses. The attempt to apply the sol-gel technique for the preparation of catalyst material is relatively new as evidenced by very few publications.<sup>4-8</sup>

In this chapter, an attempt has been made to demonstrate the fundamental benefits of sol-gel technology with a special emphasis on catalyst preparation, particularly supported metal catalysts.

### *4.1.1. What is the sol-gel process ?*

The sol-gel process involves the hydrolysis of a metal alkoxide solution to form a *sol* followed by condensation and polymerization to form a *gel*. A *sol* is a dispersion of solid particles in a liquid phase where the particles are small enough to remain suspended indefinitely by Brownian motion.<sup>9</sup> A *gel* is a solid containing a liquid component and an internal network structure so that both the solid and the liquid are in a highly dispersed state. All the sols can not be converted in to gels. There should be a strong particle-solvent interaction so that at least part of the solvent is bound. In essence, the sol-gel process involves the dissolution of the required metal ions either as

alkoxide or other metallo-organic salts in a suitable alcoholic solvent or as inorganic salts in water to form the sol. This is followed by the gelation step in which the fluid sol is transformed to a semi-rigid solid gel. Two types of gels are usually formed, colloidal and polymeric. Colloidal gels are formed from metal salt solutions and oxides and hydroxide sols. On the other hand, polymeric gels are formed from metal alkoxide based sols. The gel is dried and calcined (if necessary). On heating the gel, it generally undergoes the following changes.<sup>10</sup>

- i) loss of solvents and pyrolysis of the organics;
- ii) structural rearrangement and densification;
- iii) crystallization.

Conventional evaporative drying such as heating a gel in an oven, induces capillary pressure associated with the liquid-vapour interface within a pore resulting in the collapse of the porous network. The sample thus obtained is called a *xerogel*, which has a relatively low surface area and pore volume. In supercritical drying, on the other hand, these deleterious effects are minimized due to differential capillary pressure and the resultant materials are known as *aerogels*. Consequently, they have high pore volumes, surface areas and lower bulk densities. A third method of drying involves the freeze drying of the solvents at low temperature under reduced pressure. This method is similar to the lyophilization technique adopted in pharmaceutical industries and the product is called *cryogel*. Yet another method of drying is subjecting the gel to ultrasonic vibration at room temperature to remove the solvent. The gel thus obtained is called a *sonogel*.

The typical preparation route by the sol-gel process is presented in Fig. 4.1.

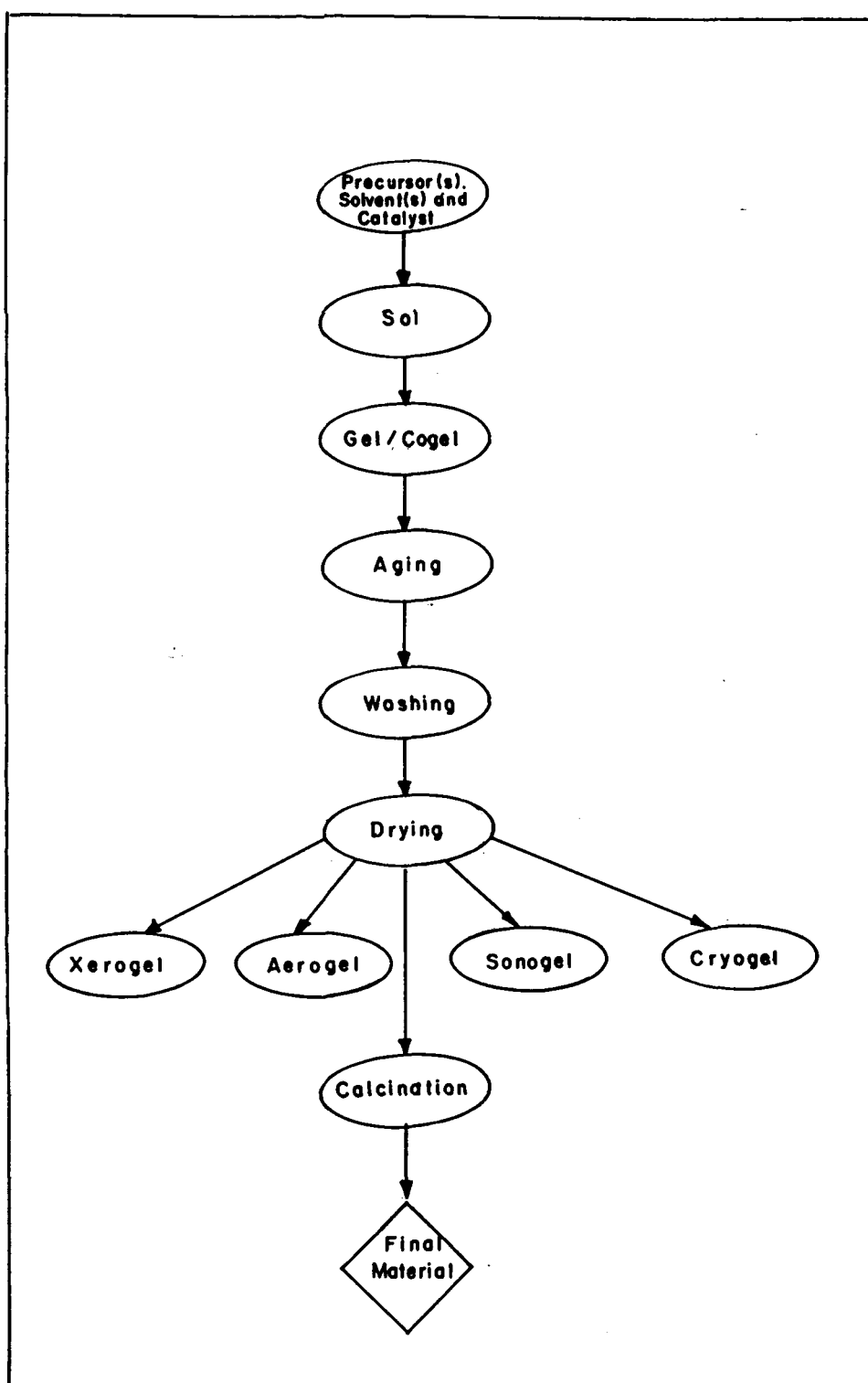
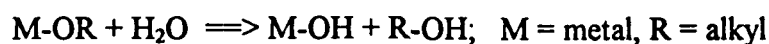


**Fig. 4.1 :** Steps involved in a typical sol-gel preparation

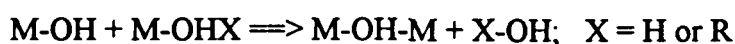
### 4.1.2. Chemistry of sol-gel process

The chemistry of the process which occurs during the sol-gel synthesis is represented below.<sup>11</sup>

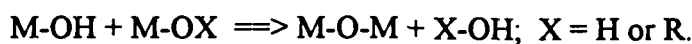
#### *Hydrolysis of metal alkoxide*



#### *Condensation to form hydroxy bridges*



#### *Condensation to form oxygen bridges*



Most sol-gel reactions involve hydroxylated species and can be described as nucleophilic substitutions. The chemical reactivity of metal alkoxides toward hydrolysis and condensation then depend on the positive charge of the metal atom,  $\delta_M$ , and its ability to increase its coordination number,  $N$ . As a general rule the electronegativity of the metal atom decreases, their size increases and the chemical reactivity of the corresponding alkoxides increases when going down the periodic table. To increase the hydrolysis and condensation rates usually acid or base catalysts have to be used. The mechanism and the rate of the above reactions are dependent on several factors, including the pH, the temperature and the rate of water addition.

### 4.1.3. Conditions for Sol-gel synthesis

One advantage of the sol-gel synthesis is the possibility of tailoring catalyst properties by tuning various conditions of the sol-gel process. Some of them are :

***pH of the hydrolysis*** : The pH during hydrolysis mainly decides the nature of the pores and surface area apart from the density of the materials. Acid catalyzed hydrolysis gives a microporous network, while base catalyzed hydrolysis leads to the formation of mesoporous networks.

***Rate of addition of water*** : The rate of addition of water during the preparation of the sol affects the rate of hydrolysis and condensation which in turn influence the texture and morphology of the gel.

***Temperature of gelation*** : The rate of gelation depends on the temperature at which the sol is aged or heated to remove the solvent or for the facilitation of hydrolysis. If the temperature is lower, the rate of hydrolysis will be slower and the particle size will be relatively smaller. This results in reduced pore collapse and yield to a well defined porous network.

***Aging*** : Removal of the solvent from the solid matrix encapsulating a solvent (gel) is an important step in the sol-gel synthesis. The time between the formation of a gel and its drying is known as *aging*. During aging also the gel continues to undergo hydrolysis and condensation.<sup>12</sup> In addition, syneresis, which is the expulsion of the solvent due to the gel shrinkage, and coarsening, which is dissolution and reprecipitation of the particles, can occur. These phenomena can affect both the chemical and structural properties of the gel after its initial formation.

***Drying conditions*** : Drying conditions affect the structure and morphology of the sol-gel derived materials. Conventional evaporative drying such as heating a gel in an oven, induces capillary pressure associated with the liquid-vapour interface within a pore. In a sample with a distribution of pore sizes this would result in the collapse of the porous network. To overcome the problem of differential capillary pressure

*supercritical drying* is shown to be useful.<sup>13</sup> The resultant materials have high surface area, porous structure and low density.

***Drying control chemical agents (DCCA)*** : Various drying control chemical agents are useful in controlling the porosity and bulk density. Some of the prominent DCCAs include formamide, glycerol and oxalic acid. The presence of DCCA will have significant influence on the particle texture and morphology.

***Calcination temperature*** : The temperature of calcination is also important in controlling the pore size and density of the material. For instance, calcination at temperature above 1273 K may cause collapse of the porous net work, but results in material with high density.

#### ***4.1.4. Advantages of the sol-gel method***

Advantages of sol-gel method in the preparation of catalyst materials are listed below :

- \* better homogeneity in products
- \* lower reaction temperature
- \* less contamination and loss
- \* ultrafine particle size (less than 100 Å)
- \* possibility of many new composites
- \* very low atomic density
- \* very high porosity and surface area
- \* lower thermal conductivity



- \* textural and structural stability at high temperatures
- \* control over composition
- \* the ability to control structure and composition at a molecular level.
- \* the ability to introduce several components at a single step.
- \* stabilizing the metastable phases by imposing kinetic constraints on a system
- \* tracing the genesis of the active species and fine tuning activation behaviour.

### ***Scope of the present chapter***

In the present chapter, application of sol-gel method of preparation on structure and activity of copper metal catalysts supported on silica is described. A comparison is made with the copper- silica prepared by conventional co-precipitation method. The advantage of sol-gel method of preparation on the hydrogenation and dehydrogenation activity of the catalysts is explained in terms of "*restricted grain growth model*".

### ***4.1.5. Supported metal catalysts : Where do we stand ?***

Many industrial applications require supports which combine a high specific surface area with good thermal and chemical stability. Several attempts are reported where an easy accessibility to the reactant is considered to be the prime requirement. According to Trimm and co-investigators supports must possess a well- developed mesoporous texture.<sup>14</sup>

Hydrogenation reactions have gained ground due to their industrial importance. Heterogeneous catalyzed hydrogenation reactions involve the use of molecular hydrogen in presence of metal catalysts. The effect of metallic loading, the metal-

support interactions, decoration effect, hydrogen spill-over and structure sensitivity are some of the well established phenomena in this direction. However, there is hardly any attempt known where the effect of preparation on the physical and catalytic properties are made. In this regard, our present approach of comparing the sol-gel derived supported catalyst with that of conventionally prepared catalyst would be interesting. Justification for choosing sol-gel method is described in the next section.

#### ***4.1.6. Preparation of supported metal catalysts***

Several methods are known for the preparation of supported metals. The most common among them are impregnation and ion exchange.<sup>15</sup> These preparation methods greatly influence the particles size, the electronic properties and structural features of the catalysts.<sup>16-18</sup>

Another parameter which controls the properties of the supported metal catalysts is the structure of metal precursors.<sup>19-21</sup> Catalysts prepared by these traditional methods undergo rapid sintering under identical conditions.<sup>22,23</sup> If the structure of the metal crystallites could be matched to the pore diameter, surface diffusion is inhibited and crystal growth will not occur. At higher metal loadings, metal particles may also be present outside the pore systems. These particles are more prone to get sintered at higher temperature. In this direction, sol-gel method could be considered as advantageous.

Sol-gel method is one of the newer techniques employed recent times for the preparation of supported metal catalysts.<sup>24-26</sup> Sol-gel method has particularly caught the attention of catalytic chemists due to the possibility of controlling dispersion and particles size of the active metal phase and in turn activity and selectivity since several

hydrogenation and hydrogenolysis reactions depends critically on the particle size.<sup>27,28</sup> The potential advantages of the sol-gel processing include purity, homogeneity and controlled porosity combined with ability to form large surface area materials at lower temperatures.

More commonly practiced method involve the acid or base catalyzed hydrolysis of metal alkoxides in presence of the metal. Under acid catalyzed conditions, highly hydroxylated catalysts are obtained . At base catalyzed conditions, the strong interaction of silanol groups with the metals is observed.<sup>29</sup> Although, acid catalyzed sol-gel samples have high surface area ( $400 - 600 \text{ m}^2 \text{ g}^{-1}$ ), they are microporous. These micropores tend to get blocked due to the deposition of coke with eventual deactivation of the catalyst. On the other hand, catalysts prepared under base catalyzed conditions show tendency to sinter due to the agglomeration of the metal particles as a result of which, surface area decreases.<sup>30</sup> Therefore, a proper control of the pH of the preparation condition is warranted to get tailored metal catalysts. In addition, care should be taken that the metal crystallites should neither get sintered nor get buried inside the pore. Therefore, preparation conditions should be chosen in such a way that it should overcome the limitations of the conventional preparation technique.

#### ***4.1.7. Supported copper catalysts***

Copper based catalysts are applied in a variety of industrial process.<sup>31-36</sup> More particularly, copper catalysts supported on oxidic support has been widely used in various reactions such as dehydrogenation of alkanes, aldehydes and ketones or some

hydrogenation reactions. They are particularly interesting due to their selective properties in reactions involving hydrogen.<sup>37</sup>

The most prominently used catalysts include Cu-SiO<sub>2</sub><sup>38-41</sup> and Cu-Al<sub>2</sub>O<sub>3</sub><sup>42-45</sup> which are most intensively studied by various techniques.

#### ***4.1.8. Aniline through hydrogenation of nitrocompounds***

Aniline is an industrially important chemical which finds wide spread applications.<sup>46</sup> The major use of use of aniline is in the manufacture of polymers, rubber, agricultural chemicals, dyes and pigments, pharmaceuticals and photographic chemicals. Approximately 65 % of the world production of aniline is used in the manufacture of rigid polyurethanes and reaction injection molded parts for the construction, automobiles and durable goods industries.

Catalytic reduction of nitrobenzene is the predominant process for the manufacture of aniline.<sup>47-50</sup>

The reduction of nitrocompounds has been comprehensively studied by many investigators with the aid of metal acid systems<sup>51</sup> and molecular hydrogen<sup>52,53</sup> or by hydride ion transfer.<sup>54,55</sup> over Fe, Ni or Pd catalysts supported on silica or alumina<sup>56,57</sup> In a number of cases they are promoted by various additives such as magnesium, calcium and zirconium, thorium, vanadium or chromium.<sup>58,59</sup> Recently, kieselghur supported copper catalyst has been used for this.<sup>60</sup>

The conversion of nitrobenzene to aniline is expected to predominate at high partial pressures of hydrogen. The hydrogen molecule, being small in size, can penetrate in to the internal part of the catalyst grain more easily than the nitrobenzene molecule. Therefore, the concentration gradient of the hydrogen molecule along the

radius of the grain is negligible in relation to that of nitrobenzene. As a result of this, the concentration of the coke precursors along the radius will be dependent mainly on the diffusion in to the catalyst grain which is proportional to its gas phase concentration.

To the best of our knowledge, the application of sol-gel method for developing industrial aniline catalysts is not there in practice. Realizing the importance of metal crystallite size, metal dispersion and sintering inhibition for the hydrogenation reactions, an attempt has been made to tailor make Cu-SiO<sub>2</sub> catalysts by sol-gel method for hydrogenation and dehydrogenation applications.

#### ***4.1.9. Dehydrogenation of Secondary butyl alcohol.***

Methyl ethyl ketone is a highly versatile petrochemical solvent which finds application in diverse industries.<sup>61</sup> The natural advantages which make it a popular solvent are:

- high solvent power
- favourable evaporation rate
- good miscibility with organic solvent
- greater diluent tolerance
- low density
- unsaponifiability.

Methyl ethyl ketone finds application in dewaxing of lubricating oils, in audio, video and computer tapes. It is used for coating of magnetic iron oxide on polyester

film. MEK is also used as a chemical reactant for manufacture of vitamin A and as a solvent for film coating.

Methyl ethyl ketone is generally manufactured via catalytic hydrogenation of secondary butyl alcohol over a suitable catalyst.<sup>62</sup> The dehydrogenation of secondary butyl alcohol is carried out over a catalyst bed of copper, zinc oxide, silver on pumics, etc. For the selective formation of MEK, the side reaction such as the dehydation of alcohol with the formation of olefins is to be avoided.

Although, a variety of reaction parameters are studied, the influence of the preparation parameter, particularly the sol-gel preparation conditions is not yet studied to the best of our knowledge. Therefore, an attempt has been made to compare the conventional Cu-SiO<sub>2</sub> with that of sol-gel derived catalyst. Since our emphasis is on the industrial development of Cu-SiO<sub>2</sub> catalysts, the comparison has been made at higher conversion.

## 4.2. EXPERIMENTAL

### 4.2.1. Preparation of the Cu-SiO<sub>2</sub> catalysts

A series of samples of copper-silica with copper contents ranging from 5 to 50 wt % were prepared by sol-gel method. The procedure involves hydrolysis and condensation of stoichiometric mixtures of tetraethyl orthosilicates (TEOS) and aqueous solution of copper nitrate at neutral medium using deionised water; the molar ratio of TEOS : Ethanol : Water = 1 : 2 : 20. The resultant blue coloured sol was kept at 323 K for time ranging from 3 to 12 hours to get a thick gel. It was then kept for drying at 383 K for 12 hour and subsequently calcined at 573 K for 8 h. For

comparison, sample with copper content ranging from 5 to 50 wt % was prepared by co-precipitation method using the same source of Cu and Si and ammonium hydroxide as the precipitating agent.

The specific surface area, mean cylindrical pore diameter and pore volume were determined by the BET method from the N<sub>2</sub> adsorption isotherms at 77 K measured in an 'Omnisorp 100 CX' surface area analyzer. BET surface areas were calculated in a relative pressure range between 0.05 and 0.2 assuming a cross sectional area of 0.162 nm for the nitrogen molecule. The pore size distributions were calculated by applying BJH model and Horwath-Kawazoe model. The temperature programmed reduction experiments were carried out on a 'Sorbstar' (Institute of Isotopes, Hungary) apparatus using 5 % H<sub>2</sub> in N<sub>2</sub>.

#### ***4.2.2. Metal area estimation :***

The standard degree of reduction (% DR) of the sample were obtained from the temperature programmed reduction experiments. The metal area was calculated by using the formula,<sup>63</sup>

$$\text{metal area} = [(DR/100)*4310]/ \text{crystallite size},$$

where, the crystallite size was estimated from the X-ray line broadening. Although, this method is based on the accuracy of the crystallite size determination, relative trends can be assessed.

#### ***4.2.3. Catalytic reaction :***

The catalytic test reaction of hydrogenation of nitrobenzene were conducted at nitrobenzene LHSV value between 0.007 and 0.01 h<sup>-1</sup>. These values are similar to

those of industrial conditions. The feed molar ratio between hydrogen and nitrobenzene was from 20 : 1 to 40 : 1 which is once again at par with industrial conditions. The reaction was conducted at atmospheric pressure and at temperature ranging from 503 to 563 K. The temperature of the catalyst was kept constant by means of an electronic thermoregulator with an accuracy of  $\pm 1$  K. Liquid nitrobenzene was admitted to the reactor by a Alcott, 760 model pump. The analysis of the reaction products was carried out on a 'HP 5880' gas chromatograph equipped with capillary column.

The catalyst was placed in the reactor and dried in a stream of nitrogen for two h at 393 K. Then the temperature was slowly increased to 473 K under the flow of mixtures of  $H_2/N_2$ . Further, the catalyst bed was kept at the same temperature for three hours. Finally the temperature of the reactor was raised to 523 K and after three h the feed was introduced. The schematic diagram of the reactor system used is shown in Fig. 2.18 (Chapter two).

Similarly, dehydrogenation of secondary butyl alcohol was carried out in a fixed bed plug flow reactor.

## 4.3. RESULTS AND DISCUSSION

### 4.3.1. X-ray diffraction studies

The powder X-ray diffraction profiles of reduced Cu-SiO<sub>2</sub> with 5, 10, 20, 30 and 50 wt % copper prepared by sol-gel method is presented in Fig. 4.2 (profiles a to e, respectively). For comparison, CuO-SiO<sub>2</sub> prepared by co-precipitation with 10, 20, 30 and 50 wt % of copper loading is presented in Fig. 4.3 (profiles a to d).



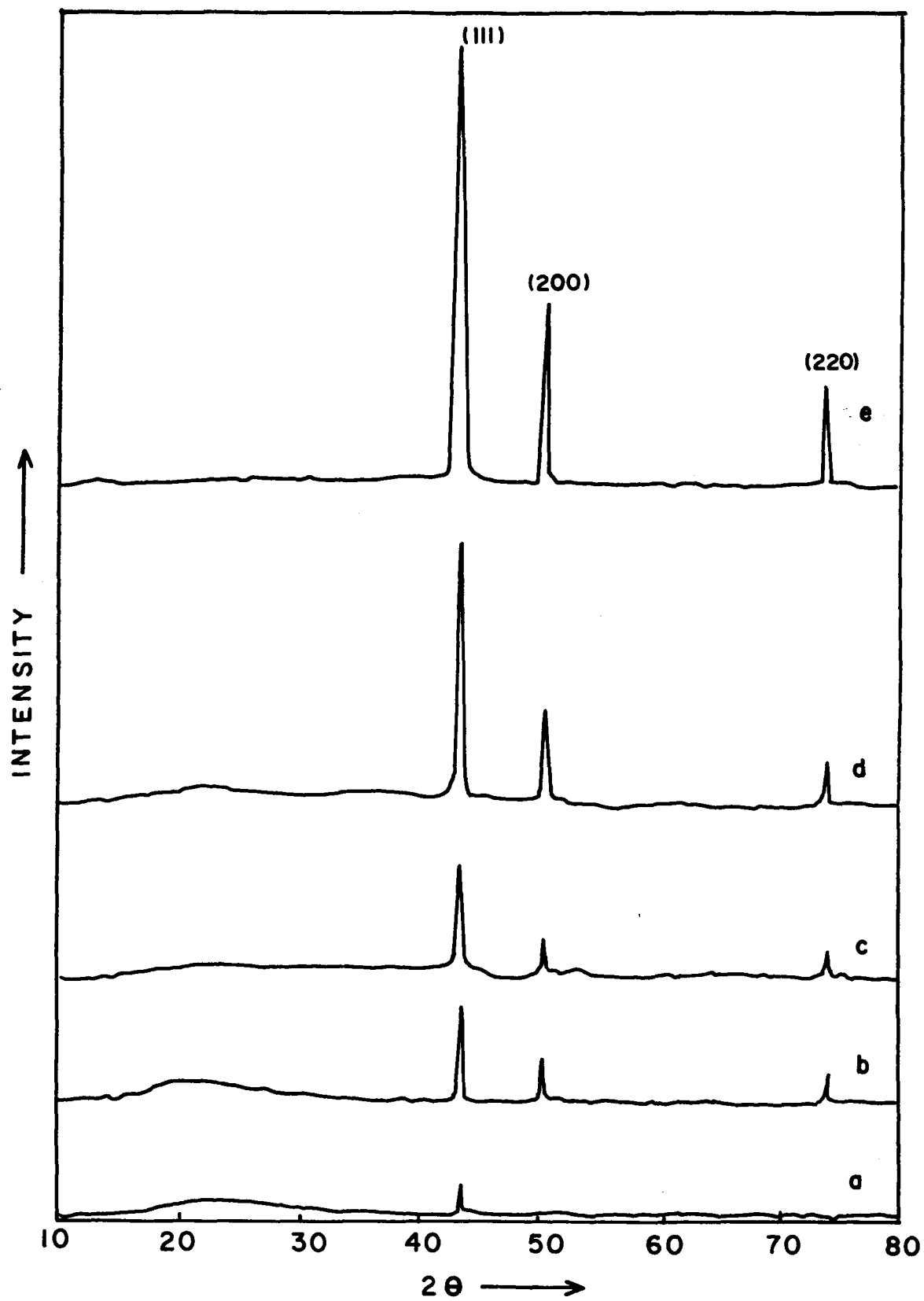


Fig. 4.2 : X-ray diffraction patterns of reduced Cu-SiO<sub>2</sub> catalysts prepared by sol-gel method with Cu loading of 5, 10, 20, 30 and 50 wt% (a to e).

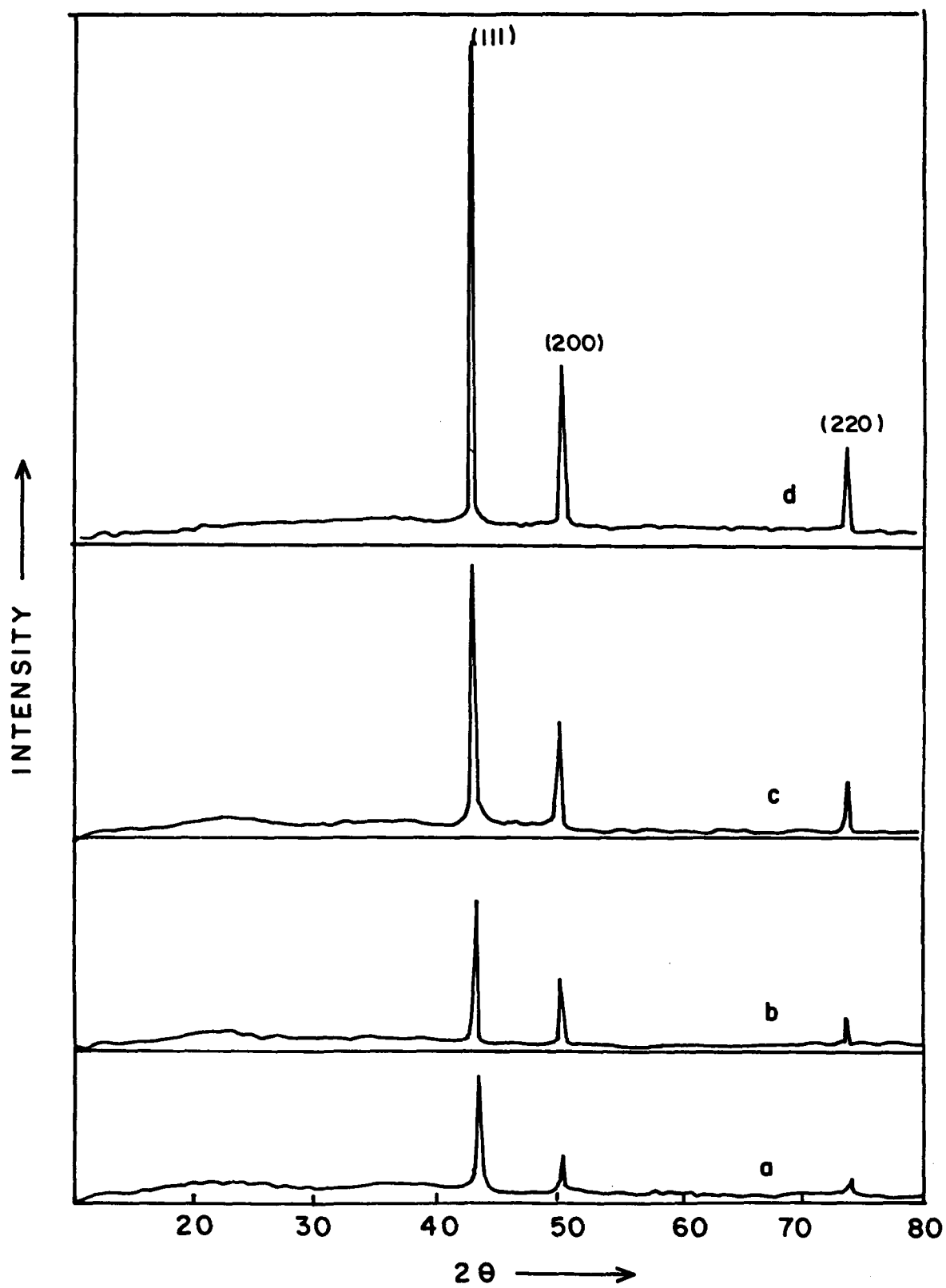


Fig. 4.3 : X-ray diffraction patterns of reduced Cu-SiO<sub>2</sub> catalysts prepared by co-precipitation method, with Cu loading of 10, 20, 30 and 50 wt % (a to d, respectively).

comparative look at the most significant peaks corresponding to (111), (200), and (220) reflections the samples prepared by sol-gel method have smaller crystallites. The corresponding crystallite sizes calculated by applying Debye-Scherrer formula on (200) reflection are tabulated in Table 4.1.

Crystallite size of sol-gel derived copper catalysts is in the range of 45 to 55 Å whereas, the corresponding size of the sample prepared by co-precipitation method is relatively higher, ranging from 55 to 80 Å. Thus it can be inferred that the sol-gel method gives smaller metal crystallites.

**Table 4.1**

**Crystallite sizes of Cu-SiO<sub>2</sub> prepared by sol-gel and co-precipitation route.**

Copper loading, (wt%)	Cu crystallite size, Å	
	Sol-gel	Co-precipitation
5	45	55
10	49	60
20	51	70
30	54	77
50	56	80

### ***4.3.2. Textural Properties***

The adsorption - desorption isotherms of representative samples of reduced Cu-SiO<sub>2</sub> catalysts containing 20 wt % of Cu, prepared by sol-gel method and co-

precipitated method are presented in Fig. 4.4. In the case of co-precipitated samples, the adsorption-desorption branches show considerable hysteresis and conform to BET type II isotherms, indicating the presence of mesopores. On the other hand, the sol-gel derived Cu-SiO<sub>2</sub> catalysts showed Type IV isotherms and the unusual hysteresis with two significant loops indicate the coexistence of micropores.<sup>64</sup> A comparison of physical properties of two representative samples prepared by sol-gel and co-precipitation method is presented in Table 4.2. Also, the surface area (BET) of the two samples are drastically different. For example, surface area of the Cu-SiO<sub>2</sub> sample prepared by sol-gel method is 380 m<sup>2</sup> g<sup>-1</sup> whereas that of co-precipitated sample is 160 m<sup>2</sup> g<sup>-1</sup>. Similarly, there is significant difference in the pore diameter. Sol-gel route results in the formation of meso pores with pore diameter of about 48 Å, whereas the sample prepared by co-precipitation method has meso pores with pore radii of about 200 Å. This is further corroborated through the pore size distribution curves. (Fig. 4.5). Copper metal area is also significantly higher in the case of sol-gel method of preparation.

**Table 4.2**

**A comparison of physical properties of Cu-SiO<sub>2</sub> catalysts (20 wt% of copper) prepared by sol-gel and co-precipitation method.**

Sample	S <sub>BET</sub> (m <sup>2</sup> g <sup>-1</sup> )	Pore dia, Å	Cu - area, m <sup>2</sup> g <sup>-1</sup>	Cryst. size, Å
Sol-gel	380	48	74.3	51
Co-precipitation	160	200	43.1	70

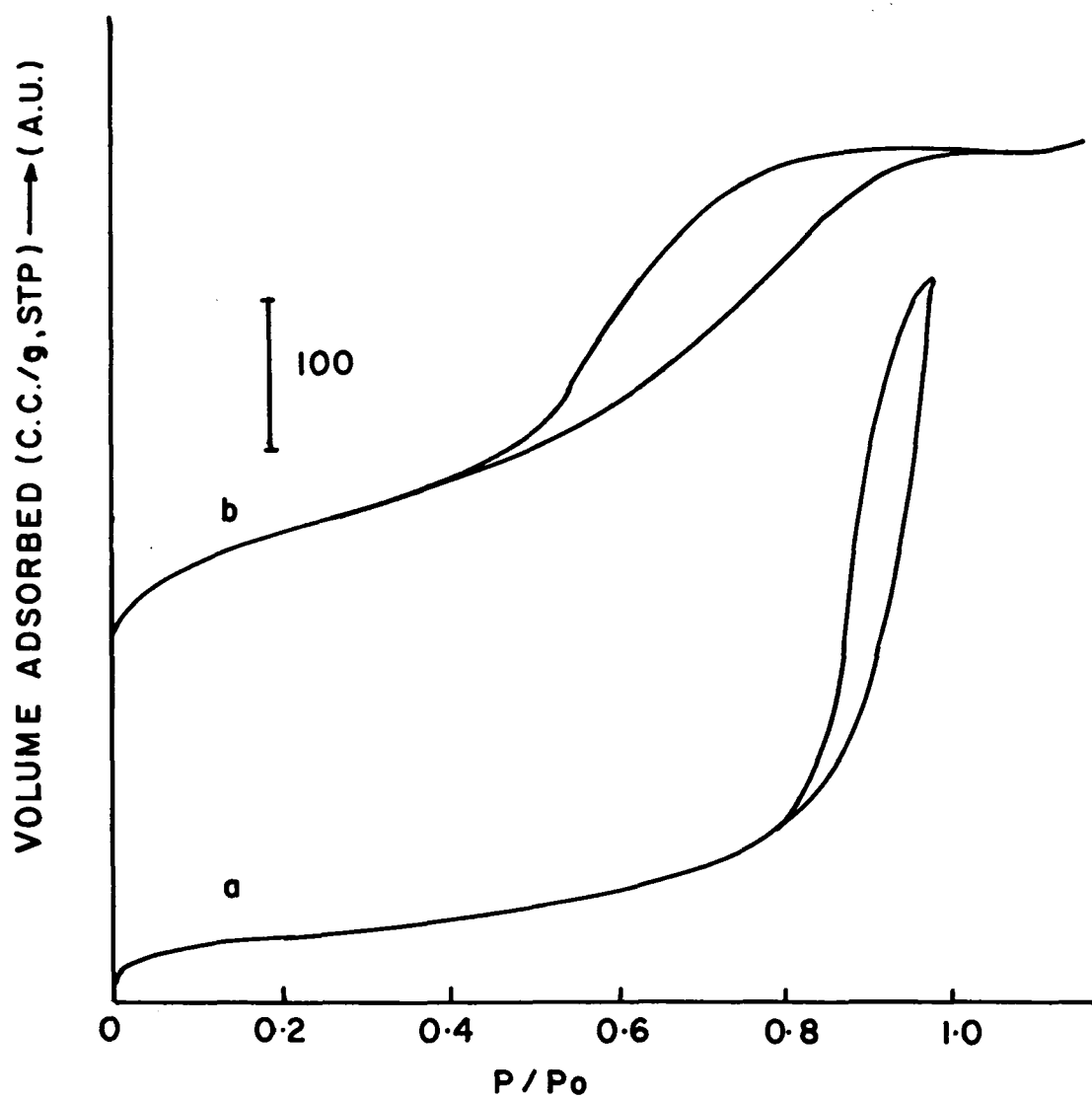


**Fig. 4.4 :** N<sub>2</sub> adsorption - desorption isotherms of reduced Cu-SiO<sub>2</sub> (20 wt % of Cu) catalysts prepared by co-precipitation method (a) and sol-gel method (b)

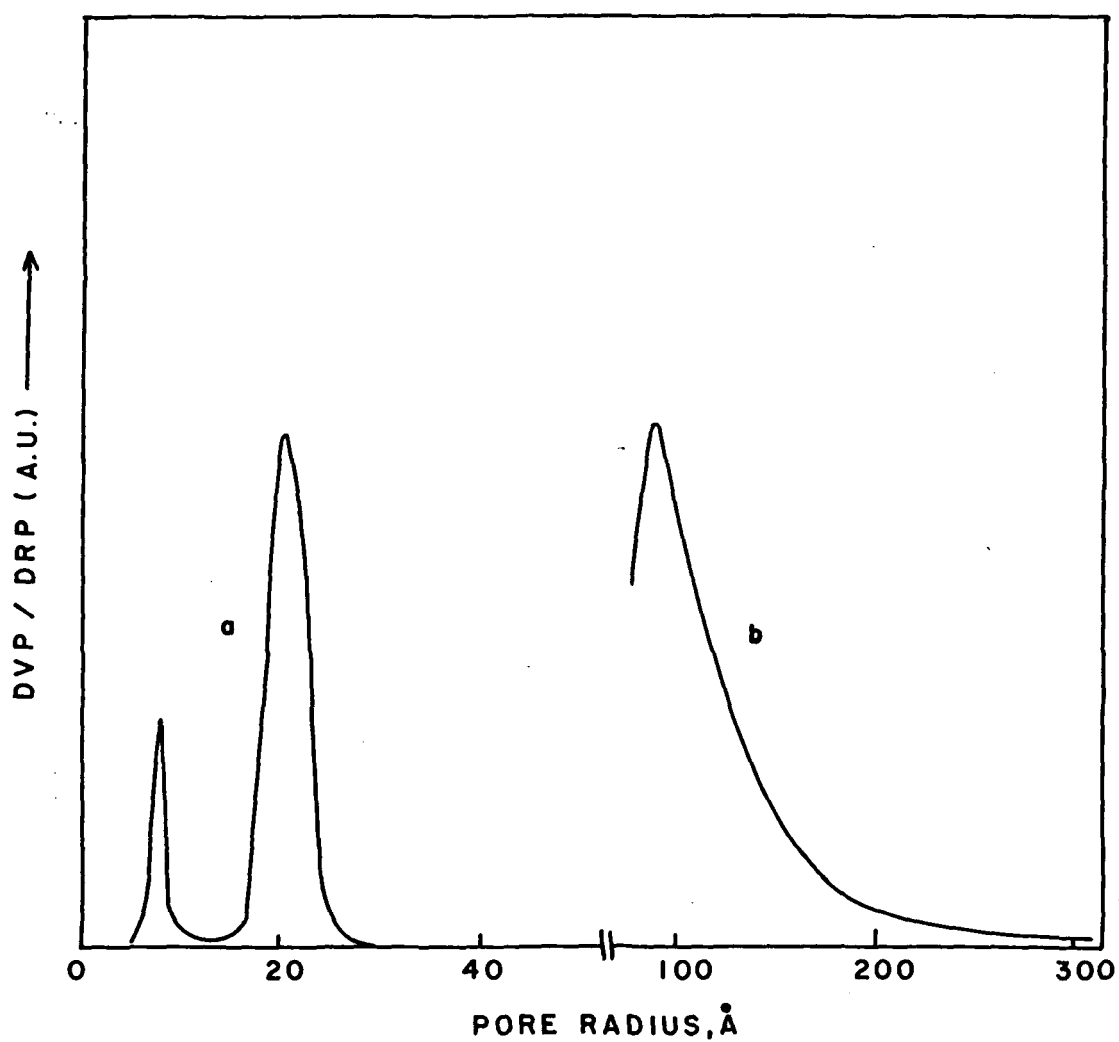


Fig. 4.5: Pore size distribution of Cu-SiO<sub>2</sub> catalysts with 20 wt % of Cu prepared by sol-gel method (a) and co-precipitation method (b).

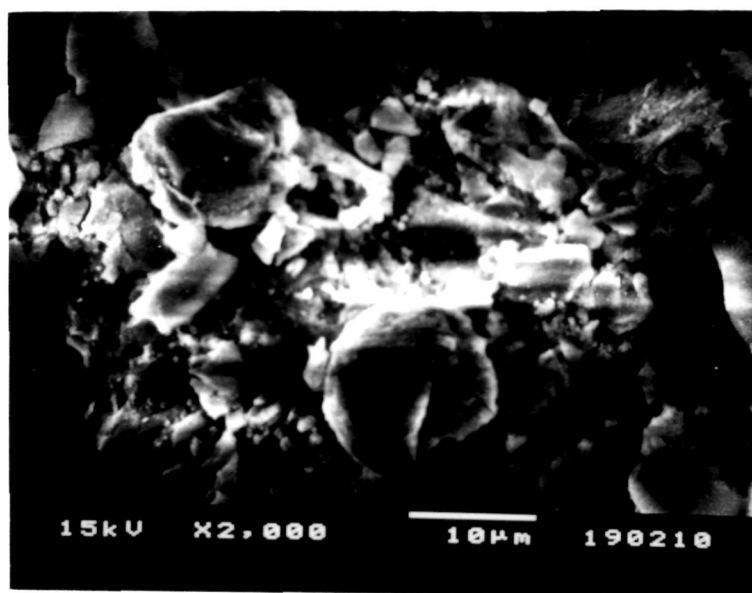
### ***4.3.3. Scanning Electron Microscopy***

The scanning electron micrographs of two representative samples with copper loading of 20 wt %, prepared by Co-precipitation and sol-gel method are shown in Fig. 4.6 a and b, respectively. The sol-gel method gives uniform particles with relatively smaller size ( less than 3 microns), whereas the sample prepared by co-precipitation method gives larger particles and shapes are not regular. However, there is a drastic difference between the particle size and the corresponding crystallite size, probably the particle size is also due to the contribution from silica.

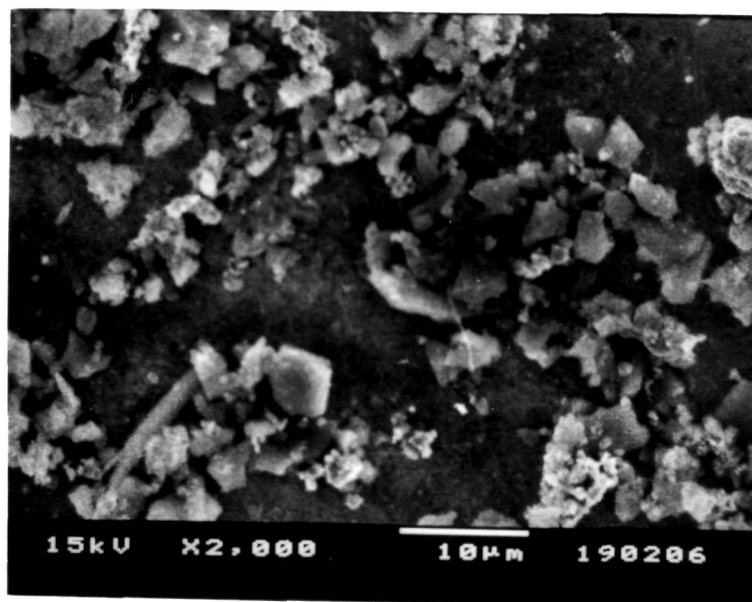
### ***4.3.4. Temperature Programmed Reduction***

The temperature programmed reduction is an useful tool because it can distinguish highly dispersed metal oxide from that of the bulk metal oxide on the basis of the ease of reducibility.

Fig. 4.7 shows the TPR profiles of CuO-SiO<sub>2</sub> catalysts (with 30 wt % of copper) prepared by sol-gel method and co-precipitation method. Since Cu(II) nitrate trihydrate decomposes at 443 K, an optimum temperature of 573 K was chosen for the calcination of the catalysts prior to reduction.<sup>65</sup> From the figure it can be seen that the sample prepared by sol-gel route reduces in two steps with T<sub>max</sub> at 580 K, whereas the other prepared by co-precipitation method require higher temperature, T<sub>max</sub> being 715 K. The increased ease of reduction of supported oxide as compared to bulk oxide is probably due to higher dispersion, which provides a larger surface area, therefore high concentration of defects at which reduction reaction can start.<sup>66</sup>



b



a

**Fig. 4.6 :** Scanning electron micrographs of reduced  $\text{Cu-SiO}_2$  with 20 wt % of Cu prepared by sol-gel (a) and co-precipitation method (b)



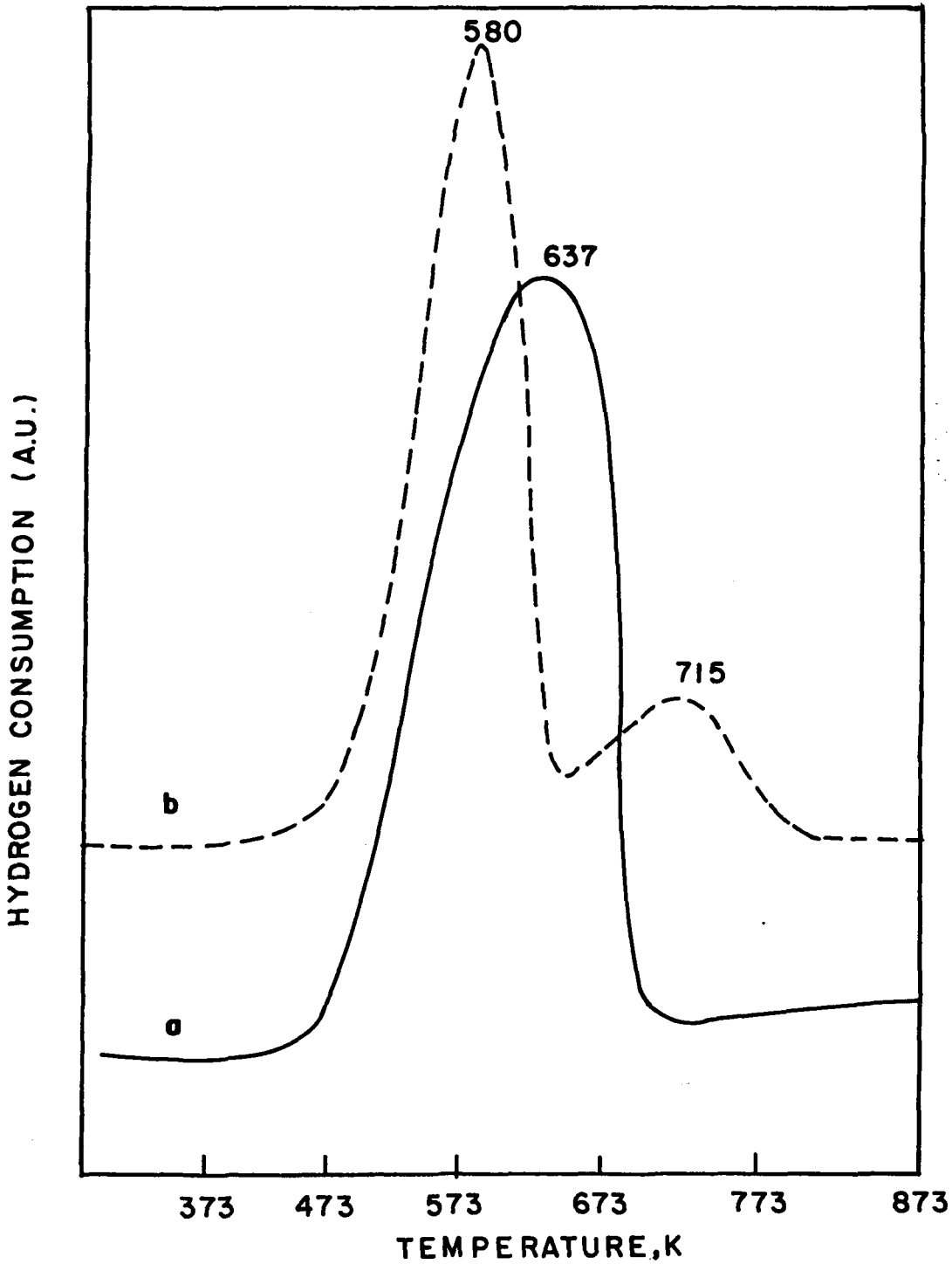


Fig. 4.7: Temperature programmed reduction profiles of Cu-SiO<sub>2</sub> catalysts prepared by co-precipitation method (a) and sol-gel method (b).

### ***4.3.5. Catalytic activity***

#### ***4.3.5.1. Dehydrogenation of secondary butyl alcohol***

Variation in the percentage conversion of secondary butyl alcohol with reaction time on Cu-SiO<sub>2</sub> catalyst with copper content of 20 wt %, prepared by co-precipitation (a) and sol-gel method (b) is presented in Fig. 4.8. The former sample shows a conversion efficiency of about 80 % in the beginning and after about 40 h there is a gradual decrease in the conversion which reaches to 60 % at the end of 112 h. In contrast to this, sol-gel derived sample is stable with respect to long term activity. Apart from this, a commendable differences in the selectivity patterns is observed depending on the preparation method, the details of which are not presented here.

#### ***4.3.5.2. Hydrogenation of nitrobenzene***

Another reaction studied is the hydrogenation of nitrobenzene to aniline. This is also run under industrial conditions. The effect of temperature (A) and space velocity (B) on the conversion of nitrobenzene over Cu-SiO<sub>2</sub> catalysts with 20 wt % of Cu loading prepared by sol-gel method (a) and co-precipitation method (b) is represented in Fig. 4.9. Once again, the superiority of the sol-gel method is demonstrated by the observation that the sol-gel derived sample gives almost 100 % conversion at all space velocity, ranging from 2.5 to 15 h<sup>-1</sup> (Fig. 4.9 B, curve a). On the other hand, over the co-precipitated sample, there is a sharp decline in the activity with increase in the space velocity. Similarly, the temperature also shows a favourable

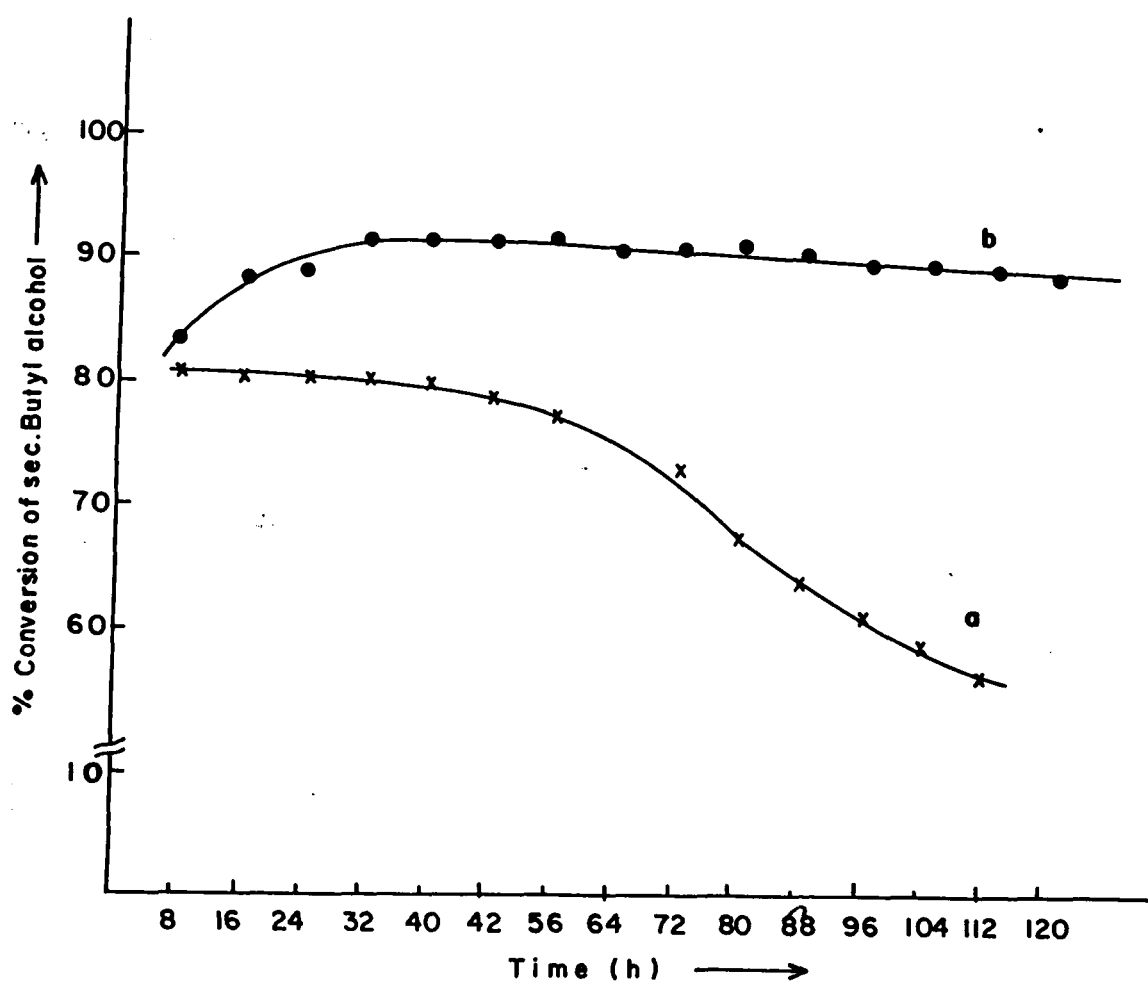


Fig. 4.8: Variation in the percentage conversion of secondary butyl alcohol with reaction time on Cu-SiO<sub>2</sub> catalyst prepared by co-precipitation (a) and sol-gel method (b).

influence on the sol-gel derived sample relative to that of co-precipitated sample. . (Fig. 4.9 A, curve a and b, respectively).

Effect of temperature on the selectivity to aniline during the hydrogenation of nitrobenzene is depicted in Fig. 4.10 A. The temperature plays a crucial role in controlling the structure sensitivity of the catalysts, and therefore, influences the selectivity. Up to 220 K, both the catalysts have almost similar selectivity. However, above 220 K, the sol-gel Cu-SiO<sub>2</sub> shows selectivity up to 99.5 % (curve b) whereas, the co-precipitated sample shows a decline in the selectivity (98.5 %). The influence of temperature on the selectivity is mainly due to the difference in the crystallite sizes of the sample (Table 4.2). The effect of reaction time on the selectivity is indicated in Fig. 4.10 B. Once again, the sample prepared by sol-gel method shows better selectivity (100 %) (curve b), while the latter sample shows a decline in selectivity after about 72 h..

The meritorious effects of sol-gel derived catalysts are due to its ability in controlling the crystallite size of the metal, metal area and, the sintering inhibition properties. This is illustrated by Fig. 4.11, where a comparison of crystallite size (XRD) of the two representative sample, before and after reaction. It can be seen that, in the sol-gel derived copper - silica, the crystallite size remains intact even after using it for more than 200 hours, which is not the case with co-precipitated catalysts. Thus the agglomeration of the crystallites are hindered in sol-gel derived samples. To explain the cause of stabilization of high surface area of the support and smaller metal crystallites a simple two dimensional "*restricted grain growth model*" is proposed.

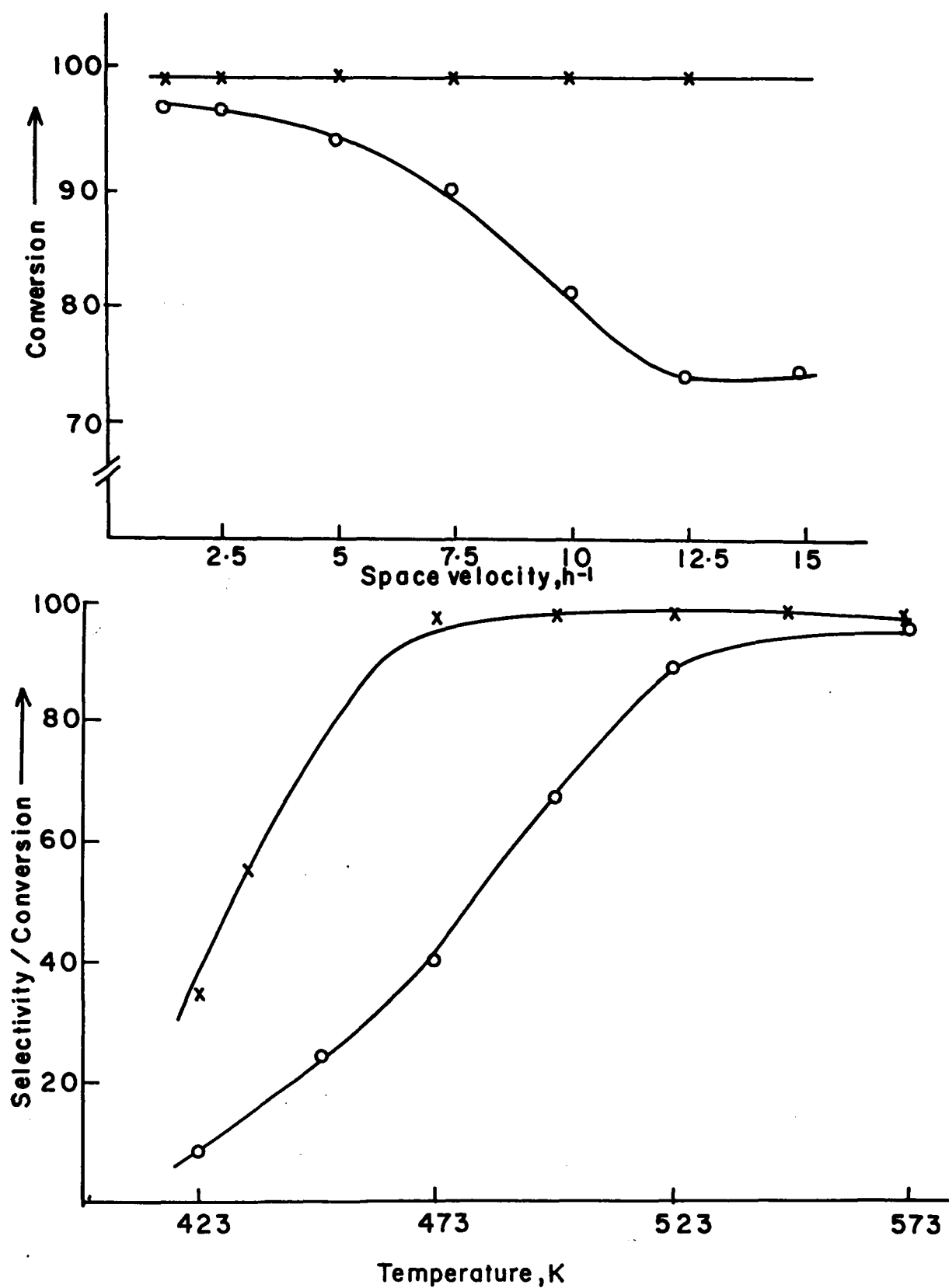


Fig. 4.9: Effect of temperature (A) and space velocity (B) on the conversion of nitrobenzene over  $\text{Cu-SiO}_2$  catalysts with 20 wt % of Cu loading prepared by sol-gel method (a) and co-precipitation method (b).

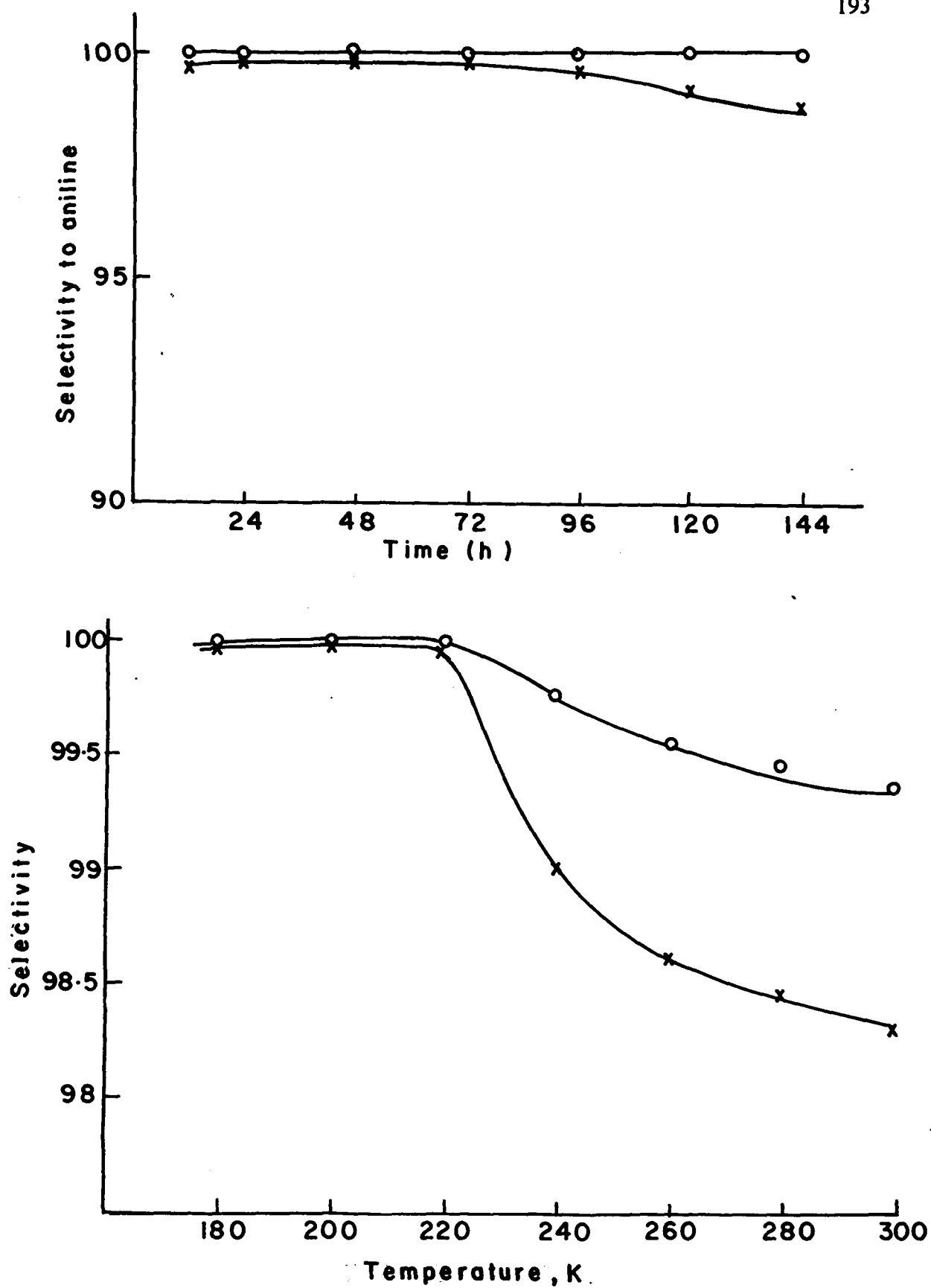
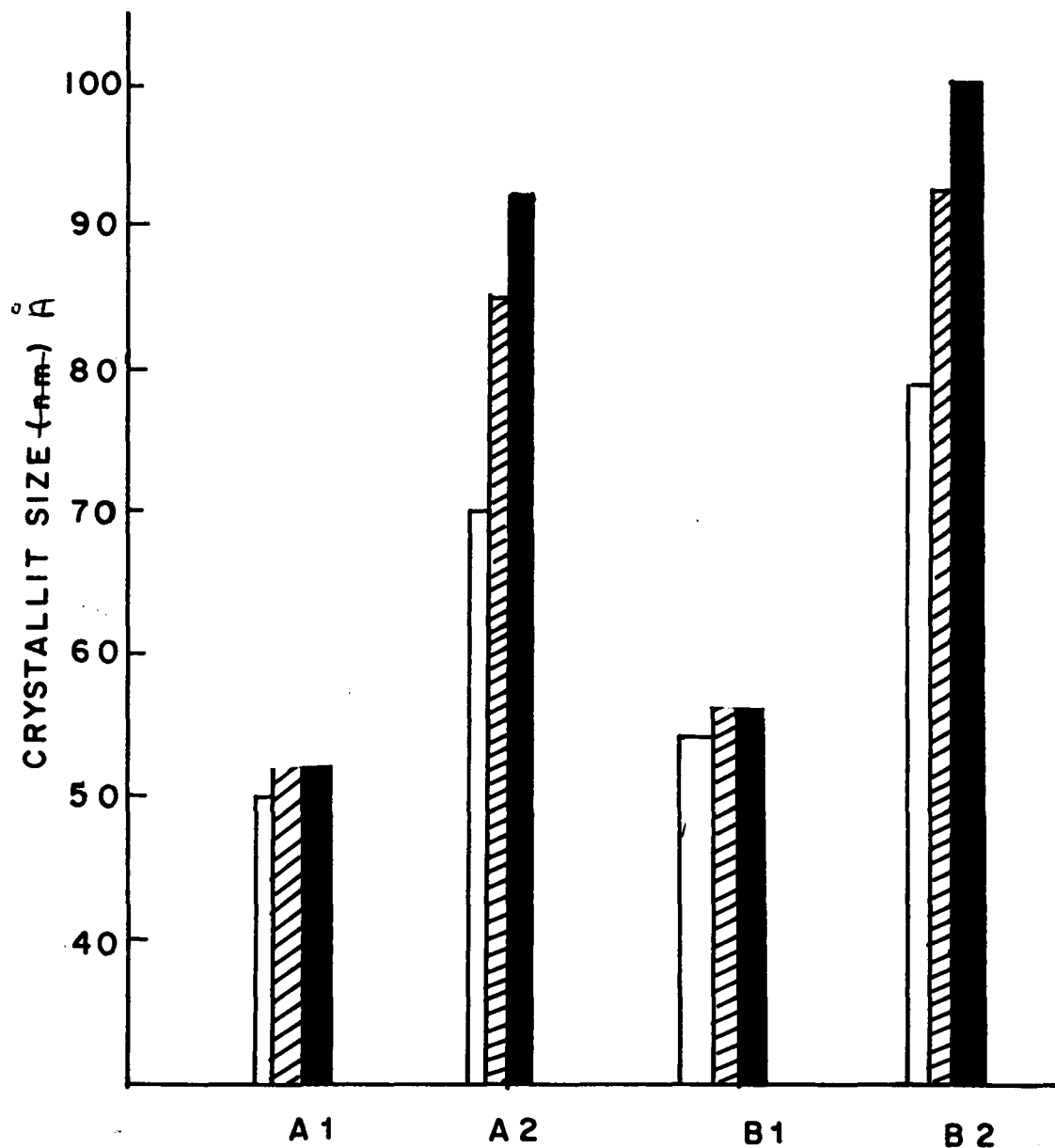
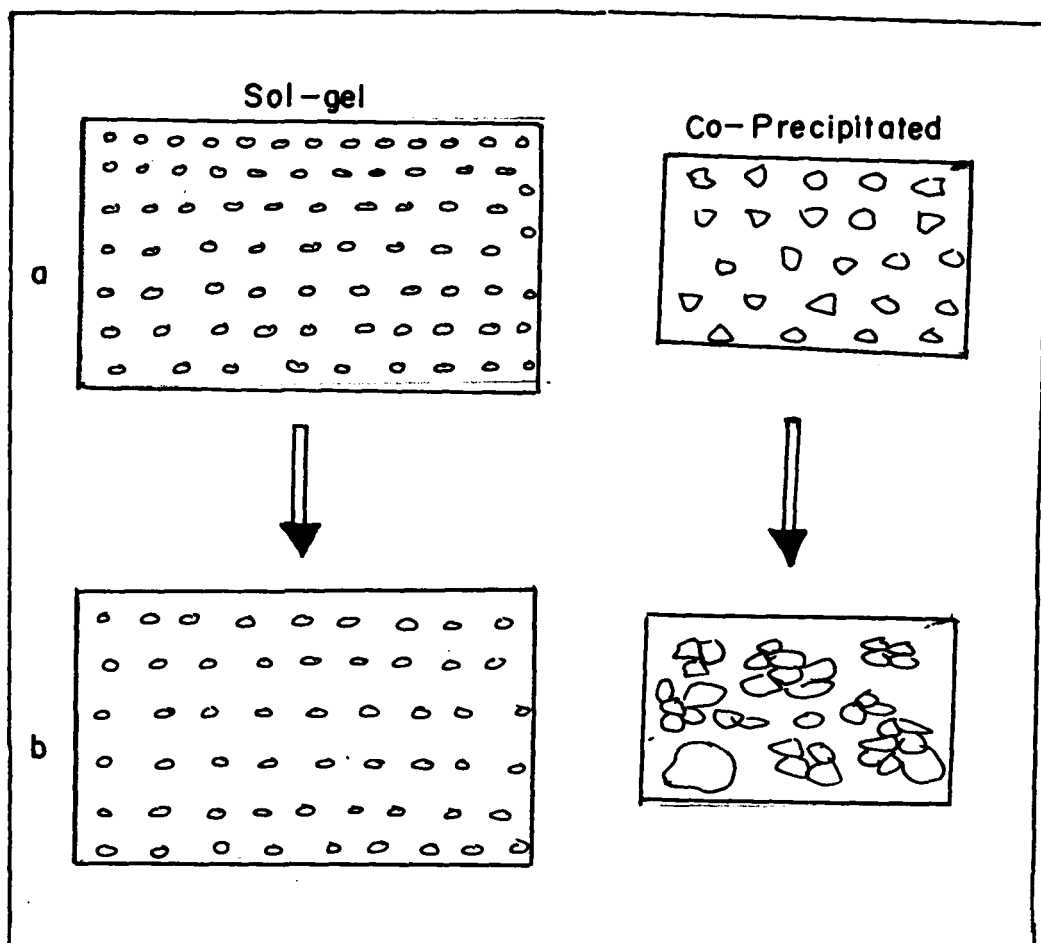


Fig. 4.10 : Effect of temperature (A) and time on stream (B) on the selectivity to aniline during the hydrogenation of nitrobenzene over Cu-SiO<sub>2</sub> with 20 wt % of Cu prepared by co-precipitation method (a) and sol-gel method (b).



**Fig 4.11 :** A comparison of crystallite size of Cu-SiO<sub>2</sub> with 20 and 30 wt % of Cu before reaction (white), 100 h after reaction (shaded) and 200 h after reaction (dark). A1 and A2 refer to samples prepared by sol-gel and Co-ppt method with 20 wt % of Cu; B1 and B2 refer to corresponding samples with 30 wt % of Cu.



**Fig. 4.12 :** Two dimensional schematic diagram of proposed *restricted grain growth model*; a and b refer to the status of the metal crystallites before and after hydrogenation reaction.



### ***4.3.6. Restricted grain growth model***

The activity and selectivity of supported copper catalyst prepared by sol-gel method can be explained in terms of restricted grain growth model. According to this model, both the *support* as well as the *metal* plays a crucial role. The sol-gel method of preparation enables one to get support, silica in the present case, with high surface area. In addition, it also leads to smaller crystallites. Due to these two-fold benefits of the sol-gel method the ability of the metal to resist sintering increases unlike the case of conventionally prepared catalysts. This can be better understood by looking at Fig. 4.12 which represents a two dimensional view of restricted grain growth model. Fig. 4.12 a shows that even after a long term use under hydrogen flow at reaction temperature, the Cu crystallites are separated well apart, mainly due to the high surface area and smaller crystallite size of the sol-gel derived catalysts. In contrast, the catalysts prepared by co-precipitation method have lower surface area and bigger crystallites. Therefore during the continuous exposure to hydrogen under severe temperature conditions, these crystallites tend to agglomerate together thereby causing decrease in metal area.

## **4.4. SUMMARY AND CONCLUSION**

Sol-gel method is found to be one of the most suitable methods for preparing supported metal catalysts with smaller crystallite size and larger surface area. In particular, mesoporous Cu-silica sample with pore diameter of around 40 - 60 Å and crystallite size ranging from 45 - 60 Å is obtained by this method. The TPR data indicates the ease of reducibility of the sol-gel derived catalysts, probably due to the

well dispersed metal crystallites. All these advantages are further supported by the utility of these catalysts in hydrogenation and dehydrogenation reactions. In conclusion, sol-gel method of preparation is a beneficial method for developing industrial supported metal catalysts. Further investigations with the influence of several preparation conditions, optimization of metal loading, etc would be interesting.

## References

1. M. Ebleman, *Ann. Chim. Phys.*, **16** (1846) 129.
2. R. Roy, *Science*, **238** (1987) 1664.
3. J. Livage, M. Henry and C. Sanchez, *prog. Solid State Chem.*, **18** (1988) 259.
4. M. Azomoza, T. Lopez, R. Gomez, and R. D. Gonzalez, *Catal. Today*, **15** (1992) 547.
5. R. Tleimat-Manzolji, T. Manzolji and G. M. Pajong, *J. Non-Cryst Solids*, **147** (1992) 744.
6. L. K. Campbell, B. E. Na, and E. I. Ko, *Chem. Mater.*, **4** (1992) 1329.
7. D. A. Ward, and E. I. Ko, *Chem. Mater.*, **5** (1993) 956.
8. D. A. Ward, and E. I. Ko, *J. Catal.*, **150** (1994) 18.
9. A. Keshavaraja, V. Ramaswamy, H. S. Soni, A. V. Ramaswamy and P. Ratnasamy, *J. Catal.*, **157** (1995) 501.
10. A. Keshavaraja, S. G. Hegde and A. V. Ramaswamy, (Unpublished results).
11. C. Sanchez, and J. Livage, *New J. Chem.* **14** (1990) 513.
12. A. Keshavara, J. V. Samuel, and A. V. Ramaswamy (submitted for publication)
13. G. Cerrato, C. Morterra, G. M. Pajonk, F. Pinna, M. Signoretto and G. Strukul, *Proc. First World Conference on Environmental Catalysis, Pisa, May 1995*.
14. D. L. Trimm, in *Design of Industrial Catalysts, Chemical Engineering Monographs - II*, Elsevier, Amsterdam, 1980.
15. T. A. Doorling, B. W. J. Lynch and R. L. Moss, *J. Catal.*, **20** (1971) 190.
16. J. M. Dartiques, A. Chambellan, S. Corolleur, F. G. Gault, A. Renouprez, B. Moraweck, P. Bosch and G. Dalmai-Imelik; *Nouv. J. Chem.* **3** (1979) 691.
17. P. Bosch, D. Acosta, J. Zenith, D. M. Nicolson and B. C. Gates, *J. Mol. Catal.*, **31** (1985) 73.
18. T. Lopez, P. Bosch, M. Asomoza and R. Gomez, *J. Catal.*, **133** (1992) 247.
19. T. Lopez, J. Mendez, T. Zamudio, and M. Villa, *Mater. Chem. Phys.* **30** (1992) 161.
20. T. Lopez, M. Moran, J. Navarrete, L. Herrera and R. Gomez, *J. Non-Cryst. Solids*, **147** (1992) 773
21. Y. A. Ryndin, M. Stenin, A. Boronin, V. Bukhtiyarov and E. Zairovssky, *Appl. Catal.* **54** (1989) 277.
22. E. Ruckenstein and B. Pulvermacher, *J. Catal.*, **29** (1973) 224.
23. E. Ruckenstein and B. Pulvermacher, *J. Catal.*, **37** (1975) 416.
24. T. Lopez, M. Asomoza, P. Bosch, E. Garcia-Figuera and R. Gomez, *J. Catal.*, **138** (1992) 463.
25. W. Zou, R. D. Gonzalez, *Catal. Lett.*, **12** (1992) 73.
26. T. Lopez, P. Bosch, M. Asomoza and R. Gomez, *J. Catal.*, **133** (1992) 247.
27. S. Fuentes and F. Figueras, *J. Catal.*, **74** (1978) 997.;
28. Z. Karpinski, J. B. Butt and W. M. H. Sachtler, *J. Catal.*, **119** (1989) 521.

29. T. Lopez, P. Bosch, J. Navarrete, M. Asomoza and R. Gomez, *J. Sol-gel Sci. and Tech.*, **1** (1994) 193.
30. T. Lopez, P. Bosch, M. Moran and R. Gomez, *J. Phys. Chem.*, **97** (1993) 1671.
31. E. G. M. Kuipers, R. B. Tjepkema, W. J. J. van der wal, C. M. A. M. Mesters, S. F. G. M. Spronck and J. W. Geus, *Appl. Catal.*, **25** (1986).
32. M. Kobayashi, N. Takezawa, C. Minochi and N. Takahashi, *Chem. Lett.*, (1980) 1197.
33. K. Takahashi, N. Takazawa, and H. Kobayashi, *Appl. Catal.*, **2** (1982) 363.
34. D. M. Monti, M. S. Wainwright, D. L. Trimm and N. W. Cant, *Ind. Eng. Chem. Prod. Res. Dev.* **24** (1985) 397.
35. 139. D. W. Monti, N. W. Cant, D. L. Trimm and M. S. Wainwright, *J. Catal.*, **100** (1986) 17.
36. K. Klier, *Adv. Catal.*, **31** (1983) 243.
37. F. Pepe, C. Angletti, S. De Rossi and M. Lo. Jacono, *J. Catal.*, **91** (1985) 69.
38. C. A. Leon y Leon and M. A. Vannice, *Appl. Catal.*, **69** (1991) 291.
39. C. A. Leon y Leon and M. A. Vannice, *Appl. Catal.* **69** (1991) 269.
40. J. L. Robbins, E. Iglesia, C. P. Kelkar and B. Dekites, *Catal. Lett.*, **10** (1991) 1.
41. M. J. Sandoval and A. T. Bell, *J. Catal.*, **144** (1993) 227.
42. J. T. Wehrli. D. J. Thomas, M. S. Wainwright and D. L. Trimm, *Appl. Catal.*, **70** (1991) 253.
43. B. R. Strohmeirer, D. E. Leyden, R. S. Field and D. M. Hercules, *J. Catal.*, **94** (1985) 514.
44. M. C. Marion, E. Garbowski and M. Primet, *J. Chem. Soc. Farad. Trans.*, **86** (1990) 3027.
45. R. M. Friedman and F. W. Lytle, *J. Catal.*, **55** (1978) 10.
46. Kirk-Othmer Encyclopaedia, Vol-2 (4<sup>th</sup> Edition), Wiley Interscience
47. O. C. Karkalitis, S. M. Vanderwaart and F. Houghton, U.S. Pat 2,891,094 (1959)
48. K. Pilch and H. Sperber, U. S. Pat 3,538,018 (1970).
49. H. Thelen and K. Halcour, US Pat. 3,882,048 (1975).
50. U. Birkenstock, B. Lachmann, J. Metten and H. Schmidt., US Pat., 4,265,834 (1981).
51. J. March, *Advances in Organic Chemistry : Reaction mechanism and structure*, 3<sup>rd</sup> edition, John Wiley, New York (1985) p-1103.
52. P. Rylander, *Catalytic Hydrogenation over platinum metals*, Academic Press Inc., New York, (1967) p-168.
53. T. Cole, R. Ramage, C. Cann and R. Pettit, *J. Amer. Chem. Soc.*, **102** (1980) 6182.
54. N. A. Cortesse, R. F. Heck, *J. Org. Chem.*, **42** (1977) 3491.
55. D. C. Dittmer and J. M. Koyler, *J. Org. Chem.* **27** (1962) 56.
56. E. A. Braude, R. P. Linsted and P. W. D. Mitcheell, *J. Chem. Soc.*, (1954) 3578.
57. G. Brieger, T. J. Nestrick and T. H. Fu, *J. Org. Chem.*, **44** (1979) 1876.
58. N. Takezawa, M. Shimokawabe, H. Hiramatsu, H. Sugiura, H. Asakawa and H. Kobayashi, *React. Kinet. Catal. Lett.* **33** (1987) 191.

59. G. K. Boreskov, in proceeding of the sixth international congress on catalysis, London, Chemical Soc. London, 1976, p-204.
60. L. Petrov, K. Kumbilieva, N. Kirkov, *Appl. Catal.*, **59** (1990) 31.
61. M. Mukherji, *Chem. Eng. World*, **4** (1992) 91.
62. A. Sing and N. R. Narayanan, *Chem. Eng. World*, **4** (1992) 87
63. J. W. E. Coenen, B. G. Linsen, in B. G. Linsen (Ed), Physical and chemical aspects of adsorbents and catalysts, Academic Press, New York.
64. K. S. W. Sing, D. H. Everette, R. A. W. Haul, L. Moscou, R. A. Pierotti, J. Rouquerol, T. Siemieniewska, *Pure and Appl. Chem.*, **57** (1985) 603.
65. R. C. Weast, *Hand book of chemistry and physics*, 63<sup>rd</sup> Ed., CRC Press, Boca raton, 1982
66. J. Van der Berg, J. A. Van Dillen, J. Vander Meyden and J. W. Geus, in G. P. Bonnelle, B. Delmon, and E. Derouane, (Eds), Surface properties and catalysis by non-metals, NATO ASI series, Reidel, Dordrecht, 1983, p-493.

## CHAPTER FIVE

# Sol-gel derived Metallosilicate Catalysts

---

Amorphous analogs of crystalline titanium and aluminium silicates are dealt with in this chapter. Amorphous titanium silicates prepared at different pH values and at neutral pH were characterized by FTIR, UV-Vis and other spectroscopic techniques. Generation of isolated active sites and their role in catalytic activity are discussed. Similarly, the sol-gel derived aluminosilicates prepared under neutral and basic conditions are compared with respect to their acidic and catalytic properties.

---

*A part of this chapter is published in J. Catal. 157 (1995) 501., and a part is submitted to J. Catal. for publication.*

## ***Objectives of Chapter-Five***

The present chapter is divided into five sections. Section 5.1 gives a brief introduction. In the section 5.2, an attempt is made to understand the role of pH during the preparation of titanium silicates by sol-gel method, on their physico-chemical properties. This is accomplished by correlating the pH of the sol-gel processing with the textural properties, coordination of Ti species and acidic properties of the material through adsorption isotherms, UV-visible, SEM, TEM and FTIR studies. An attempt is also made to quantitatively estimate the isolated Si-O-Ti linkage, surface hydroxyls and the extent of the pyridine adsorption on the prepared samples, as a function of pH during the preparation. Section 5.3 deals with the synthesis of micro-mesoporous, amorphous titanosilicates (designated as MMATS) in the absence of nitrogenated organic bases.<sup>55</sup> These materials are able to oxyfunctionalize organic molecules with aqueous H<sub>2</sub>O<sub>2</sub>, with an activity and selectivity somewhat similar to those of TS-1. MMATS have been additionally characterized by x-ray diffraction/scattering, ESCA, IR/UV-Vis/Raman spectroscopies, SEM, TG/DTA, TPR, <sup>29</sup>Si MAS-NMR and sorption (argon, water, benzene, cyclohexane, mesitylene, 1,3,5-tri-isopropyl benzene) techniques. Section 5.4 deals with systematic study of the properties of amorphous aluminosilicates prepared under basic (pH = 8) and neutral pH conditions. Particularly, the role of pH in controlling the acidic properties and its consequences on catalytic properties in the isomerization of 1,3,5-trimethylbenzene was studied. Section 5.5 summarizes the whole chapter.

---

## 5.1

# INTRODUCTION

---

The introduction of aluminosilicate zeolites as catalysts in the early sixties had a significant impact on industrial catalysis. Since then, small pore (erionite), medium pore (ZSM-5) and large pore (faujasites, mordenite, L and beta) zeolites have been used extensively for various (mainly acid-catalyzed) chemical transformations. The recent entry of titanium in the area of zeolites has attracted a great deal of attention. More particularly, in the early eighties, the advent of titanosilicate molecular sieve, TS-1, with MFI structure represented the next major innovation and this enabled shape-selective oxidations to be carried out on an industrial scale<sup>1</sup>. Subsequently, other titanosilicate molecular sieves like TS-2 (MEL)<sup>2</sup>, TS-48 (the titanium analog of ZSM-48)<sup>3</sup> and TS-beta (titano-aluminosilicate analog of zeolite beta)<sup>4,5</sup> were synthesized broadening the scope of oxidation catalysis with molecular sieves. Among these, titanium silicate molecular sieves, TS-1 and TS-2, are an interesting class of compounds capable of catalyzing several oxidation reactions.<sup>6,7</sup> All these materials are microporous with an average pore radius less than 1.0 nm, thereby imposing a constraint on the size of the organic substrate that can be oxyfunctionalised. Apart from these, mesoporous molecular sieves are also among the attractive materials in the focus of research. For example, very recently, Tanev et al.<sup>8</sup> announced the synthesis of titanium-containing hexagonal mesoporous silica (Ti-HMS) with a pore diameter of



around 2.8 nm possessing significant catalytic activity in the oxidation of bulky molecules like 2,6-ditert-butyl phenol. Almost simultaneously, Corma *et al.*<sup>9</sup> and Franke *et al.*<sup>10</sup> reported the preparation and properties of Ti-containing MCM-41. Its catalytic utility in the oxidation of alpha terpineol and norbornene using tert-butyl hydroperoxide as the oxidant has also been reported.<sup>9</sup> A common characteristic of all the titanosilicate molecular sieves mentioned above, including Ti-HMS, is that they are all crystalline materials prepared in the presence of nitrogenated organic bases.

Amorphous variants of crystalline titanium silicates i.e., TiO<sub>2</sub>-SiO<sub>2</sub> mixed oxides have been extensively used as catalyst supports,<sup>11-13</sup> as ceramic materials<sup>14-17</sup> and as catalysts.<sup>18-22</sup> An interesting feature of these catalysts is their redox properties. Thus, the possibility of tuning them as oxidation catalysts by the proper control of preparation methods has recently led to serious research activities all over the world. By varying any one of the preparation parameters such as solvents, alkoxide to water ratio, temperature, pH, stirring and complexing agents, it is possible to vary properties including catalytic activity.

For example, recently, Toba *et al.*<sup>23</sup> have compared different methods of preparation of titania-silicas (Si/Ti = 0.5 - 25) and concluded that those prepared using diols as complexing agents are more homogeneous and yield materials with significant amount of Ti-O-Si bond. However, there is no mention in their report of the most important behaviour, namely, their catalytic activity. Also, among the various preparation parameters, the role of pH during the preparation in controlling the catalytic properties is not well understood.

Another class of materials of importance in the frontier area of research during pre-zeolite era and which still continues to be the centre of attention due to their

widespread utility as solid acid catalysts is amorphous aluminosilicates.<sup>24-41</sup> The major reason for their popularity can be attributed to the flexibility of designing and developing them as novel catalyst materials by altering the preparation parameters. For example, changing the amount of alumina content or using different types of additives during the preparation results in materials with distinct properties.<sup>42-53</sup> In contrast to the conventional method of preparation of aluminosilicates, these techniques of preparation have opened up new vistas. This combination of the old and the new techniques involves either the impregnation of aluminium salt on silica gel and calcination or the co-precipitation of the silica sol and an aluminium salt as mixed hydroxides, followed by drying and calcination. Particularly, it is the entry of the sol-gel chemistry that yields known materials with novel properties and applications.<sup>47-53</sup>

The advent of sol-gel research in catalyst preparation has led to the development of nano composites which are low density and porous materials with high surface areas.<sup>52</sup> The interesting observation in the sol-gel method of preparation is that a minor change in the use of starting substances or temperature of gelation or the mode of addition of solvent drastically alters the properties of the prepared materials. Recent investigations have shown that the catalytic activity of amorphous alumino-silicates depends greatly on the amount of alumina present in them.<sup>45</sup> However, no systematic investigations have been made on the effect of pH of sol-gel preparation on the acidity and catalytic activity of amorphous aluminosilicates.

---

## 5.2

# AMORPHOUS TITANO-SILICATES PREPARED AT DIFFERENT pH

---

### 5.2.1. WHY AT DIFFERENT pH ?

As discussed in the introduction, pH is one of the important parameters to be considered while preparing any material by the sol-gel technique. A small change in the pH drastically affects the physico-chemical characteristics of the materials and thus their catalytic properties. Therefore it is necessary to choose the right pH depending on the requirements. A comparison of the series of titanium silicates prepared by sol-gel method at different pH would give a broad view of the importance of pH in catalyst design.<sup>54</sup>

### 5.2.2. EXPERIMENTAL

#### 5.2.2.1. *Preparation*

A series of samples of titanium silicates with Si/Ti ratio of 17 were prepared at pH values ranging from 1 to 13. The procedure involves hydrolysis and condensation of stoichiometric mixtures of tetraethyl orthosilicates and titanium isopropoxide separately at different pH conditions by using nitric acid or deionised water or ammonium hydroxide as required, along with the necessary quantity of water and isopropanol mixture and kept for periods ranging from 4 to 24 h to get a gel. The

molar ratio of titanium isopropoxide (TiIP), tetraethylorthosilicate (TEOS), water and isopropyl alcohol is 17 : 1 : 71 : 18. The gel was dried under reduced pressure ( $\approx 1$  torr) at 353 K for 24 h and calcined at 773 K for 8 h to get the final product.

#### ***5.2.2.2. Characterization***

The specific surface area, mean cylindrical pore diameter and pore volume were determined by the BET method from the  $N_2$  adsorption isotherms at 77 K as determined in an 'Omnisorp 100 CX' surface area analyzer. BET surface areas were calculated in a relative pressure range between 0.05 and 0.2 assuming a cross sectional area of  $0.162 \text{ nm}^2$  for the nitrogen molecule. The pore size distribution was calculated by applying the BJH model<sup>57</sup> in the mesopore region and the Horwath-Kawazoe model<sup>58</sup> in the micropore region.

UV-visible spectra were recorded on a 'Shimadzu UV-2101PC' scanning spectrophotometer equipped with an integral sphere using  $BaSO_4$  as a reference. FTIR spectra were recorded with a Nicolet 60 SXB spectrometer. For the spectrum in the framework region, a sample with KBr (1:300) was pressed in to pellets. Its spectrum was recorded with  $4 \text{ cm}^{-1}$  resolution and averaged over 100 accumulations. The acidic properties were evaluated by pyridine adsorption on self supported wafers ( $4\text{-}9 \text{ mg/cm}^2$ ) in an IR cell equipped with greaseless stopcocks and KBr windows. The samples were outgassed at 673 K and  $10^{-6}$  torr for 4 h, cooled to 323 K and their spectra were recorded by averaging over 500 scans. The samples were equilibrated with pyridine vapour (10 mm) and excess pyridine was removed by evacuation at 323, 373 and 423 K before recording the spectrum. The scanning electron micrographs of

samples were taken with a 'Jeol Model 5200' instrument. The transmission electron micrographs and the selected area electron diffraction patterns of the samples were taken with a Jeol (model 1200 EX) electron microscope.

## 5.2.3. RESULTS AND DISCUSSION

### 5.2.3.1. $N_2$ adsorption studies

Surface area, t-area and pore volumes of titanium silicates prepared by the sol-gel method at different pH values are presented in Table 1. The samples prepared under acidic conditions have surface areas in the range of 400-550  $m^2g^{-1}$  and there is a

**Table 5.1**

**Textural properties of titanium silicates prepared at various pH**

pH	Surface area ( $m^2 g^{-1}$ )	t-area ( $m^2 g^{-1}$ )	Pore volume ( $ml g^{-1}$ )	
			micropore	mesopore
1	550	64	0.20	0.04
3	437	84	0.17	0.08
5	418	172	0.16	0.15
7	484	205	0.12	0.23
9	419	317	0.01	0.27
11	75	73	-	0.17
13	41	40	-	0.08

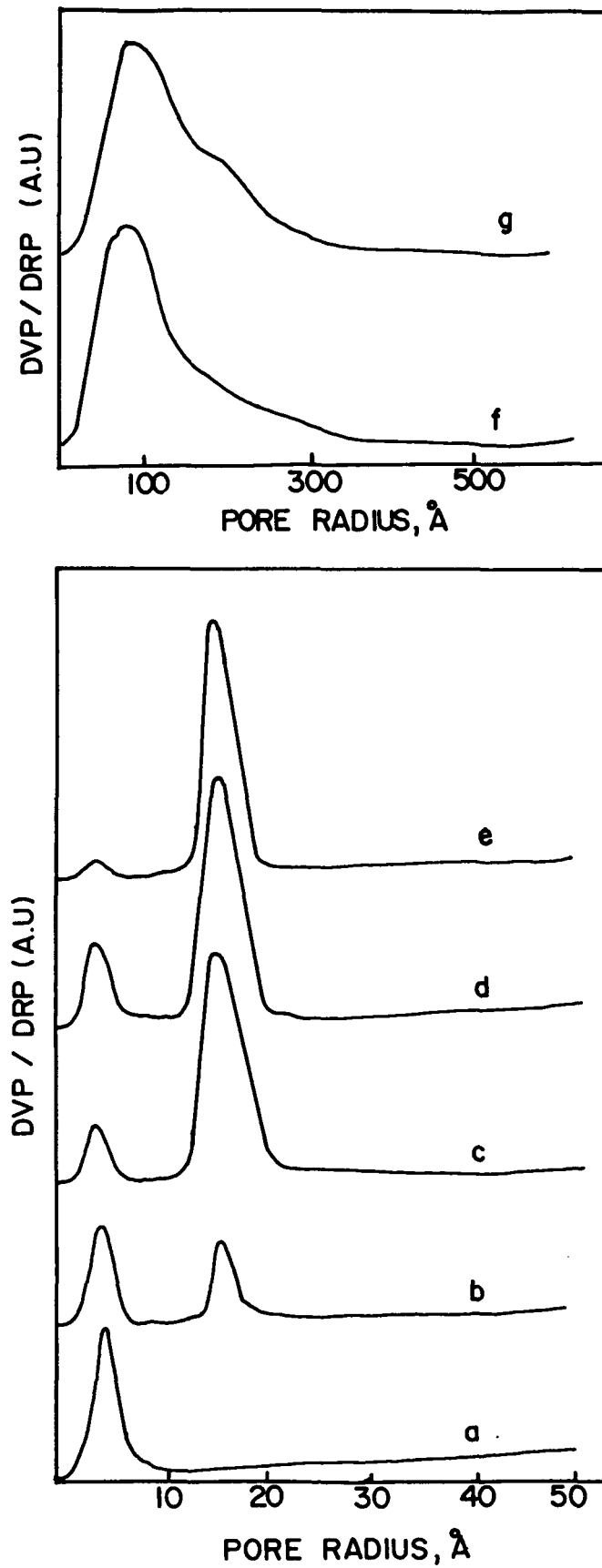


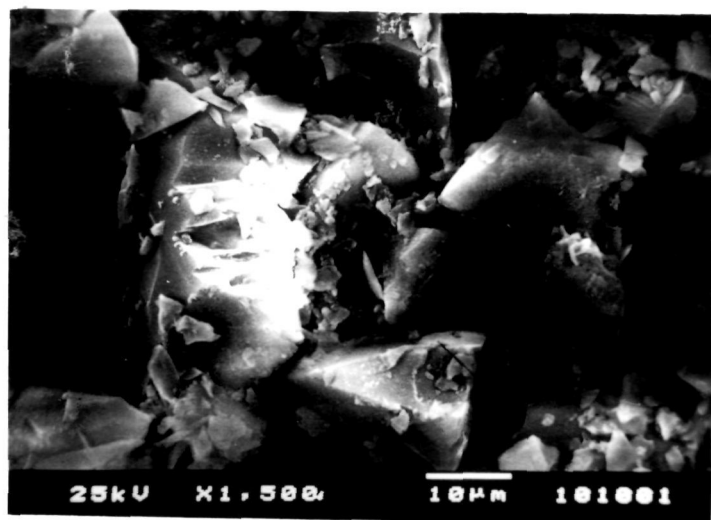
**Fig. 5.1 : Pore size distribution of titanium silicates prepared at different pH  
(curves 'a' to 'g' refers to pH 1,3,5,7,9,11, and 13, respectively)**

linear decrease in the surface areas as the pH is increased from 1 to 5. At neutral pH the surface area increases to  $484 \text{ m}^2\text{g}^{-1}$ . Under base catalyzed conditions, the surface area decreases drastically due to the total absence of micropores. But the mesopore area given by the t-plot increases up to a pH of 9. Thus pH seems to play a major role in controlling the surface area and nature of pores of these materials.

This is further illustrated by the pore size distributions (Fig. 5.1) of the various samples. The sample prepared at pH 1 contain predominantly micropores (curve 'a'), while those prepared at pH 3 to 7 have both micro and meso pores (curves 'b' to 'd'). However, under basic conditions, mesopores are present in considerable amount. Particularly, samples prepared at pH 11 and 13 have only mesopores (curves 'f' and 'g'). In the case of acid hydrolysis, gelation occurs with the formation of a linear chain polymer which on calcination yields micropores. In the case of base catalyzed hydrolysis,  $\text{OH}^-$  ion attacks  $\text{Si}^{4+}$  and  $\text{Ti}^{4+}$  in the Si-O-C and Ti-O-C bonds resulting in the formation of a 3D network which results in mesopores upon calcination.<sup>59</sup> Under neutral pH, hydrolysis is the rate determining step and condensation is also slow, resulting in bimodal pores. Apart from the porous properties, the pH of the sol-gel preparation also influences the particle morphology.

### ***5.2.3.2. Scanning Electron Microscopy***

The Scanning electron micrographs of the samples prepared at pH 1, 7 and 13 are presented in Fig. 5.2. Dense and agglomerated particles are observed in the sample prepared at acidic pH (pH 1) [A]. On the other hand, at very high pH (pH 13) the particles attain an elongated shape [C] with particle size ranging from 1 to 3 microns. At neutral pH conditions, the particles are fairly uniform in size [B] ( $\approx 2$  microns).



b

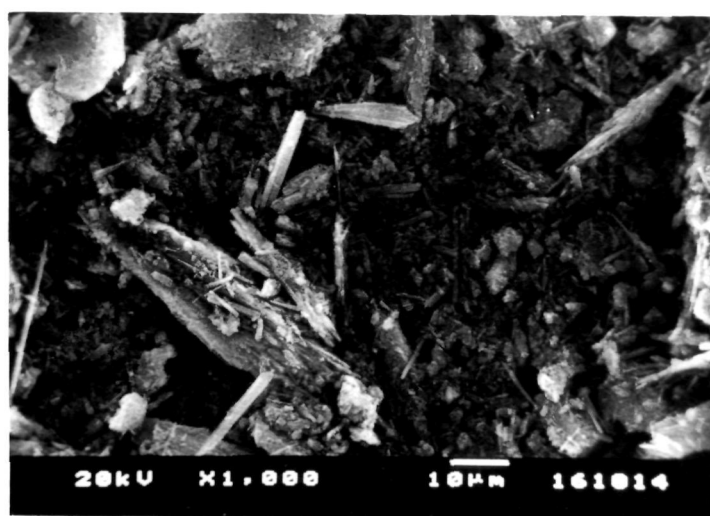
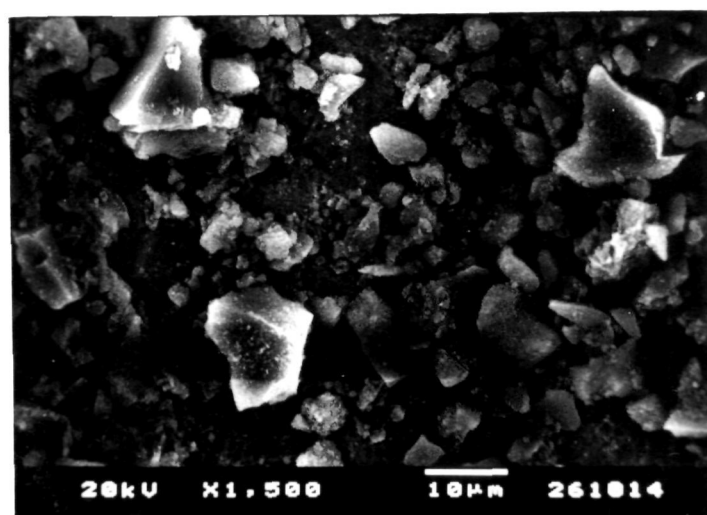


Fig. 5.2: Scanning electron micrographs of the samples prepared at pH 1, 7 and 13 (a, b and c, respectively)



### ***5.2.3.3. TEM and Electron Diffraction***

The effect of pH on the texture and morphology and long range order of the samples can be understood from the transmission electron micrographs samples and the corresponding electron diffraction patterns of the representative samples (Fig. 5.3). The sample prepared at neutral pH shows a halo pattern while two samples prepared at pH 5 and 9 correspond to the electron diffraction patterns of the anatase and rutile phases. The morphology of the sample prepared under neutral pH conditions possesses a uniform particle size.

### ***5.2.3.4. UV-visible spectra***

The coordination spheres of  $Ti^{4+}$  in the sample is one of the important characteristics in the application of these titanium silicates as catalysts. In the present case, it is influenced by the pH conditions of preparation as seen from the UV-vis DR spectra of the representative samples (Fig. 5.4). The sample prepared at neutral conditions has a peak maxima on the relatively higher energy side (curve 'a') compared to that of samples prepared at the other two extreme pH conditions. As the pH increases to 13, the tendency to acquire an octahedral coordination increases as indicated by the band around 330-350 nm in the UV-Visible spectra (curve 'c'). Although, the titanium content is the important parameter that decides the coordination, in the present case, it is to be inferred that the pH of the preparation conditions also plays a prominent role in the design of the titanium silicate catalysts with the desired coordination.

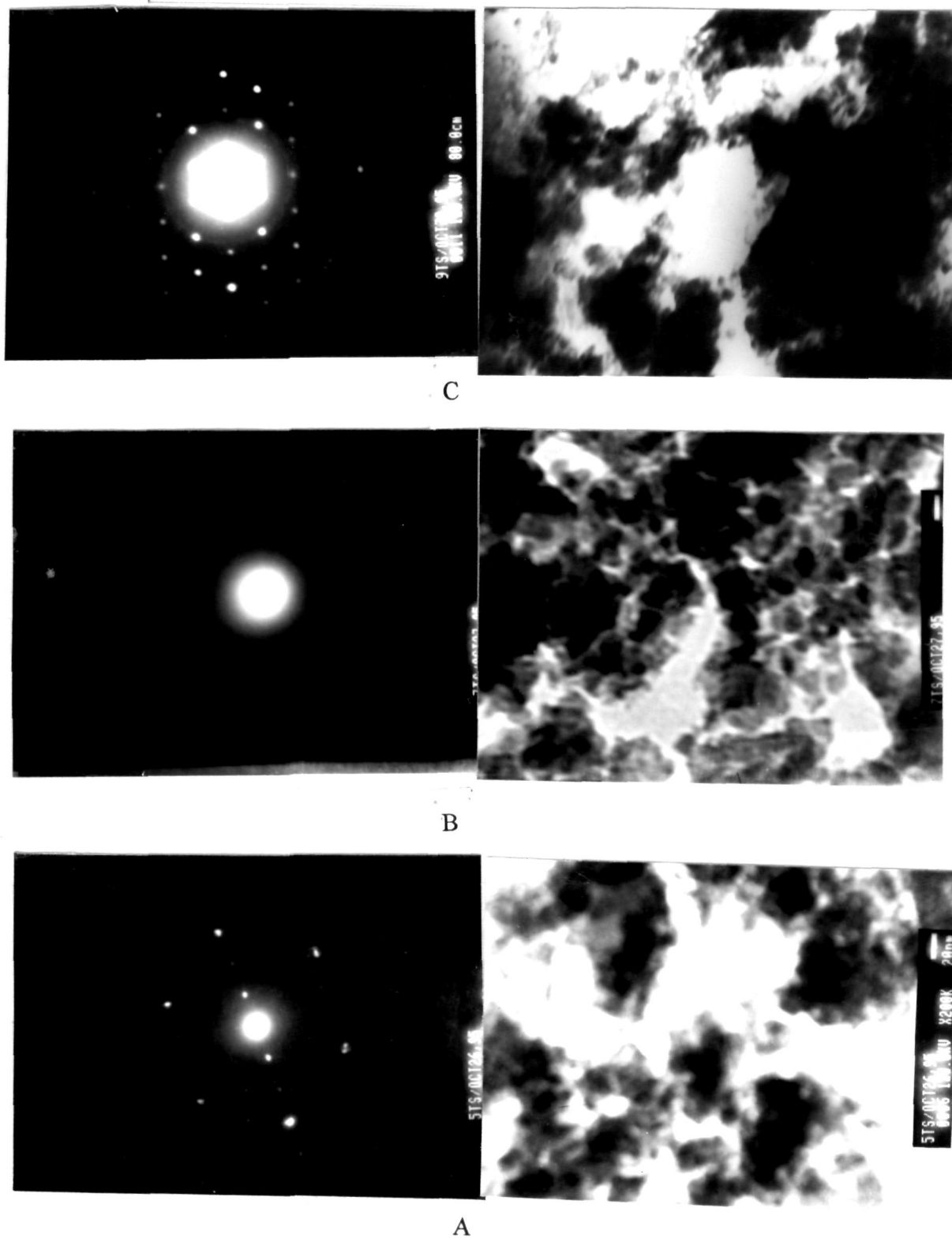
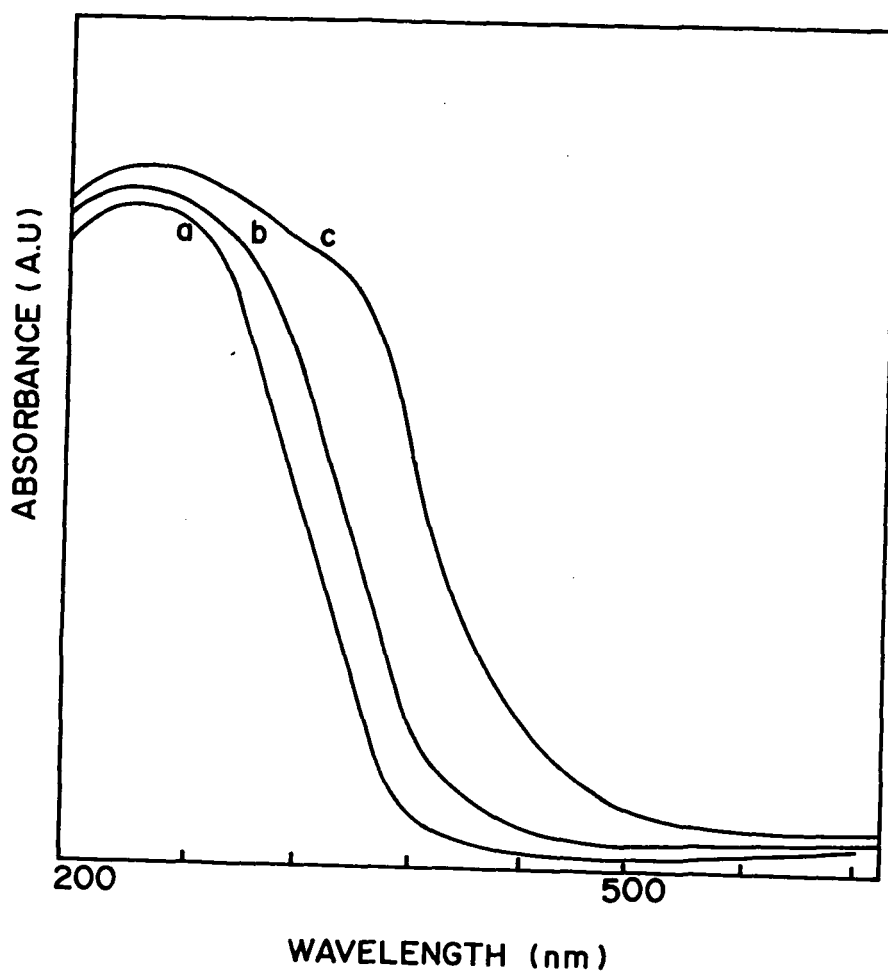


Fig. 5.3: Electron diffraction patterns and corresponding transmission electron micrographs of titanosilicates prepared at pH 5, 7 and 9 (A, B and C, respectively)



**Fig. 5.4: UV-visible spectra of titanium silicate samples prepared at pH 7, 1 and 13 ( curves a, b, and c, respectively)**

### 5.2.3.5. FTIR in framework vibration region

The FTIR spectra of titanium silicate samples prepared by the sol-gel method can give valuable information about the dispersion of  $\text{TiO}_2$ .<sup>18, 60-63</sup> There are three main absorption regions which are assigned to the asymmetric, symmetric and the corresponding deformation vibrations of (Ti)Si-O-Si(Ti) stretching.

In the spectra of the samples (Fig. 5.5) there are peaks at 960 (m), 1080 (s) and 1220  $\text{cm}^{-1}$  (sh) in the asymmetric region, at 810  $\text{cm}^{-1}$  (m) in symmetric region and at 575 (sh) and 475  $\text{cm}^{-1}$  (s) in the deformation vibration region. Incorporation of  $\text{TiO}_2$  in  $\text{SiO}_2$  matrix is characterized by a band at 960  $\text{cm}^{-1}$  for titanium substituted silicalites<sup>64</sup> and at 940-950  $\text{cm}^{-1}$  for  $\text{SiO}_2$  -  $\text{TiO}_2$  gels.<sup>65-67</sup> The presence of the distinct peak at 960  $\text{cm}^{-1}$  is clearly observed in all the samples. However, for better evaluation of the FTIR results, attempt to deconvolute the composite spectrum in 1450-650  $\text{cm}^{-1}$  region was made according to the procedure described by Dutoit *et al.*<sup>60</sup> By applying the FOCAS deconvolution programme (Nicolet) and by choosing 1402, 1296, 1211, 1089, 954 and 806  $\text{cm}^{-1}$  as the starting peak values, the spectrum was deconvoluted into Gaussian curves. The deconvolution band positions were observed at 800 - 810, 950-960, 1070-1080 and 1207-1220  $\text{cm}^{-1}$ . The individual deconvoluted curves (curve a) and the original spectra of a representative sample (prepared at pH 7) (curve b) are given in Fig. 5.6 for illustration. Further, the ratio of peak intensity of Si-O-Ti band (960  $\text{cm}^{-1}$ ) to that of Si-O-Si band (1220  $\text{cm}^{-1}$ ) which is defined as Si-O-Ti connectivity or Ti dispersion was calculated. This connectivity ratio is plotted against the pH of the preparation condition of the sol to gel transformation, which is depicted in Fig. 5.7.

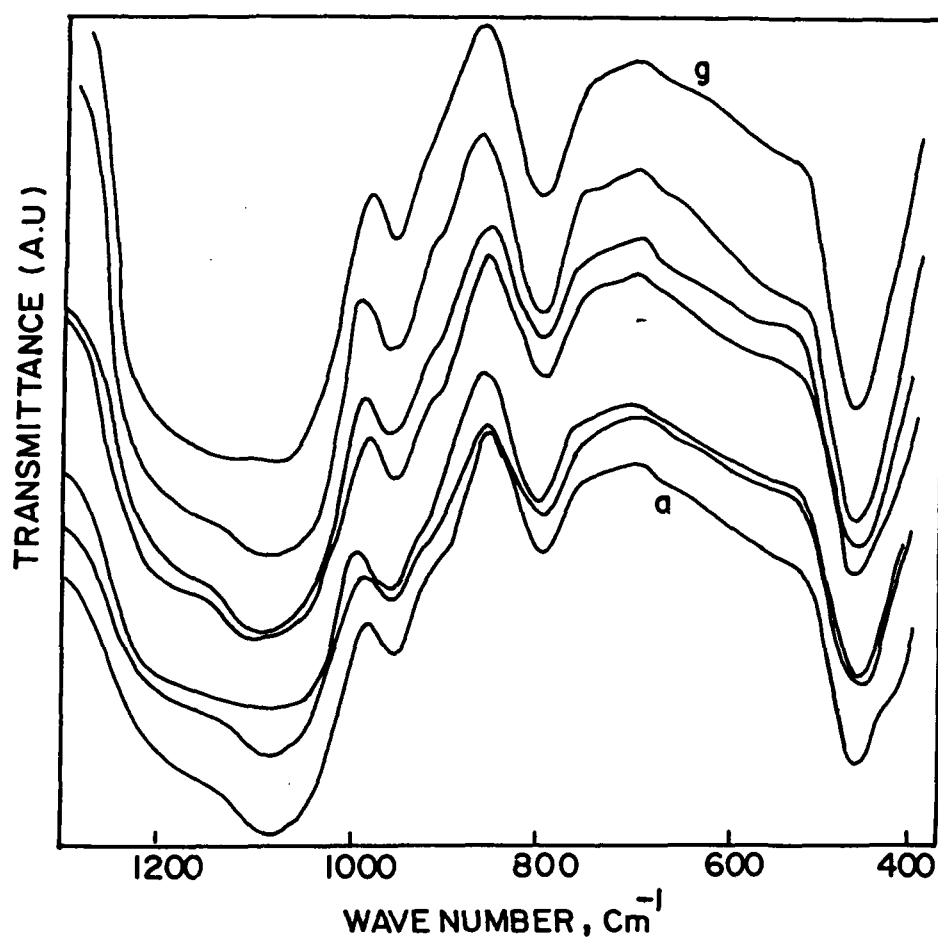


**Fig. 5.5:** FTIR spectra in the framework region; curves 'a' to 'g' corresponds to pH 1,3,5,7,9,11 and 13, respectively

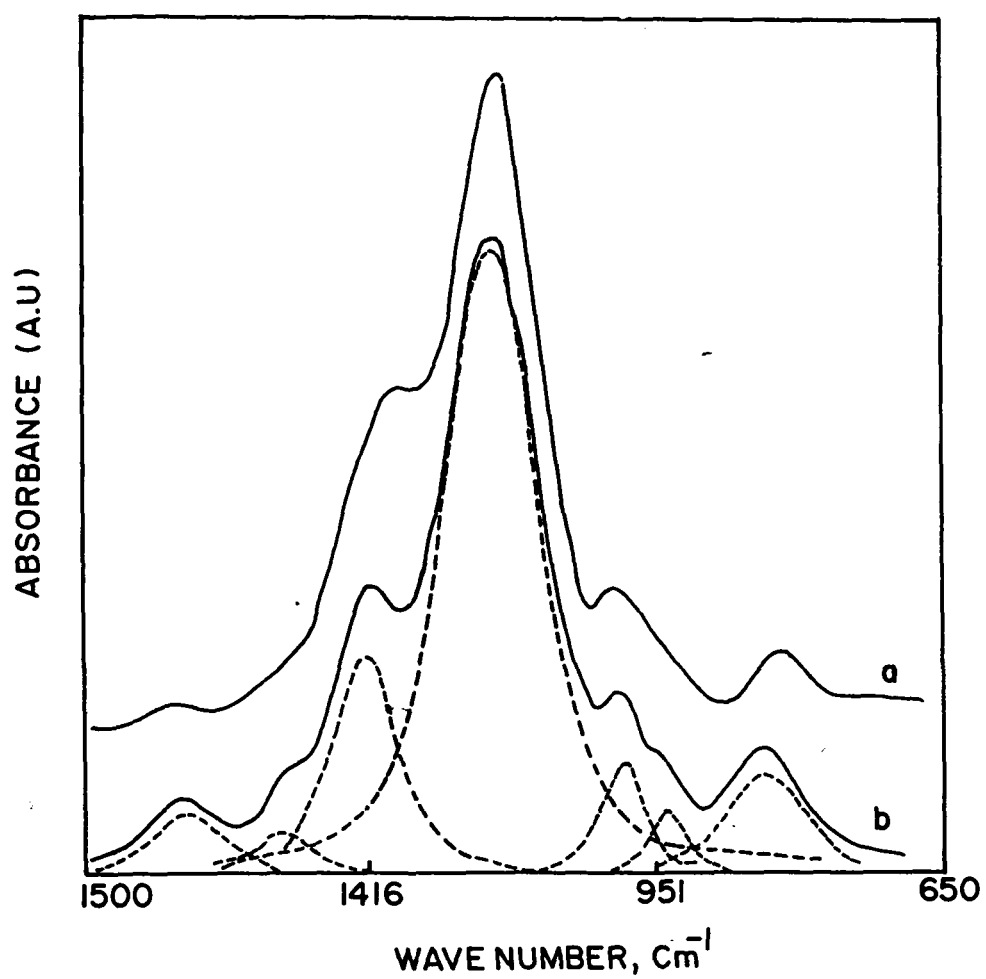


Fig. 5.6: Deconvoluted FTIR spectra of the titanium silicate prepared at pH 7.

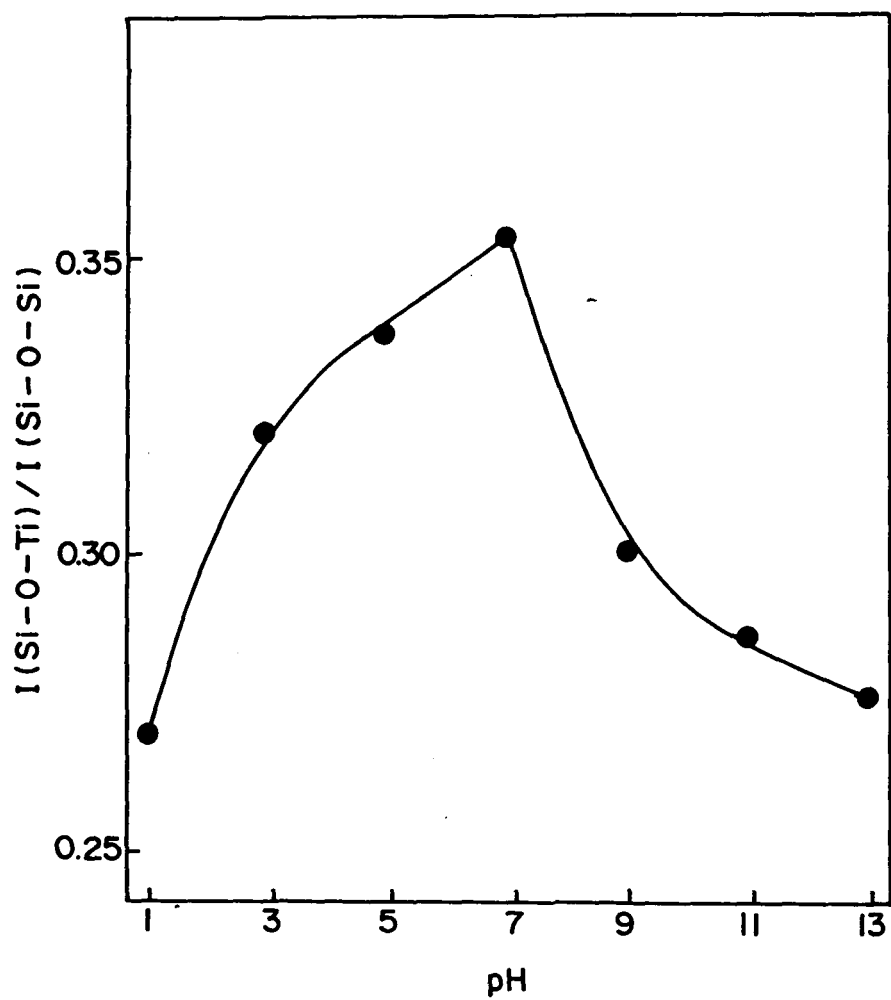


Fig. 5.7: Variation of Si-O-Ti connectivity ratio as a function of pH

It is clear therefore that the Ti dispersion increases from acidic medium to neutral medium then drops suddenly as the pH is increased further. At very high pH, it is probable that the dissolution of silica decreases the Ti dispersion. In other words, Ti dispersion is maximum under neutral conditions.

### 5.2.3.6. FTIR spectra of framework hydroxyl groups

The FTIR spectra of dehydrated titanium silicate samples prepared under various pH conditions are presented in Fig. 5.8. In all forms of silica, there are two major types of hydroxyl groups,<sup>68</sup> a sharp band around  $3740\text{ cm}^{-1}$  attributable to isolated silanol groups and a broad band in the region  $3700 - 3200\text{ cm}^{-1}$  attributable to hydrogen bonded hydroxyl groups. The spectrum of pure  $\text{TiO}_2$  samples shows a sharp band at  $3710\text{ cm}^{-1}$  together with a broad band with a peak at  $3670\text{ cm}^{-1}$ . Odenbrand *et al.*<sup>18</sup> have reported peaks at  $3730$  (sh),  $3710$  (s),  $3680$  (s),  $3670$  (s),  $3640$  (sh) and  $3610\text{ cm}^{-1}$  (sh) for  $\text{TiO}_2$  (anatase). However, when a minor amount of  $\text{TiO}_2$  is substituted in the tetrahedral position of  $\text{SiO}_2$  a significant decrease in the isolated silanol at  $3740\text{ cm}^{-1}$  has been reported by Fereres.<sup>61</sup> The results presented in the Fig. 5.8 also show a general decrease in the silanol groups at  $3740\text{ cm}^{-1}$ . In addition, in the region of  $3720 - 3200\text{ cm}^{-1}$  a significant broadening is observed in all the samples. It is possibly due to the destruction of surface hydroxyls by the presence of titanium in the second co-ordination spheres. In Fig. 5.09, the integral intensity of absorption in the region  $3700 - 3200\text{ cm}^{-1}$  is plotted as a function of pH of the sol-gel preparation. It should be noted that the concentration of surface hydroxyls passes through a maximum for pH 7. When titanium assumes tetrahedral coordination in TS-2, titanium silicalite<sup>69</sup>



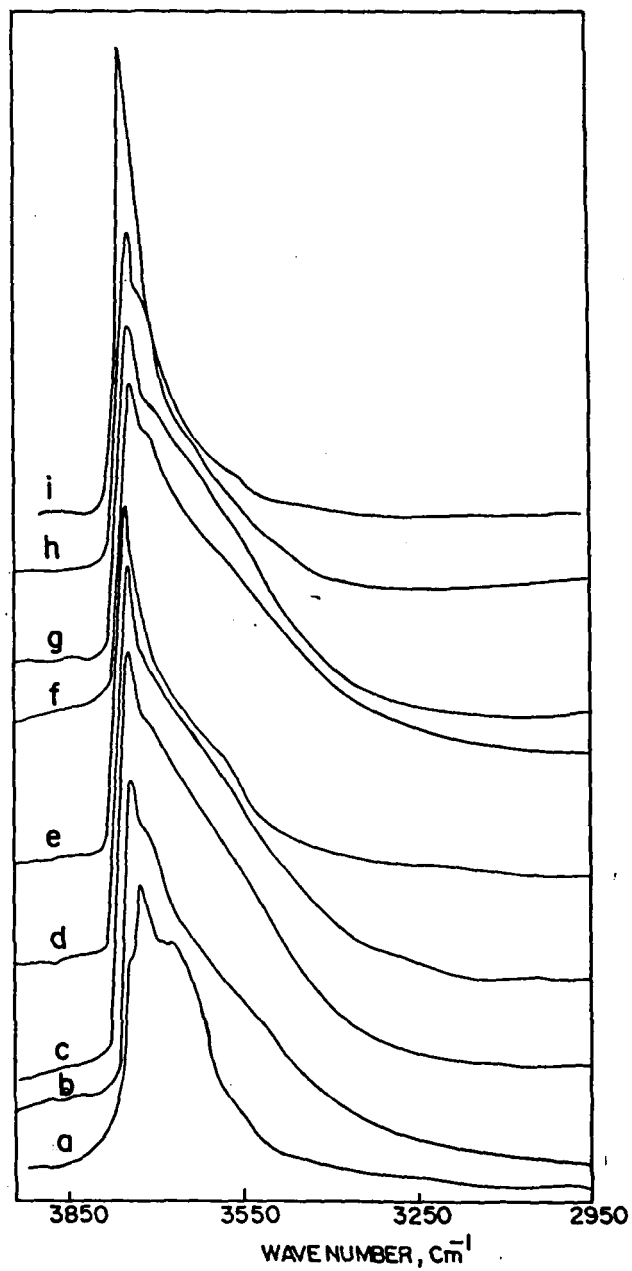


**Fig. 5.8:** FTIR spectra of framework hydroxyls of titanium silicates prepared at pH 1 to 13 (curves 'b' to 'h') and that of pure  $\text{TiO}_2$  (curve 'a') and pure  $\text{SiO}_2$  (curve 'i')

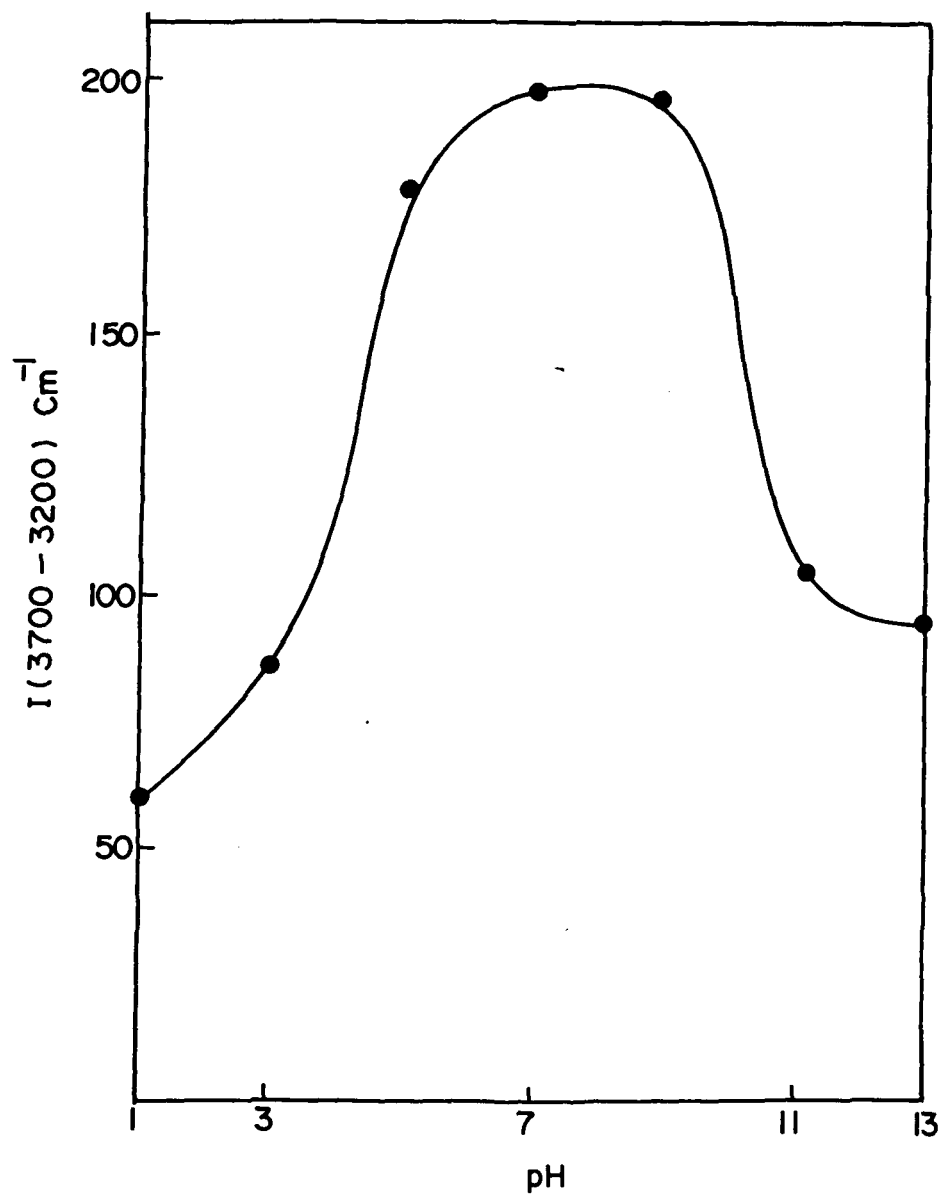
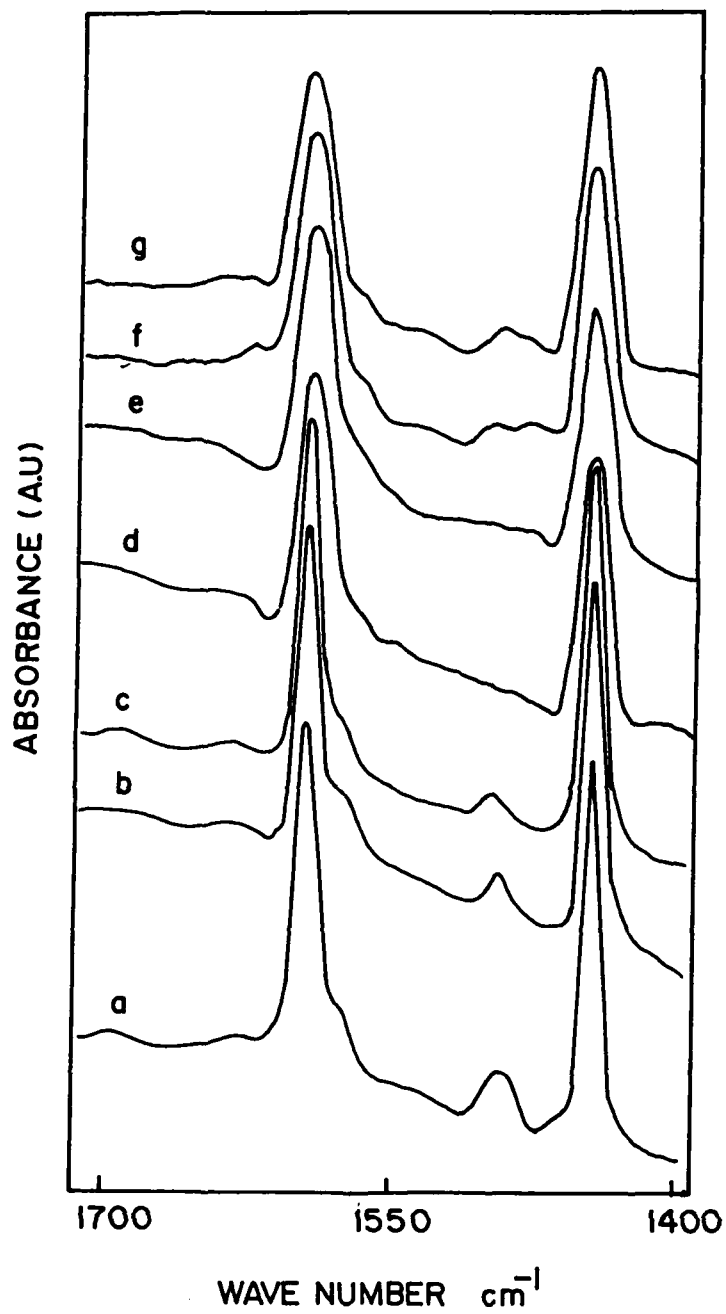


Fig. 5.9: Variation of surface hydroxyl intensity,  $I(3700-3200 \text{ cm}^{-1})$  with pH.

or when vanadium occupies tetrahedral position in vanadium silicalite molecular sieve, VS-2,<sup>70</sup> the concentration of hydrogen bonded hydroxyl groups increases. This can be attributed to the increase in defect sites created by the Si-O-Ti and Si-O-V connectivity. One can conclude that at pH 7, the incorporation of Ti in the silica lattice is most efficient under the experimental conditions.

### 5.2.3.7. FTIR spectra of adsorbed pyridine

The infrared spectra of the pyridine adsorbed on the solid catalysts can be used for characterizing the nature and the strength of surface acid sites.<sup>71</sup> Pyridine adsorbed on silica alone showed two major absorption bands at 1445 and 1598  $\text{cm}^{-1}$ , which correspond to *19b* and *8a* modes of physically adsorbed pyridine.<sup>71</sup> This is further confirmed by Ferers *et. al*, who have studied pyridine adsorption on a series of  $\text{TiO}_2$  -  $\text{SiO}_2$  mixed oxides and reported an increase in both Brønsted and Lewis acidity with the increase in  $\text{TiO}_2$  content.<sup>61</sup> In the present study, IR spectra of adsorbed pyridine at 323, 373 and 423 K were recorded as described before. In Fig. 5.10 the spectra of pyridine adsorbed at 323 K are presented. Adsorbed pyridine on acid sites gives bands due to ring vibrations at 1596, 1580, 1483 and 1438  $\text{cm}^{-1}$  for hydrogen bonded pyridine, at 1609, 1570-1580, 1487 and 1446  $\text{cm}^{-1}$  for coordinatively bound pyridine, and at 1640, 1600-1620, 1487 and 1545  $\text{cm}^{-1}$  for pyridinium ion. In the spectrum of the sample prepared at pH 7 (Fig. 5.10), bands at 1596 (s), 1580 (sh) and 1446 (s)  $\text{cm}^{-1}$  are assigned to the hydrogen bonded pyridine molecule. At 373 K, the intensity of these bands decreases and, at 423 K, disappears totally. The samples prepared at acidic and basic media ( Fig. 5.10) show an additional band at 1490  $\text{cm}^{-1}$  whose



**Fig. 5.10: FTIR spectra of adsorbed pyridine on titanium silicate samples prepared at pH 1 to 13 (curves 'a' to 'g')**

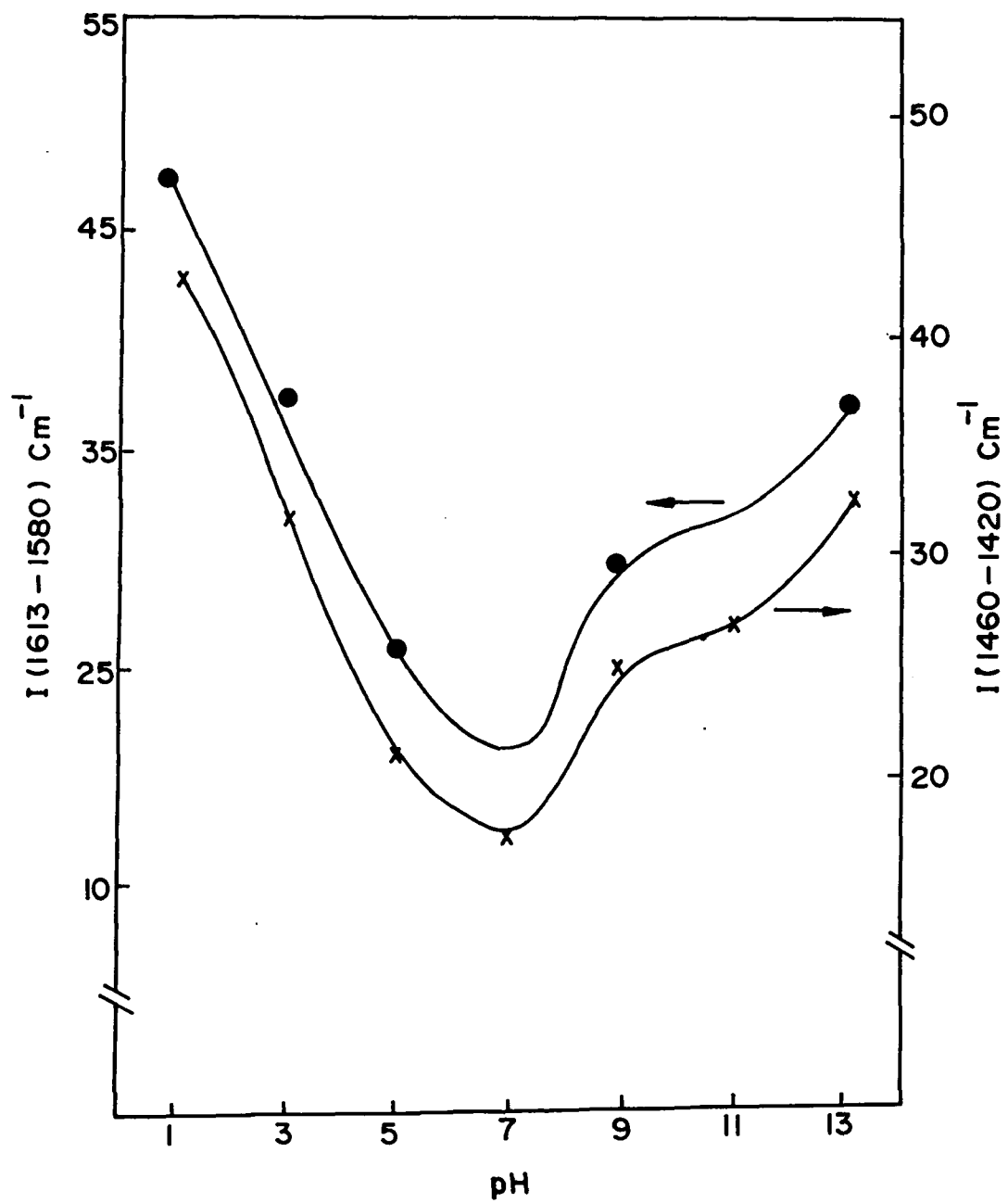


Fig. 5.11: Variation of  $I(1613-1580 \text{ cm}^{-1})$  and  $I(1460-1420 \text{ cm}^{-1})$  with pH

intensity increases with the increase in acidity or increase in basicity of the preparation medium. It can be either due to small Lewis acidity or due to the hydrogen bonded pyridine, since the intensity of this band is reported to be variable.<sup>71</sup>

In Fig. 5.11, the normalized intensity of peaks in the region 1460 - 1420 and 1613 - 1580  $\text{cm}^{-1}$  are plotted against the pH of the preparation. It should be noted that the concentration of adsorbed pyridine decreases with the increase in pH up to 7; it then increases on further increase in pH. The acidity of titanium silicates wholly depends on the state of the Ti in the sample because  $\text{SiO}_2$  is neutral and adsorbs pyridine weakly by hydrogen bonding. Characterization of the sample indicates that there are Si-O-Ti linkages and such linkages are highest at pH 7. However, if the concentration of  $\text{TiO}_2$  is low, such a bridging framework does not produce acidity in titanium silicate molecular sieves.<sup>72,73</sup> As the concentration of Ti falls within this range, Ti must be incorporated isomorphously in the silica framework in this sample also. Under these conditions, no charge imbalance is expected as proposed by Tanabe,<sup>74</sup> and the results on the acidity of the titanium silicate samples studied in the present investigation are as expected.

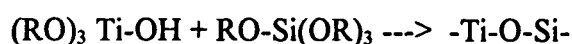
### ***5.2.3.8. General Discussion***

The problem of preparing homogeneous and controlled heterogeneous  $\text{SiO}_2$  -  $\text{TiO}_2$  from TEOS and TiIP is due to the large difference between the hydrolysis and condensation rates.<sup>43</sup> In acidic medium, hydrolysis reaches completion before condensation starts, whereas, in basic and neutral medium, condensation occurs as soon as hydrolysis is over. Since hydrolysis rate itself is very slow in neutral medium,

it should be a better condition for controlling the properties of the product. However, the hydrolysis rate of TiIP is reported to be more than five times that of TEOS in neutral medium. This problem was investigated in detail by Schmidt.<sup>75</sup> He discovered that if a small quantity of water is generated homogeneously in the mixture,  $\text{Si(OR)}_4$  is partly hydrolysed producing  $-\text{Si-OH}$ , which immediately binds with  $\text{Ti(OR)}_4$ , and prevents it from uncontrolled hydrolysis and precipitation.



In the preparation method used in the present study in the neutral medium, in particular, because of excess rate of hydrolysis of TiIP compared to that of TEOS, generation of partially hydrolysed  $-\text{Ti-OH}$  species in a large amount of unhydrolysed silicon alkoxide may be expected. Under this condition, the following reaction would probably takes place predominantly.



Thus, neutral pH seems to be an ideal condition for obtaining isolated Si-O-Ti linkages in the amorphous titanium silicate materials. This aspect is discussed in detail in a subsequent section of this chapter.

---

## 5.3.

### AMORPHOUS TITANIUM SILICATES PREPARED AT NEUTRAL pH (MMATS)

---

#### 5.3.1. WHY NEUTRAL MEDIUM ?

In the previous section, a systematic study of the effect of control of pH during the sol-gel preparation of amorphous titanium silicates (ATS) was described. It is evident from the study that neutral pH is more suitable for the generation of isolated Si-O-Ti linkages with the tetrahedral coordination. Therefore, a detailed study of the amorphous titanosilicate catalysts was carried which is reported in this section. Titanium silicates with different Si/Ti ratios were prepared and since they contained both micro and meso pores, they were named as *micro-meso porous amorphous titanium silicates* (MMATS).

#### 5.3.2. EXPERIMENTAL

##### 5.3.2.1. Preparation of MMATS

These were prepared by a modified sol gel method. Typically, 1 mole of tetraethyl orthosilicate (TEOS) (Aldrich, 99%) in ethanol was slowly added to 0.06



mole of titanium butoxide (Aldrich, 99%) in isopropanol at 313 K at neutral pH over a period of 6 h. Deionised water mixed with 2-propanol was then added to the above mixture in a controlled manner (0.1 ml per min) to produce a clear, transparent gel. The material was aged for 24 h at 313 K and then water and alcohol were removed by vacuum treatment. The resultant semi-dry gel was further dried at 383 K for 24 h under reduced pressure ( $\approx 1$  torr) and then calcined in air at 723 K for 24 h. Three such samples with Si/Ti ratios of 17, 34 and 51 (designated as samples A, B and C, respectively) were prepared. For the purpose of comparison, a Ti-free silica was also prepared from TEOS in a similar way along with a microporous, crystalline, titanosilicate (TS-1) with MFI structure using tetrapropylammonium hydroxide as the organic base as per the procedure described elsewhere<sup>76</sup>. The samples were chemically analyzed by atomic adsorption spectroscopy using a Hitachi model spectrometer.

### ***5.3.2.2. Characterization***

The x-ray scattering measurements were made with Cu K $\alpha$  radiation on a computer-controlled XRD (Rigaku, D-Max/III VC model) instrument, equipped with a reflection geometry, NaI scintillation counter, a curved graphite crystal monochromator and a nickel filter. The scattered intensities were collected from 3.5° to 130° (2 $\theta$ ) by scanning at 0.5° (2 $\theta$ ) steps with a counting time of 15 s at each step. The sample was rotated throughout the scanning period. The intensities were corrected for air scattering, polarization and absorption effects and then normalized to convert the corrected intensities to electron units. Using the theoretical values of the Compton scattering intensities of silicon, titanium and oxygen as a function of  $\sin \theta/\lambda$  the normalized radial distribution function was computed.<sup>77</sup>

The framework IR spectra of the samples were recorded in a Nicolet (60 SXB model) FTIR instrument, after depositing the sample as a thin film on a Si plate and subsequently removing the background vibration due to Si. The Laser Raman (Spex 1403 spectrometer, Ar ion laser) spectra of self supported, thin pellet of the samples were recorded after evacuation of the sample to  $10^{-3}$  torr. The  $^{29}\text{Si}$  MASNMR (Bruker, MSL-300) spectra of the samples were recorded at 59.6 MHz and referenced to  $\text{Me}_4\text{Si}$ . The XPS measurements were carried out in a VG Scientific ESCA-3 MK2 electron spectrometer with an Al  $K_\alpha$  x-ray source. A binding energy of 285 eV for C1s level was used as the internal standard. The sorption measurements were carried out gravimetrically in a (Cahn, 2000 G) electrobalance at 298 K and at a fixed  $p/p_0$  of 0.5 after equilibration for 10 h. The samples were evacuated at 673 K to  $10^{-6}$  torr for 6 h before adsorption measurements. The surface areas (BET), the micro and meso pore volume and pore size distributions were calculated from the Ar adsorption/desorption isotherms at liquid  $\text{N}_2$  temperature in a Coulter (Omnisorp 100 CX) instrument. The micropore size distributions were calculated from the low pressure region ( $p/p_0 = 10^{-4}$  to 0.1) of the isotherms following the Horvath and Kawazoe model<sup>58</sup> and the mesopore distribution from the desorption isotherm using the BJH model<sup>57</sup>. Scanning electron micrographs were taken in a Jeol (model 5200) instrument. TEM and electron diffraction of the sample were carried out in a Jeol (model 1200 EX) electron microscope. Simultaneous TG and DTA of the samples were performed in a TG/DTA-92 model (Setaram, France) instrument in an air flow of  $100 \text{ cm}^3 \text{ min}^{-1}$  with a heating rate of  $10 \text{ K min}^{-1}$  up to 1270 K. Temperature-programmed reduction of the samples was carried out in a Sorbstar (Hungary) instrument using 5 vol %  $\text{H}_2 - \text{N}_2$  mixture at a heating rate of  $18 \text{ K min}^{-1}$ .

### 5.3.2.3. *Catalytic activity*

The hydroxylation and oxidation reactions were carried out in a batch reactor using benzene, phenol and toluene as organic substrates and aqueous H<sub>2</sub>O<sub>2</sub> (26 wt.%) as the oxidant. Invariably, a substrate to catalyst (wt.) ratio of 10 and a substrate to H<sub>2</sub>O<sub>2</sub> (mole) ratio of 3 have been employed using either acetone, water or acetonitrile as the solvent. Other details of the reaction and of product analysis are given elsewhere.<sup>78</sup>

## 5.3.3. RESULTS AND DISCUSSION

### 5.3.3.1. *X-ray, Electron diffraction, and TEM*

The X-ray diffraction patterns of the samples did not contain any sharp reflections except a broad diffuse band similar to that of amorphous silica. In particular, no separate crystalline phases of TiO<sub>2</sub> (like anatase) could be detected. These materials are hence completely amorphous without any long range order. Even samples calcined above 1073 K did not show the formation of a separate anatase or rutile phase and there was no indication of crystallization of either the silica or titania after such thermal treatment. The electron diffraction patterns of sample A showed only a halo pattern and its TEM image did not indicate the presence of any crystalline TiO<sub>2</sub> (Fig. 5.03, B). This strongly confirms that regions with short range order similar to that in crystalline TiO<sub>2</sub> are absent in the samples studied. However, Imamura *et al*<sup>79</sup> and Saito<sup>80</sup> have argued that very fine crystalline particles could be present even in samples which are apparently amorphous to electron diffraction and TEM imaging.

### 5.3.3.2. X-ray photoelectron spectroscopy

The bulk chemical composition (from wet chemical analysis) and surface composition (from XPS) in terms of Si/Ti ratios of the three samples (A-C) are given in Table 5.2. There is an apparent surface enrichment of Si. Surface depletion of TiO<sub>2</sub> has been observed in many titania - silica systems<sup>79</sup> including TS-1 (Table 5.2) and Ti glasses.<sup>81</sup> A plausible explanation is that occupancy of Ti is energetically less favoured than that of Si on the surface where the silica network is disrupted.<sup>79,81</sup> Fig. 5.12 shows the Ti2*p* photoelectron peaks of samples A-C in comparison with those of pure TiO<sub>2</sub> and TS-1 after compensation for work function shifts due to specimen charging. The ESCA binding energies of Si and Ti (Table 5.2) are found to be those expected for Si<sup>4+</sup> and Ti<sup>4+</sup> ions. The actual peak separation for TS-1 is smaller (4.7 eV) compared to that for MMATS samples (5.2 to 6.4 eV). For pure TiO<sub>2</sub>, the Ti 2*p*<sub>3/2</sub> binding energy value is 458.9 eV. There is a small but significant increase in the binding energy of Ti 2*p*<sub>3/2</sub> electrons in samples A, B and C (459.5, 459.6, and 459.8 eV, respectively), while that of Si 2*p*<sub>1/2</sub> decreases marginally. These trends are similar to those observed by Imamura *et al*<sup>79</sup> for their titania - silica samples and indicate the formation of Si-O-Ti species through an interaction between Ti and Si atoms. The difference in binding energies has been attributed to four coordination with oxygen (of Ti) in Ti silicate glasses.<sup>81,82</sup> The binding energy shift is more prominent in TS-1 (1.6 eV). The O1*s* spectra of the samples shown in Fig. 5.13 provide further evidence for the formation of Si-O-Ti linkages. The symmetrical O1*s* peaks of pure SiO<sub>2</sub> and pure TiO<sub>2</sub> appear at 533.5 and 530.2 eV, respectively, whereas the samples A, B and C show asymmetry due to the presence of a minor Si-O-Ti and a major Si-O-Si

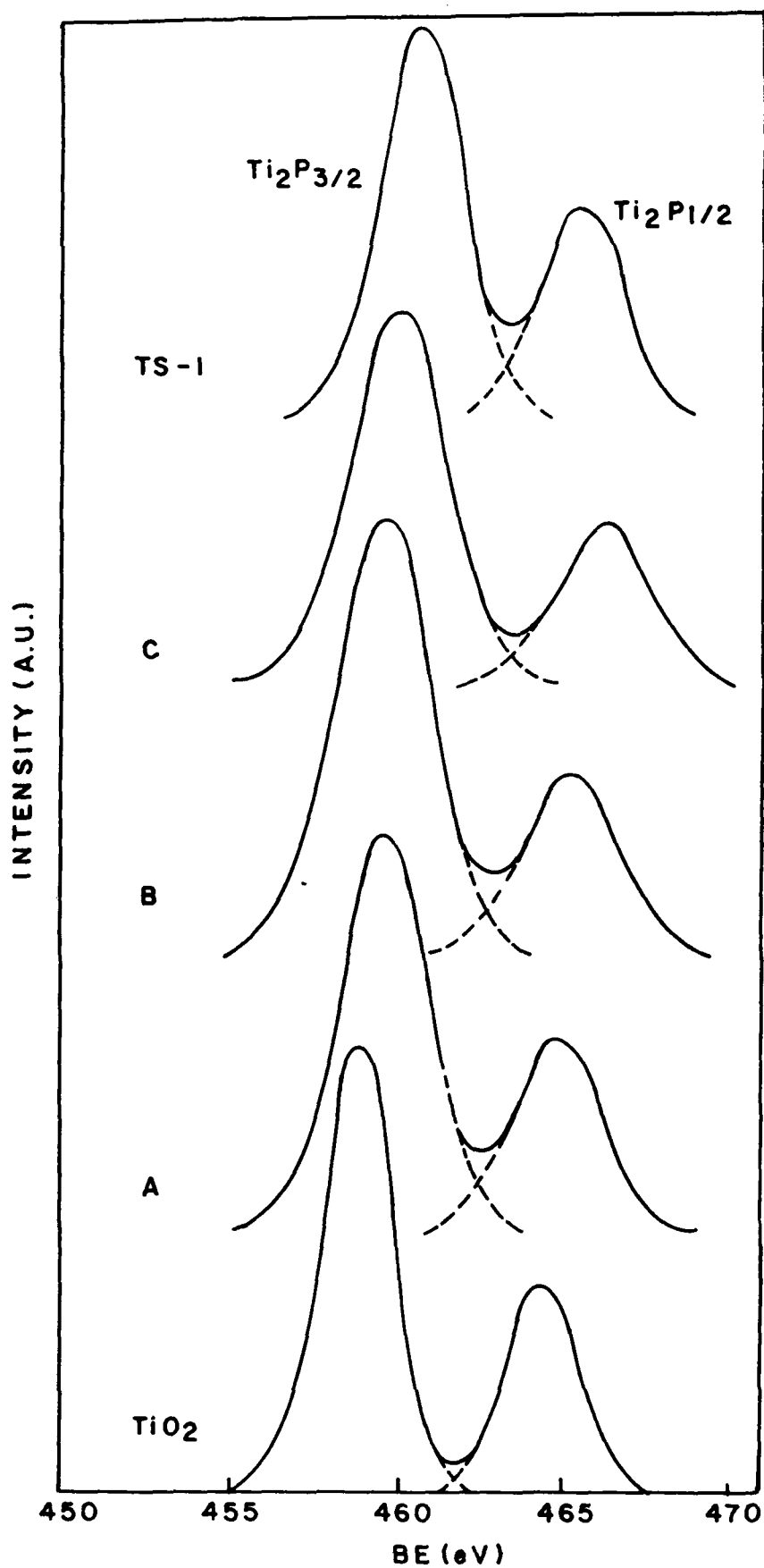


Fig. 5.12: Ti 2p photoelectron spectra of  $TiO_2$ , MMATS samples A to C and titanium silicalite, TS-1.

Table 5.2

XPS data of MMATS samples A-C, SiO<sub>2</sub>, TiO<sub>2</sub> and TS-1

Sample	Si/Ti ratio (mol)		B.E. (eV) (XPS)	
	Bulk	Surface	Si 2p <sub>1/2</sub>	Ti 2p <sub>3/2</sub>
A	17	32	103.6	459.5
B	34	53	103.6	459.6
C	51	81	103.6	459.8
SiO <sub>2</sub>	-	-	104.0	-
TiO <sub>2</sub>	-	-	-	458.9
TS-1	32	125	103.9	460.5

component. The core electron binding energy of the oxygen atom is decreased when a Si-O-Si bond is replaced by Ti-O-Si. In addition, the O1s peaks in Ti-doped silica are wider than those of pure silica, whereas the FWHM of this peak varies linearly with increasing Ti content (2.5, 2.7 and 3.1 eV, respectively). These observations are similar to those reported for amorphous titania-silica glasses.<sup>82-84</sup>

Fig. 5.14 shows the corresponding Si2p spectra of SiO<sub>2</sub> and MMATS A, B and C respectively. (a to d). Here also the shift in the Si 2p is a clear indication of the formation of Si-O-Ti linkages. Apart from these qualitative data, an attempt was also made to estimate the extent of tetrahedrally coordinated Si-O-Ti on the basis of the ratio of integral area of the two O1s peaks pertaining to oxygen of Si-O-Si and Si-O-Ti linkages. When this ratio, the fraction of tetrahedral Si-O-Ti connectivity, was plotted with the Ti content, a linear trend was observed (Fig. 5.15).

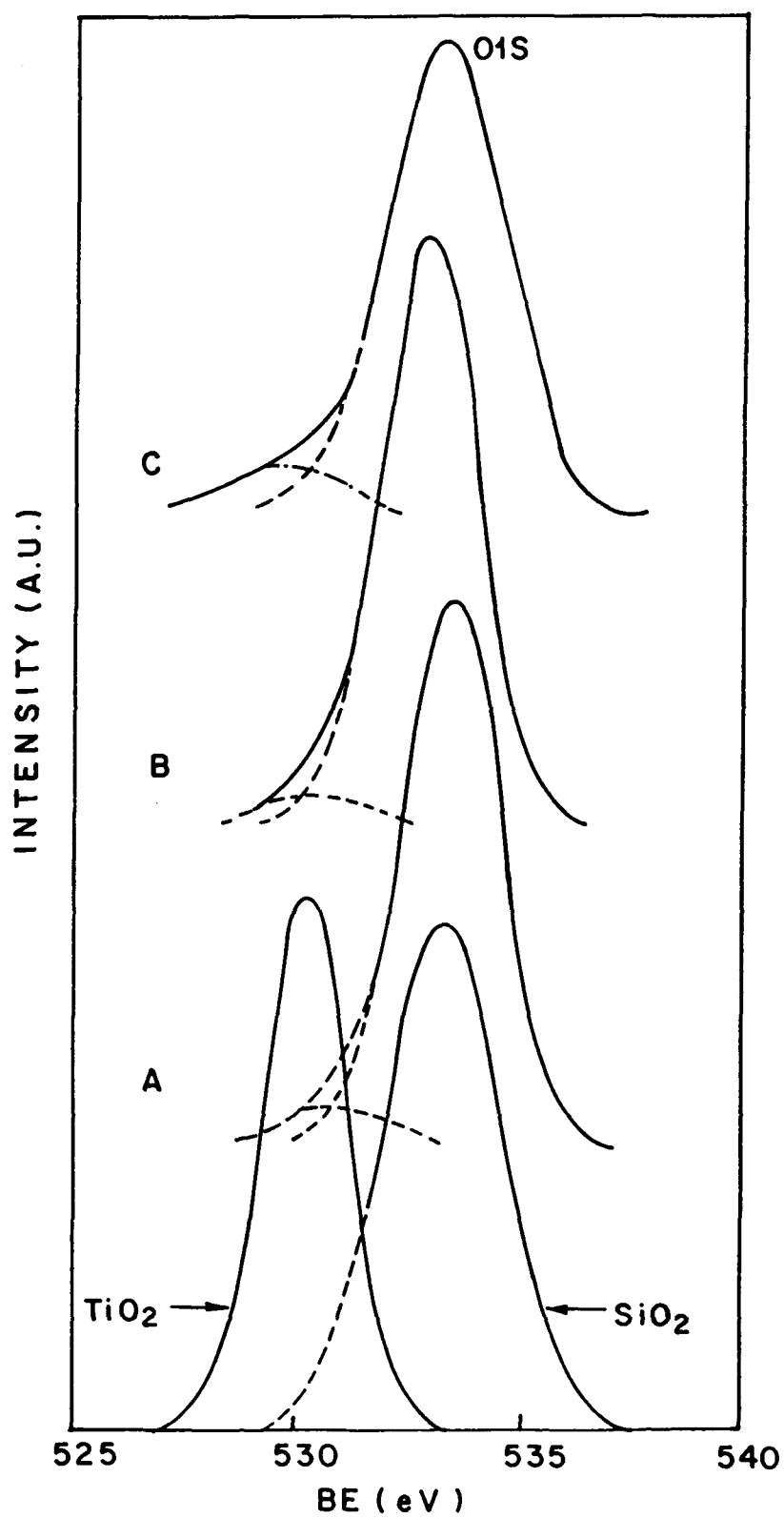


Fig. 5.13: O 1s photoelectron spectra of TiO<sub>2</sub>, SiO<sub>2</sub> and MMATS samples A to C

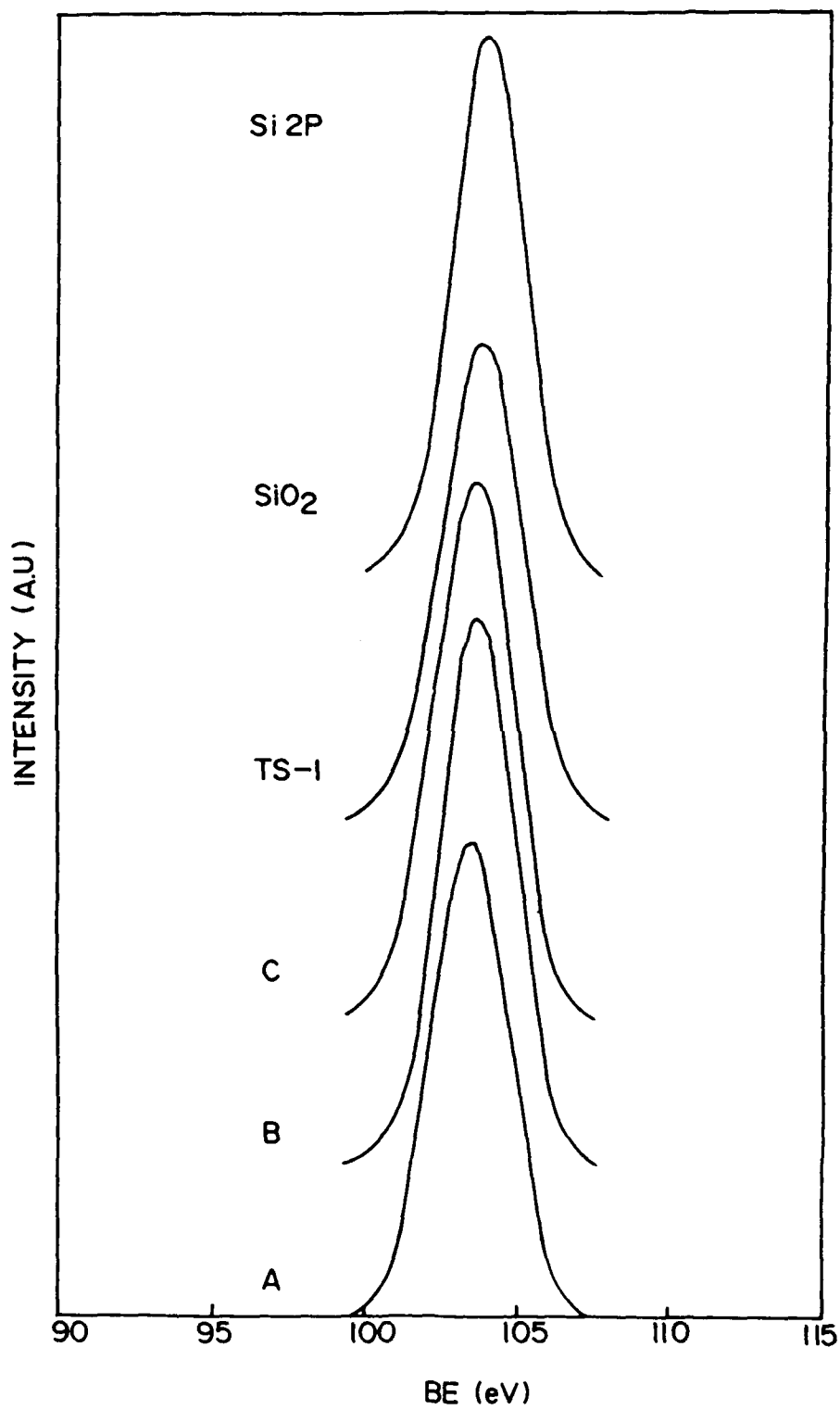
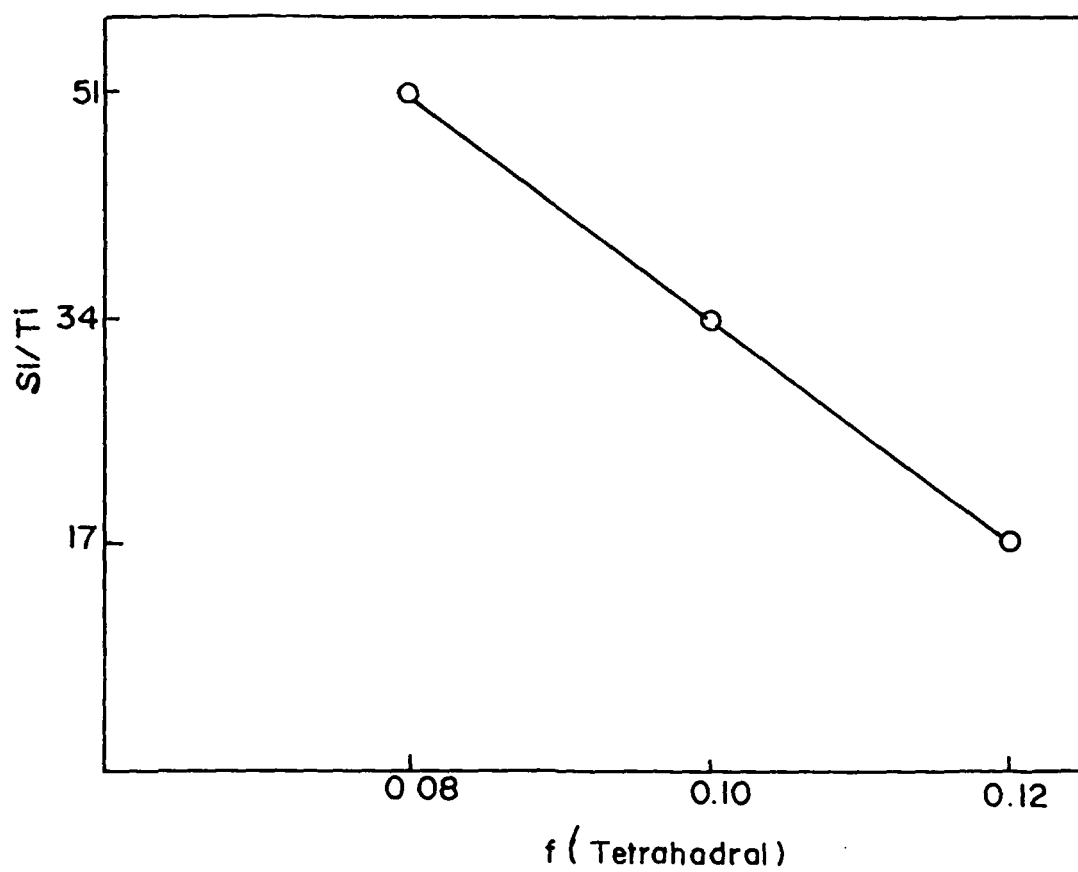


Fig. 5.14: Si 2p photoelectron spectra of MMATS samples A to C, TS-1 and SiO<sub>2</sub>.





**Fig. 5.15: Variation of Si-O-Ti connectivity ( $f$  (tetrahedral)) as estimated by O 1s spectra with Si/Ti ratio**

### 5.3.3.3. Adsorption.

Some of the textural properties of these samples are given in Table 5.3. The Ar adsorption-desorption isotherm of one of the samples is shown in Fig. 5.16 (inset) along with those of silica and titania prepared in a similar manner. Three stages can be observed in the plot for the MMATS sample: a sharp linear increase passing through the origin at a very low partial pressure of Ar due to monolayer-multilayer adsorption in micropores, a more gradual increase at higher partial pressures of Ar indicative of multilayer adsorption in mesopores and finally a capillary condensation above  $p/p_0 = 0.4$ . The mesopore area (from the t-plot) and the total surface area (BET) values are also indicated in Table 5.3. As the Ti content increases, the surface area of mesopores increases significantly. A corresponding increase in mesopore volume is also noticed on increasing the Ti content. In fact, the increase in pore volume due to Ti incorporation is due entirely to the generation of mesopores (Table 5.3). The porewidth of the micro- and mesopores was calculated to be around 0.85 and 3.6 nm, from the respective Horvath-Kawazoe and the BJH plots. These materials, hence, possess a bimodal and a fairly narrow pore size distribution. In general, when a material is prepared by sol-gel method under basic pH conditions, the hydrolysis rather than condensation is the rate determining step and the resulting material is essentially mesoporous. Under acidic condition, condensation is the rate determining step and one would get microporous material. During the preparation the pH was almost neutral which probably led to a bimodal pore size distribution in the samples irrespective of Si/Ti ratio. In addition, it has been observed that the rates of hydrolysis and condensation of TEOS is influenced by the presence of even small concentrations of Ti

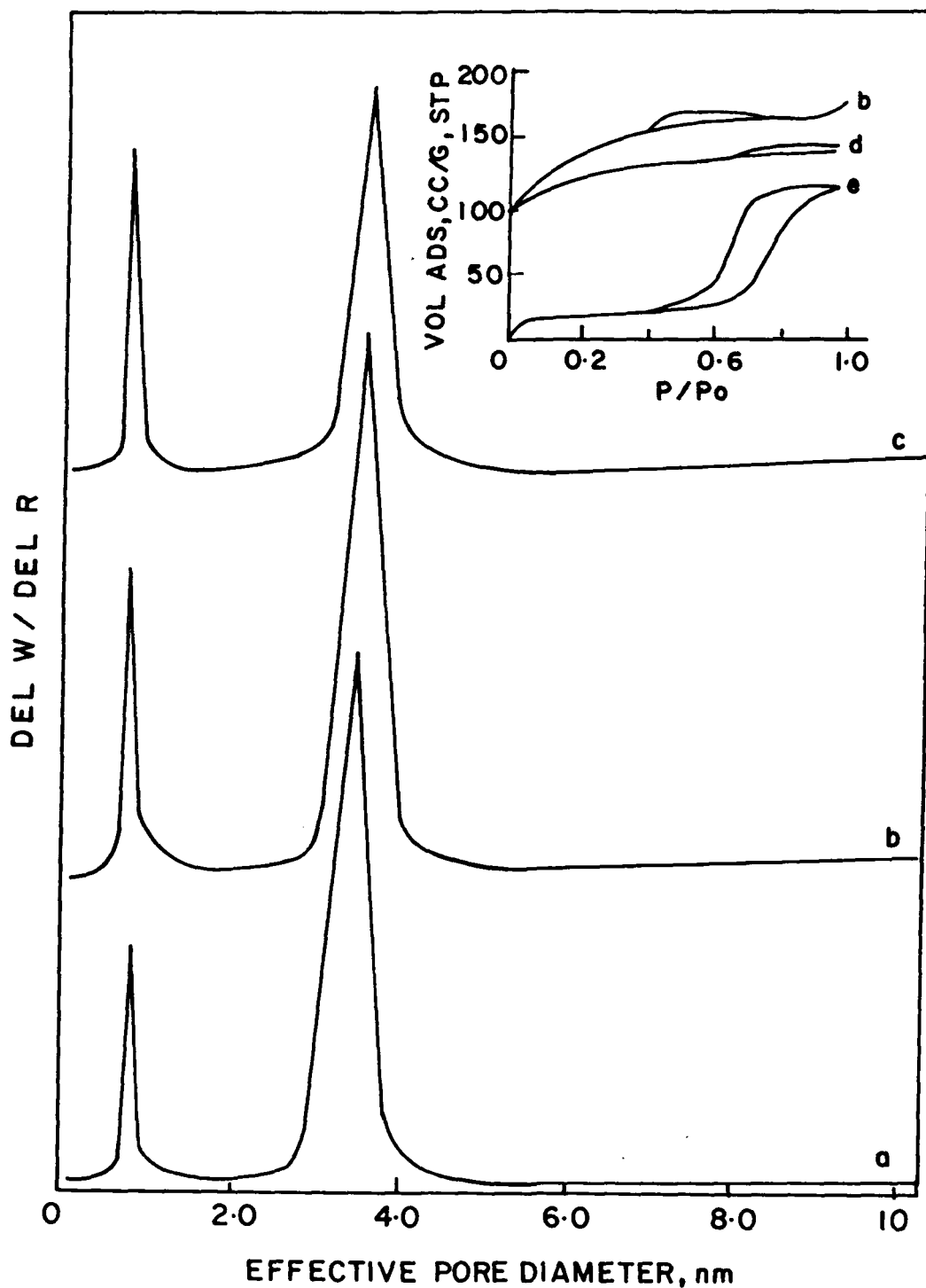


Fig. 5.16: Pore size distribution in MMATS samples A to C (curves a to c, respectively). Inset : Ar adsorption-desorption isotherms at 77K, of samples B (curve b), pure silica (curve d), and pure  $\text{TiO}_2$  (curve e)

alkoxides. A major part of the surface area is contributed by pores with a diameter characteristic of micropores (less than 2.0 nm). A smaller but significant part is due to mesopores with a pore diameter between 2.0 and 20 nm (Table 5.3). In contrast, the Ti-free silica prepared from TEOS is found to be essentially microporous, whereas pure TiO<sub>2</sub> (anatase) has a low surface area, owing to the presence of meso-pores with a broad pore size distribution. The surface area of MMATS samples decreases sharply on calcination above 923 K (Fig. 5.17) owing to loss of micropores.

**Table 5.3**

**Surface area and pore volume data of MMATS samples A-C, SiO<sub>2</sub>, TiO<sub>2</sub> & TS-1**

Sample	Surface area (m <sup>2</sup> g <sup>-1</sup> )			Pore volume (ml g <sup>-1</sup> )			Av. pore dia (nm)	
	Micro	Meso	Total	Micro	Meso	Total	Micro	Meso
A	462	162	624	0.22	0.11	0.33	0.85	3.6
B	478	105	583	0.21	0.09	0.30	0.86	3.6
C	506	46	552	0.22	0.04	0.26	0.85	3.6
SiO <sub>2</sub>	563	31	594	0.22	0.02	0.24	0.75	-
TiO <sub>2</sub>	-	47	47	-	0.22	0.22	-	18.8
TS-1	400	15	415	0.18	-	0.18	0.58	-

The sorption capacity of MMATS samples and of pure SiO<sub>2</sub> for H<sub>2</sub>O and some hydrocarbons is summarized in Table 5.4. For all the adsorbates including the bulkier molecules like 1,3,5-trimethyl- and 1,3,5-triisopropylbenzenes, the amount adsorbed at

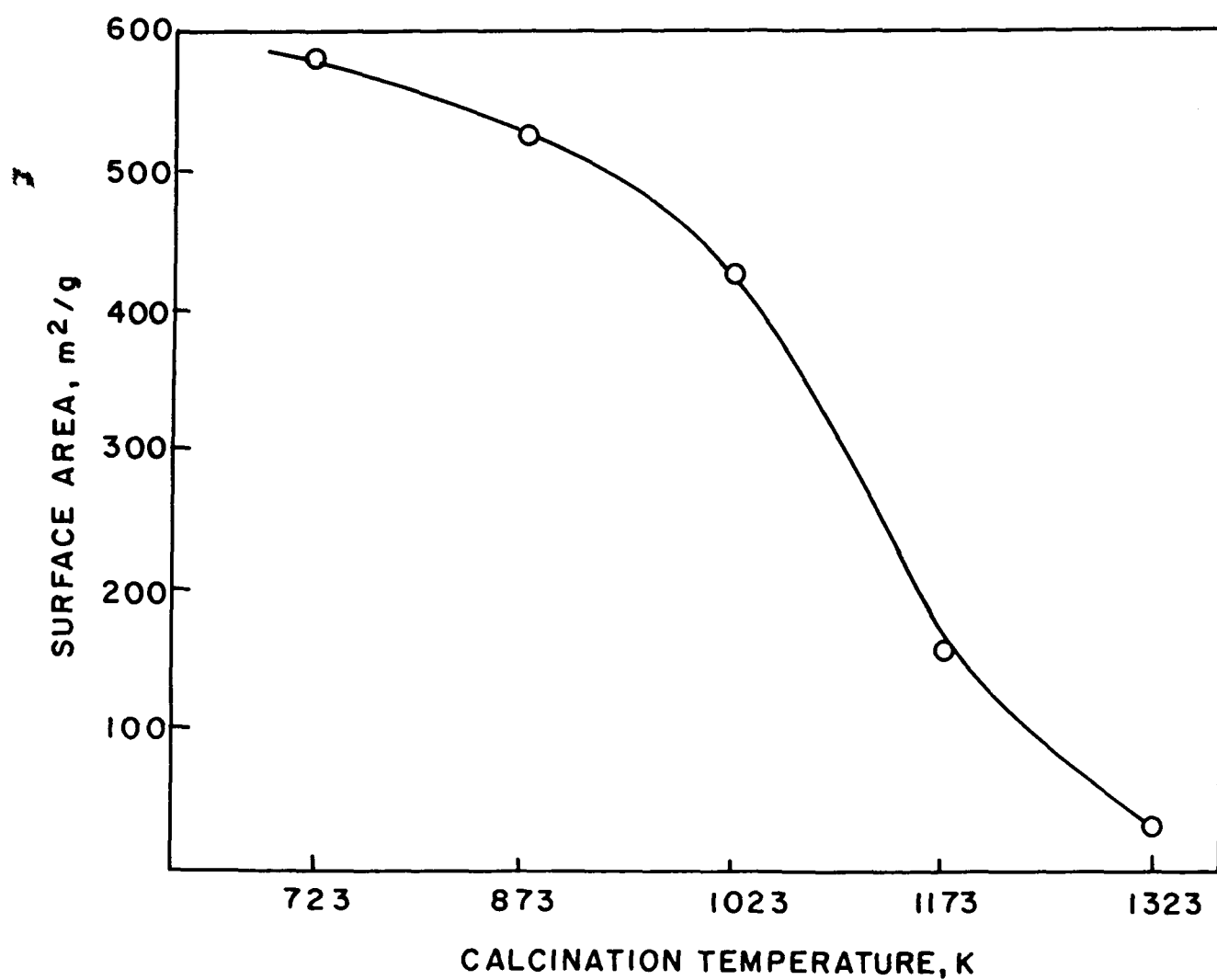


Fig. 5.17: Influence of calcination temperature on the surface area (BET) of MMATS-B sample (Si/Ti = 34)

**Table 5.4.**  
**Sorption Capacity of MMATS samples (Wt%)<sup>a</sup>**

Adsorbate	Samples			
	MMATS-A	MMATS-B	MMATS-C	SiO <sub>2</sub>
Water	25.1	21.0	21.9	17.6
n-Hexane	16.8	14.2	11.3	9.7
Cyclohexane	19.3	14.1	10.0	8.4
Benzene	26.0	19.5	16.7	13.7
1,3,5-trimethylbenzene	23.0	18.2	14.6	9.7
1,3,5-triisopropylbenzene	18.8	15.0	11.4	1.3

<sup>a</sup> Gravimetric adsorption in Cahn Electrobalance at  $p/p_0 = 0.5$  and at 298 K

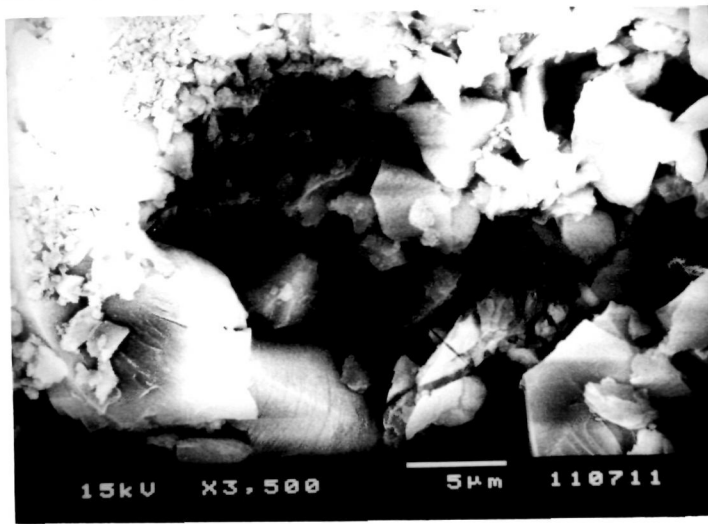
the conditions given in Table 5.4 is significant and it increases with the Ti content in the sample in parallel with the increase in the mesopore volume and the surface area of the samples (Table 5.4). In the absence of the corresponding values for the other mesoporous titanium silicates known so far, viz., Ti-MCM-41 and Ti-HMS<sup>8,9</sup>, it is difficult to compare the relative adsorption capacities of all three materials. It can be seen from the Table 5.4 that the sorption capacity of pure silica, which is essentially microporous, is relatively less than that of the MMATS samples.

#### ***5.3.3.4. Scanning electron microscopy.***

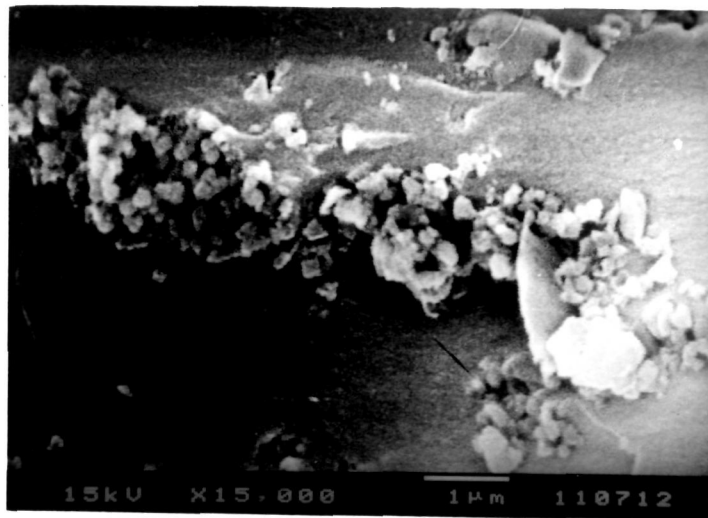
The scanning electron micrographs of samples A-C are shown in Fig. 5.18. The average particle size is between 0.2 and 0.5  $\mu\text{m}$ . As expected for amorphous materials, they are irregular in shape but fairly uniform in size.

#### ***5.3.3.5. Thermal analysis.***

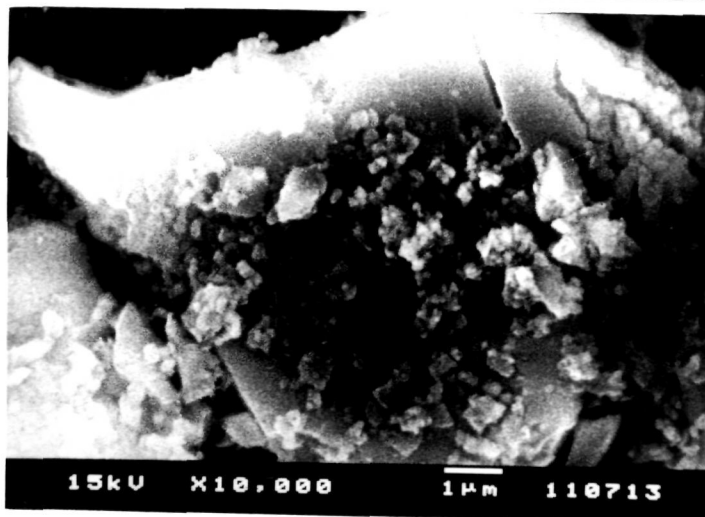
The TG/DTA thermograms of samples A-C (Fig.5.19) reveal only the endothermic loss of water in the temperature range, 273-500 K. No exotherm due to crystallization and segregation of a  $\text{TiO}_2$  phase is seen up to about 1200 K in any of the three samples. We may therefore, conclude that no separate phase of  $\text{TiO}_2$  (like anatase) is present in samples A-C. The Ti-O-Si bond is quite stable to thermal treatment. The latter feature is reminiscent of TS-1 and the titano-aluminosilicate-1,<sup>76</sup> which are also quite stable to thermal treatment up to 1200 K. Hence, eventhough MMATS samples lack the long-range order of TS-1, the Ti-O-Si bonds in both have similar characteristics, at least with respect to thermal stability.



A



B



C

Fig. 5.18: Scanning electron micrographs of MMATS samples A, B and C



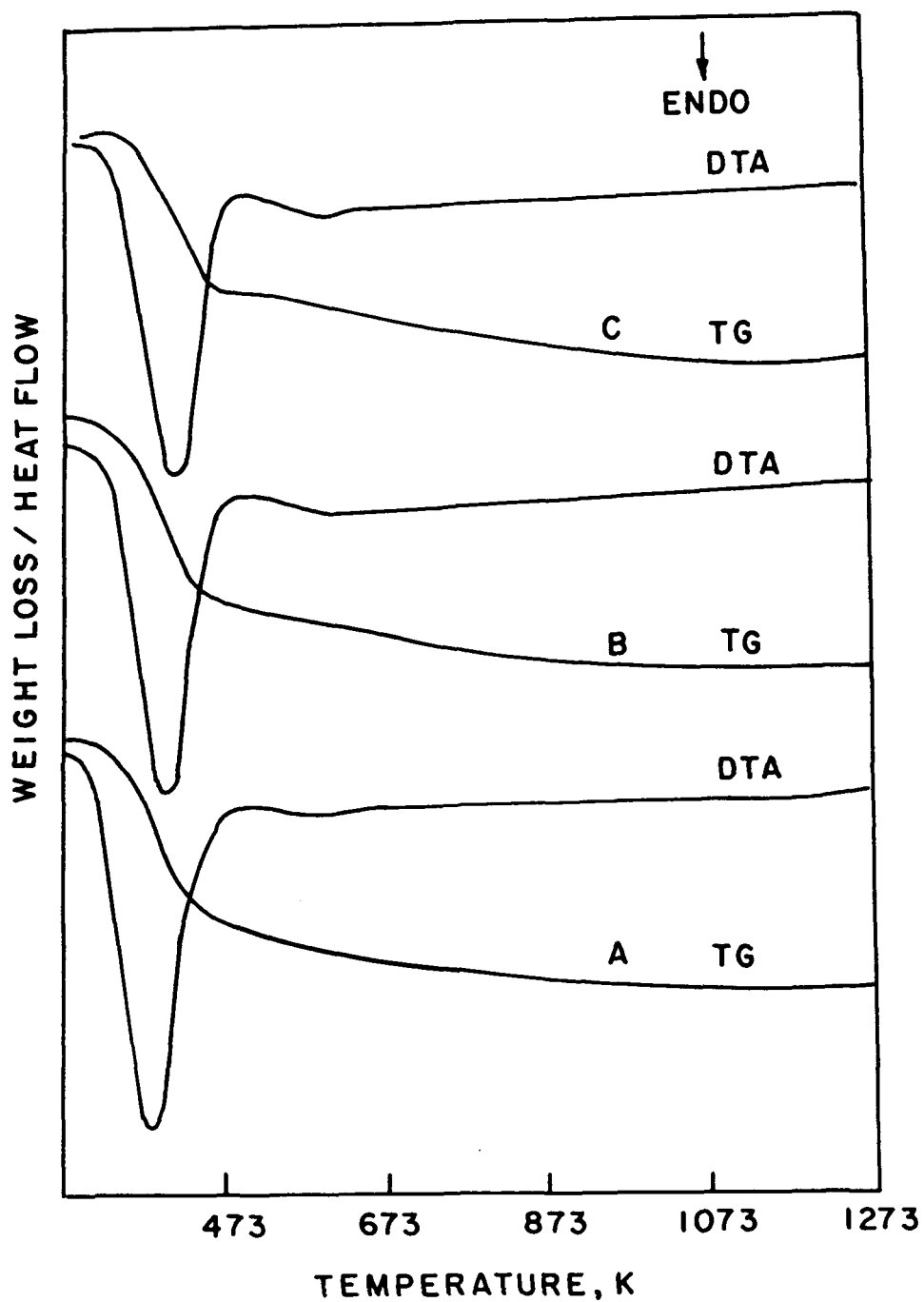


Fig. 5.19: Simultaneous TG-DTA thermograms of samples A, B, and C (curves A, B and C, respectively)

### 5.3.3.6. Framework IR and UV-VIS spectroscopy.

The framework IR and UV-VIS spectra of these samples are shown in Figs. 5.20 and 5.21, respectively. The presence, in the IR spectra of samples A-C, of the  $960\text{ cm}^{-1}$  band, probably due to a Si-O bond 'perturbed' by Ti<sup>85</sup> is a further indication of the presence of Si-O-Ti linkages in MMATS. Both TS-1 and TS-2 exhibit this band and its intensity correlates with the Ti content in their framework<sup>86</sup>. The band at  $550\text{ cm}^{-1}$  observed for TS-1 (Fig. 5.20) is due to the presence of five membered rings (pentasil structure) in the crystalline material. This vibration is obviously not present in the amorphous titanosilicates. The UV spectra of MMATS (Fig. 5.21) is more complex. In addition to strong absorption around 220 nm, which is characteristic of Ti<sup>4+</sup> in tetrahedral symmetry, there is also significant absorption in the region 220-300 nm, suggesting that, compared to TS-1 (which has a sharp absorption band at 220 nm), the coordination of Ti<sup>4+</sup> in MMATS is more heterogeneous. In other words, the Ti atoms are well dispersed in the amorphous silica matrix. The Ti ions are most probably also present in other distorted tetrahedral/octahedral environment (see *Raman spectroscopy*). In these materials, the Ti coordinates to four oxygen atoms, but because of its larger covalent radius, it can interact with one or two more ligands such as H<sub>2</sub>O. This expands its coordination five or six-fold. It is noteworthy that anatase (absorption at 330 nm) is not found in samples A-C (Fig. 5.21). To summarize, framework IR and UV-VIS spectra indicate that : (i) in MMATS samples Si-O-Ti linkages exist; (ii) the Ti<sup>4+</sup> ions are present in a tetrahedral (and probably also in octahedral) environment; and (iii) a separate, crystalline TiO<sub>2</sub> phase like anatase, is absent. However, the IR spectrum of MMATS differs from that of TS-1 with respect

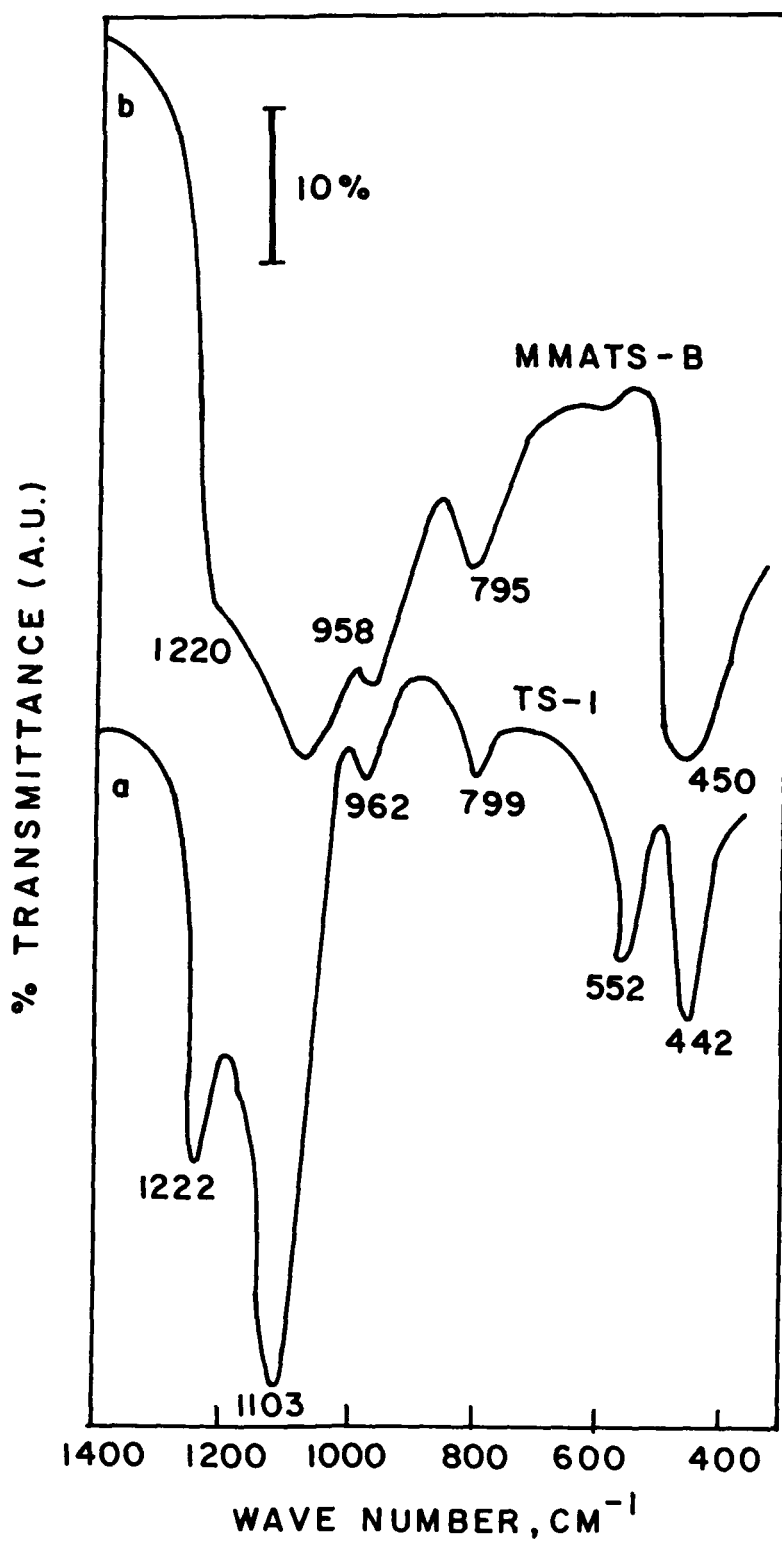


Fig. 5.20: FTIR spectra of crystalline TS-1 (curve a) and MMATS-B (curve b).

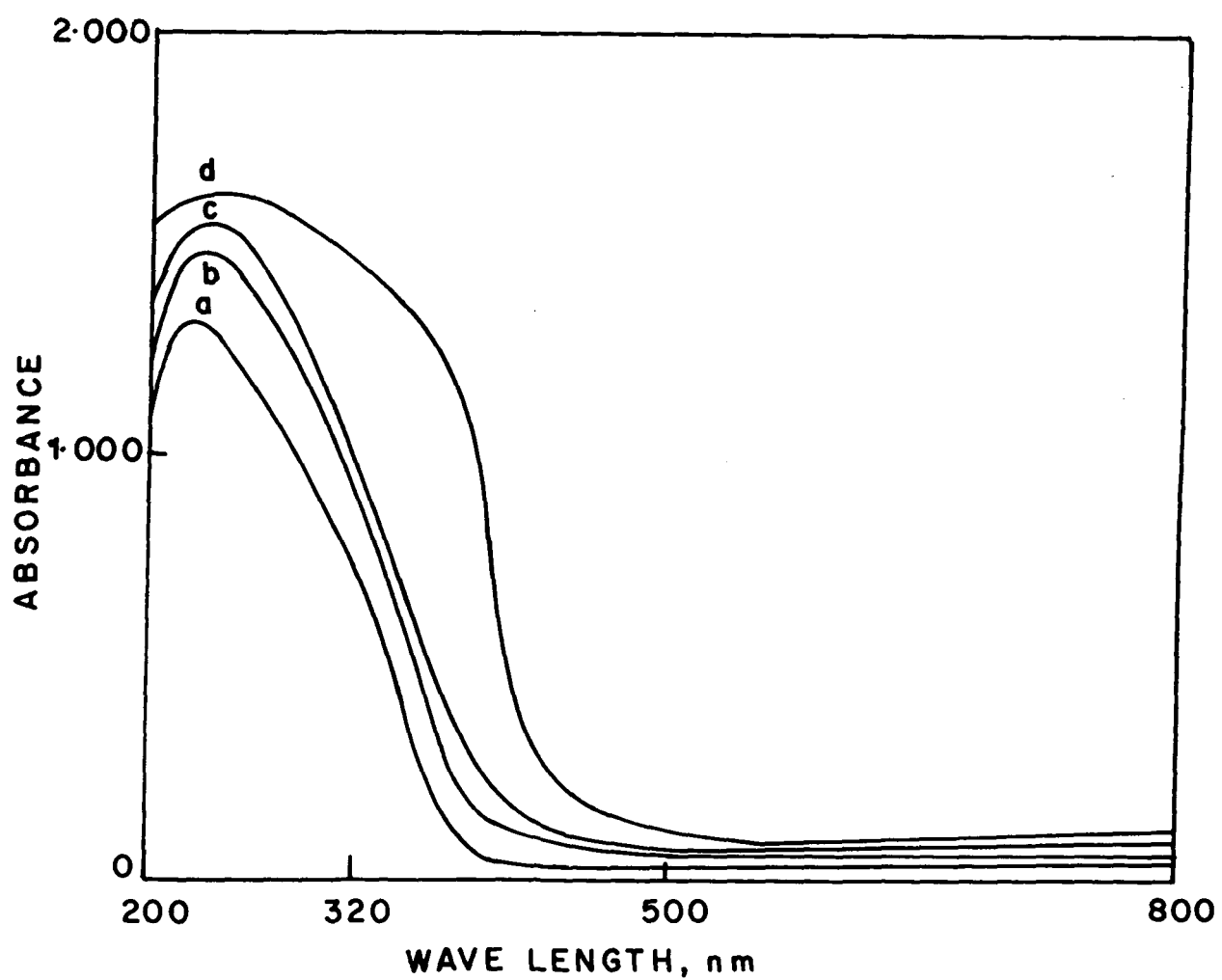


Fig. 5.21: UV-VIS spectra of MMATS samples A-C (curves a-c, respectively) and pure TiO<sub>2</sub> (curve d)

to the band at  $550\text{ cm}^{-1}$ , which is present in the latter case owing to the presence of five membered rings.

### 5.3.3.7. Raman spectroscopy.

The Raman spectra of samples A-C (curves a - c) and a sample of  $\text{SiO}_2$  prepared by the alkoxide method (curve d) along with anatase form of  $\text{TiO}_2$  (curve e) are shown in Fig. 5.22.  $\text{TiO}_2$  has strong bands at  $640, 518, 400\text{ cm}^{-1}$  (Fig. 5.22) as well as at  $368, 248$  and  $146\text{ cm}^{-1}$  (not shown in Fig. 5.22). These values for anatase are similar to those of Deo *et al*<sup>87</sup> ( $637, 513, 386$  and  $144\text{ cm}^{-1}$ ) and Srinivasan *et al*<sup>88</sup> ( $643, 520, 399, 244$  and  $144\text{ cm}^{-1}$ ). From the presence of a broad band around  $640\text{ cm}^{-1}$  and its increase with Ti content (Fig. 5.22), it may be concluded that, although a segregated, crystalline anatase phase may be absent,  $\text{Ti}^{4+}$  ions in a distorted octahedral symmetry is probably present in all the samples, A to C. Another feature of the spectra in Fig. 5.22 is the enhanced intensity of the Raman scattering in samples A-C (compared to  $\text{SiO}_2$ , curve d) around  $800\text{-}850, 950\text{-}1000$  and  $1100\text{-}1150\text{ cm}^{-1}$ . While investigating the substitution of Ti in the crystalline silicalite-1 lattice, Deo *et al*,<sup>87</sup> have also observed enhanced Raman scattering at  $970$  and  $1125\text{ cm}^{-1}$  in TS-1 compared to silicalite-1 samples. While both these bands are essentially due to silicon-oxygen vibrations, the enhancement in their intensity, perhaps, indicates formation of Si-O-Ti bond. All solid titania compounds exhibit Raman scattering below  $900\text{ cm}^{-1}$  as per earlier reports.<sup>87,88</sup>

Thus Raman spectroscopy provides additional evidence for the formation of isolated Si-O-Ti linkage in the present amorphous titanium silicate samples.

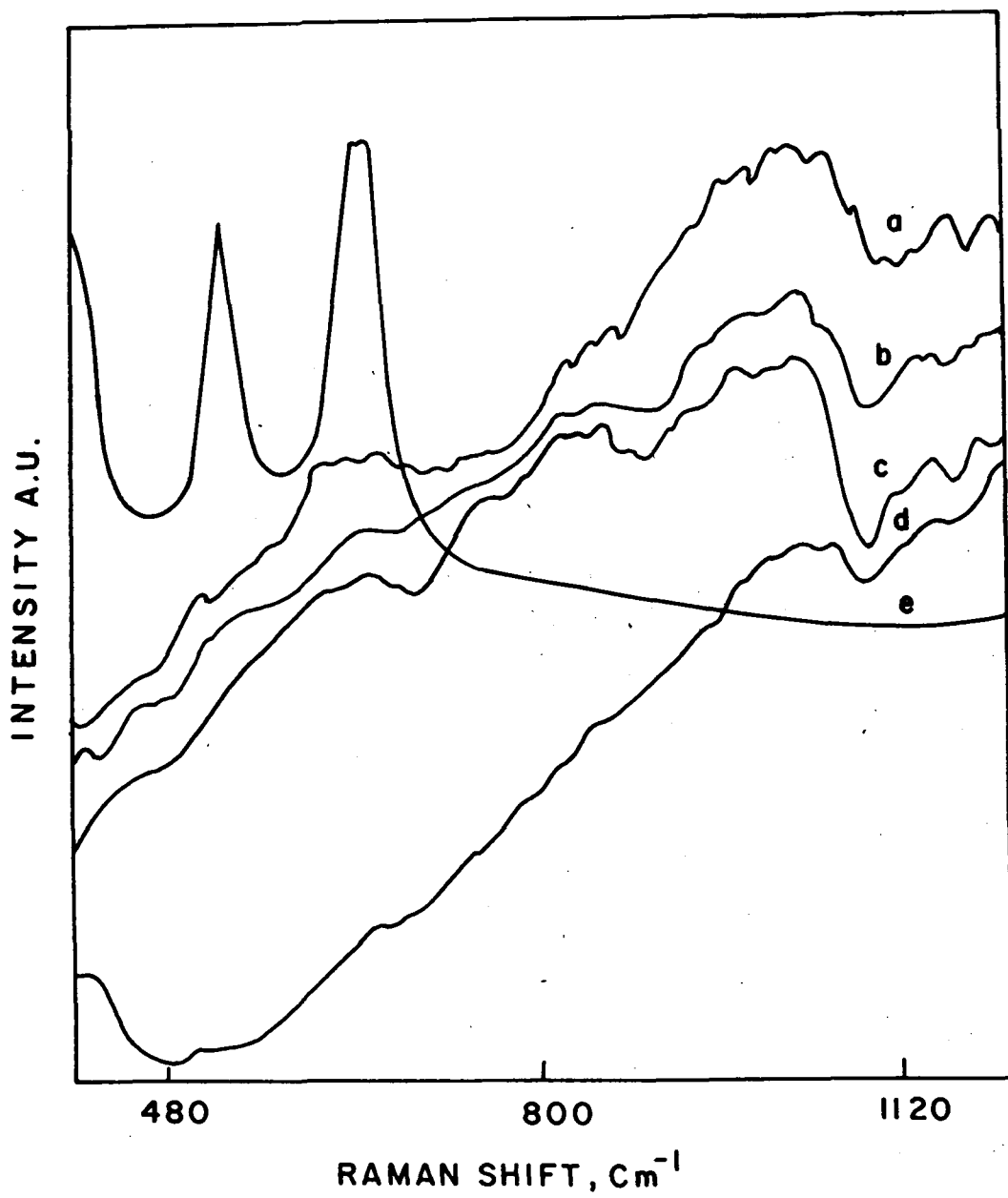


Fig. 5.22: Raman spectra of MMATS samples A-C (curves a-c, respectively), pure  $\text{SiO}_2$  (curve d) and pure  $\text{TiO}_2$  (curve e).

#### **5.3.3.8. $^{29}\text{Si}$ MASNMR spectroscopy.**

The structural connectivity of Ti to Si through Si-O-Ti bonds is again suggested by the  $^{29}\text{Si}$  MASNMR spectra (Fig. 5.23). The broadening of the  $^{29}\text{Si}$  lines in samples A-C compared to those in pure  $\text{SiO}_2$  (prepared by a similar procedure) suggest that species such as  $\text{Si}(\text{OSi})_{4-n}(\text{OTi})_n$  exist in these samples resulting from a replacement of Si in  $\text{Si}(\text{OSi})_4$  by Ti in the second coordination sphere. In the completely homogeneous sol gel method of preparation, as the miscibility of silica/titania increases the Ti-O-Si bond formation occurs more easily.<sup>23</sup>

#### **5.3.3.9. Temperature Programmed Reduction**

The stability of the Si-O-Ti bond in MMATS with respect to reduction in hydrogen by temperature-programmed reduction indicates that the  $\text{Ti}^{4+}$  ions are not reduced in flowing dry hydrogen, at least up to 1100 K. The non-reducibility of MMATS in hydrogen is probably due to the absence of a separate  $\text{TiO}_2$  phase in them. Alternatively, this is also indicative of the presence of strong Si-O-Ti linkage, and, in this respect, it is similar to TS-1. However, this is an indirect evidence for the formation of isolated active site and therefore, further evidence is sought by X-ray scattering studies.

#### **5.3.3.10. X-ray scattering.**

The results from the characterization studies discussed above suggest that although MMATS materials are amorphous and lack long-range order, there are broad similarities between them and titanosilicate molecular sieves, like TS-1 as regards the

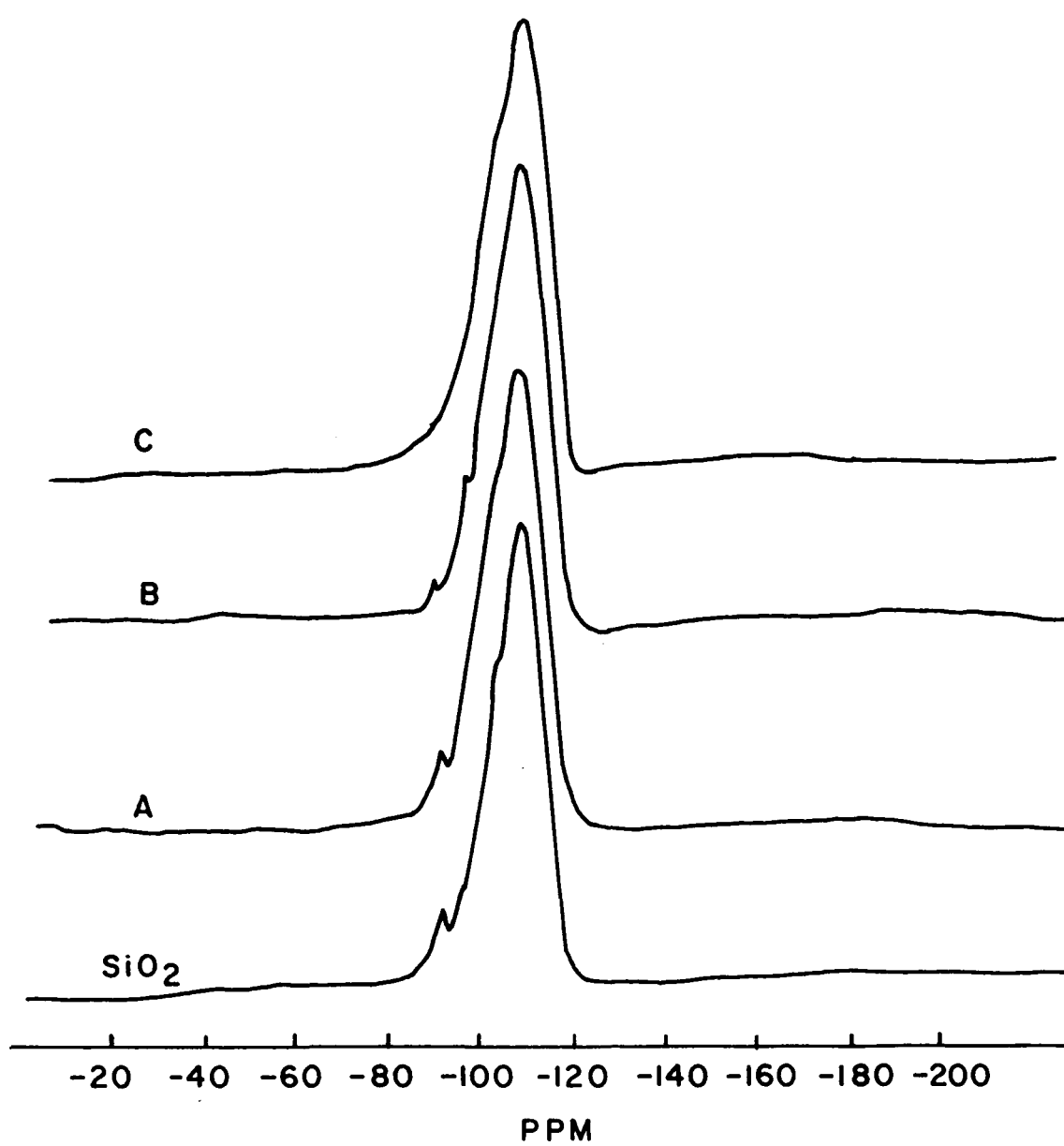


Fig. 5.23:  $^{29}\text{Si}$  MAS NMR spectra of  $\text{SiO}_2$  and MMATS samples A, B and C.



local environment around  $\text{Ti}^{4+}$ . The local environment around Si and Ti in samples A-C was investigated using x-ray scattering techniques.<sup>10</sup> The radial electron density distribution plots for a sample of  $\text{SiO}_2$  prepared by the sol-gel method (see **Experimental**), along with samples A-C and  $\text{TiO}_2$  (anatase), are shown in Fig. 5.24. Values of interatomic distances derived from Fig. 5.24 are given in Table 5.4. Values for  $\text{SiO}_2$  ((1.63 ( $\text{Si}_1\text{-O}_1$ ); 2.61 ( $\text{O}_1\text{-O}_1$ ); 3.39( $\text{Si}_1\text{-Si}_2$ ); and 4.24 Å ( $\text{O}_1\text{-O}_2$ )) are in the range usually observed for amorphous  $\text{SiO}_2$ .<sup>89</sup> The  $\text{TiO}_2$  sample has the interatomic vectors at 1.99, 2.98, 3.93 and 4.74 Å. Two conclusions of a qualitative nature may be drawn from Fig. 5.24 on the effects of introduction of Ti in the silica matrix : (i) there is no evidence for the presence of anatase or an anatase-like phase in any of the amorphous titanosilicate samples MMATS, A-C. The r.e.d. curve for  $\text{TiO}_2$  (anatase) is completely different from that of MMATS (Fig. 5.24); the peak at 2.98 Å, very significant in  $\text{TiO}_2$  is absent in the MMATS samples. (ii) As the Ti content increases (from MMATS-C to MMATS-A), there is a gradual broadening of the peaks at 2.61 and 3.39 Å due to the  $\text{O}_1 - \text{O}_1$  and  $\text{Si}_1 - \text{Si}_2$  ( $\text{Si}_1 - \text{Ti}_1$ ), respectively. A plausible explanation is that the Ti atom is being inserted in the second coordination sphere of Si (oxygen atoms occupy the first coordination sphere) progressively in the order :



As expected, the introduction of Ti does not change the  $\text{Si}_1\text{-O}_1$  distances significantly (Table 5.5). The statistical average of the  $\text{Si}_1\text{-Si}_2$  and  $\text{Si}_1\text{-Ti}_1$  vectors in the second coordination sphere varies from 3.29 to 3.40 Å. MMATS-C with the lowest content of Ti does not show any significant distortion as the  $\text{Si}_1\text{-Si}_2$  vector is shifted to lower value on introduction of Ti. In MMATS-B and, MMATS-A in particular, both of which contain higher amounts of Ti, the  $\text{Si}_1\text{-Si}_2$  vector is shifted to lower values on

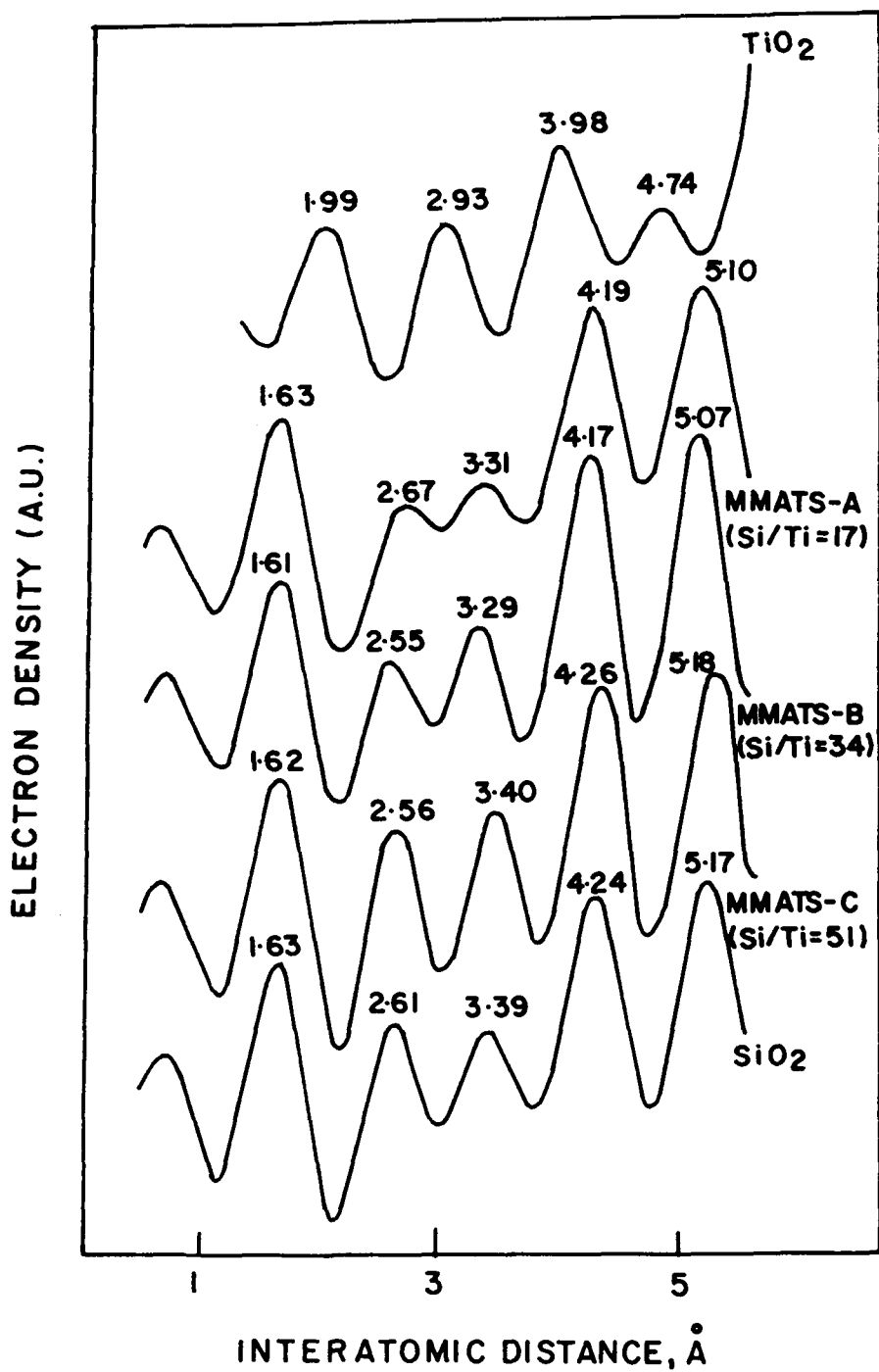


Fig. 5.24: Radial electron density distribution function curves for SiO<sub>2</sub>, MMATS (A-C), and TiO<sub>2</sub> samples.

introduction of Ti. Blasco *et al*<sup>90</sup> have recently studied the local environment of Ti and Si in titano-aluminosilicates, isomorphous with zeolite beta, by the EXAFS technique and obtained a good fitting of the data for a model involving four silicon atoms in the second shell of Ti at a distance of about 3.23 Å, implying the existence of isolated TiO<sub>4</sub> units. The shift (from 3.39 for SiO<sub>2</sub> to 3.29 Å for MMATS) observed in the peak due to Si<sub>1</sub>-Si<sub>2</sub> distance in Fig. 5.25 can arise from a contribution from a vector at 3.23 Å due to Si<sub>1</sub>-Ti<sub>1</sub> from isolated TiO<sub>4</sub> tetrahedra present in the MMATS samples.

Table 5.5

## Interatomic Distance Vectors in Silica, Titania and Titanosilicates

Sample	Si/Ti ratio	Interatomic vectors (Å)				
		Si <sub>1</sub> -O <sub>1</sub>	O <sub>1</sub> -O <sub>1</sub>	Si <sub>1</sub> -Si <sub>2</sub> (Si <sub>1</sub> -Ti <sub>1</sub> )	O <sub>1</sub> -O <sub>2</sub> (Si <sub>1</sub> -O <sub>2</sub> )	Si <sub>1</sub> -Si <sub>3</sub> (O <sub>1</sub> -O <sub>3</sub> )
SiO <sub>2</sub>	-	1.63	2.61	3.39	4.24	5.17
C	51	1.62	2.56	3.40	4.26	5.18
B	34	1.61	2.55	3.29	4.17	5.07
A	17	1.63	2.67	3.31	4.19	5.10
TiO <sub>2</sub>	-	1.99	2.98	3.93	4.74	-
		(Ti <sub>1</sub> -O <sub>1</sub> )	(O <sub>1</sub> -O <sub>1</sub> )	(Ti <sub>1</sub> -Ti <sub>2</sub> )	(Ti <sub>1</sub> -O <sub>2</sub> )	

### 5.3.4. CATALYTIC ACTIVITY

The catalytic activity of MMATS in the oxidation (using aqueous  $\text{H}_2\text{O}_2$  as oxidant) of benzene, toluene and phenol was investigated (Tables 5.6 and 5.7). The amorphous titanosilicates have significant catalytic activity in the oxidation of benzene to phenol and phenol to hydroquinone and catechol. In contrast, both pure  $\text{TiO}_2$  and Ti-impregnated silica were found to have negligible activity in these reactions. Hence, the catalytic activity must be due to the isolated  $\text{TiO}_4$  species present in MMATS samples. The course of the hydroxylation of phenol on the three samples is shown in Fig. 5.25. The reaction occurs with an induction period and catechol is the first dihydroxybenzene obtained. However, *para*-benzoquinone is formed as soon as the reaction starts. A large concentration of  $\text{H}_2\text{O}_2$  in the beginning of the reaction probably leads to a fast overoxidation of hydroquinone in the reaction medium. From the initial rates, the intrinsic activity of TS-1 appears to be high (Table 5.7). However, under the conditions given in Table 5.7 (phenol/ $\text{H}_2\text{O}_2$  (mol) = 3), the  $\text{H}_2\text{O}_2$  efficiencies for TS-1 and MMATS-A at the end of the reaction are found to be 91 and 93 %, respectively. The lower  $\text{H}_2\text{O}_2$  efficiency observed for samples B and C due to their lower concentration of isolated Ti species, which are probably covered with tar during the initial stages of the reaction. In the absence of fresh Ti surface, there is a self decomposition of  $\text{H}_2\text{O}_2$  predominantly and hence the efficiency of utilization of  $\text{H}_2\text{O}_2$  in the hydroxylation of phenol is low. The main difference between TS-1 and MMATS-A lies in the product distribution and, due to the mesoporous nature of the material, no shape selectivity is seen in the latter. In the MMATS-catalyzed oxidation of phenol, for example, the ratio of the *ortho*- to *para*- isomer (catechol/hydroquinone)

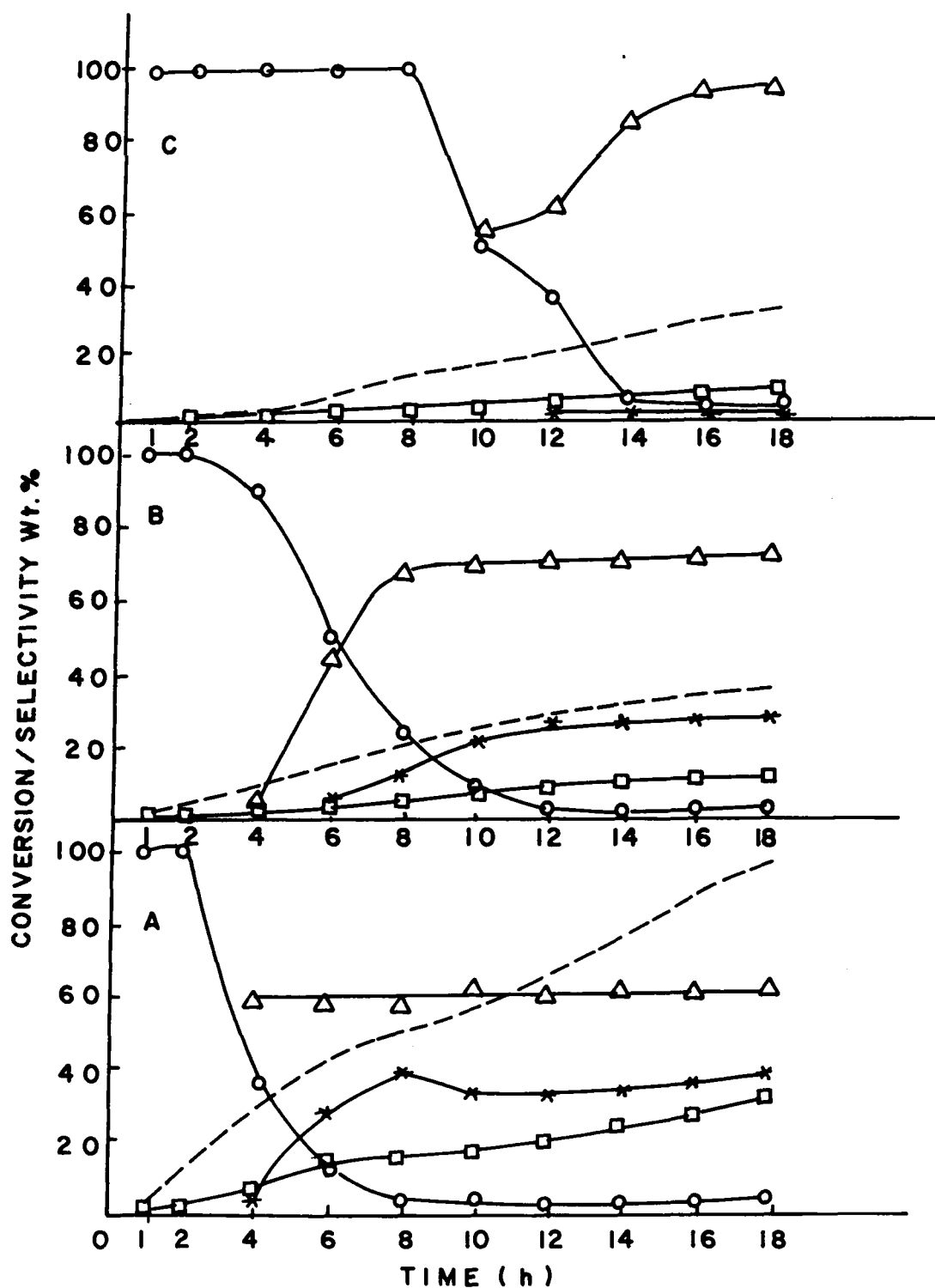


Fig. 5.25: Conversion (mol%) and selectivity (%) to different products in the hydroxylation of phenol over MMATS samples A to C as a function of time. (◻) phenol conversion; (Δ) catechol; (x) hydroquinone; (○) p-benzoquinone; (---) H<sub>2</sub>O<sub>2</sub> efficiency (mol %)

Table 5.6

Hydroxylation of Phenol over Amorphous Titanosilicate (MMATS) samples<sup>a</sup>

Sample	Turnover frequency	H <sub>2</sub> O <sub>2</sub> efficiency (%) <sup>c</sup>	Product distribution (wt%)	
			Catechol	Hydro- and p-benzoquinones
A	2.5	93.0	63.2	36.8
B	1.6	31.5	71.4	28.6
C	1.2	26.4	90.0	10.0
TS-1	5.5	91.2	47.5	52.5
TiO <sub>2</sub>	negligible	-	-	-
SiO <sub>2</sub>	no activity	-	-	-
Ti impr SiO <sub>2</sub>	no activity	-	-	-

<sup>a</sup> Catalyst: A-C (Si/Ti = 17,34, and 51, respectively); Temperature: 353 K, Phenol/catalyst (wt) = 10; Phenol/H<sub>2</sub>O<sub>2</sub> (mol): 3; Solvent (water): 20g. Duration = 18h

<sup>b</sup> Initial rates, moles converted per hour per Ti atom.

<sup>c</sup> Moles of H<sub>2</sub>O<sub>2</sub> consumed in the formation of dihydroxy benzenes excluding tar.

is around 2, in contrast to the TS-1 catalyzed oxidation in which the ratio drops to a value of around 1 or even less due to the shape selectivity of the medium pores in the titanosilicate molecular sieve (Table 5.6)<sup>91</sup>

The catalytic activity and the product distribution in the oxidation of benzene and toluene over sample A ( $\text{Si/Ti} = 17$ ) are summarized in Table 5.7. In the oxidation of benzene, the selectivity to phenol is almost 100 % at a conversion of 13.3 mol % of benzene ( $\text{benzene/H}_2\text{O}_2$  (mol) = 3), while the  $\text{H}_2\text{O}_2$  efficiency is 40 %. The latter value is lower for the other two mesoporous titanium silicates, Ti-HMS and Ti-MCM-41 in the oxidation of benzene<sup>6</sup> where, conversions of only 37 and 68 %, respectively, have been observed even at a nine-fold higher concentration of  $\text{H}_2\text{O}_2$  ( $\text{benzene/H}_2\text{O}_2 = 0.35$ ).

**Table 5.7**

**Catalytic activity of MMATS in the oxidation of benzene and toluene<sup>a</sup>**

Substrate	Solvent	Substrate (mol %)	conv.	$\text{H}_2\text{O}_2$ efficiency (mol %)	Product distribution (wt%)
Benzene	acetone	13.3		40	Phenol: 100
Toluene	acetonitrile	26.6		39	benzyl alcohol: 16.0 benzaldehyde: 49.1 benzoic acid : 3.9 <i>o</i> -cresol : 14.0 <i>p</i> -cresol : 16.5 others : 0.5

<sup>a</sup> Catalyst sample : A ( $\text{Si/Ti} = 17$ ); Temperature : 353 K; Substrate/Catalyst (wt) = 10;

Substrate/ $\text{H}_2\text{O}_2$  (mol): 3 (for benzene) and 1 (for toluene); solvent: 20 g; duration = 18h

<sup>b</sup>  $\text{H}_2\text{O}_2$  efficiency based on utilization of  $\text{H}_2\text{O}_2$  for the formation of all oxidized products.

In the oxidation of toluene (Table 5.7), a surprising observation is the formation of products due to the oxidation of the side chain (methyl group) of toluene (benzyl alcohol, benzaldehyde and benzoic acid) in addition to the formation of cresols. In fact, the oxidation of the methyl substituent in toluene is more predominant (69 % product selectivity) than aromatic hydroxylation (31 %). Such a phenomenon, while common in the case of vanadosilicates, VS-2 and V-NCL-1<sup>92,93</sup>, has so far not been observed over titanosilicates, TS-1 or TS-2. The latter selectively produces only cresols in the oxidation of toluene.<sup>94</sup> The mechanism of oxyfunctionalization of the organic substrates over MMATS is hence different from that over TS-1 or TS-2, and probably involves free radical routes. The ability of the amorphous titanosilicates to utilize aqueous H<sub>2</sub>O<sub>2</sub> in the oxidation reaction is an additional evidence for the presence of Ti<sup>4+</sup> ions in tetrahedral coordination in the silicate matrix.



---

## 5.4. AMORPHOUS ALUMINOSILICATES

---

### 5.4.1. WHY ALUMINOSILICATES ?

In previous sections the role of pH on the characteristic features of titanium silicate samples was discussed. In this section, an attempt has been made to know whether the same trend holds good for aluminosilicate samples also. The preparation and characterization of amorphous aluminosilicates prepared by sol-gel method at neutral and basic media are described. More emphasis is laid on the acidic properties since aluminosilicates are well known as acid catalysts. Apart from the pore size, acidity contributes to the activity and selectivity of many isomerization reactions. The isomerization of 1,3,5-trimethylbenzene over amorphous aluminosilicates prepared under basic and neutral conditions was investigated. The observed activity and selectivity to isomerization and disproportionation reactions are correlated to acidic properties. Thus the major objective here is to understand the role of pH of the sol-gel preparation in tailoring the acidic properties of the catalysts and therefore a typical acid catalyst, aluminosilicate is chosen.

## 5.4. 2. EXPERIMENTAL

### 5.4.2.1. *Catalyst Preparation*

Amorphous alumino-silicates with silica to alumina ratios of 5, 10, 20 and 40 were prepared by the sol-gel method in neutral medium using deionised water as the hydrolysing agent. The procedure consists of a gradual addition of deionised water to a stoichiometric mixture of aluminium isopropoxide in isopropanol and tetraethyl orthosilicate under constant stirring. A transparent gel was obtained on ageing at 313 K for 24 h which was subsequently calcined at 723 K for 16 h. The samples are designated as SA-5N, SA-10N, SA-20N and SA-40N, where N denotes neutral medium and 5, 10, etc. the silica to alumina ratio.

Similarly, amorphous alumino-silicate samples with a silica to alumina ratio in range from 5 to 40 were prepared in basic medium by adding aqueous ammonia (10%) into a stoichiometric mixture of aluminium isopropoxide in isopropanol and tetraethylorthosilicate with vigorous stirring, until the pH was about 8, to get a thick viscous gel instantaneously. The gel was thoroughly washed with deionised water and subsequently dried under reduced pressure ( $\approx 1$  torr) at 383 K for 24 h and calcined at 723 K for 18 h. The samples are designated as SA-5B, SA-10B, SA-20B and SA-40B, where B stands for basic medium, and 5, 10, etc. the silica to alumina ratio.

### 5.4.2.2. *Characterization of catalysts*

Chemical analysis of the samples was carried out by wet chemical methods. The ammonium ion exchange capacity of the samples was determined by treating

about 1g of the sample with 10 ml of 1M aqueous ammonium nitrate solutions under reflux for about 6 h, filtering, washing and drying at 393 K. The same procedure was repeated three times to ensure maximum exchange. The presence of tetrahedral aluminium was verified by calculating the amount of exchanged ammonia. Simultaneous TG-DTA of the samples were performed in a TG-DTA-92 model (Setaram, France) instrument in a flow of air (rate :  $100 \text{ cm}^3 \text{ min}^{-1}$ ) at a heating rate of  $10 \text{ K min}^{-1}$  up to 1273 K. The surface area and the pore size distribution of the samples were determined from nitrogen adsorption-desorption isotherms obtained using an Omnisorp -100 CX sorptometer. The scanning electron micrographs were taken on a Jeol Model 5200 microscope. Solid state MAS NMR spectra were obtained at room temperature with a Bruker AM 300 high resolution multinuclear NMR spectrometer at a resonance frequency of 400 M. Hz.  $[\text{Al}(\text{H}_2\text{O})_6]^{3+}$  and trimethyl silane were used as external standards for  $^{27}\text{Al}$  and  $^{29}\text{Si}$  NMR, respectively. The  $^{29}\text{Si}$  MAS NMR spectra were taken at 79.5 M Hz and a spinning rate of 3k Hz. with radio frequency pulses of 2.3 micro seconds, while the  $^{27}\text{Al}$  MAS NMR spectra were run at 104.3 M. Hz at a spinning rate of 4k Hz with a radio frequency pulses of 4 micro seconds. The framework IR spectra were recorded in a Nicolet (60 SXB) FTIR instrument using thin films of the samples on a silicon plate.

#### ***5.4.2.3. Acidity measurements***

The total acid sites and strength distributions were measured by gravimetric determination of chemisorbed pyridine at various temperatures using a McBain spring balance as per methods reported earlier.<sup>95</sup> The FTIR spectra of the adsorbed pyridine

were used to identify the type of acid sites and the relative amounts of Brønsted and Lewis acidity.<sup>96</sup> The IR spectra of adsorbed pyridine were obtained using self supported wafers of the sample ( $5\text{mg}/\text{cm}^2$ ). The sample was outgassed *in-situ* at 673 K at a pressure of  $10^{-6}$  torr for 6 h and cooled to 373 K before recording the spectra. The spectra were averaged for 500 scans with  $2\text{ cm}^{-1}$  resolution. The samples were then equilibrated in pyridine vapour (10 mm v-p) for 1 h and the excess pyridine was removed by evacuating the sample cell at 373, 473, 573 and 673 K for 1 h before recording the spectra.

#### ***5.4.2.4. Catalytic test reactions.***

The catalytic test reaction of isomerization of 1,3,5-trimethylbenzene was carried out in a tubular down flow silica reactor at temperatures ranging from 473 to 673 K and WHSV ranging from 2 to  $10\text{ h}^{-1}$ . The catalyst (1 g) was activated in a flow of air for 8 h prior to the reaction. A syringe pump was used to introduce the reactant over the catalyst bed at atmospheric pressure. The reaction products were analyzed by temperature programmed gas chromatography (Shimadzu) using a 5 % bentone + 5 % di-isodecyl phthalate column. Initially the temperature was held at 333 K for 5 min and then raised to 393 K at the rate of  $5\text{ K min}^{-1}$  and held for 30 min. The mass balance of the reaction products were routinely carried out with an accuracy of over 98 %. The details of the procedure followed and the apparatus used are described elsewhere.<sup>97</sup>

### 5.4.3. RESULTS AND DISCUSSION

#### 5.4.3.1. *Preparation of the catalyst*

A marked difference was observed between the aluminosilicate samples prepared in neutral and basic media. In the former case, a transparent silica-alumina sol from aluminium isopropoxide in isopropanol and tetraethylorthosilicate in ethanol, slowly transformed into gel after a gelation time of about 24 h. In the latter case, a quick formation of an opaque gel was observed due to the base-catalyzed hydrolysis of mixed alkoxides of aluminium and silicon followed by immediate condensation into  $\text{SiO}_2\text{-Al}_2\text{O}_3$  gel. On the other hand, the sol-gel method under neutral hydrolysis conditions gives a more homogeneous sample with a higher surface area than those obtained under base-catalyzed conditions mainly because of the molecular level mixing in the former case. This provided the motivation to explore its detailed properties by means of various techniques.

#### 5.4.3.2. *TG-DTA Studies*

The TG-DTA profiles of the representative samples, SA-5N (silica to alumina ratio 5) prepared by sol-gel method at neutral conditions are compared with those of the sample SA-5B, prepared in a basic medium (Fig. 5.26). In SA-5B sample, the weight loss (32.4 %) due to dehydration of the gel occurs in two distinct stages whereas in SA-5N it occurs in a single stage with a weight loss of about 22 % (curves

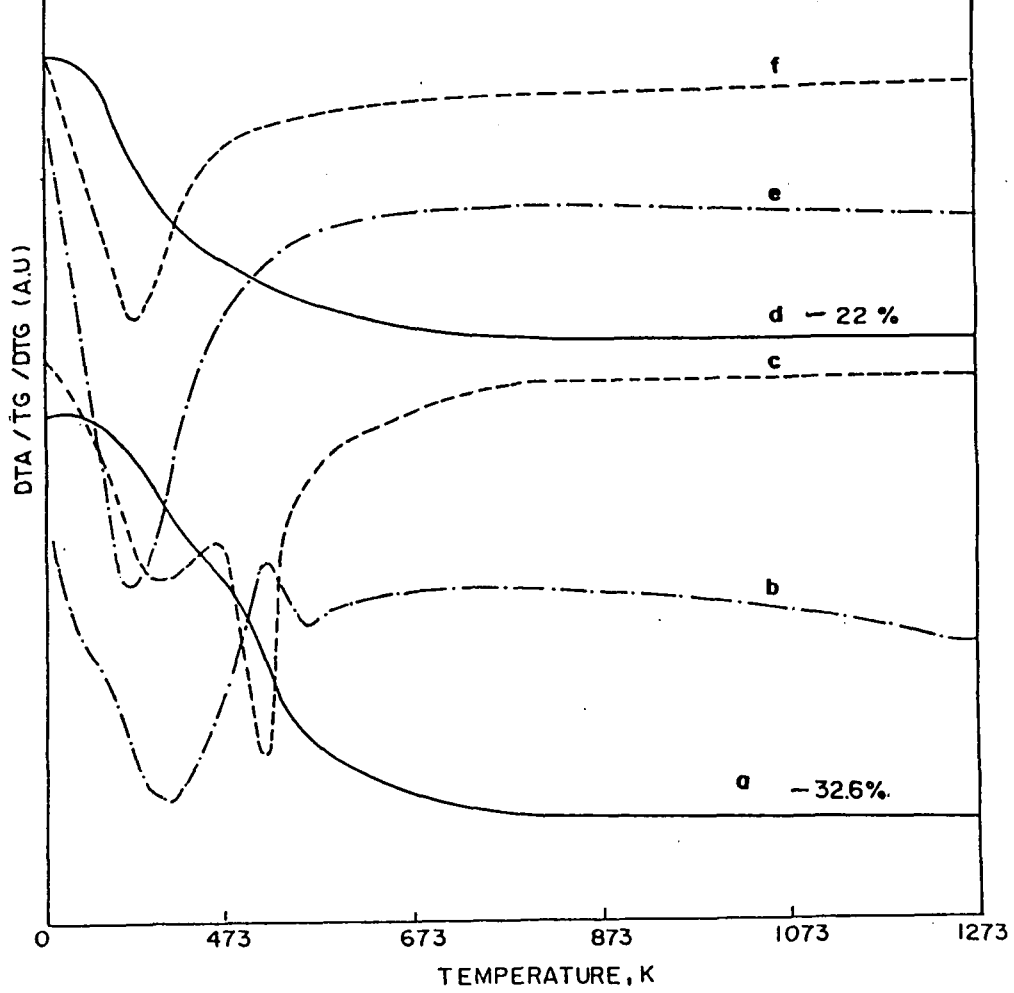


**Fig. 5.26: TG-DTG profiles of aluminosilicate gel ( $\text{SiO}_2/\text{Al}_2\text{O}_3 = 5$ ) prepared under basic and neutral medium (a,c, and d, f, respectively) and corresponding DTA curves (b and e, respectively).**

a and d). It indicates that the silica-alumina hydrogel species are not the same in both the samples. The difference in weight loss in the two samples may be attributed to the difference in the nature of hydrolysis products of aluminium alkoxide in the presence of alkoxide of silicon. Under neutral conditions, aluminium alkoxide is known to give  $\text{AlO}(\text{OH})$  whereas in the case of base-catalyzed hydrolysis it forms  $\text{Al}(\text{OH})_3$ .<sup>97</sup>

The corresponding DTA curves are also depicted in Fig. 5.26 (curves c and f). Here, two endotherms corresponding to the two steps of dehydration are observed in the case of the sample prepared under basic conditions (Fig. 5.26, curve c), whereas, the sample prepared in a neutral medium decomposes with a single endotherm. In both the cases, an exotherm indicating the crystallization of any dense phase of alumina is absent. A comparative analysis of the TG-DTA profiles of the samples prepared under the two conditions indicates that neutral medium gives a more homogeneously mixed alumino-silicate.

### ***5.4.3.3. Chemical Analysis***

The results of chemical analysis by wet chemical method and X-ray fluorescence technique are given in Table 5.8 in terms of silica to alumina ratios. Samples prepared under neutral pH conditions have a silica to alumina ratio almost similar to that of the input. Within the limits of experimental error there is an agreement between the silica to alumina ratios. Invariably, in the samples prepared in basic medium, the output ratio is somewhat lower than that of the samples prepared in a neutral medium. This is due to the dissolution of some silica.

#### 5.4.3.4. $N_2$ - Adsorption studies

Table 5.8 lists  $N_2$  physisorption data of sol-gel derived aluminosilicates prepared under neutral and basic conditions. The surface areas of the catalysts were calculated by applying the BET equation<sup>98</sup> to the nitrogen adsorption data in the relative pressure ( $p/p_0$ ) range of 0.05 - 0.30. A decrease in the silica to alumina ratio or an increase in the alumina content decreases the surface area. Apart from the

**Table 5.8**

**Physico-chemical properties of amorphous alumino-silicates prepared at neutral and basic conditions**

Sample name	Silica to alumina ratio		Surface area, $m^2 g^{-1}$	Pore volume, $ml g^{-1}$	
	by chemical analysis	by XRF		micropores	mesopores
SA-5N	5.0	4.9	378	0.12	0.10
SA-10N	10.0	9.7	393	0.13	0.11
SA-20N	19.6	19.5	421	0.15	0.13
SA-40N	38.9	39.1	440	0.17	0.14
SA-5B	4.8	4.8	340	-	0.18
SA-10B	9.2	9.4	375	-	0.21
BSA20B	18.1	18.4	410	-	0.25
SA-40B	36.2	33.5	430	-	0.28



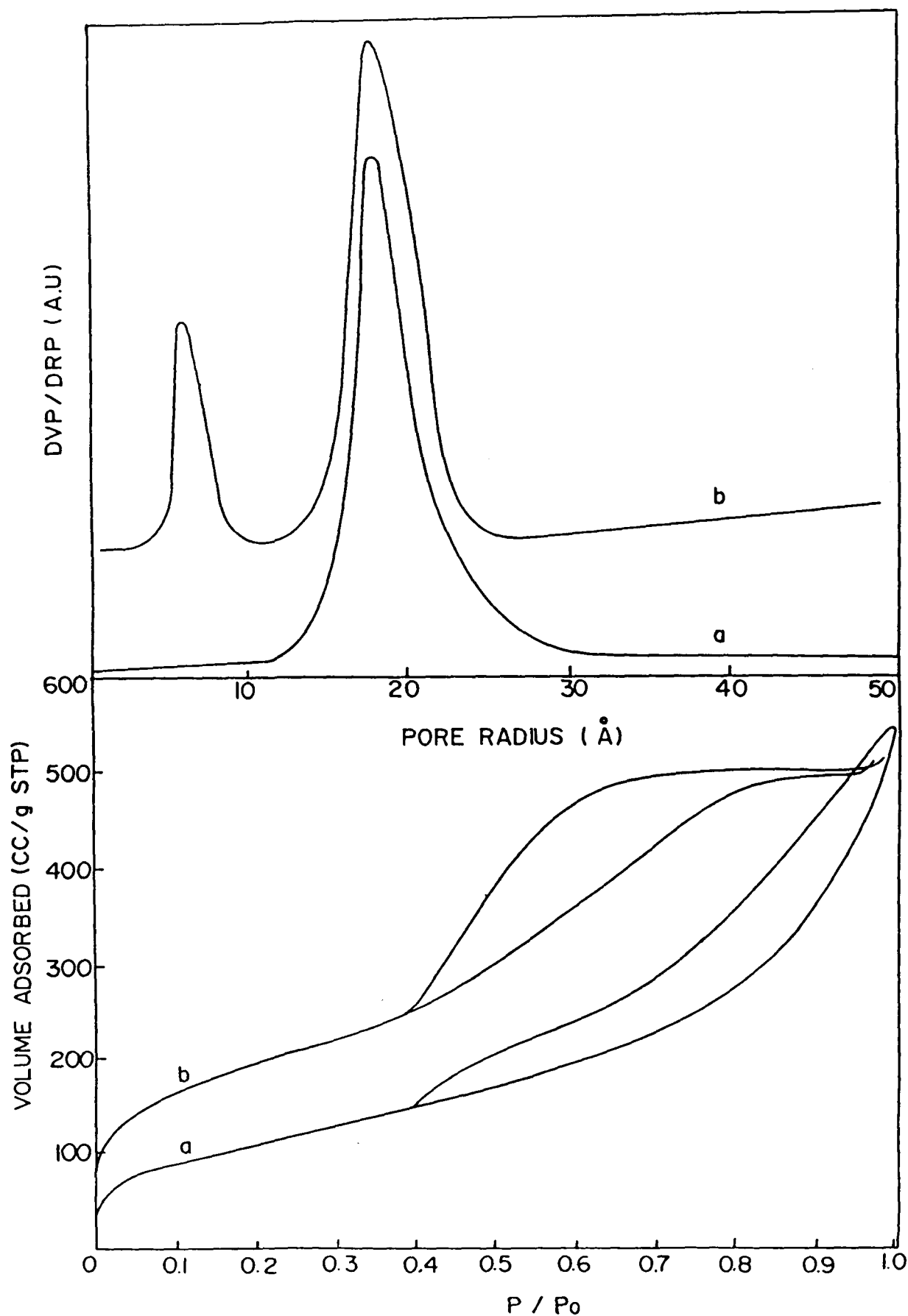


**Fig. 5.27:** N<sub>2</sub> adsorption-desorption isotherms of amorphous aluminosilicate samples, SA-5B and SA-5N calcined at 773 K (a and b, respectively) and the corresponding pore size distribution.

alumina content, the pH of the sol-gel preparation influences the distribution of the pore volume of the samples. For SA-5N samples, the surface area is due to the contribution from both micro and mesopores, which exist in almost similar proportions. This is clearly reflected by the pore volume data given in Table 5.8. In the base-catalyzed hydrolysis during the preparation of aluminosilicates by sol-gel method, only mesopores are observed in all the samples due to the highly cross linked nature of the gels. Under neutral conditions, hydrolysis leads to both micro and mesopores probably due to the presence of both linear as well as cross linked polymeric network.

The adsorption-desorption isotherms of SA-5N and SA-5B samples prepared under neutral and basic conditions with a silica to alumina ratio of 5 are given in Fig.5.27 along with the respective pore size distributions. It can be seen that both the samples have type IV hysteresis typical of mesoporous materials. The pore size distribution was calculated by applying the expanded form of BJH equation<sup>57</sup>, for the desorption data. The micropore size distributions were calculated from the low pressure region ( $p/p_0 = 10^{-4}$  to 0.1) of the isotherms by the Horwath-Kawazoe model.<sup>58</sup> These calculations indicate that the mesopore radius is around 20 Å in both the samples, while, in SA-5N micropores (radius = 8 Å) are also formed in addition to mesopores (curves a and b, Fig. 5.27).

#### 5.4.3.5. Solid state MAS NMR

##### $^{27}\text{Al}$ MAS NMR :

Fig. 5.28 shows the  $^{27}\text{Al}$  MAS NMR spectra of aluminosilicates SA-5N and SA-5B before calcination (a and b) and after calcination at 723 K (c and d, respectively). The intense peak at 56.3 ppm corresponds to tetrahedrally coordinated aluminium in the sample SA-5N, before calcination. In addition, a small peak around 4.7 ppm can be attributed to Al species present in the octahedral environment.<sup>100</sup> The sharpness of the peak at 56.3 ppm may be accounted for by an increase in the symmetry of the aluminium site and a consequent relaxation of the lattice strain due to the presence of water. The sample SA-5B also showed peaks at 57.1 ppm and 2.8 ppm corresponding to tetrahedral and octahedral aluminium species respectively. However, the peaks are relatively broader due to the asymmetry of the aluminium site (curves a and b).

The broadening of the peaks observed after calcination of the sample may be an indication of the dehydration of hydroxyls and the presence of some of the Al species in the distorted tetrahedral environment. In addition, a relative increase in the intensity of the peak at 2.4 ppm in SA-5B sample (curve d) compared to the corresponding peak of SA-5N (curve c) indicates an increase in the octahedral aluminium species in the former sample.

The  $^{27}\text{Al}$  MAS NMR spectra of aluminosilicate samples of different silica to alumina ratio, prepared at neutral pH are presented in Fig. 5.29 (curve a to d). The

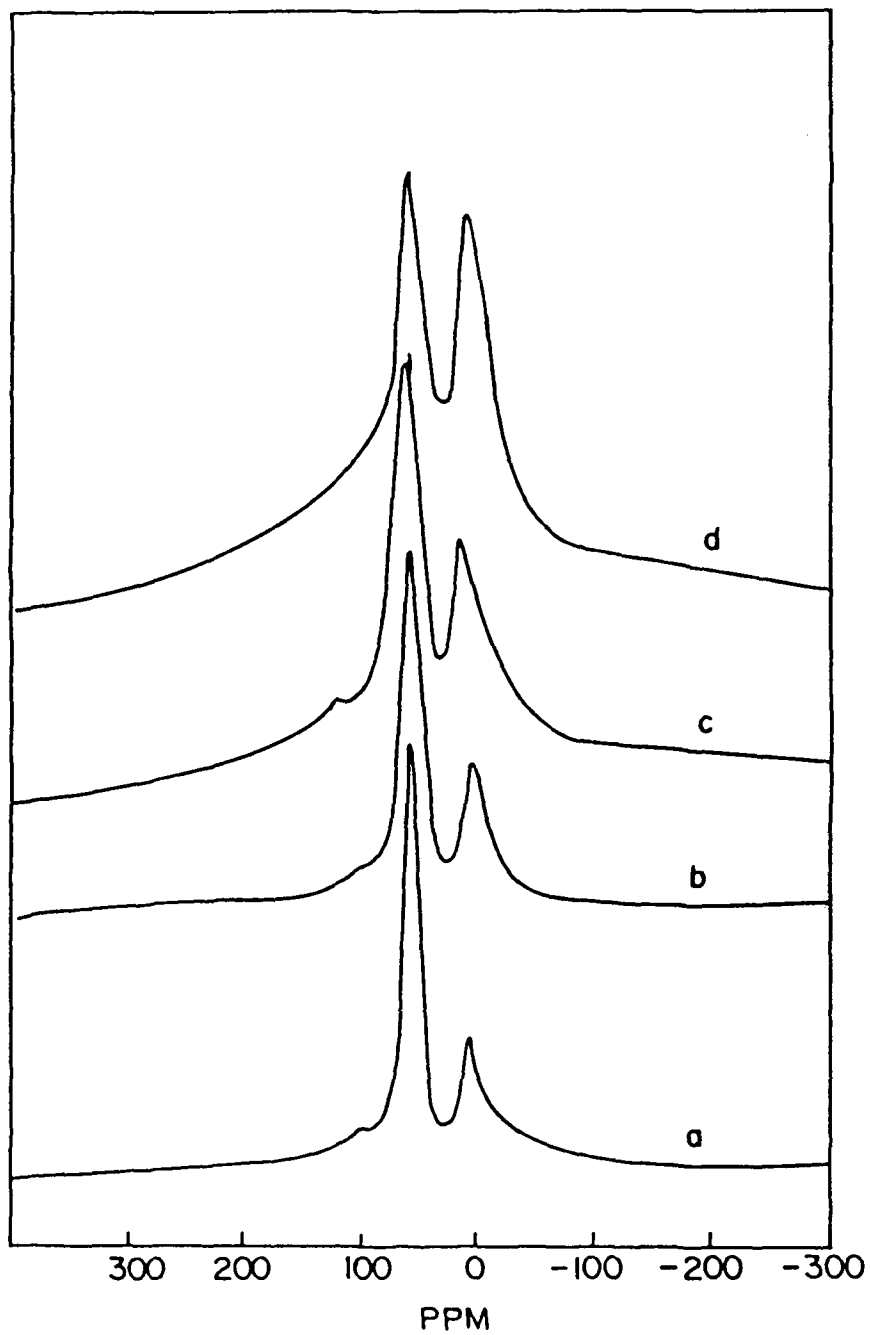


**Fig. 5.28:**  $^{27}\text{Al}$  MAS NMR spectra of aluminosilicate samples, SA-5N and SA-5B before calcination (a and b, respectively) and after calcination at 723 K (c and d, respectively)

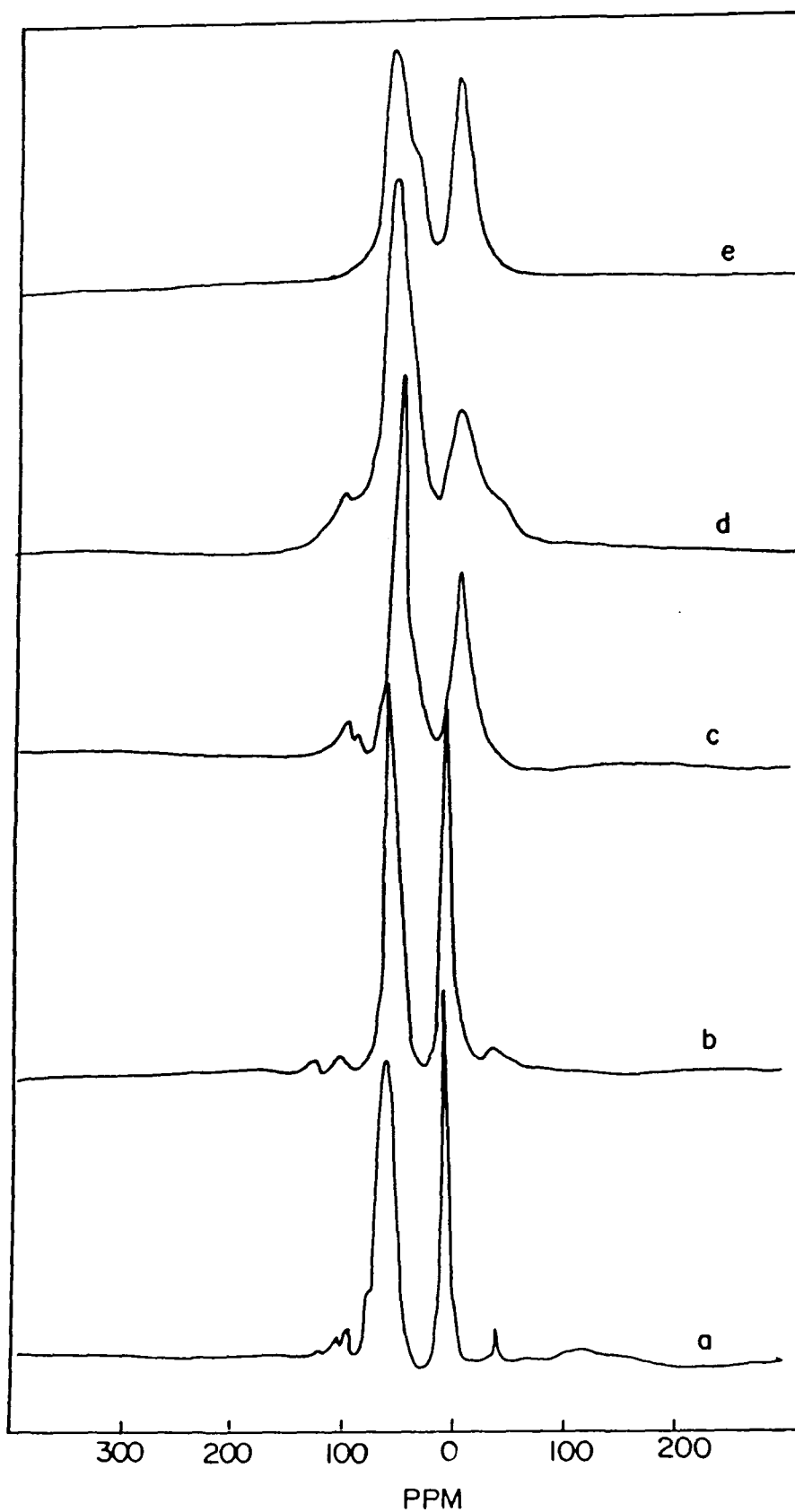


Fig. 5.29:  $^{27}\text{Al}$  MAS NMR spectra of aluminosilicate samples prepared under neutral conditions, SA-40N, SA-20N, SA-10N and SA-5N (a,b,c, and d, respectively) compared to that of a representative sample prepared under basic condition, SA-5B (e).

spectra have mainly two resonances; one around 50 - 60 ppm and other at around 0-5 ppm corresponding to 4 and 6 coordinated aluminium, respectively. One of the prominent features in the  $^{27}\text{Al}$  MAS NMR spectra is that aluminium shows different chemical shifts depending on the configuration of the Al ions.<sup>101</sup> The observed range of chemical shift can be separated into three regions: (i) alkyl aluminium compounds with 150 ppm shift or more to low field; (ii) a tetrahedrally coordinated aluminium with chemical shift between 140 and 40 ppm; and (iii) an octahedrally coordinated aluminium between 40 and -46 chemical shift. Accordingly, the percentage of the tetrahedral configuration was estimated from the spectra by taking the ratio of integral areas of the peaks at 50 - 60 ppm and at 0 - 5 ppm and the resultant values are presented in Table 5.9.

**Table 5.9.**

**$^{27}\text{Al}$  MAS NMR and  $^{29}\text{Si}$  MAS NMR spectral data of different samples.**

Samples	$^{27}\text{Al}$ MAS NMR peaks at (ppm)		$^{29}\text{Si}$ MAS NMR peak at (ppm)	% tetrahedral alumina	
				by $^{27}\text{Al}$ MAS NMR	by ammonia exchange
SA-40N	57.21	4.09	-109.4	70.5	73.0
SA-20N	55.75	3.33	-109.0	72.4	75.3
SA-10N	55.63	1.72	-109.1	72.2	75.4
SA-5N	58.40	-0.39	-107.4	73.0	76.0
SA-5B	57.95	2.46	-107.0	53.4	55.0

A comparison of these with the amounts of tetrahedral aluminium species obtained from ammonium ion exchange experiments reveals a good agreement between the two estimations. All the samples prepared under neutral conditions have greater than 70 % of tetrahedral aluminium species, while the base-catalyzed hydrolysis yields an equal amount of octahedral aluminium species. Tetrahedral configuration can be caused by effective Al-O-Si bond formation. According to the acid hypothesis<sup>102</sup>, the number of Al-O-Si bond should be proportional to the number of acid sites of mixed oxides. What is evident from this is that in the case of neutral preparation conditions, the slower rate of hydrolysis results in the homogeneous distribution of Al and Si. In the base-catalyzed hydrolysis, Al-O-Al chains are formed faster than the Al-O-Si and Si-O-Si chains because of the large difference in the rates of hydrolysis of aluminium isopropoxide and tetraethylorthosilicate. This results in a phase segregation, leading to a less uniform distribution of alumina in silica matrix. The most distinguishing feature of the <sup>27</sup>Al MAS NMR spectra of the samples with different silica to alumina ratios is that, as the alumina content increases, the line broadening increases. This may be once again due to decrease in the symmetry of the aluminium sites as alumina content increases.

### *<sup>29</sup>Si MAS NMR*

Fig. 5.30 presents the <sup>29</sup>Si MAS NMR spectra of SA-5N and SA-5B before calcination (a and b, respectively) and after calcination (c and d, respectively). In both the samples, a resonance centered at -109, -102 and -93 ppm appear as major peaks

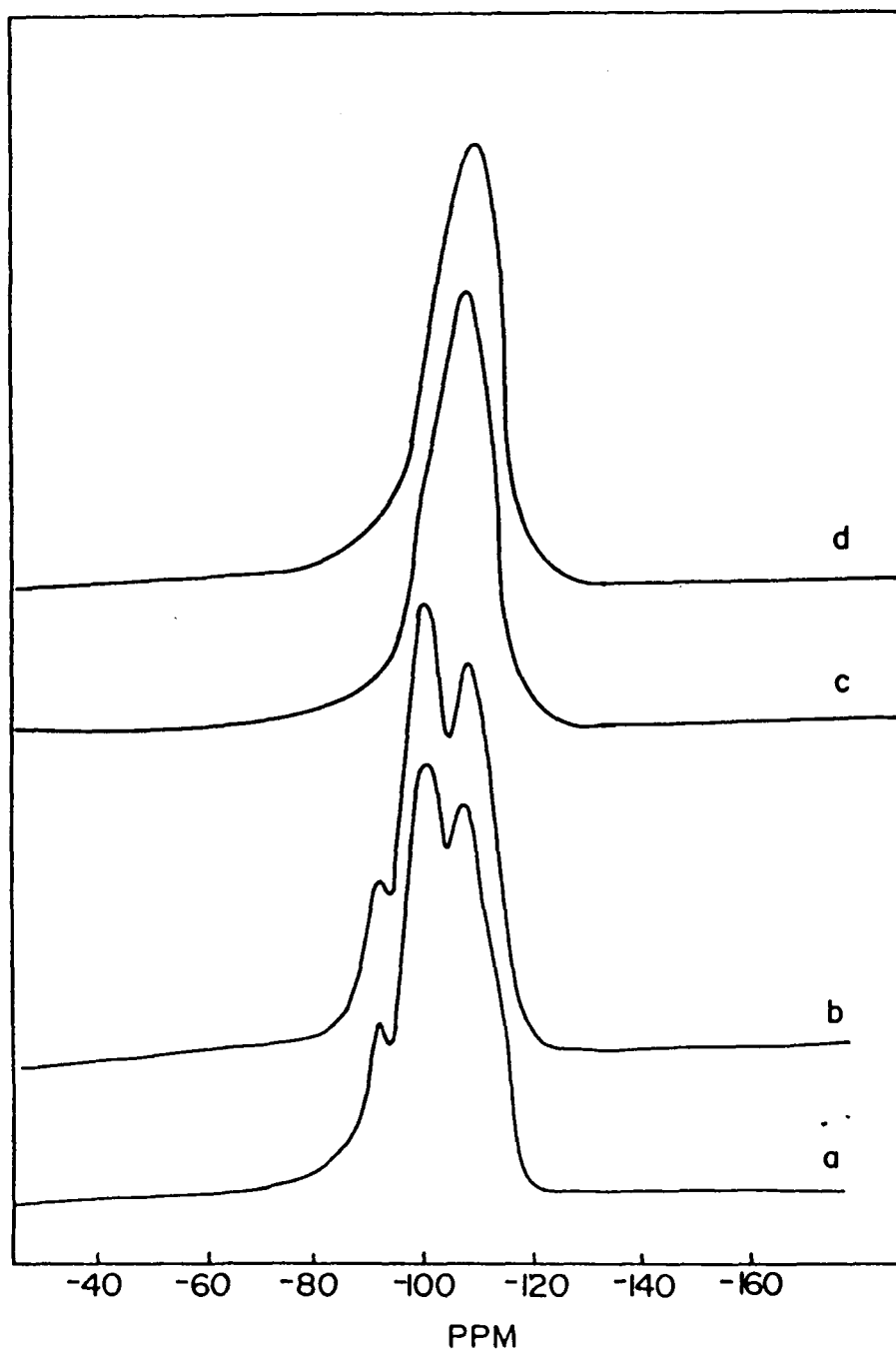
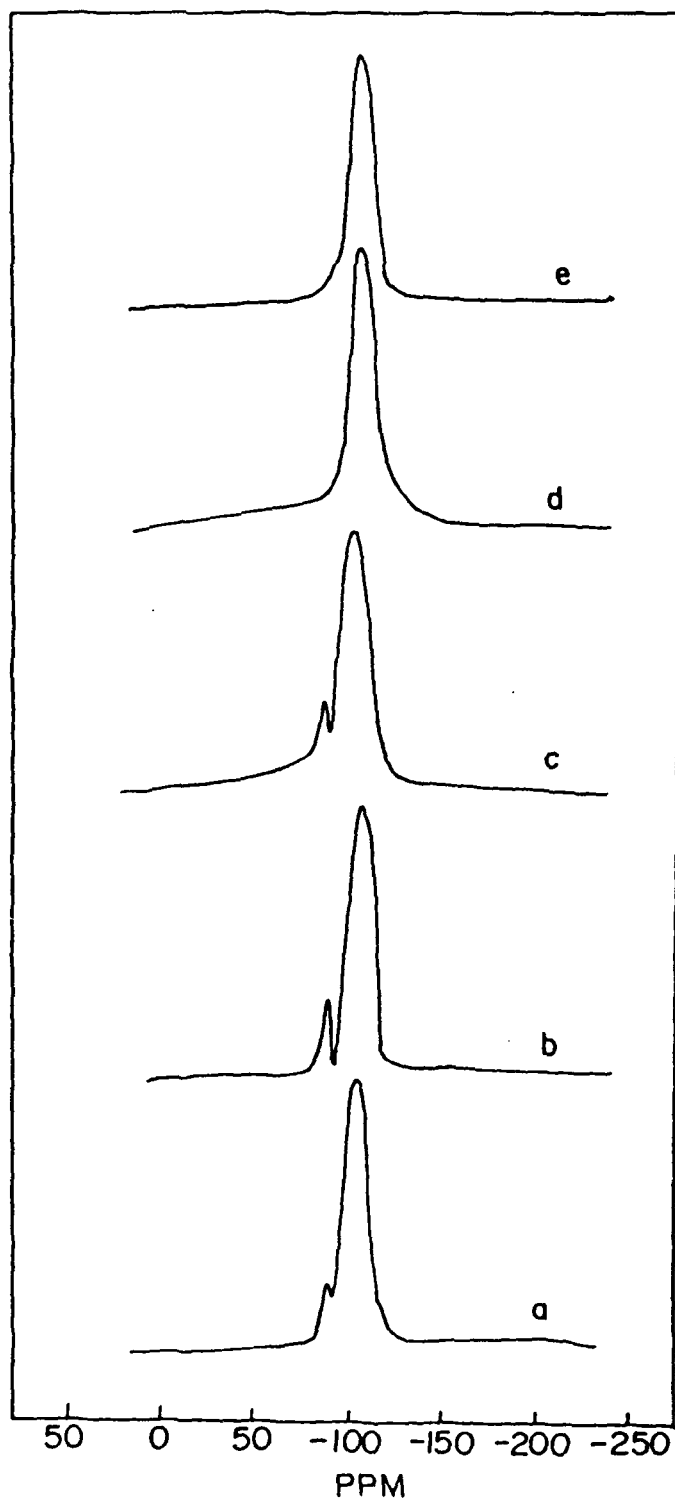


Fig. 5.30:  $^{29}\text{Si}$  MAS NMR spectra of SA-5N and SA-5B, before calcination (a and b) and after calcination at 723 K (c and d).





**Fig. 5.31:**  $^{29}\text{Si}$  MAS NMR spectra of aluminosilicate sample prepared under neutral condition, SA-40N, SA-20N, SA-10N and SA-5N (a, b, c and d, respectively) compared to that of a representative sample prepared under basic condition, SA-5B (e).

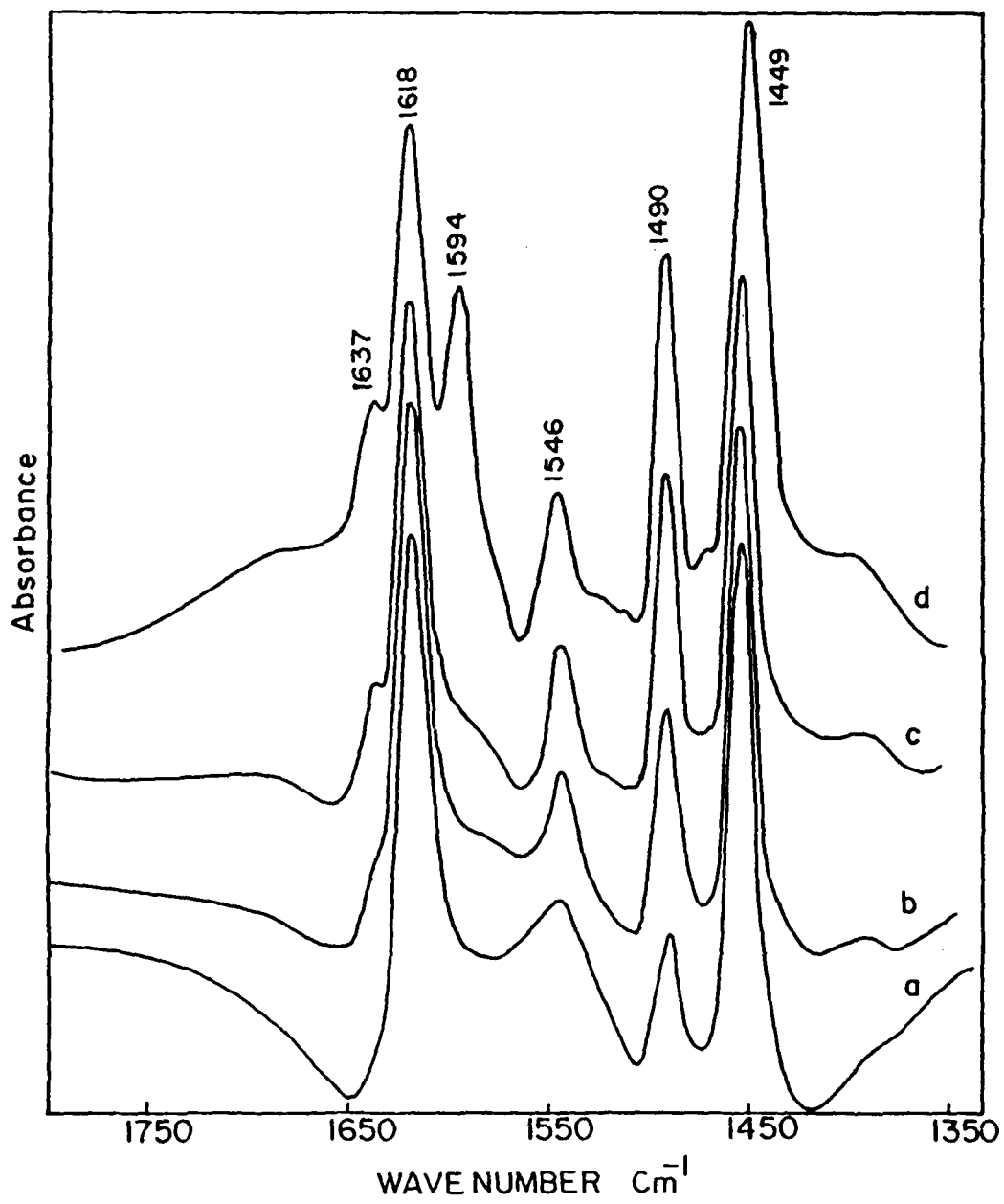
prior to calcination. It has already been reported that the silicon in  $\text{Si}(\text{OSi})_4$ ,  $\text{Si}(\text{OSi})_2(\text{OAl})_2$  and  $\text{Si}(\text{OAl})_4$  show peaks at -110, -100 and -85 ppm, respectively.<sup>103</sup> However, after calcination, a broad peak centered at -109.7 ppm is observed which corresponds to four -O-Si- linkages around each Si atom (curves a and d).

Fig. 5.31 shows  $^{29}\text{Si}$  MAS NMR spectra of the calcined samples SA-40N, SA-20N, SA-10N, SA-5N and SA-5B (curves a to e respectively). In addition to the resonance at around -109 ppm, a small peak at -88 ppm was observed in high silica samples. This can be attributed to two bridging oxygen atoms in  $(\text{HO})_2\text{Si}(\text{O-Si})_2$ <sup>103</sup>. In general, in crystalline zeolitic materials, high silica zeolites have considerable amount of silanols and they decrease with increasing aluminium content. Probably, the same trend is valid in amorphous materials also.

#### ***5.4.3.5. On the nature and strength of acidity.***

Pyridine is known to chemisorb on solid acids mainly in two ways : on Lewis acid sites (co-ordinatively unsaturated or electron pair acceptor sites) by coordination of nitrogen with a lone pair of electrons and on Brønsted acid sites by the transfer of a proton from the site to the nitrogen. Therefore, chemisorption of pyridine leads to the formation of pyridinium ions represented by bands in the region of 1632, 1490 and 1550  $\text{cm}^{-1}$  and coordinated species represented by bands in the region of 1620, 1490 and 1450  $\text{cm}^{-1}$ .<sup>104-106</sup>

Since isomerization reactions are acid catalyzed, it is likely that the difference in behaviour of the two sets of catalysts prepared by the two methods with respect to activity and selectivity can be correlated with the acidic characteristics. The FTIR



**Fig. 5.32:** FTIR spectra of adsorbed pyridine on amorphous aluminosilicate sample, SA-5N prepared under neutral medium, at 673, 573, 473 and 373 K (a, b, c and d, respectively)

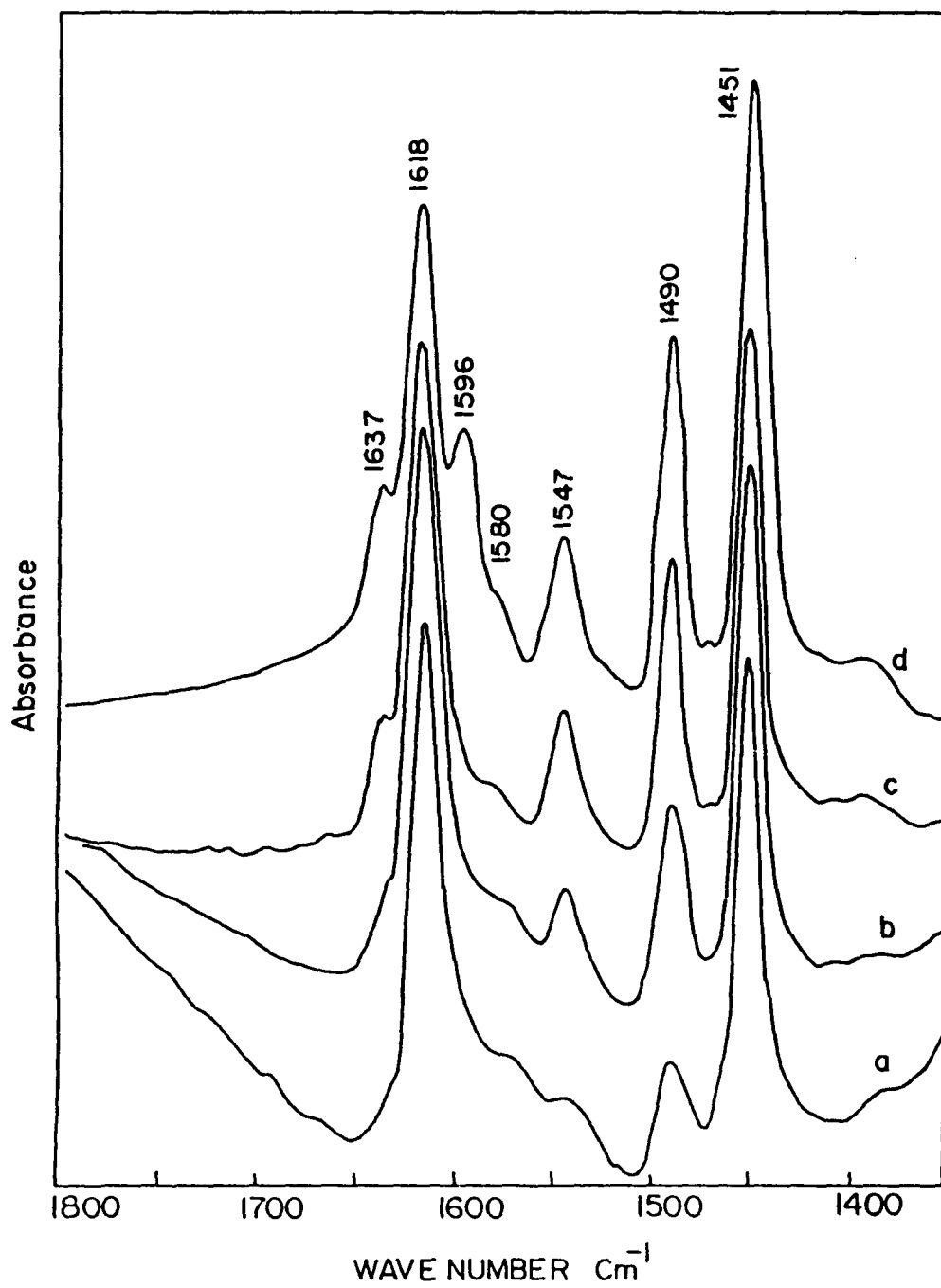


**Fig. 5.33:** FTIR spectra of adsorbed pyridine on amorphous aluminosilicate sample, SA-5B prepared under basic medium, at 673, 573, 473 and 373 K (a, b, c and d, respectively)

spectra of adsorbed pyridine on two samples, SA-5N and SA-5B are given in Fig. 5.32 and 5.33, respectively. Curves a to d refer to spectra of chemisorbed recorded after thermal treatment of the samples at 373, 473, 573 and 673 K and subsequent degassing of pyridine. The bands at 1449-1451  $\text{cm}^{-1}$ , 1618 and 1490  $\text{cm}^{-1}$  are due to pyridine adsorbed on Lewis acid sites while the bands at 1630, 1547 and 1490  $\text{cm}^{-1}$  are assigned to pyridine adsorbed on Bronsted acid sites. Although the main features of the FTIR spectra of adsorbed pyridine on the samples prepared under neutral and basic hydrolysis conditions are similar, the variation of the intensity of 1546  $\text{cm}^{-1}$  and 1450  $\text{cm}^{-1}$  bands with temperature of chemisorption are remarkably different. The intensity of the peak at 1450  $\text{cm}^{-1}$  remains reasonably high at all temperatures in both the samples indicating the presence of strong Lewis acid sites. However, there is a significant difference with respect to peak at 1546  $\text{cm}^{-1}$ . In SA-5N, even after degassing at 673 K, there is a strong absorption indicating the presence of Bronsted acid sites. In contrast, the peak at 1547  $\text{cm}^{-1}$  disappears completely on degassing the pyridine adsorbed on SA-5B at 673 K. It can be, therefore concluded that SA-5N has a relatively higher amount of Brönsted acid sites.

In Fig. 5.34, The total amounts of chemisorbed pyridine on SA-5B and SA-5N (curves a and b) at different temperatures, determined gravimetrically, are plotted for comparison. The variation of normalized relative amount of Lewis to Bronsted sites (L/B) of SA-5N and SA-5B (curves c and d) with temperature of chemisorption is also depicted in the same figure. The latter is obtained by taking the ratio of integral areas of peaks at 1450 and 1546  $\text{cm}^{-1}$  and plotting them as a function of temperature. The difference in the acid site distribution in the two samples are now clearly noticeable. The total acidity of SA-5N is more than that of SA-5B at all temperatures. The acidity

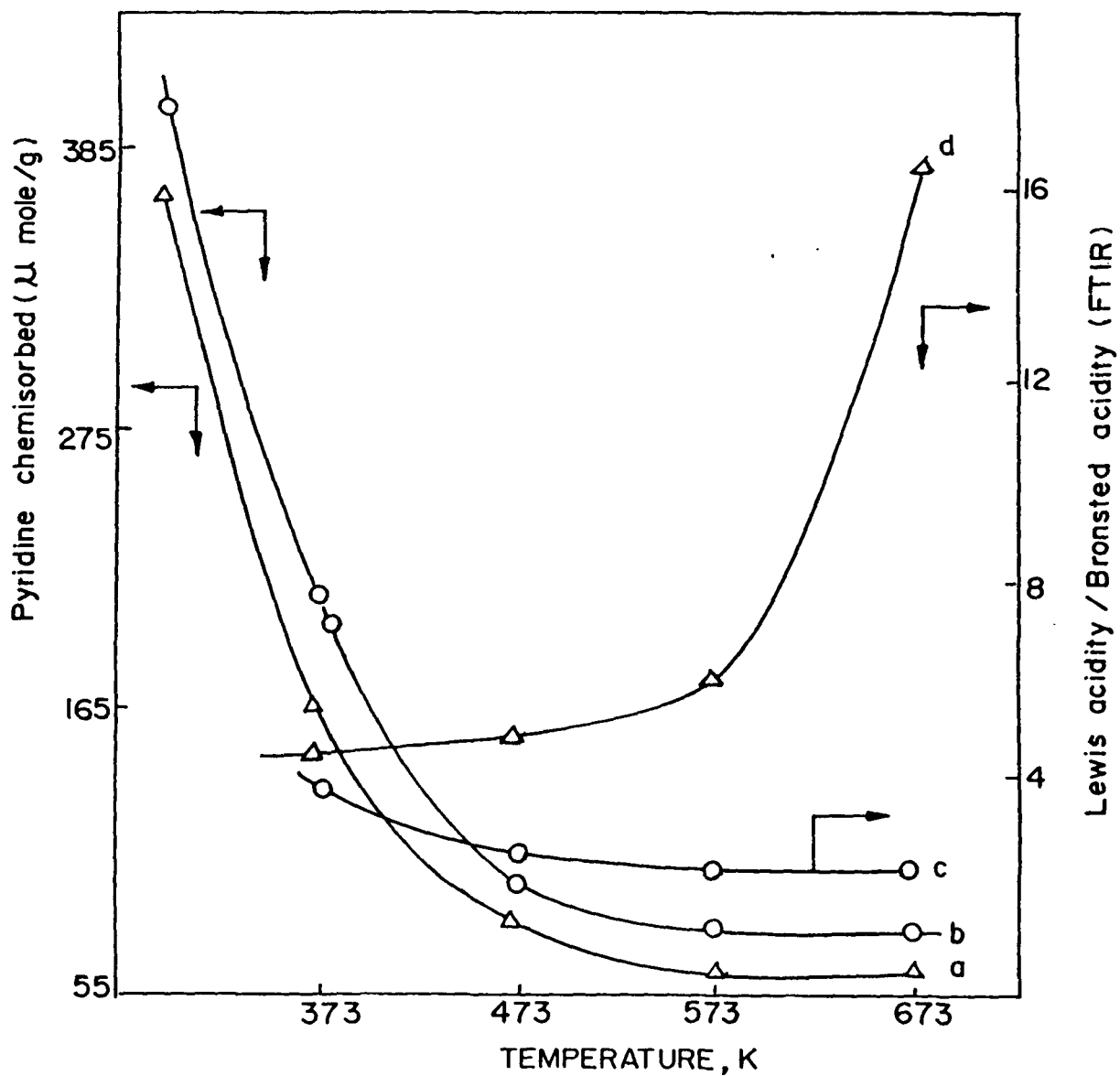


**Fig. 5.34:** Variation of total acidity (gravimetric adsorption of pyridine) and Lewis/Bronsted acidity ratio (FTIR) of SA-5N (b and d) and SA-5B samples (a and c) with temperature.

of SA-5B sample decreases beyond 573 K with a relative decrease in the amount of Bronsted acid sites as reflected by a sharp increase in L/B from 5 to 16. SA-5N is more acidic than SA-5B, the Brönsted acidity is relatively higher and the L/B ratio remains in the range 5 - 2.5. It can therefore be concluded that the higher acidity of SA-5N sample is due to the contribution from the Brönsted acidic sites. The formation of Brönsted acidity of silica - alumina is linked to the formation of the Si-O-Al bond.<sup>107</sup> As per the FTIR study of pyridine adsorption, sol-gel derived samples prepared in neutral media show higher Brönsted acidity and hence significant Si-O-Al linkages. This is in agreement with the <sup>27</sup>Al MAS NMR spectral observations discussed earlier.

#### ***5.4.3.6 Isomerization of 1,3,5-trimethylbenzene***

Table 5.10 and 5.11 present the results of isomerization and disproportionation of 1,3,5 trimethylbenzene over SA-5N and SA-5B samples, respectively, at different temperatures. With similar silica to alumina ratios, similar conversion and product selectivity may be expected. However, there is considerable difference with respect to activity and product selectivity which needs to be accounted for. At all temperatures, conversion on SA-5N is higher, particularly between 573 and 673 K, than on SA-5B. But the extent of isomerization relative to disproportionation, as reflected by their ratio (I/D), is always more on SA-5B than on SA-5N. Since both the samples have mesopores, this difference cannot be attributed exclusively to the nature of pores. A comparison of I/D as a function of temperature is made in Fig. 5.35. There is a commonality in the trend shown by the two samples with respect to I/D ratio (Fig. 5.35) and the corresponding L/B (Lewis acidity/Brönsted acidity) ratio (Fig. 5.34).

Thus, the product distribution is directly controlled by the nature of the acidic sites which is, in turn, controlled by the pH of the sol-gel preparation. The SA-5N sample which has relatively higher acidity and higher Brönsted acid sites shows a higher conversion and also yields more disproportionation products. It was also found that

**Table 5.10**

**Isomerization and disproportionation of 1,3,5 trimethyl benzene over SA-5N.**

Temperature, K		573	623	673	723
Conversion, mole %		20.0	34.5	59.2	69.7
<b>Product distribution</b>					
Toulene (mole %)		-	-	0.1	0.1
Xylenes (mole %)	para	0.05	0.1	0.7	1.10
	meta	0.40	0.60	2.9	3.0
	ortho	0.2	0.2	1.0	1.6
Trimethyl benzenes, (mole %)	1,3,5	80.0	65.5	40.8	30.3
	1,2,4	14.1	25.2	43.5	50.5
	1,2,3	0.9	3.2	5.5	7.7
Tetramethylbenzenes (mole %)	1,2,4,5	3.3	4.3	4.8	5.3
	1,2,3,5	1.05	0.9	0.7	0.5
Isomerizaion/Disproportionation (I/D)		3.1	4.7	4.9	5.1



the quantities of xylenes formed were almost equal to those of tetramethyl benzenes and, therefore, dealkylation reactions do not take place. The variation of the activity and selectivity of the reaction with time was also studied. The extent of deactivation was less in SA-5N than in SA-5B and also crystalline porous materials like HY. The I/D ratio increases showing that disproportionation reaction deteriorates

**Table 5.11**

**Isomerization and disproportionation of 1,3,5 trimethyl benzene over SA-5B.**

Temperature, K		573	623	673	723
Conversion, mole %		9.9	20.7	42.0	62.3
Product distribution					
Toulene		-	-	0.1	0.1
Xylenes	para	0.05	0.1	0.3	0.5
	meta	0.2	1.0	1.3	1.7
	ortho	0.1	0.1	0.6	0.8
Trimethyl benzenes	1,3,5	90.1	79.3	58.0	37.7
	1,2,4	7.1	17.7	34.2	49.7
	1,2,3	0.6	1.2	4.0	6.7
Tetramethylbenzenes	1,2,4,5	1.8	0.6	1.3	2.3
	1,2,3,5	0.05	0.1	0.2	0.5
Isomerization/Disproportionation, (I/D)		3.5	9.9	10.3	9.8

with time, unlike trend displayed by zeolites where, disproportionation increases with time on stream.<sup>97</sup> The amount of coke deposited after 8 h of reaction was also estimated. It was found that the extent of coke formation was only about 2 % in the case of SA-5N, whereas in SA-5B, it was about 5 %. This also accounts for the difference in the deactivation behaviour observed in the samples prepared by the two methods.

To study the stability of catalysts under hydrothermal conditions, the catalysts with a silica to alumina ratio of 5 were heated to 1033 K under steam for 8 h and then tested for their isomerization activity. The results are presented in Table 5.12. Even after the steam treatment the sample prepared under neutral condition shows significant catalytic activity (with only 35 % loss in activity) and selectivity to isomerization products, while the sample prepared under basic condition shows a 57 % decline in the activity after steam treatment.

Trimethyl benzenes undergo both disproportionation and isomerization during conversions over solid acid catalysts such as LaY zeolite.<sup>97</sup> Although, a commendable amount of work on the mechanistic features of these reactions has been reported, the exact reason for the difference in activity and selectivity is not well understood. The primary reason for the formation of various products in zeolite based materials is believed to be the existence of pores, which is why the isomerization of m-xylene and 1,3,5 trimethyl benzene can be used as a test reaction for assessing the nature of pores in the crystalline porous materials. However, besides pore size differences, several other factors play a significant role in isomerization and disproportionation selectivity.<sup>107</sup> For example, it is known that disproportionation requires stronger acid sites, in particular, Lewis and Brønsted acid sites.<sup>108</sup>

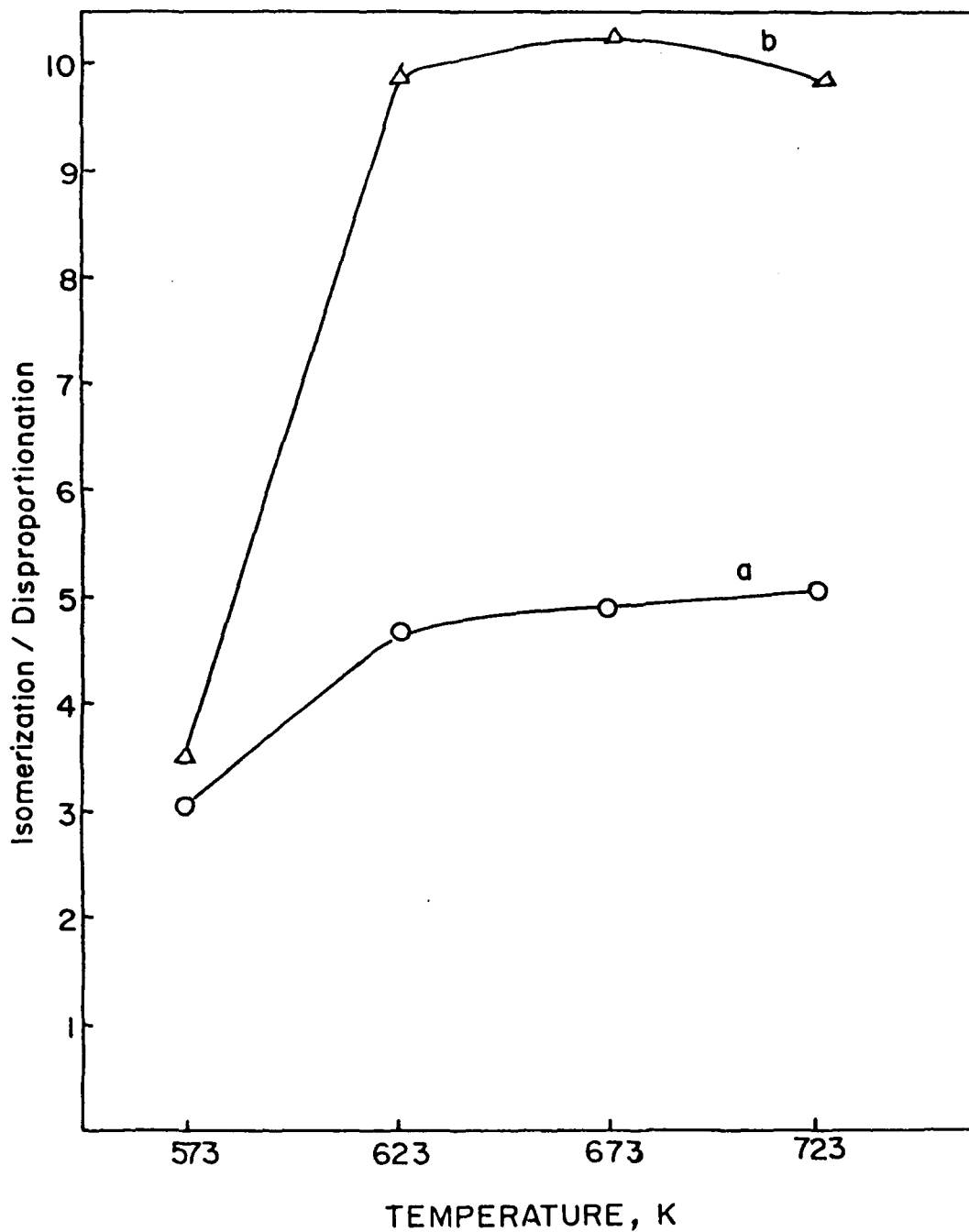


**Fig. 5.35: Variation of isomerization/disproportionation ratio as a function of temperature for the isomerization of 1,3,5-trimethylbenzene shown by SA-5N and SA-5B samples ( a and b, respectively)**

Table 5.12

**Isomerization and disproportionation of 1,3,5 trimethyl benzene at 673 K over SA-5N and SA-5B before and after steam treatment at 673 K**

Sample	SA-5N		SA-5B	
	before steam treatment	after steam treatment	before steam treatment	after steam treatment
Conversion, mole %	59.2	38.1	42.0	18.0
Product distribution				
Toulene	0.1	-	0.1	-
Xylenes	para	0.7	0.2	0.3
	meta	2.9	1.2	1.3
	ortho	1.0	0.5	0.6
Trimethyl benzenes	1,3,5	40.8	61.9	58.0
	1,2,4	43.5	31.1	34.2
	1,2,3	5.5	3.8	4.0
Tetramethylbenzenes	1,2,4,5	4.8	1.1	1.3
	1,2,3,5	0.7	0.2	0.2
Isomeriztaion/Disproportionation, (I/D)	4.9	10.9	10.3	11.8

In the present case, since SA-5N sample has an almost equal number of Lewis and Brönsted acid sites as reflected by lower L/B ratio, the lower value of I/D seems reasonable. Among the various existing routes for the preparation of amorphous aluminosilicates, the hydrolysis at neutral conditions is shown to be better in obtaining significantly high Brönsted acidity than hydrolysis at basic conditions.

---

## 5.5. Summary

---

The versatility of the sol-gel process is evidenced by the rapid increase of the number of catalytic materials prepared as aerogels. Sol-gel methods have been applied to prepare single-component oxides, multiple-component oxides, solid solutions, supported metals, bimetallic catalysts, superacids, amorphous materials, etc. Plenty of scope exists in exploiting the sol-gel technology in the preparation of catalytic materials.

The influence of pH of preparation on the sol gel-derived amorphous titanium silicate catalysts was investigated through SEM, N<sub>2</sub> adsorption, UV-visible and FTIR spectroscopic techniques, which led to some meaningful conclusions. Surface area and pore size distribution are largely dependent on the pH prevailing during the sol-gel formation. The acidity or otherwise of the medium has a marked effect on the surface area and the nature of the pores. An acidic medium leads to a high surface area (550 m<sup>2</sup>/g) with predominant micropores; a neutral medium, a high surface area (480 m<sup>2</sup>/g) with both micro and meso pores; and under basic conditions a low surface area (>100 m<sup>2</sup>/g) with meso/macro pores is obtained. UV-visible spectra indicated that at neutral

medium, tetrahedral coordination of Ti in silica framework is favoured. Quantitative FTIR spectroscopic measurements were carried out in the framework region, the surface hydroxyl stretching region and the ring vibration region of adsorbed pyridine. The ratio of intensities of the  $960\text{ cm}^{-1}$  band and the  $1220\text{ cm}^{-1}$  band (Si-O-Ti/Si-O-Si), which is a measure of the Ti dispersion, passes through a maximum at neutral pH. The integrated area of hydrogen bonded hydroxyl groups ( $3700 - 3200\text{ cm}^{-1}$ ), which is a measure of defect sites, also passes through a maximum at neutral pH. The spectra of the pyridine chemisorbed on the sample, prepared at neutral pH, shows that it is only hydrogen bonded whereas the spectrum of the sample prepared in acidic and basic media shows traces of weak Lewis acidity. The concentration of the adsorbed pyridine also passes through a minimum at neutral pH. From these observations, it is concluded that sol-gel formation in neutral medium is the best condition to achieve isomorphous substitution of Ti in the silica framework in  $\text{SiO}_2$ - $\text{TiO}_2$  materials.

Novel, amorphous titanosilicates with a bimodal, fairly narrow pore size distribution with an average pore width around 0.85 and 3.6 nm were synthesized from the corresponding alkoxides, at neutral pH in the absence of nitrogenated organic bases, acids or other bases. The  $\text{Ti}^{4+}$  ions are well dispersed in these materials and form Ti-O-Si bonds. There is no evidence for the presence of a separate  $\text{TiO}_2$  phase. TG/DTA analysis and temperature-programmed reduction in  $\text{H}_2$  indicate that these Ti atoms do not migrate and sinter to form  $\text{TiO}_2$  at elevated temperatures, nor are they reduced easily to lower oxidation states in  $\text{H}_2$ . X-ray scattering studies suggest that at least a part of the Ti atoms are in a tetrahedral environment of oxygen atoms. These titanosilicates are active in oxidation reactions using  $\text{H}_2\text{O}_2$  as the oxidizing agent. In some cases, as in the oxidation of phenol to catechol and hydroquinone, their activity

and selectivity is comparable (in some respect even superior) to the titanium molecular sieve, TS-1 and the new mesoporous materials like Ti-HMS and Ti-MCM-41. MMATS is unique among the solid catalysts investigated so far in yielding more catachol than hydroquinone in the oxidation of phenol by  $H_2O_2$ . The oxyfunctionalization of the methyl substituent in toluene to give benzyl alcohol, benzaldehyde and benzoic acid, in addition to cresols, distinguishes MMATS from TS-1 or TS-2

Amorphous aluminium silicate samples with various silica-to-alumina ratios were prepared by the sol-gel method at neutral and basic pH conditions. The effect of pH on the textural properties was studied by  $N_2$  physisorption studies. The sample prepared in a basic medium is mesoporous, and the sample prepared under neutral conditions contains both micro and mesopores. The  $^{29}Si$  and  $^{27}Al$  MAS NMR data threw light on the role of pH on the formation of tetrahedrally coordinated Al-O-Si linkages. The amount of tetrahedral Al as indicated by NMR data is in agreement with the ammonia exchange capacity. FTIR spectra of adsorbed pyridine on the samples revealed the extent of Lewis and Brønsted acid sites. Gravimetric study of pyridine chemisorption indicated that the sample prepared in a neutral medium is more acidic, as reflected in its activity in the isomerization and disproportionation of 1,3,5-trimethyl benzene. A relationship was found to exist between the selectivity and acidity expressed in terms of isomerization/disproportionation ratio (I/D) and the Lewis acidity/Bronsted acidity (L/B) ratio.

## REFERENCES

1. M. Taramasso, G. Perego and B. Notari, US Patent 4,410,50 (1983); B. Notari, *Stud. Surf. Sci. Catal.*, **60** (1991) 343.
2. J. S. Reddy, R. Kumar and P. Ratnasamy, *Appl. Catal.*, **58** (1990) L1.
3. D. P. Serrano, Li Hong-Xin and M. E. Davis, *J. Chem. Soc. Chem. Commun.*, (1992) 745.
4. M. A. Camblor, A. Corma, A. Martinez and J. Perez-Parient, *J. Chem. Soc., Chem. Commun.*, (1992) 8.
5. M. A. Camblor, A. Corma and J. Perez-Pariente, *Zeolites*, **13** (1993) 82.
6. J. S. Reddy and R. Kumar, *J. Catal.*, **130** (1991) 440.
7. U. Romano, A. Esposito, F. Maspero, C. Neri, M. G. Clerici, *La Chimica & L'Industria*, **72** (1990) 610.
8. P. T. Tanev, M. Chibwe and T. J. Pinnavaia, *Nature*, **368** (1994) 321.
9. A. Corma, M. T. Navarro, J. Perez-Pariente and F. Sanchez, *J. Chem. Soc. Chem. Commun.*, (1994) 147.; *Stud. Surf. Sci. Catal.*, **84** (1994) 69.
10. O. Franke, J. Rathonsky, G. Schulz-Ekloff, J. Starek and A. Zukal, *Stud. Surf. Sci. Catal.*, **84**, (1994) 77.
11. C. J. Brinker, *J. Non-Cryst. Solids*, **100** (1988) 31.
12. B. E. Handy, A. Baiker, M. S. Marth and A. Wokaun, *J. Catal.*, **133** (1992) 1.
13. T. Shikada, K. Fujimoto, T. Kunugi and H. Tominaga, *J. Chem. Tech. Biotechnol.*, **33** (1983) 446.
14. T. Hayashi, T. Yamada and H. Saito, *J. Mater. Sci.*, **18** (1983) 3137.
15. B. Yoldas, *J. Non-Cryst. Solids*, **38** (1980) 81.
16. K. Kamiya and S. Sakka, *J. Mater. Sci.*, **15** (1980) 2937.
17. P. C. Schultz, *J. Amer. Ceram. Soc.*, **59** (1976) 214.
18. C.U.I Odenbrand, S.L.T.Anderson, J.M.G. Brandin and G. Busca, *J. Catal.*, **125** (1990) 541.
19. S. Imamura, S. Ishida, H. Tarumoto, Y. Saito and T. Ito, *J. Chem. Soc. Farad. Trans.*, **89** (1993) 757.
20. R. Hutter, D. C. M. Dutoit, T. Mallat, M. Schneider and A. Baiker, *J. Chem. Soc. Chem. Commun.*, (1995) 163.
21. H. Nakabayashi, *Bull. Chem. Soc. Jpn.*, **65** (1992) 914.
22. J. R. Sohn and H. J. Zang, *J. Catal.*, **132** (1991) 563.
23. M. Toba, F. Mizukami, S. Niwa, T. Sano, K. Maeda, A. Annila and J. Komppa, *J. Mol. Catal.*, **91** (1994) 277.
24. C. L. Thomas, *Ind. Eng. Chem.*, **41** (1949) 2564.
25. R. W. Blue and C. T. Eagle, *Ind. Eng. Chem.*, **43** (1951) 494.
26. C. V. Holm, C. G. Balley, and A. Clark, *J. Phys. Chem.*, **63** (1959) 129.



27. A. Clark., *J. Catal.*, **1** (1962) 244.
28. V. C. Hom and A. Clark, *J. Catal.*, **2** (1963) 16.
29. A. Leonard, S. Suzuki, J. J. Fripiat and de Kimpe, *J. Phys. Chem.*, **68** (1964) 2608.
30. D. Barthomeuf, *C. R. Acad. Sci.*, **259** (1954) 3520.
31. J. W. Ward and R. C. Hansford, *J. Catal.*, **13** (1969) 154.
32. B. D. Flockhart, K. Y. Lieu and R. C. Pink, *J. Catal.*, **32** (1974) 10.
33. R. F. Vogel, G. Mercelin and W. L. Kohl, *Appl. Catal.*, **12** (1984) 237.
34. R. J. Pelet, C. S. Blackwell and J. A. Robo, *J. Catal.*, **31** (1988) 10.
35. A. Corma, V. Fornes, V. Martines, F. Melo and O. Pallota, *Studies in Surface Science and Catalysis*, **37** (1988) 375.
36. R. A. Comelli and N. F. Figolli, *Appl. Catal.*, **36** (1988) 299.
37. P. Barteau, B. Delmon, J. L. Dallons and A. van Gysel *Appl. Catal.*, **70** (1991) 307.
38. Y. Mao and J. K. Thomas, *J. Chem. Soc. Chem. Commun.*, (1993) 1257.
39. S. Rajagopal, T. L. Grimm, D. J. Collins and R. Miranda, *J. Catal.*, **137** (1992) 453.
40. R. A. Comelli and N. F. Figolli, *React. Kinet. Catal. Lett.*, **47** (1992) 213.
41. R. J. Bonton, *J. Chem. Soc. Chem. Commun.* (1993) 1257.
42. V. Y. Borekov, A. A. Alexev and V. B. Kazansky, *J. Catal.*, **80** (1983) 462.
43. R. Snell, *Appl. Catal.*, **11** (1984) 174.
44. R. Snell, *Appl. Catal.*, **12** (1984) 189.
45. P. Yarlagadda, C. R. F. Lund and E. Ruckenstein, *J. Catal.*, **125** (1990) 421.
46. R. K. Sato, P. F. Mc Millan, P. Dennison and R. Dupree, *J. Phys. Chem.*, **95** (1991) 4483.
47. T. Sato, T. Sodesawa F. Nozaki and H. Shoji, *J. Mol. Catal.*, **66** (1991) 343.
48. T. Lopez, *React. Kinet. Catal. Lett.*, **47** (1992) 21.
49. F. Hatekayama and T. Maekawa, *J. Amer. Ceram. Soc.*, **100** (1992) 163.
50. C. Dessables, I. Biay, F. Colenda, J. F. Quinson and J. P. Reymond, *J. Non-Cryst. Solids*, **147/148** (1992) 141.
51. O. Franke, *J. Chem. Soc. Chem. Commun.*, (1993) 724.
52. S. Komarneni, R. Roy, U. Selvaraj, P. Malla and E. Brevel, *J. Mater. Res.*, **8** (1993) 3163
53. M. Toba, F. Mizukami, S. Niwa, T. Sano, K. Maeda and H. Shoji, *J. Mater. Res.*, **4** (1994) 1131.
54. A. Keshavaraja, S. G. Hegde and A. V. Ramaswamy, (Submitted for publication)
55. A. Keshavaraja, V. Ramaswamy, H. S. Soni, A. V. Ramaswamy and P. Ratnasamy, *J. Catal.*, **157** (1995) 501.
56. A. Keshavaraja, S. G. Hegde and A. V. Ramaswamy, *J. Catal.*, (submitted for publication).
57. E. P. Barrett, L. G. Joyner, and P. P. Halenda, *J. Amer. Chem. Soc.*, **73** (1951) 373.
58. G. Horwath and K. Kawazoe, *J. Chem. Eng. Jpn.*, **16** (1983) 470.

59. J. Fricke and A. Emmerling in "Structure and Bonding"- 77, R. Reisfeld (Ed) p - 38, Springer Verlag, Budapest, 1992.
60. D. C. Dutoit, M. Schneider and A. Baiker, *J. Catal.*, **153** (1995) 165.
61. M. Galon-Feres, R. Mariscal, L. J. Alemany, J. L. G. Fierro and J. A. Anderson, *J. Chem. Soc. Farad. Trans.*, **90** (1994) 3711.
62. M. Galon-Feres, L. J. Alemany, R. Mariscal, M. A. Benares, J. A. Anderson and J. L. G. Fierro, *Chem. Mater.*, **7** (1995) 1342.
63. Z. Liu and R. J. Davis, *J. Phys. Chem.* **98** (1994) 1253.
64. P. A. Jacobs in "Selective Oxidation in petrochemistry", Proc. Of DGMK Conf, 192, p-171.
65. I. M. M. Salvado and J. M. F. Novoro, *J. Non-Cryst. Solids*, **147** (1992) 256.
66. U. Brautigam, K. Meyer and H. Burger, in "Eurogel 91", Vilminet *et al* (Ed), Elsevier, Amsterdam (1992) p-335.
67. M. Beghi, P. Chiurlo, L. Casta, M. Palladino and M. F. Pirini, *J. Non-Cryst. Solids*, **145** (1992) 175.
68. M. Srinivasan, A. K. Datye and M. H. Smith and C. H. F. Peden, *J. Catal.*, **145** (1994) 565.
69. J. S. Reddy, R. Kumar and P. Ratnasamy, *Appl. Catal.*, **58** (1990) L1.
70. P. R. H. P. Rao, A. A. Belhekar, S. G. Hegde, A. V. Ramaswamy and P. Ratnasamy, *J. Catal.*, **141** (1993) 595.
71. E. P. Parrey, *J. Catal.*, **2** (1963) 371.
72. Z. Liu, J. Dobra and R. Davis, *J. Catal.*, **149** (1994) 117.
73. G. Deo, A. M. Turek, I. E. Waches, D. R. Huybrechts and P. A. Jacobs, *Zeolites*, **13** (1993) 365.
74. K. Tanabe, in "New solid acids and bases" K. Tanabe, M. Misono, Y. Ono, H. Hattori (Eds), Kodansha and Elsevier, Tokyo, Vol 51, Chapter 3.
75. H. Schmidt in "Structure and Bonding - 77", R. Reisfeld (Ed), p-119, Springer Verlag, 1992.
76. A. Thangaraj, R. Kumar, S. P. Mirajkar and P. Ratnasamy, *J. Catal.*, **143** (1993) 273.
77. P. Ratnasamy and A. J. Leonard, *Catal. Rev.* **6** (1972) 293.
78. Ramesh Reddy, A. V. Ramaswamy and P. Ratnasamy, *J. Catal.*, **143** (1993) 273.
79. S. Imamura, S. Ishida, H. Tarumoto and Y. Sato, *J. Chem. Soc. Farad. Trans.*, **89** (1993) 757.
80. Y. Saito, *J. Phys. Soc. Jpn.*, **53** (1994) 4230.
81. S. M. Mukhopadhyay and S. H. Garofalini, *J. Non-Cryst. Solids*, **107** (1988) 65.
82. A. B. Rosenthal and S. H. Garofalini, *J. Non-Cryst. Solids*, **107** (1988) 65.
83. K. Kusabarak, *J. Non-Cryst. Solids*, **95,96** (1987) 411.
84. Hanase, T., Aikawa, T., and Saga, N., *J. Amer. Ceram. Soc.*, **67**, 52 (1984).
85. Boccuti, A.R., Rao, K.M., Zecchina, A., and Leofanti, G., *Stud. Surf. Sci. Catal.*, **48**, 133 (1988).
86. Huybrechts, D.R.C., Buskans, P.L., and Jacobs, P.A., *J. Mol. Catal.*, **71**, 129 (1992)

87. Deo, G., Turek, A.M., Wachs, I.E., Huybrechts, D.R.C., and Jacobs, P.A., *Zeolites*, 13, 365 (1993).
88. Srinivasan, S., Datye, A.K., Hampden-Smith, M., Wachs, I.E., Deo, G., Jehng, J.M., Turek, A.M., and Peden, C.H.F., *J. Catal.*, 131, 260 (1991).
89. Fripiat, J.J., Leonard, A., and Barake, N., *Bull. Soc. Chem. France*, 122 (1963)
90. Blasco, T., Cambor, M.A., Corma, A., and Perez-Pariente, J., *J. Am. Chem. Soc.*, 115, 11806 (1993).
91. A. Thangaraj, R. Kumar and P. Ratnasamy, *J. Catal.*, 131 (1991) 294.
92. P. R. Hari Prasad Rao, A. A. Belhekar, S. G. Hegde, A. V. Ramaswamy and P. Ratnasamy, *J. Catal.*, 141 (1993) 595.
93. Hari Prasad Rao, P.R., Ramesh Reddy, K., Ramaswamy, A.V., and Ratnasamy, *Stud. Surf. Sci. Catal*, 78 (1993) 385.
94. A. V. Ramaswamy, S. Sivasanker and P. Ratnasamy, *Microporous Materials*, 2 (1994) 451.
95. T. Kakatoka and J. A. Dumesic, *J. Catal.*, 112 (1988) 66.
96. D. Chen, S. Sharma, N. C. Martinez, J. A. Dumesic, V. A. Bell, G. D. Hodge and R. Madon, *J. Catal.*, 136 (1992) 392.
97. D. J. Collins, C. B. Quiery, J. E. Fertig and B. H. Davis, *Appl. Catal.*, 28 (1986) 35.
98. O. Rodriguez, F. Gonzalez, P. Bosch, M. Portilla and T. Viveros, *Catal. Today*, 14 (1992) 243.
99. S. Brunauer, P. H. Emmett and E. Teller, *J. Amer. Chem. Soc.*, 60 (1938) 309.
100. E. Dollimore and G. R. Heal, *J. Appl. Chem.*, 14 (1964) 109.
101. C. Y. Chen, H. X. Li and M. Davis, *Microporous Mater.*, 2 (1995) 27.
102. C. Doremieux-morin, C. Martin, J. M. Breocault, J. Fraissard, *Appl. Catal.*, 77 (1991) 149.
103. F. Hatakayama and T. Maekawa, *J. Ceram. Soc. Jpn.*, 100 (1992) 163.
104. B. Yoldas, *J. Non-cryst. Solids*, 83 (1986), 375.
105. H. C. Kung and H. H. Kung, *Catal. Rev. Sci. Eng.*, 27 (1985) 425.
106. Tanabe, K., in J. R. Anderson, and M. Boudart, (Eds.), *Catal. Sci. And Technol.*, Vol-2, Springer - Verlag, Berlin, 1981, p-231.
107. G. Conneli, J. A. Dumesic, *J. Catal.*, 102 (1986) 216.
108. M. L. Poutsma, in J. Rabo Ed., *Zeolite Chemistry and Catalysis* (ACS Monograph No. 171), (1976) 437.
109. J. A. Martens, J. P. Pariente, E. Sastre, A. Corma and P. A. Jacobs, *Appl. Catal.*, 45 (1988) 85.

## CHAPTER - SIX

### Summary

---

*Over all summary of the thesis is presented in this chapter.*

The present thesis gives an account of preparation, characterization and catalytic applications of a variety of mixed metal oxide catalysts.

In the *first chapter* salient features of catalyst development with particular emphasis on mixed metal oxide catalysts are discussed. The scope and objectives of the present thesis is also briefly mentioned.

The *chapter two*, is a brief compilation of various experimental techniques used in the present study. It includes X-ray diffraction, X-ray scattering, X-ray fluorescence, X-ray photoelectron spectroscopy, UV-vis, FTIR, laser Raman, NMR, SEM, TEM, N<sub>2</sub> adsorption studies, TG-DTA, TPR, particle size analysis, gas chromatography and reaction techniques.

In the *chapter three* a comparative study of crystalline stabilized zirconia catalysts with different dopants is made. Solid solutions of zirconia with various amounts of Mn-oxide are prepared by the co-precipitation method. X-ray diffraction data indicate the formation of cubic phase with fluorite type structure which is further confirmed by FTIR and Raman studies. In addition, XPS and cyclic voltammetric studies demonstrate the redox ability of these catalysts. Their application as a complete oxidation catalysts is then established by n-butane and carbon monoxide oxidation reactions. Similarly, other 3d-transition metal oxides such as oxides of Cr, Fe, Co and Ni are also used for stabilizing zirconia and their efficacy as complete oxidation catalysts is illustrated.

*Chapter four* pertains to application of sol-gel method of preparation for the development of industrial hydrogenation catalysts. Accordingly, copper metal supported on silica is prepared by sol-gel method and is compared with that of co-

2/10  
me

precipitated catalyst. The distinct advantages offered by sol-gel method is illustrated in terms of surface area, crystallite size and metal area of the Cu-silica catalysts which is further reflected in their efficient role as hydrogenation catalysts. The observed activity and improved life of the catalyst in the hydrogenation of nitrobenzene and dehydrogenation of secondary butyl alcohol is explained through the *restricted grain growth model*.

In chapter five, the influence of the pH of the preparation on the sol-gel derived titanosilicates is investigated using SEM, N<sub>2</sub> adsorption, UV-visible and FTIR spectroscopic studies. Surface area and pore size distributions are largely dependent on the pH prevailing during the preparation. FTIR spectra of adsorbed pyridine and UV-vis studies indicate that the sample prepared under neutral conditions tend to form Si-O-Ti linkages most efficiently. Accordingly, the titanosilicate samples with different Si/Ti ratio are prepared at neutral pH in the absence of nitrogenated organic bases and named as micro-mesoporous amorphous titanosilicates. The unique property of this catalyst in the oxidation of phenol in presence of H<sub>2</sub>O<sub>2</sub>, with selective formation of catachol is interesting. Similarly, it could oxidize toluene to give relatively more amount of benzaldehyde.

Another system studied in chapter five is the amorphous aluminosilicates prepared by sol-gel method at neutral and basic conditions. FTIR and gravimetric sorption studies indicate that the aluminosilicates prepared under neutral conditions is more acidic as reflected in its activity in the isomerization and disproportionation of 1,3,5-trimethyl benzene. A relationship is established between the selectivity and acidity of these type of catalysts. This is explained in terms of the mutual relation

between Lewis acidity/Bronsted acidity ratio and Isomerization/Disproportionation values. Following conclusions can be drawn from the present study.

### **Conclusions:**

- Co-precipitation as mixed hydroxides followed by calcination at 773 K is a convenient route for crystallizing active elements such as Mn, Cr, Fe, Co or Ni in multiple valence, as solid solutions in the lattice of zirconia. The stabilized zirconia formed thus, has high surface area ( $\sim 80 - 120 \text{ m}^2 \text{ g}^{-1}$ ), and resist sintering. The enhanced redox ability of these materials as demonstrated by various techniques is further manifested in the catalysis of complete oxidation of n-butane and carbon monoxide. The superiority of these fluorite based oxides over the known oxidation catalysts as demonstrated by the low temperature oxidation (100 % conversion of CO at about 473 K) is due oxygen ion vacancies, and the reducibility of the active transition element.
- Sol-gel technique is an appropriate method for the preparation of supported copper catalysts due to the possibility of decreasing crystallite size (50 Å in contrast to above 80 Å of co-precipitated samples). This is further corroborated by their application in the hydrogenation of nitro benzene and dehydrogenation of secondary butyl alcohols. The predominance of the sol-gel derived supported copper over their conventional counterparts is illustrated in terms of enhanced activity, improved selectivity and sustainable life. These improvements can be explained in terms of restricted grain growth model.
- Yet another advantage of sol-gel method is elucidated by amorphous titanosilicates prepared at various pH. Among a series of samples prepared, one prepared under neutral condition is shown to be better with respect of

Si-O-Ti linkages, surface area and pore size distribution. Their utility is for the oxidation/hydroxylation of benzene, phenol and toluene. Phenol was converted to the extent of 91 % with  $H_2O_2$  efficiency of more than 90 %, whereas, the oxidation of toluene resulted in the formation of benzaldehyde to a major extent (~ 40 %). Similarly, when aluminosilicates are prepared under neutral conditions by sol-gel route, they gain dominating edge with respect to acidity over the conventionally prepared catalysts as illustrated by their activity in the isomerization and disproportionation of 1,3,5-trimethylbenzene. Supremacy of the sol-gel derived metallosilicates is mainly due to the site isolation.



# Publications

1. An yttrium based strong Lewis acid catalysts for the heterogeneous catalysis of Diels-Alder reactions.  
A. Keshavaraja, V. R. Hegde, B. Pandey, A. V. Ramaswamy, P. Kumar, and T. Ravindranathan, *Angew. Chem. Int. Ed. Engl.* **34** (19) (1995) 2143-2144.
2. Preparation and characterization of novel micro-mesoporous titanosilicates.  
A. Keshavaraja, V. Ramaswamy, H. S. Soni, A. V. Ramaswamy and P. Ratnasamy, *J. Catal.*, **527** (1995) 501-511.
3. Low temperature stabilization of zirconia by Mn through co-precipitated hydroxide gel route.  
A. Keshavaraja and A. V. Ramaswamy,  
*J. Mater. Res.*, **9** (1994) 837-840
4. Thermal decomposition of co-precipitated oxide hydrates of zirconium and manganese.  
A. Keshavaraja, N. E. Jacob, and A. V. Ramaswamy,  
*Thermochim. Acta*, **254** (1995) 267-275.
5. 3d-Transition metal oxide -stabilized zirconia as novel catalysts for complete oxidation of hydrocarbons.  
A. Keshavaraja and A. V. Ramaswamy,  
*J. Chem. Soc. Chem. Commun.*, (in press).
6. Mn-stabilized zirconia catalysts for complete oxidation of n-butane.  
A. Keshavaraja and A. V. Ramaswamy,  
*Appl. Catal.(B) Environmental*, (in press).
7. A comparative study of LaCoO<sub>3</sub> prepared by various wet chemical methods.  
A. Keshavaraja and A. V. Ramaswamy,  
*Ind. J. Engg. Mater. Sci.*, (1994) 229-236 .
8. Effect of surface modification due to superacid species in controlling the sensitivity and selectivity of SnO<sub>2</sub> gas sensors.  
Keshavaraja, B. S. Jayashri, A. V. Ramaswamy and K. Vijayamohan, *Sensors and Actuators*, **21** (1995) 75-81.
9. Use of solid superacid as efficient catalyst in the facile trans esterification of ketoesters.  
S. P. Chavan, P. K. Zubaidha, S. W. Dantale, A. Keshavaraja, A. V. Ramaswamy and T. Ravindranathan.  
*Tetrahedron Letters*, **37** (1996) 233-236.
10. Facile deprotection of allylestere mediated by solid superacid (sulfated SnO<sub>2</sub>).  
S. P. Chavan, P. K. Zubaidha, S. W. Dantale, A. Keshavaraja, A. V. Ramaswamy and T. Ravindranathan, *Tetrahedron Letters*, **37** (1996) 237.
11. Efficient synthesis of acetals promoted by yttrium based strong Lewis acid catalysts.  
G. C. G. Pais, A. Keshavaraja, K. Saravanan and P. Kumar,  
*J. Chem. Res.*, (accepted).

12. Yttrium based strong Lewis acid catalysts for silylation of alcohols with 1,1,1,3,3,3-hexamethyldisilazane.  
P. Kumar, G. C. G. Pais and A. Keshavaraja,  
*J. Chem. Res.*, (accepted)
13. A better Technology for LAB from NCL.  
A. Keshavaraja and K. R. Srinivasan,  
*Chem. Ind. Digest.*, 1995.
14. Thermal characterization of mixed phase precursors of La and Co in the formation of  $\text{LaCoO}_3$ .  
A. Keshavaraja and A. V. Ramaswamy,  
Thermal Analysis, Proceedings of the 9<sup>th</sup> National Symposium on Thermal Analysis, Indian Thermal Analysis Society, at Goa, 1993.
15. Mechanistic features of novel Mn-stabilized zirconia in catalytic oxidation of CO.  
A. Keshavaraja, K. Vijayamohan and A. V. Ramaswamy,  
in N. M. Gupta and D. K. Chakraborty, (Eds), Catalysis : Modern Trends, Proceedings of the 12<sup>th</sup> National Symposium on Catalysis, Catalysis Society of India, Bombay, 1994.
16. Sol-gel Technology for catalyst synthesis.  
A. Keshavaraja,  
*Bull. Catalysis Soc. India*, Jan (1996) 3.
17. Amorphous aluminosilicates prepared by sol-gel method under neutral and basic pH.  
A. Keshavaraja, S. G. Hegde and A. V. Ramaswamy,  
*J. Catal.* (submitted)
18. Mn-Stabilized zirconia for complete oxidation of carbon monoxide.  
A. Keshavaraja, S. P. Katdare and A. V. Ramaswamy,  
*Appl. Catal. (B) Environmental*, (to be communicated).

#### Papers presented at Symposia/Conferences.

1. The effect of A-site substitution in  $\text{LaCoO}_3$  in the  $\text{H}_2\text{O}_2$  decomposition activity.  
A. Keshavaraja and A. V. Ramaswamy,  
Presented at 11<sup>th</sup> National Symposium on catalysis, Catalysis Society of India, at Hyderabad, 1993.
2. Novel silica and zirconia based metal oxides : Preparation, characterization and catalytic applications.  
A. Keshavaraja,  
Presented at 12<sup>th</sup> National Symposium on Catalysis, Catalysis Society of India, at Bombay, 1994.
3. Fluorite type oxide catalysts for complete oxidation of CO.  
A. Keshavaraja, S. P. Katdare and A. V. Ramaswamy,  
National Workshop on Catalysis, Bhavanagar, India, 1995.

4. Solid super acids as efficient catalysts in facile transesterification of ketoesters.  
S. P. Chavan, P. K. Zubaidha, S. W. Dantale, A. Keshavaraja and T. Ravindranathan,  
Presented at 10<sup>th</sup> International Conference on Organic Synthesis, Bangalore, 1994.
5. Yttrium supported strong Lewis acid catalysts for acceleration of Diels-Alder reaction.  
V. R. Hegde, A. Keshavaraja, B. Pandey, P. Kumar and T. Ravindranathan,  
Presented in the 10<sup>th</sup> International Conference on Organic Synthesis, (IUPAC) Bangalore,  
India, Dec. 1994.
6. On the development of fluorite based metal oxide catalysts for the abatement of  
autoexhaust emission.  
A. Keshavaraja,  
Young Scientist Award Lecture at the 83<sup>rd</sup> Indian Science Congress, Patiala, 1996.

## Patents

1. An improved process for the surface modification of semiconducting metal oxides for use  
as gas sensors.  
A. Keshavaraja, K. Vijayamohan and A. V. Ramaswamy,  
Indian Patent 642/DEL/94.
2. A process for the complete oxidation of hydrocarbons and carbon monoxide.  
A. Keshavaraja, P. Ganguly, A. V. Ramaswamy and I. S. Mulla,  
Indian Patent NF-76/94.
3. An improved process for the preparation of partially stabilized zirconia with high surface  
area useful in oxidation reactions.  
A. Keshavaraja, A. V. Ramaswamy and V. Ramaswamy,  
Indian Patent 629/DEL/94.
4. An improved process for the preparation of Copper-silica catalysts  
A. Keshavaraja and A. V. Ramaswamy,  
Indian Patent, 1260/DEL/94.
5. An improved process for the preparation of aniline from nitrobenzene using an improved  
copper-silica catalysts.  
A. Keshavaraja and A. V. Ramaswamy,  
Indian Patent, 1725/DEL/94
6. An improved process for the dehydrogenation of secondary butyl alcohol to methyl ethyl  
ketone using an improved copper-silica catalysts.  
A. Keshavaraja, J. V. Samuel, and A. V. Ramaswamy,  
Indian Patent, NF 175/94.
7. A process for the preparation of micro-mesoporous amorphous titanosilicates.  
A. Keshavaraja, V. Ramaswamy, A. V. Ramaswamy and P. Ratnasamy,  
Indian Patent, 1508/DEL/95.
8. A process for the preparation of micro-mesoporous amorphous titanosilicates.  
A. Keshavaraja, V. Ramaswamy, A. V. Ramaswamy and P. Ratnasamy,  
US Patent, 08/510,574, 1995.

9. An improved process for the selective oxidation of hydrocarbons.  
A. Keshavaraja, A. V. Ramaswamy and P. Ratnasamy,  
Indian Patent 1722/DEL/95
10. An improved process for the selective oxidation of hydrocarbons.  
A. Keshavaraja, A. V. Ramaswamy and P. Ratnasamy,  
US Patent, 08/510,291, 1995.
11. A process for the preparation of sulphated mixed metal oxides.  
A. Keshavaraja, S. G. Hegde and A. V. Ramaswamy,  
Indian Patent, NF 175/95
12. A process for the transesterification of ketoesters using solid acids.  
A. Keshavaraja, A. V. Ramaswamy, S. W. Dantale, S. P. Chavan and T.  
Ravindranathan,  
Indian Patent, NF 176/95.
13. An improved process for the C-C bond forming reactions using solid acids as catalysts.  
A. Keshavaraja, A. V. Ramaswamy, V. R. Hegde, P. Kumar and T. Ravindranathan,  
Indian Patent, NF 177/95.
14. An improved process for the preparation of zirconia based catalyst composites with fluorite type structure.  
A. Keshavaraja, P. Ganguly and A. V. Ramaswamy, (Indian Patent, Filed)
15. An improved process for the complete oxidation of carbon monoxide using partially stabilized zirconia catalysts.  
A. Keshavaraja, S. P. Katdare and A. V. Ramaswamy, (Indian Patent, Filed)